The Effects of Overprinting on Isotopic Ages and Rock Fabrics: The Lewisian Gneiss Complex as a Case Study

Thesis submitted in accordance with the requirements of the University of Liverpool for the degree of Doctor in Philosophy by

John Murdoch MacDonald

September 2012

Abstract

Zircon is a key mineral in understanding tectonothermal overprinting in metagranitoid rocks of the continental crust, principally through radiometric dating. Exposed examples of such rocks are often Precambrian in age and have undergone multiple tectonothermal events. This thesis aims to understand the overprinting effects of deformation and metamorphism in multiple tectonothermal events on zircon, using the Precambrian Lewisian Gneiss Complex (LGC) of Northwest Scotland as a case study.

Deformation of zircon at the grain-scale, in the form of distortion of the crystal lattice, was found to heterogeneously affect Ti, Rare Earth Elements (REEs) and U-Pb systematics. Ti and REE abundances increased or decreased as dislocation planes caused by distortion enabled diffusion of elements in or out of the crystal lattice. Pb isotopes were also lost, resulting in discordant young ages relative to undistorted zircon. Zircons with lattice distortion may therefore record information about tectonothermal events not recorded in undistorted zircon.

Investigating the effects of multiple metamorphic episodes on zircons from the LGC revealed that different metamorphic events could not be reliably distinguished due to the occurrence of volume diffusion of Pb. A ~600Ma concordant age spread was interpreted to have been caused by volume diffusion; all other possible explanations were eliminated and age patterns from individual zircon crystals supported this hypothesis. Volume diffusion would have required ~3-500Myr at temperatures of 875-975°C.

As well as these more generic findings about the effects of overprinting on zircon, zircon U-Th-Pb, REE and Ti data were analysed to investigate meta-igneous gneisses and metasediments of the Assynt Terrane, a key part of the LGC. The oldest cores yield a mean age of 2958±7Ma, a possible magmatic protolith crystallisation age but volume diffusion of Pb in zircon may have affected these zircon core ages. The period of volume diffusion of Pb in zircon is interpreted to have ended at ~2482Ma with the peak of granulite-facies metamorphism shortly before this. Zircons in the metasediments have relatively flat chondrite-normalised heavy REE profiles (low Yb/Gd ratios) which suggest they equilibrated with granulite-facies metamorphic garnet. Ti-in-zircon thermometry records average crystallisation temperatures of 790°C for zircons from the magmatic protolith to the meta-igneous gneisses and 823°C for zircons from the metasediment. The zircons in the metasediments are interpreted to be detrital and the calculated temperatures are interpreted to record zircon crystallisation in a currently unknown protolith.

Acknowledgements

Firstly thanks to my many supervisors: Simon Harley, University of Edinburgh for help and advice with the ion microprobe and various geochemical and geochronological discussion; Quentin Crowley, Trinity College, Dublin for lots of discussion on geochronological data; Kathryn Goodenough, British Geological Survey for help on the field side as well as her ability to tease out the main points from my confused writing!; Elisabetta Mariani, University of Liverpool for microstructural advice and latterly to Dan Tatham who stepped in; and of course to John Wheeler, University of Liverpool who was the main man and whose desire to understand the Lewisian was the starting point for this project. Thanks also to Eddie, Carmel, Dave P and Dan T for help with those troublesome SEMs while Mark, Dave M and many others helped me to settle in and to get me going with the work.

It's not just been work though. I've played sport with lots of people in Liverpool: Willem and Chris for tennis; Andy, Katrien and Ludo for badminton; Ceri's Soccer School, Armo, Oshaine and all the other football lads; and latterly Paddy and Rhodri for squash. Thanks to all those who came hillwalking: Rhodri, Goz, Jutley, Paddy, Gemma, Megan & James, Kirstie and Tash.

Liverpool also saw a pick-up in my bagpiping and may thanks to all those in the Wirral Pipe Band who I had a great time with, whether competing, doing a gig or just at Wednesday practice.

A big thanks too to all those in the department who were around for tea break (Kirstie), Boswell lunch and pub on a Friday (and other days!). Particularly to Tash, Paddy, Gem & Gem, Vic and Jutley, the original RCA.

And to my parents whose love of the outdoors got me into geology in the first place, without which this work would never have been done.

Contents

List of Figures

List of Tables

1. Introduction

Definitions and Importance

Radiometric dating is crucial to understanding the evolution of Precambrian high grade metamorphic regions, where meta-igneous rocks dominate and relict metasediments are unfossiliferous. Such regions can have complicated histories including protolith igneous rocks of various ages as well as multiple tectonothermal (metamorphism and/or deformation) events, each 'overprinting' previous mineral assemblages and structures. It is important to understand these rocks and their history as they may be a window into the evolution of the early Earth and a possible analogue for current processes in the lower continental crust. Zircon is the key mineral chronometer in understanding high-grade Precambrian complexes and has several attributes desirable for recording complex high-grade tectonothermal histories:

- it is widespread in the dominant metagranitoid rocks
- it incorporates a range of trace elements and their isotopes in its crystal lattice which record aspects of the geological history
- it is a relatively mechanically- and chemically-durable mineral so can often partially withstand high-grade tectonothermal activity and retain pre-existing element and isotopic compositions; a high enough grade of tectonothermal event will often also be recorded in the resetting of part of the existing zircon or growth of some new zircon

The trace elements incorporated allow a range of interpretations to be made about the zircon and its host rock. The U^{4+} cation can occupy the Zr site in the zircon lattice while Pb is largely excluded due to its incompatible charge and ionic radius. With little Pb present on crystallisation, most of the Pb present is radiogenic daughter Pb isotopes from the decay of the radioactive U; measurement of ratios of U and Pb isotopes allows calculation of a radiometric age (e.g. Davis et al., 2003; Ireland and Williams, 2003; Kosler and Sylvester,

2003; Parrish and Noble, 2003). As well as its importance for radiometric dating, zircon incorporates a range of other trace elements which allow for other interpretations of the geological history. These include: Ti which is proportional to crystallisation temperature depending on rutile activity (Watson et al., 2006); Lu-Hf which can be used to infer the origin of the source melt and to calculate melt extraction model ages (Kinny and Maas, 2003); and Rare Earth Elements (REEs) which can be used to distinguish crystal zones of different age (Whitehouse and Kamber, 2003) and link them to major phases such as garnet which also sequester REEs (Kelly et al., 2006; Taylor et al., 2007). Isotopes of oxygen may also be used to infer the origin of the melt (Valley, 2003).

Zircon is therefore a key mineral in understanding many rock types, including Precambrian meta-igneous complexes. Radiometric dating has been a major step forward in building a chronology of large- and small-scale geological events in the Precambrian, while the insights from other trace elements in zircon has supplemented the picture and can support and inform interpretation of radiometric ages.

The Problem

In Precambrian meta-igneous complexes which have undergone high temperature metamorphism and high strain deformation (often on multiple occasions), zircon evolves in multifaceted ways to the changing conditions. Metamorphism and deformation are often heterogeneous in their intensity and distribution and zircon may respond heterogeneously via a range of mechanisms with different geochemical characteristics. This results in a complex record of zircon U-Pb ages, which do not clearly relate to the relative chronology constructed from mineral assemblages and structures observed in the field. The rocks for this case study, the Lewisian Gneiss Complex (LGC) of northwest Scotland, are a good example of the difficulty of interpretation of radiometric age patterns (e.g. Kinny et al., 2005; Park, 2005 and references therein; Corfu, 2007).

The Aims

The overall aim of this PhD is to undertake a detailed and systematic characterisation of the response of zircon to overprinting by metamorphism and deformation. Under this, there are both process- and regionally-motivated objectives:

- a generic understanding of how radiometric ages and other geochemical systems in zircon are affected by multiple episodes and varying intensities of metamorphism and deformation i.e. process-motivated
- a better understanding of the formation and evolution of the case study rocks, the Lewisian Gneiss Complex, through geological mapping, petrography, microstructure and element/isotope zircon measurements i.e. regionally-motivated

The first of these objectives will be addressed by obtaining a suite of element and isotope measurements from zircons from samples that have been carefully characterised by detailed field mapping, petrography and microstructural analysis so as to provide a clear framework on which to base zircon interpretations. This framework will show the metamorphic and deformation history of the host rocks, which will be the context for examining the effects of overprinting on zircon. Detailed examination of the different zircon response mechanisms and their geochemical characteristics will be made and linked to the tectonothermal context. To what extent does metamorphism have an effect on the zircons and how do they respond to more than one episode of elevated temperature? How does deformation at the grain-scale affect zircon? These questions will be asked in tackling this process-motivated objective.

The second objective has arisen from a desire to understand the host rocks of the LGC better. Despite many field, geochemical and geochronological studies, the geological history of this classic Precambrian high-grade region remains unclear. Radiometric dating of zircon (Friend and Kinny, 1995; Kinny and Friend, 1997; Friend and Kinny, 2001; Kinny et al., 2005; Friend et al., 2007; Love et al., 2010) has challenged the traditional structural and

metamorphic interpretation (Sutton and Watson, 1951) and continues to generate lively debate (e.g. Park et al., 2005). It is hoped that combining radiometric zircon dating with field, geochemical, petrographic and microstructural constraints, and supporting evidence from other trace elements in zircon, in this project will improve understanding of the tectonothermal evolution of the LGC.

The Location

The rocks of the Lewisian Gneiss Complex (LGC) of northwest Scotland are the case study for this project and are reviewed in detail in Chapter 2.2. The protolith was dominantly a tonalite-trondhjemite-granodiorite (TTG) suite, with minor mafic and sedimentary rocks. In the TTG gneisses, the oldest mineral assemblage is a granulite-facies assemblage, termed the Badcallian (Park, 1970), of orthopyroxene, clinopyroxene, plagioclase and quartz (Sutton and Watson, 1951) with gneissic layering and granoblastic texture; it is unclear whether this is simply the same as the original TTG mineralogy or was formed during a granulite-facies tectonothermal event. It is only preserved in part of the LGC and there is no evidence for it in the majority of the complex. An age of either ~2730Ma (Corfu et al., 1994) or ~2490Ma (Friend and Kinny, 1995; Kinny and Friend, 1997) has been assigned to this assemblage based on U-Pb zircon dating. A subsequent tectonothermal event, the Inverian (Evans, 1965), heterogeneously overprints Badcallian structures in the form of discrete shear zones up to several kilometres wide. The timing of large areas of static retrogression of orthopyroxene and clinopyroxene to hornblende is still unclear. The Inverian event has been assigned U-Pb zircon ages of either 2490Ma (Corfu et al., 1994) or 2490-2400Ma (Kinny et al., 2005). The heterogeneity of distribution and differing interpretation of zircon and monazite (Zhu et al., 1997) dates of both these two events has led to some controversy. The traditional model of Sutton and Watson (1951), based on field criteria around which later zircon U-Pb dates were fitted, invokes a single block of crust undergoing a common history with the heterogeneity in distribution of assemblages and structures of

each event being attributed to different levels of the crust. A more recent interpretation, based mainly on the heterogeneity of zircon dates across the complex, has suggested that the LGC comprises many disparate terranes with different tectonothermal histories (Kinny et al., 2005). Following the Inverian event, there was an episode of mafic dyke intrusion (the Scourie dykes) and another amphibolite-facies tectonothermal event, termed the Laxfordian (Sutton and Watson, 1951), which overprinted much of the exposed LGC. The Scourie dykes and Laxfordian are common to the whole complex but the distribution of the earlier events and the terrane hypothesis are still disputed.

Thesis Structure

This thesis is structured around three distinct but interlinked manuscripts (chapters 5-7) which address the aims outlined above. These manuscripts have been or will be submitted to internationally-recognised peer-review journals and as there are common themes between the three manuscripts, there are overlaps in content including geological background and methodology. In this thesis, these manuscripts have figures and tables embedded in the text but are otherwise formatted for journal submission. Each of the three manuscripts contains only a brief description of the geological setting, methodology employed and sample petrography, which are largely the same or at least overlapping, as the focus of each manuscript is on zircon. Not all samples and not all analytical techniques were necessarily used in each of the three manuscripts. As a result, there are dedicated chapters comprehensively describing: the geological setting (chapter 2b); all methodologies deployed in sample characterisation and in the manuscripts (chapter 3); and detailed characterisation of all samples from which zircons were analysed in each manuscript (chapter 4). Chapter 8 synthesises the themes from the three manuscripts and suggests further work. As there are common themes running through all chapters, references are frequently used in more than one chapter. As a result, references from all chapters and collated in a single list at the end.

A brief synopsis of each chapter is now given:

Chapter 2: *Reviews.* This chapter is split in two parts, the first reviewing the properties and geological applications of the mineral zircon, and the second reviewing the rocks which have been used a case study for the investigations carried out during the PhD.

Chapter 3: *Methodology.* A wide range of methods has been deployed ranging from geological field mapping through to micro-beam isotope analysis. Each technique is described in much more detail than is required for peer-review publication so as to provide a more thorough account of the analytical techniques used than that which is given in the manuscript chapters.

Chapter 4: *Sample Characterisation.* This chapter is split into three parts: the first gives detailed descriptions of the field localities and the petrography of samples taken from them which have been analysed; the second part analyses the whole-rock and mineral chemistry of these samples; and the third part discuss the heterogeneity of the rocks of the Lewisian Gneiss Complex and the representativeness of the samples.

Chapter 5: *The Effects of Crystal Lattice Distortion on Trace Element Mobility and U-Pb Isotope Systematics in Zircon: Examples from the Lewisian Gneiss Complex, Northwest Scotland.* This manuscript investigates the effects of crystal lattice distortion on a population of zircons as would typically be used in a geochronological/geochemical study. Electron backscatter diffraction (EBSD) analysis identified crystal lattice distortion in a small but significant percentage of zircons in the population. This was found to disturb U-Pb, REE and Ti geochemical systems heterogeneously. Weighted Burgers vectors (WBV) analysis suggested that the lattice distortion formed either during crystallisation of the zircons or through post-crystallisation plastic deformation. U-Pb data suggests that distorted zircons

could be used to approximately date amphibolite-facies tectonothermal activity not recorded by undistorted zircons.

Chapter 6: *Volume Diffusion of Pb in Zircons from the Lewisian Gneiss Complex, Northwest Scotland*. Evidence is presented for the occurrence of volume diffusion of Pb in zircons, a phenomenon generally regarded as impossible in normal crustal conditions. Other possible explanations for a spread of concordant U-Pb ages are eliminated and the age and chemical zoning patterns of individual grains are used to illustrate the occurrence of volume diffusion.

Chapter 7: *New Insights on the Assynt Terrane of the Lewisian Gneiss Complex of NW Scotland from Zircon U-Th-Pb, REEs and Ti-Thermometry.* This manuscript brings together the zircon U-Th-Pb, rare earth element (REE) and Ti data collected during the PhD and applies it in a regional context. Volume diffusion of Pb in zircon (see chapter 6) renders protolith and metamorphic ages unsafe which informs the controversy over Lewisian chronology. REEs indicate zircons in the meta-igneous gneisses were a relatively closed-system through tectonothermal activity but zircons in metasediments interacted with garnet. Ti-in-zircon thermometry is used to calculate a crystallisation temperature range for the magmatic protolith.

Chapter 8: *Synthesis and Further Work*. The final chapter in this thesis summarises the main points from the manuscripts in Chapters 5-7 in the context of the initial thesis aims. Although advances in understanding have been made through the work presented here, it has inevitably raised further questions which could not be addressed due to the time constraints of a PhD. Some such points are discussed in this final chapter.

Manuscript Status

The manuscripts for submission to peer-review journals are listed below along with the authors and their contributions and the status of the manuscript at the time of thesis submission.

The Effects of Crystal Lattice Distortion on Trace Element Mobility and U-Pb Isotope Systematics in Zircon: Examples from the Lewisian Gneiss Complex, Northwest Scotland (Chapter 5) has been submitted to Contributions to Mineralogy and Petrology and has been peer-reviewed. Reviewers' comments are currently being acted upon prior to publication.

John MacDonald – data collection and processing, interpretation and discussion of data, principal author

John Wheeler – Burgers vectors modelling, discussion and manuscript review

Kathryn Goodenough – discussion and manuscript review

Quentin Crowley – discussion and manuscript review

Simon Harley – discussion and manuscript review

Elisabetta Mariani – discussion and manuscript review

Daniel Tatham – discussion and manuscript review

Volume Diffusion of Pb in Zircons from the Lewisian Gneiss Complex, Northwest Scotland (Chapter 6) will benefit from further work (modelling of Pb diffusion and possible TOFSIMS analysis), which will be carried out in future before submission to a journal (possibly Earth and Planetary Science Letters).

John MacDonald – data collection and processing, interpretation and discussion of data, principal author

John Wheeler –discussion and manuscript review

Kathryn Goodenough – discussion and manuscript review

Quentin Crowley – discussion and manuscript review

Simon Harley – discussion and manuscript review

Elisabetta Mariani – discussion and manuscript review

Daniel Tatham – discussion and manuscript review

New Insights on the Assynt Terrane of the Lewisian Gneiss Complex of NW Scotland from Zircon U-Th-Pb, REEs and Ti-Thermometry (Chapter 7) will be updated with Hf isotope data and submitted to a journal (Precambrian Research) in the near future.

John MacDonald – data collection and processing, interpretation and discussion of data, principal author

John Wheeler – discussion and manuscript review

Kathryn Goodenough – discussion and manuscript review

Quentin Crowley – discussion and manuscript review

Simon Harley – discussion and manuscript review

Elisabetta Mariani – discussion and manuscript review

Daniel Tatham – discussion and manuscript review

2. Chapter 2 – Reviews

2a: Zircon

What is Zircon and Why is it Useful?

Zircon is a tetragonal orthosilicate with the chemical formula $ZrSiO_4$ (Fig. 2.1). It is the main mineral with Zr as a structural component and is the host for significant whole-rock percentages of the elements Hf, U, Th and the REEs (Hoskin and Schaltegger, 2003). The lattice is composed of SiO_4 tetrahedra and ZrO_8 dodecahedra; the space group is $I4_1/amd$ (Finch and Hanchar, 2003). It has a hardness of 6.5 on the Mohs scale and is chemically durable in resisting volume diffusion and incorporation of trace elements which makes it an important mineral for geochronological and petrogenetic investigations of a wide range of rocks. It originates dominantly in Si-saturated igneous rocks and is recycled into, or occasionally grows in, a range of metamorphic and sedimentary rocks; it is an accessory mineral where present and although it occurs in low abundances, it is widespread.

For these reasons zircon is commonly analysed in geochronological and petrogenetic studies. Zircon chemical zoning and microstructure can be imaged in a scanning electron microscope (see chapter 3) and high-precision and high spatial-resolution geochemical and isotopic data can be obtained by a variety of methods. These techniques are discussed in detail later in this chapter.

Formation of Zircon

Zircon can form through a variety of mechanisms involving new growth or recrystallization of pre-existing zircon. Each mechanism has a range of physical and chemical characteristics, which may allow it to be distinguished; this can be important contextual information when interpreting geochemical data.

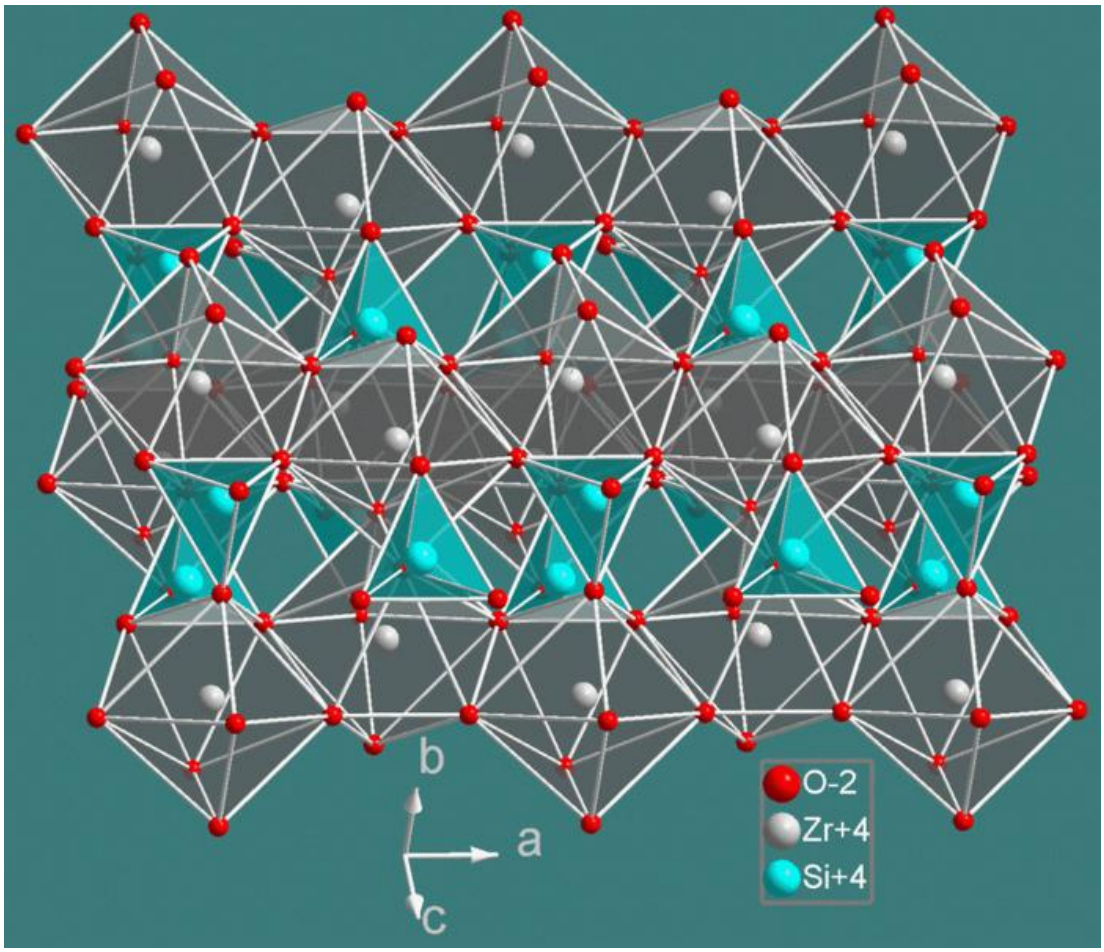

Fig. 2.1 Zircon crystallographic structure.

Magmatic Growth

Primary zircon forms from intermediate to silica-saturated magmas when these magmas reach saturation in Zr (Hoskin and Schaltegger, 2003). Primary zircon crystallisation is dependent on both the concentration of Zr in the magma, the water content and the temperature and this allows crystallisation temperatures to be calculated based on Zr saturation conditions (Hanchar and Watson, 2003). Zircon can also be resorbed in Si- and Zr-undersaturated melts and can be altered sub-solidus with changes in temperature and water content (e.g. metamorphic events). Primary magmatic zircon can be euhedral to anhedral depending on how early Zr saturation conditions are reached in the magma. Magmatic zircons usually contain internal growth zoning; this is most clearly seen in cathodoluminescence (CL) imaging (see chapter 3) where the growth zones are seen as

alternating CL-bright and CL-dark stripes, starting at the core and moving outwards, often mimicking the polygonal crystal shape. This feature is known commonly as oscillatory zoning patterns (OZPs) and is thought to form from varying Zr-saturating conditions in the magma (Vavra, 1993). Recorded U-Pb ages usually reflect the age of crystallisation of the magma, unless later thermal (lattice diffusion) or microstructural effects (brittle fracturing or plastic lattice distortion) cause radiogenic Pb to move around the crystal or be lost altogether. Magmatic zircon typically has a chondrite-normalised REE pattern of increasing abundance from light REEs to heavy REEs but with a positive Ce anomaly and negative Eu anomaly. Ce exists as a 4^+ cation (as well as as the standard 3^+ REE valency) and so more of it is incorporated into the lattice than other 3^+ cations. Eu commonly exists as a 2^+ cation, which is unsuited to the zircon lattice structure and strongly partitions into plagioclase (Hoskin and Schaltegger, 2003). Magmatic zircons with high concentrations of U can become metamict; as radioactive U decays to Pb, the lattice is strained to the extent that it loses its crystallinity and eventually become amorphous (Ewing et al., 2003). With metamictisation comes redistribution of trace elements, which renders such zircons useless for dating and other petrogenetic studies.

Anatectic Growth

Primary zircon may also grow from anatectic melts, either nucleating as a new ovoid-shaped (sometimes termed ‘soccerball’) crystal or more commonly forming as a rim around pre-existing zircon. Anatectic zircon grows when small volumes of partial melt reach Zr-saturation conditions. In CL imaging, ‘fir-tree’ or ‘sector’ zoning are common textures (Hoskin and Schaltegger, 2003). REE patterns and abundances in anatectic growth zircon are likely to be different to earlier magmatic cores and may be distinguished thus. Anatectic zircon REE patterns may alter from the typical magmatic zircon pattern depending on the other phases present when the anatectic zircon is forming. For example, it will have a flat

heavy REE pattern on a typical Matsuda plot when grown in the presence of garnet (Rubatto, 2002; Whitehouse and Platt, 2003; Kelly et al., 2006; Harley and Kelly, 2007). U-Pb ages derived from anatectic growth rims should be younger than from magmatic or inherited cores, unless some Pb-loss mechanism has occurred during the high-temperature anatexis.

Growth in Net-Transfer Reactions

Some other minerals may contain significant levels of Zr, such as baddeleyite, or are present in rocks at high modal percentages such that they contain a significant percentage of the total Zr in the whole rock. Garnet (Degeling et al., 2001), hornblende (Fraser et al., 1997), biotite (Vavra et al., 1996) and ilmenite (Bingen et al., 2001) have all been shown to contain high levels of Zr. When these minerals break down, new zircon can form in net-transfer reactions. Degeling et al. (2001) showed that when garnet, sillimanite and quartz reacted to form cordierite, the Zr in the garnet could not be incorporated into the cordierite and so was released and formed new zircon. Fraser et al. (1997) calculated that new zircon could form from net-transfer reactions involving hornblende breakdown although they did not ground-truth their models using real rocks. Bingen et al. (2001) used careful petrographic observation to show that zircon had formed from breakdown of magmatic ilmenite during granulite-facies metamorphism. These examples show that net-transfer reactions may be a significant source of new zircon growth during metamorphism.

Coupled Dissolution-Reprecipitation

Zircon can also become altered in sub-solidus conditions through recrystallization, which can occur in three different ways. Recrystallisation by coupled dissolution-reprecipitation (Geisler et al., 2007) occurs when a fluid or melt comes into contact with metastable zircon. Zircon will naturally incorporate assorted trace elements but these do not necessarily sit well in the lattice; radiogenic Pb^{2+} and trivalent REEs sitting in tetravalent

sites cause a certain degree of lattice strain while in order to achieve equilibrium the zircon must be pure zircon. Without interaction with a catalyst such as fluid or melt, the zircon is essentially metastable; but when a fluid or melt does come along, the outer parts of the zircon are able to dissolve and topotactically recrystallize. Variable amounts of trace elements diffuse out of the recrystallizing zircon so analyses of zircon rims with low REE abundances are suggestive of coupled dissolution-reprecipitation (Geisler et al., 2007). As U is also expelled, these rims are also characterised by bright CL intensity; CL often reveals irregular inward-penetrating zones as pre-existing zircon of certain composition has been preferentially dissolved.

Diffusion-Driven Recrystallization of Radiation-Damaged Zircon

Diffusion-driven recrystallization of radiation-damaged zircon (Geisler et al., 2007) is similar to coupled dissolution-reprecipitation in that it involves the metastable zircon lattice moving towards equilibrium on contact with a fluid. Decay of radioactive U and emission of alpha and beta particles causes strain in the crystal lattice, which may become slightly amorphous and effectively metastable. Contact with fluid is the catalyst that allows diffusion of ions to recover the crystallinity of the lattice, although temperature is also an important factor. Zones in which this process has occurred are characterised by irregular curved inward-penetrating zones visible in CL while pattern quality in EBSD microstructural analysis is poor reflecting amorphisation of the lattice. Chemically, formula elements such as Hf, U, REEs etc are often retained in a memory of the original zircon composition while there are also high levels of non-formula elements such as Ca, Fe, Ba and common Pb, relative to other zircon-forming mechanisms (Geisler et al., 2007).

Solid-State Recrystallisation

Solid-state recrystallization (Hoskin and Black, 2000) involves internal rearrangement of ions in the crystal lattice, again with the objective of achieving

equilibrium. Reaction fronts sweep through the crystal lattice by grain boundary migration or lattice defect diffusion and trace elements are concentrated on these reaction fronts. This mechanism is characterised by CL-bright zones (often rims) transgressing earlier zoning patterns such as OZPs; the reaction front itself is seen as a very CL-bright narrow line, which reflects the high concentrations of trace elements concentrated on that front. The recrystallized zircon behind the reaction front is closer to equilibrium than before. Recrystallisation is not always efficient, which can result in mixed U-Pb ages due to partial 'memory' of the pre-existing composition. This form of recrystallization can be isochemical but there is often some limited exchange of ions with the surrounding rock.

What Geological Information Can Be Extracted From Trace Elements in Zircon?

There are several factors that make zircon amenable to geochemical investigation of a range of processes and rocks. Although only an accessory phase in most rocks, it is widespread in the crust. It incorporates a range of useful trace elements including U, Hf, Ti and the REE, the uses of which are discussed in detail below. Many minerals contain these trace elements but what marks out zircon is its physical and chemical durability. It is able to withstand high mechanical stress and has a widespread presence in highly strained lower crustal rocks. Its ability to withstand high temperatures makes it a very useful mineral in investigating high temperature rocks, particularly from the Precambrian. Cherniak and Watson (2003) measured volume diffusion of most elements in zircon and found that it is very unlikely for any of them to diffuse under normal geological conditions. Radiogenic Pb can move by volume diffusion in crystalline zircon but periods of around 100Myr at >1000°C are required, depending on crystal size; the effective closure temperature for Pb is around 800-900°C but for other trace elements it is higher still. Elements can move in the zircon lattice by other mechanisms such as by diffusion through distorted lattice or by recrystallization. In general though, zircon is able to preserve its chemical and isotopic composition for long periods of time through episodes of high temperature and pressure

(Finch and Hanchar, 2003). Zircon incorporates a range of other trace elements, which allow for various interpretations on the geological history of the zircons and their host rocks, which are described below.

U-Pb Dating

Radiometric 'dating' produces an end result that can mean different things in different contexts. Isotopic clocks such as U-Pb record the age at which they last dropped below a certain temperature when the isotopes can no longer diffuse, i.e. the closure temperature (Faure and Mensing, 2005). Different mineral chronometers have different closure temperatures so the age of crystallisation, cooling and closure can all be recorded in a single sample. Isotopic systems such as K-Ar or U-Th-He record ages of cooling and cooling rates in high-grade metamorphic rocks as they have a relatively low closure temperature. Zircon on the other hand, with its U-Pb isotopic clock, has a much higher closure temperature and generally records crystallisation ages of magmatism and high-temperature metamorphism (Faure and Mensing, 2005). It is generally regarded as the best mineral chronometer for high-grade rocks (e.g. Hoskin and Schaltegger, 2003).

The decay of radioactive isotopes of uranium to stable daughter lead is the most commonly used, best understood and highest precision geological dating system (Faure and Mensing, 2005). The principle radioactive isotopes of uranium are ^{238}U and ^{235}U, while the stable uranium isotope is ^{234}U. ^{238}U decays to ^{206}Pb with a half-life of 4.468×10^{-9} years (a decay constant of 1.55125×10^{-10} per year) while ^{235}U decays to ^{207}Pb with a half-life of 0.7038×10^{9} years (a decay constant of 9.8485×10^{-10} per year). ^{204}Pb is the non-radiogenic stable isotope of lead. Both ^{238}U and ^{235}U have complex decay systems where there are a number of intermediate daughter isotopes, which are themselves radioactive, before the final radiogenic daughter lead isotope forms (Fig. 2.2).

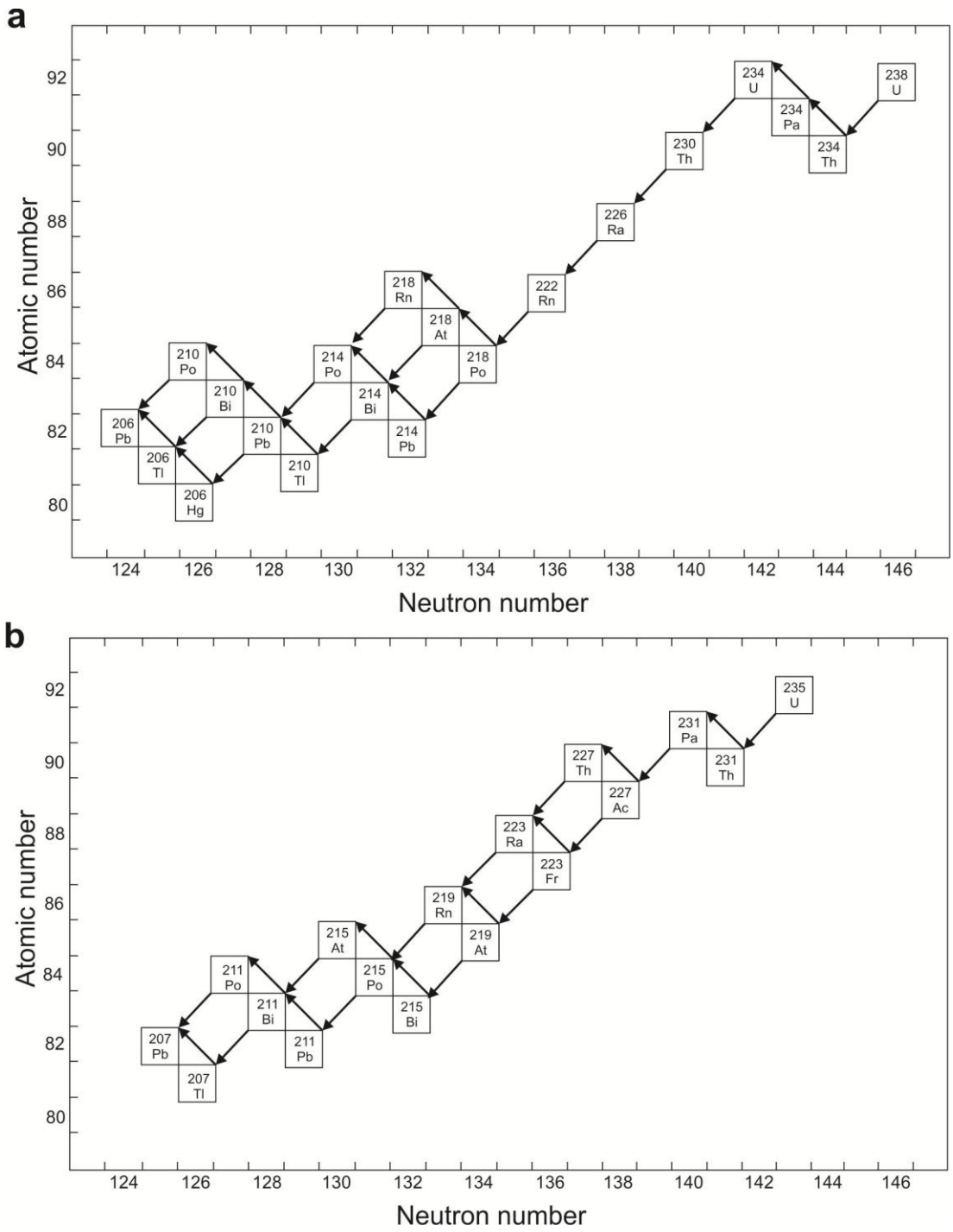

Fig. 2.2 Radioactive decay chains of ^{238}U and ^{235}U.

Certain conditions must be satisfied before reliable results can be obtained from the dating process. The mineral must remain closed to uranium and lead, and all intermediate daughters, since formation (or the last event that is to be dated) as loss or gain of any of these will yield meaningless ages. The isotopic composition of the uranium present must be normal ($^{238}U/^{235}U$ = 137.818, Hiess et al. (2012)) and should not have been

altered by isotope fractionation or by the occurrence of natural fission of ^{235}U. In the analytical stage, correct values must be used for the initial lead isotope ratios and any analyses with contamination discarded (Faure and Mensing, 2005).

Zircon is the most widely used mineral for U-Pb dating (Faure and Mensing, 2005). U^{4+} ions are substituted into the lattice for Zr^{4+} as both have a similar ionic radius of ~1Å and the same charge; Pb^{2+} ions on the other hand have a different charge and a larger ionic radius so are excluded. This means that zircon has high initial U/Pb ratios and is therefore a sensitive geochronometer. It has a high effective closure temperature for volume diffusion of Pb of >900°C (Lee and Tromp, 1995) so is more resistant to resetting and isotopic disturbance than any other mineral chronometer. As a result of this, zircon may date high-grade metamorphism whereas the closure temperatures of the other minerals are too low and their isotopic systems would be disturbed. However, with high U content, zircon suffers from radiation damage, which leads to lead-loss and discordant results.

Rare Earth Element Profiling

The trivalent rare-earth element (REE) cations substitute into the Zr site in the zircon lattice in a coupled substitution with phosphorus (Harley and Kelly, 2007). By measuring the concentration of each of the REEs and plotting a graph of atomic number against chondrite-normalised concentration (Anders and Grevesse, 1989; McDonough and Sun, 1995), a REE profile can be constructed. A typical chondrite-normalised zircon REE profile has increasing concentration with increasing atomic number, a positive Ce anomaly and negative Eu anomaly (e.g. Whitehouse and Kamber, 2003; Kelly and Harley, 2005a; Harley and Kelly, 2007). Whitehouse and Kamber (2003) analysed the concentrations of REEs from complexly zoned zircons from the Amitsoq Gneisses of southwest Greenland and found that individual zircon zones had different REE profiles. This proved that the REE chemistry of the melts from which the zircon had grown or recrystallised were distinct and in conjunction with CL imaging could be used to interpret a crystallisation history for

individual zircon. REEs are one of the main generators of cathodoluminescence (CL) in zircon (Nasdala et al., 2003).

REE patterns appear the most promising method of evaluating the metamorphic character and timing of zircon growth (Harley et al., 2007). This can be done by determining the equilibrium distribution of REEs between zircon and coexisting metamorphic minerals, which may enable the correlation of zircon growth zones to metamorphic mineral fabrics in the host rock. Experimental data on REE distribution are limited at present but that between zircon and high-temperature garnet is well known (Whitehouse and Platt, 2003); zircon grown or recrystallised contemporaneously with high-temperature garnet shows a flat heavy REE profile and strong depletion in europium (Rubatto and Hermann, 2007). There are still problems with this though as existing empirical estimates of distribution coefficients of REEs into zircon and garnet vary widely between different high-temperature and high-pressure rocks (Harley et al., 2007). It must also be remembered that these are *equilibrium* distribution coefficients and therefore careful interpretation of textural relationships between the minerals is essential. Furthermore, Rubatto (2002) pointed out that the amount of available elements may affect the composition of zircon over time, i.e. with ongoing metamorphism and garnet growth, the reservoir from which zircon takes REEs is depleted.

Harley and Kelly (2007) applied the technique to ultra high-temperature gneisses from Antarctica from which U-Pb data indicated magmatic protoliths at ~2840Ma and zircon resetting at ~510Ma while the rocks preserved a granulite-facies mineralogy. The REE distribution between zircon and the granulite-facies garnet indicated that the zircon had been unaffected by the granulite-facies event but had been altered by post-peak fluid infiltration at ~510Ma (Harley and Kelly, 2007). Clark et al. (2009) combined REE profiling with U-Pb dating and Ti-in-zircon thermometry (see below) to try to determine the P-T-t path and tectonic evolution of a Gondwanan suture. Distribution coefficients were

calculated from experimental and natural rock data for zircon/garnet and indicated that zircon grew from garnet breakdown at a certain time in the evolution of the suture. U-Pb ages and Ti-in-zircon thermometry complemented this to enable the construction of a tectonic model for the Gondwanan collision.

The Titanium-In-Zircon Geothermometer

The amount of titanium in zircon, representing the uptake of titanium during crystal growth, can be used as a geothermometer. Watson et al. (2006) grew synthetic zircons from silicate melts at a range of preset temperatures and pressures. This enabled calibration of a thermometer, which, along with analysis of natural zircons in equilibrium with rutile, has shown that the titanium content of zircon, together with the zirconium content of rutile, are temperature dependent – the more titanium, the higher the temperature. Titanium is present in zircon at up to 120ppm as a 4^+ cation substituting for zirconium 4^+ in the crystal lattice without any coupled substitution. The results of the study of Watson et al. (2006) showed that titanium concentration in zircon is relatively insensitive to pressure but is highly temperature-dependent with the potential to return temperatures of +/-10° or better for temperatures of ~400-1000°C. If the zircon crystallised in the presence of rutile (TiO_2) then the calculated temperature can be accurate to 10°C but if rutile is absent then the activity of Ti is reduced and zircon will not be able to take in an abundance of Ti proportional to the true temperature; even in this scenario, the thermometer will still record a minimum temperature. Relative temperature changes across different zones of a single grain are subject to analytical uncertainty only, which depends on the titanium content and the analytical instrument (either ion- or electron-microprobe) (Watson et al., 2006). Electron microprobe analysis is suitable for zircons with high titanium contents while an ion microprobe is necessary for precise determination of low titanium zircons.

Watson and Harrison (2005) used the technique to find out the crystallisation temperatures of the Jack Hills zircons from Western Australia – the oldest known terrestrial objects. The temperatures obtained were around 700°C suggesting growth in a granitoid melt, hence indicating that crust formation and recycling was operative as early as 4.35Ga. However, Watson et al. (2006) caution that titanium present in detrital zircon (e.g. Jack Hills) grain coatings or necessary coatings applied for microprobe analysis may result in erroneously high temperatures being calculated and hence care must be taken before analysis.

Subsequently, Ferry and Watson (2007) revised the thermometer calibrations to take into account the independently variable phase components ZrO_2 and TiO_2 in zircon. New experimental data confirmed titanium content increased with decreasing uptake of SiO_2 and hence the primary substitution of titanium is for silicon in the zircon lattice (Tailby et al., 2011). These new calibrations enable the titanium-in-zircon geothermometer to be used reliably for rocks without rutile, provided the activity of TiO_2 and SiO_2 can be independently constrained.

Fu et al. (2008) tested the thermometer by measuring titanium concentrations of 484 zircons from various different types of igneous rocks. They found temperatures to be lower than modelled and suggested a few factors that may affect the reliability of the geothermometer; perhaps the most important is that titanium does not remain immobile in the lattice through a complex geological evolution of the crystal. They also suggest that titanium behaviour may be influenced by the presence of other trace elements in the zircon lattice, as well as the possibility of non-equilibrium zircon crystallisation, e.g. in late evolved hydrous melts. Further issues regarding the thermometer's systematics were raised by Glikson (2006) and Nutman (2006) who questioned the reliability of the thermometer for melts at temperatures above ~800°C that are zircon-undersaturated. Zircon should not

crystallise until melt fractionation is well underway although Watson and Harrison (2006) argue against this on the basis of variable initial zirconium content in the melts.

Most of the application of the titanium-in-zircon geothermometer has been on igneous rocks, but Baldwin et al. (2007) applied it to ultra-high temperature metamorphic rocks. They analysed zircons from Brazilian granulites and South African lower crustal xenoliths using an electron microprobe for high titanium zircons and LA-ICP-MS for the lower (<20ppm) titanium zircons. Where zircons were zoned, they recorded different temperatures from different growth zones and applied the thermometer to zircon growth, which was interpreted to be metamorphic from textural relationships. The temperatures calculated are again lower than phase equilibria estimates but as they are higher than those recorded by Fu et al. (2008), Baldwin et al. (2007) interpreted that their calculations had not suffered from the problems that affected Fu et al. (2008) and that zircons can retain temperatures from more than one geological event.

Hafnium Isotope Petrogenetic Tracing

Hf is an abundant trace element in zircon, often reaching weight percent levels. There are both stable and radiogenic Hf isotopes in zircon: ^{176}Lu decays by beta emission to ^{176}Hf but does not easily incorporate into the zircon lattice; the stable isotope ^{177}Hf, however, does substitute into the crystal. This results in very low Lu/Hf ratios (Patchett, 1983), typically around 0.002 (Kinny and Maas, 2003). The lutetium-hafnium decay system is useful as it gives both a dating method and an isotopic tracer. Crystallisation of new zircon locks the hafnium into the lattice and hence preserves the ratio of the different isotopes as it was at the time; this renders it a useful tracer for the origin of lower crustal rocks (Faure and Mensing, 2005).

Patchett and Tatsumoto (1980) constructed a chondritic uniform reservoir line (CHUR) of the ^{176}Hf/^{177}Hf ratios against time, against which rocks derived from the mantle could be compared. This relationships is expressed using ε notation, the comparison

between the $^{176}Hf/^{177}Hf$ ratios of the sample against CHUR; positive ε(Hf) values indicate that the sample is enriched in ^{176}Hf compared to CHUR while negative ε(Hf) values are the opposite (Faure and Mensing, 2005). In fingerprinting the source of a melt from which a rock formed, an ε(Hf) value of zero falls on the CHUR line, which reflects undepleted mantle; highly positive ε(Hf) values represent a depleted mantle source while a negative value is the signature of crustal derivation or subducted ocean crust; a slightly positive or slightly negative value indicates a melt derived from depleted mantle but contaminated on ascent by crystal melts or xenoliths (Kinny and Maas, 2003). Zircon is resistant to contamination by more hafnium even during metamorphism and so even if the crystal has been subjected to high-grade metamorphism, the original ε(Hf) should be preserved (Kinny and Maas, 2003). Patchett et al. (1981) analysed the $^{176}Hf/^{177}Hf$ ratio from many rocks of different ages and found that the growth of continental crust was episodic and started at least 2.9Ga. Corfu and Noble (1992) examined hafnium isotope ratios from the 3.0Ga Superior Province in Canada and found that its source was depleted mantle indicating that the mantle had started to fractionate by this time. In the Gawler craton of Australia, Belousova et al. (2009) used the hafnium tracer to determine which of many episodes of zircon growth were from crustal sources and which were from depleted mantle sources, thus building up a picture of local crustal evolution. As well as an isotopic tracer, hafnium isotopes can also be used to calculate model ages: the age when the hafnium in a zircon separated from CHUR or Depleted Mantle and entered into the zircon crystal (Faure and Mensing, 2005).

2b: The Lewisian Gneiss Complex

Early Work

The Lewisian Gneiss Complex crops out along the northwest coast of the Scottish Highlands and on the Outer Hebrides island chain. It is unconformably overlain by Proterozoic Torridonian sediments and Cambro-Ordovician sediments and occurs west of the Moine thrust belt (Fig. 2.3). The existence of an early basement gneiss was acknowledged by the likes of MacCulloch in the first half of the nineteenth century but the first detailed investigation of the Lewisian gneiss and its component parts was carried out by the Geological Survey in the period 1883 to 1907 when the regional memoir *The Geology and Structure of the Northwest Highlands of Scotland* was published (Peach et al., 1907). Their fieldwork had led to the identification of a "Fundamental Complex" comprising a variety of banded gneisses, which they presciently recognised as being "of probably plutonic origin", with minor metasediments, all intruded by a suite of basic dykes (Peach et al., 1907). Teall (1885) examined the dykes in particular and documented their metamorphism from dolerite to hornblende-schist. Peach et al. (1907) also described foliations and lineations and although quantitative structural geology had yet to be invented, some temporal relationships of deformation and its heterogeneous nature were identified (Peach et al., 1907).

In the next fifty years or so, further research into the Lewisian Gneiss Complex was fairly limited. Jehu and Craig (1923-1934)(1923-1934) documented the Lewisian of the Outer Hebrides in five parts (Jehu and Craig, 1924; Jehu and Craig, 1925; Jehu and Craig, 1926; Jehu and Craig, 1927; Jehu and Craig, 1934) while Davidson (1944) looked at South Harris in particular. It was not until the seminal paper of Sutton & Watson (1951) that investigations into the Lewisian took off in earnest. Both authors conducted detailed observations on small parts of the outcrop so as to try and deduce the relative chronology of tectonothermal events in the Lewisian. Based on their field observations, they

introduced new chronology: the *Scourian* event, which preceded the intrusion of the metadolerite *Scourie Dyke Swarm* (they were assumed to have intruded in a single pulse), which was in turn followed by the *Laxfordian* event (Sutton and Watson, 1951). The use of the dykes as time markers proved crucial in the recognition of polyphase deformation as in places they cross-cut an existing gneissic foliation while in others were themselves foliated. Sutton and Watson (1951) also subdivided the Lewisian into three regions: Northern and Southern, which were pervasively deformed by the amphibolite-facies Laxfordian event (characterised by hornblende) and the Central region where Scourian pyroxene-bearing gneisses (referred to as 'charnockites') were locally preserved from the effects of the Laxfordian (Sutton and Watson, 1951). These chronological observations and the three-region model remained largely unchallenged until the terrane model proposed by Kinny et al. (1997; 2005), which is discussed below, and are the framework for a description of the general geology.

Geological Summary

The three-region model applies to the mainland Lewisian outcrop only (Fig. 2.4) and was proposed on metamorphic grounds (Sutton and Watson, 1951). The Central Region contains a large proportion of granulite-facies tonalite-trondhjemite-granodiorite (TTG) gneisses that contain two pyroxenes, along with more mafic gneisses and metasediments (Johnstone and Mykura, 1989). Some of the TTG gneisses in the Central Region have statically recrystallised under amphibolite-facies conditions or they were deformed and retrogressed in discrete shear zones. In both cases, the pyroxenes are progressively replaced by amphibole and biotite (Johnstone and Mykura, 1989).

The Northern Region gneisses have all been deformed at amphibolite-facies and there is no indication that they were ever subjected to an early granulite-facies metamorphic event. They are dominantly quartzofeldspathic and often migmatitic (Johnstone and Mykura, 1989). The Laxford Shear Zone was interpreted by Sutton and

Watson (1951) to be a metamorphic front that demarcated the southern edge of amphibolite-facies metamorphism in the Northern Region and the start of the Central Region of preserved granulite-facies gneisses. The Northern Region shows pervasive Laxfordian deformation (Johnstone and Mykura, 1989).

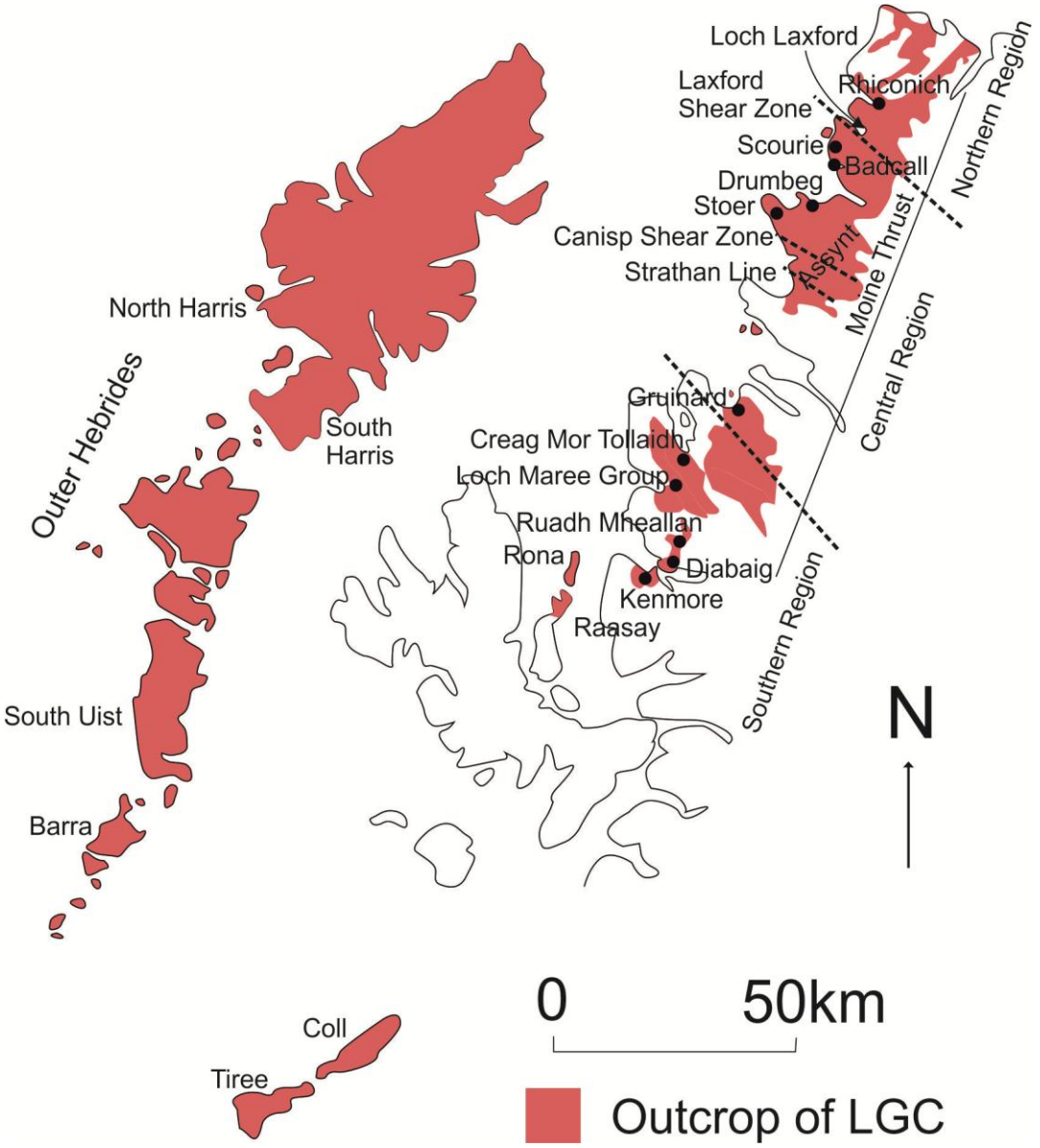

Fig. 2.3 Location and outcrop area of the foreland Lewisian Gneiss Complex with key localities mentioned in the text.

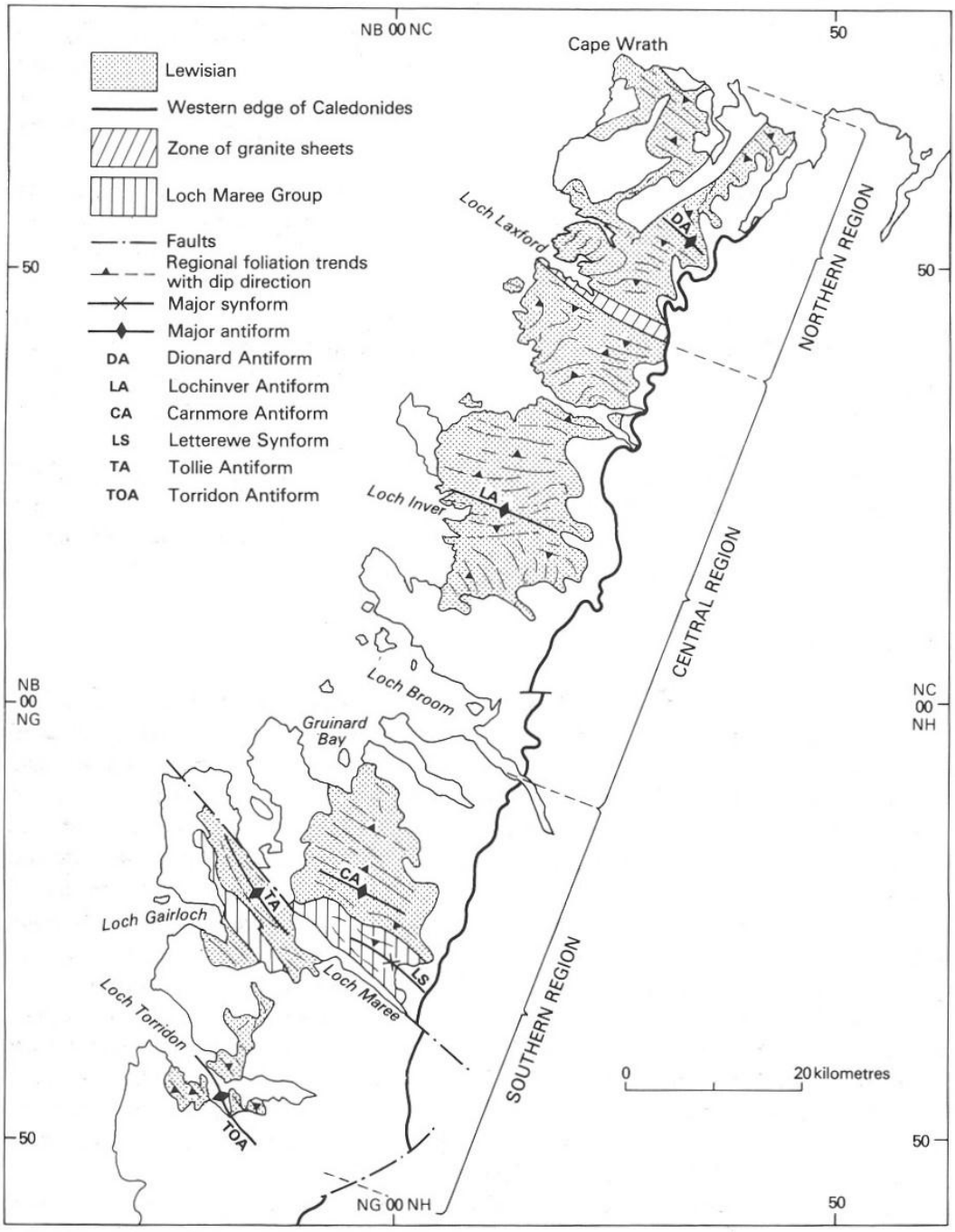

Fig. 2.4 The geographical distribution of the three-region model for the mainland Lewisian proposed by Sutton and Watson (1951). After Johnstone and Mykura (1989).

The Southern Region is also composed of amphibolite-facies gneisses although there are some areas of low strain and less migmatisation. Hornblende-gniesses are the dominant rock type with subordinate mafic and ultramafic gneisses (Johnstone and Mykura, 1989). The Southern Region contains a large metasedimentary and metavolcanic package – the Loch Maree Group. It is composed of metabasic sheets interleaved with

metasediments including garnet-mica-schists, semipelites and rare marbles (Park, 2002). They are interpreted to be Palaeoproterozoic but their contacts with surrounding gneisses are highly tectonised so the field relationships are unclear (Johnstone and Mykura, 1989).

Throughout the mainland LGC, a suite of mafic dykes – the Scourie Dyke Swarm (Sutton and Watson, 1951) – cut across the gneisses. They are mainly doleritic in composition although some picrite and olivine-gabbro dykes occur in the Assynt area, east of Lochinver (Tarney, 1973). In the Central Region, some retain their igneous mineral assemblages and textures but in areas affected by Laxfordian metamorphism and/or deformation, they are retrogressed to hornblende and plagioclase and may be deformed and transposed into sheets.

Along with the three-region model, Sutton and Watson (1951) suggested a chronology for the Lewisian Gneiss Complex. Soon after the formation of the protolith rocks, they were subjected to early Scourian granulite-facies metamorphism, termed the Badcallian event (Park, 1970); this was then followed by amphibolite-facies metamorphism and deformation – the late Scourian (Sutton and Watson, 1951) event, termed the Inverian by Evans (1965). These events can be distinguished by their respective metamorphic mineralogies. Sutton and Watson's most important insight was the use of the Scourie dykes as time markers. They used the dykes to distinguish between amphibolite-facies Inverian structures and the post-dyke Laxfordian event (also amphibolite-facies), which appear similar. The dykes cross-cut Inverian structures but are deformed by Laxfordian fabrics.

The above models apply to the mainland only but the Lewisian Gneiss Complex crops out elsewhere. There are occasional patches of hornblende gneiss east of, and within, the Moine thrust belt, which have sometimes been interpreted as inliers of Lewisian basement, but these will not be dealt with here as they have been subjected to post-Laxfordian orogenic episodes and their relationships with the main Lewisian outcrop are unknown (Johnstone and Mykura, 1989). Lewisian gneiss also crops out in the Hebrides (see

Fig. 2.3 for locations). The whole of the island of Rona and the northern part of Raasay are composed of biotite-hornblende gneisses, locally migmatitic, with mafic sheets interpreted to be transposed dykes (Lyon et al., 1973). They are very similar to the rocks around Kenmore, nearby on the mainland at the southern tip of the mainland Lewisian outcrop, and are interpreted to be contiguous (Johnstone and Mykura, 1989). Migmatitic hornblende gneisses, metasediments and amphibolite dykes crop out on the island of Iona and are interpreted to be Lewisian (Muir et al., 1994; Whitehouse and Russell, 1997) although correlation is difficult and they are interpreted to have been very close to, and therefore affected by, a major extensional structure (Potts et al., 1995). The islands of Tiree and Coll are also Lewisian. They are mostly typical migmatitic Laxfordian gneisses but western Tiree is pyroxene-bearing suggesting that granulite-facies metamorphism did occur (Westbrook, 1972a; Drury, 1973; Drury, 1974). Both islands are unusually abundant in metasedimentary bands, including garnet-biotite schists, siliceous schists and a variety of calc-silicates and marbles. Correlation is difficult due to the islands' remoteness from the main Lewisian outcrops although Westbrook (1972b) suggested a history of: granulite-facies metamorphism (Badcallian equivalent); dyke intrusion (Scourie dykes); amphibolite-facies metamorphism (Laxfordian).

The Outer Hebrides are almost exclusively composed of Lewisian gneiss of various types (Fig. 2.5). The main lithology is biotite- and hornblende-bearing TTG gneiss (Johnstone and Mykura, 1989; Fettes et al., 1992). A Laxfordian foliation and lineation is widespread, while the Inverian is represented by discrete shear zones yp to several kilometres wide (Fettes et al., 1992; Mason, 2012). The Scourie dykes also appear to be represented in the form of transposed mafic sheets as seen in the Northern and Southern regions of the mainland. Pyroxene- and garnet-bearing dioritic gneisses are found in eastern South Uist and eastern Barra although their contacts with other gneisses are tectonised so their relationships are unclear (Fettes et al., 1992). A granite vein complex occurs in west Lewis

and western North Harris and is composed of a network of granite veins and sheets ranging from centimetres to hundreds of metres in thickness (Myers, 1971). South Harris has the most diverse assemblage of the Outer Hebrides (Fig. 2.6). There is a central igneous complex of metadiorite, metatonalite, metagabbro and an older meta-anorthosite. This is flanked to the north and south by mafic metavolcanics and metasediments comprising pelitic- and graphitic-schists, quartzite and marble (e.g. Johnstone and Mykura, 1989).

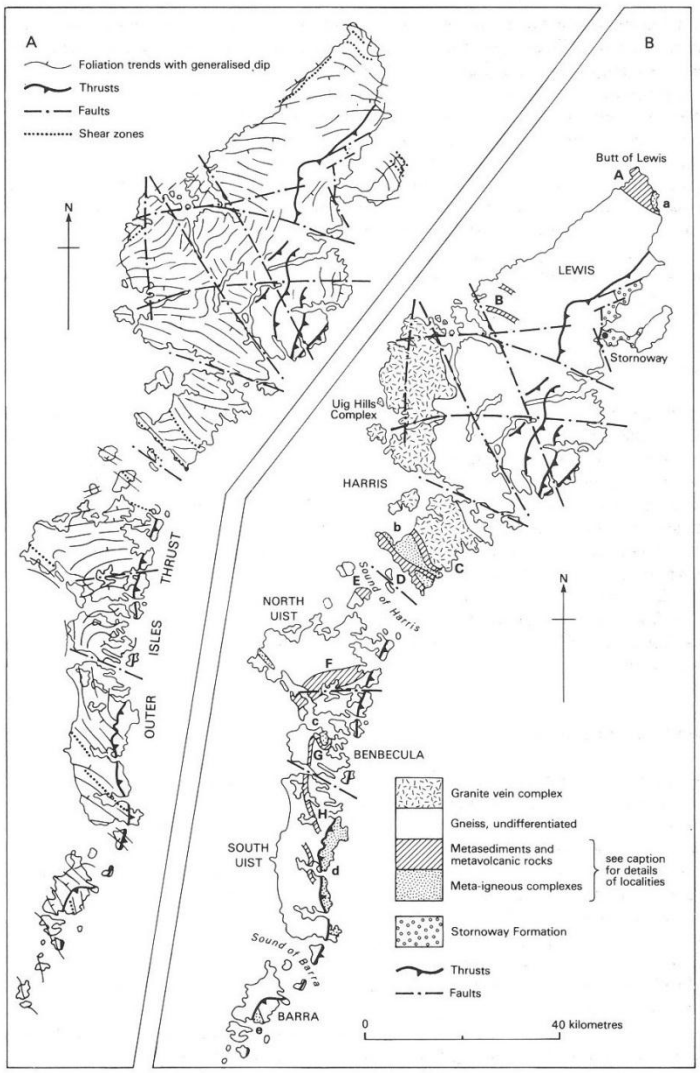

Fig. 2.5 Map of structures and lithologies of the Outer Hebrides, from Johnstone and Mykura (1989).

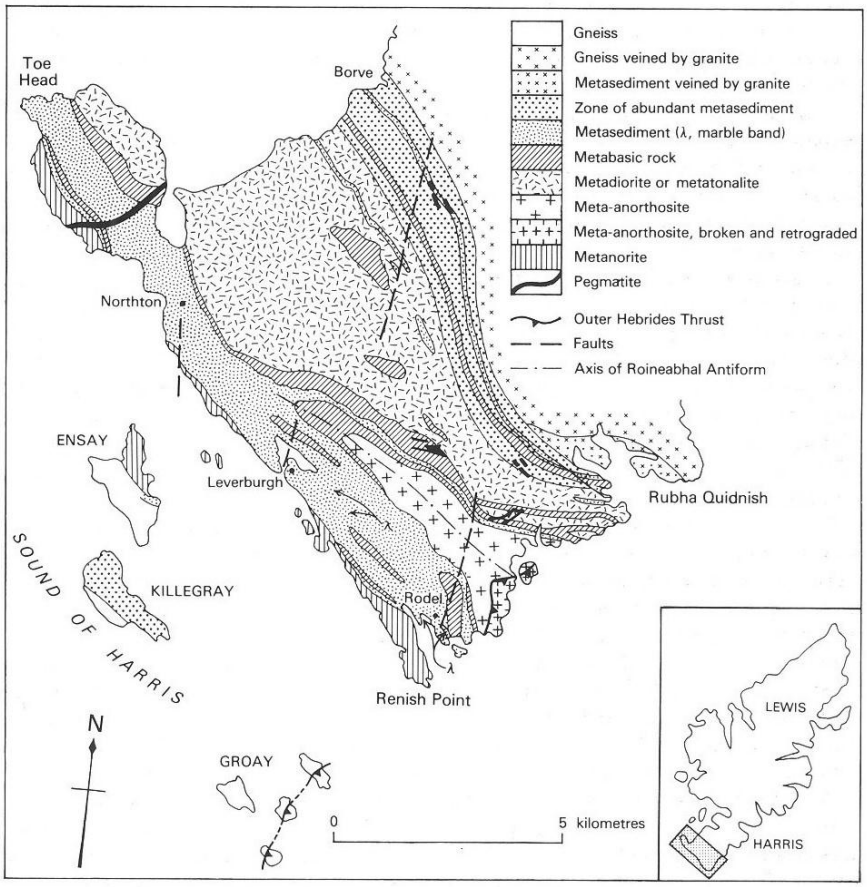

Fig. 2.6 Detailed map of the rocks of South Harris, from Johnstone and Mykura (1989).

This summarises the geological outline of the Lewisian Gneiss Complex based around the work of Sutton and Watson (1951). In the decades that followed, many advances were made in the more detailed understanding of the Lewisian Gneiss Complex, and geology in general, in the fields of structural analysis, geochemistry and metamorphism, and geochronology.

Structure

Sutton and Watson (1951) used structural features and structural relationships to define a chronology for the Lewisian. In the following decades, other workers mapped and described structures and structural relationships over a wider area of the Lewisian Gneiss Complex. Detailed mapping in the Diabaig area led Cresswell (1972) to suggest nine generations of structures, and hence nine different deformation events, between the early Scourian and late Laxfordian. Five generations of structures were pre-Scourie dyke and four

were post-dyke, while he recognised that large-scale Laxfordian structure and dyke emplacement were controlled by the pre-existing Inverian large-scale structure (Cresswell, 1972). Park (1973) took a wider view of the entire mainland Southern region, which he defined as a “Laxfordian belt”. He recognised that pre-Laxfordian structures were preserved in isolated blocks such as Ruadh-mheallan and Creag-mhor Thollaidh (Park, 1973). Park and Cresswell (1973) found that the Scourie dykes were concordant with, and were affected by, the Laxfordian foliation while they were discordant with, and cross-cut, the Inverian foliation. Concordant dykes are thinner and more frequently branched and they emphasised the structural control of pre-existing features on subsequent ones (Park and Cresswell, 1973).

Sheraton et al. (1973b) gave detailed descriptions of different generations of structures in the Assynt area. In this area, the dominant early Scourian structure was a flat-lying gneissic layering that had flattened some even earlier folds. Inverian deformation took the form of large monoclinal folds. Laxfordian deformation was concentrated in discrete shear zones (Sheraton et al., 1973b). They recognised that deformation was very heterogeneous and less intense from the Inverian onwards due to the rocks here being quite rigid, possibly due to geochemical depletion of heat-producing elements (Sheraton et al., 1973b). Further north between Scourie and Loch Laxford, Davies (1976) suggested thrusting had occurred prior to Scourie dyke emplacement, followed by multiple episodes of folding. Beach et al. (1974) found pre-dyke amphibolite-facies upright isoclinal folds just south of the Laxford Shear Zone (LSZ). Following dyke intrusion, deformation north of the LSZ took the form of a pervasive foliation while to the south it was concentrated in discrete shear zones, and a further episode of folding occurred only to the north (Beach et al., 1974). Further north still, Chowdhary and Bowes (1972) found the structure of the Northern Region between Loch Laxford and Rhiconich to be a steep, southwest-dipping Laxfordian fabric while to the north of Rhiconich the fabric flattens out into a series of

rolling folds until the major Strath Dionard antiform (Dash, 1969) where the fabric then dips steeply to the northeast up to the coast at Durness (Johnstone and Mykura, 1989).

In the 1960s and '70s, there was much development of structural ideas with the relating of foliation and lineation to strain (Flinn, 1965), and the realisation of the importance of shear zones as a style of deformation (Ramsay and Graham, 1970). This led to various workers introducing these concepts to their analyses of Lewisian structures. Graham and Coward (1973) made a point of describing the methods by which they identified heterogeneities in strain in their study of the Outer Hebrides. They found that strain variation can be attributed to lithology and ductility, for example pyroxene-bearing rocks were less deformed than amphibole-bearing rocks (Graham and Coward, 1973). Furthermore, they recognised that strain is often concentrated at the contacts between rocks of different lithology and/or ductility, for example the Scourie dykes were often highly deformed at their margins but pyroxene was preserved in the centre (Graham and Coward, 1973).

Wheeler et al. (1987) focussed on the major shear zone at Diabaig and detailed mapping revealed that it was in fact composed of multiple anastomosing shear zones separating low-strain lozenges. Shearing was suggested to have been initiated in the Inverian with individual shear zones having opposing senses: sinistral-reverse and dextral-normal (Wheeler et al., 1987). The shearing was thought to have been reactivated in the Laxfordian but strain was concentrated in the dykes, which Wheeler et al. (1987) suggested would have been more ductile.

Attfield (1987) suggested that the Canisp Shear Zone in Assynt was initiated in the Inverian as a broad belt of steep southeast-dipping foliation bounded to the south by the north limb of the Lochinver antiform, a major monoclinal fold. The Inverian lineation plunges steeply southeast indicating reverse-sense dip slip movement with a minor component of dextral strike-slip (Attfield, 1987). Laxfordian reactivation occurred in narrow

zones and the lineation plunges more shallowly to the southeast indicating dextral transpression again but strike-slip movement was dominant. Beach et al. (1974) described a similar scenario for the Laxford Shear Zone. Wynn (1995) mapped the discrete Laxfordian shear zones south of the Laxford Shear Zone and concluded that movement took place under sinistral transtension and interpreted them as accommodation structures, accommodating stress by simple shear and block rotation.

A further step in structural interpretation of the Lewisian Gneiss Complex was the attribution of structural features to wider tectonic processes and environments. Coward (1984) interpreted the offset of Scourie dykes to indicate that shear on the Laxford Shear Zone was sinistral with a small component of normal movement. Many of the major shear zones of the Lewisian were initiated in the Inverian and reactivated in the Laxfordian, which had various explanations: two collision events with the same movement direction; one large event with multiple movements; the shear zone acted to decouple the lithosphere (Coward, 1984). Further to this, the Central Region was interpreted to have been thrust obliquely northwards over the Northern Region in the Inverian then to have slid back down to the south in Laxfordian (Coward, 1990). He interpreted the exposed part of the Laxford Shear Zone to originally have been in the mid-to-lower crust (Coward, 1990).

Coward and Park (1987) interpreted the dominant flat-lying foliation of the Northern Region, Kenmore and other parts of the Southern Region, and the Outer Hebrides (Coward, 1975) to reflect a major mid-crustal flat that descended beneath the Central Region on northwest-southeast oriented shear zone ramps such as the Laxford Shear Zone. They divided the mainland Lewisian into blocks bounded by major shear zones – the Northern Region and Kenmore are lower crust while the Central Region is upper crust hence the shear zones are “mid-crustal” (Coward and Park, 1987). Goodenough et al. (2010) also interpreted that the Laxford Shear Zone was initiated in the Inverian by combining field structural observations with geochemical and geochronological data.

Coward and Park (1987) focussed on the Kenmore area and used kinematic indicators to interpret that the tectonic environment had undergone major changes during the evolution of the Lewisian – dextral-transpressional to dextral-transtensional to dextral-transpressional to sinistral strike-slip. On a crustal scale, Wheeler (2007) suggested the major shear zone at Diabaig may in fact deform by pure shear accommodated by localised simple shear in the component anastomosing shear zones. He also sounded a note of caution in showing that metre-to-kilometre scale shear does not always relate directly to this crustal-scale shearing (Wheeler, 2007).

Geochemistry and Metamorphism

Sutton and Watson (1951) recognised the importance of metamorphism in determining the history of the Lewisian Gneiss Complex. They interpreted the Laxfordian of the Northern and Southern Regions to be retrogression of the Scourian rocks still seen in the Central Region. This view has been challenged on geophysical and geochemical grounds by various workers who doubted the Laxfordian areas were cogenetic with the Central Region and that they were in fact a supracrustal sequence deposited on Scourian basement and had ever been to granulite-facies (e.g. Bott et al., 1972; Holland and Lambert, 1973; Bowes, 1978).

In the 1970s and '80s, detailed petrological analysis and geochemical measurement in conjunction with experimental work led to a new understanding of the origin and evolution of the Lewisian Gneiss Complex. Making detailed observations of mineral textures, Beach (1973) was able to deduce metamorphic reactions and their implications. He observed that biotite was the common ferromagnesian mineral in discrete Laxfordian shear zones that had formed from hydrous retrogression of hornblende (Beach, 1973). Thus he was able to say that the shearing brought about a metamorphic change as the shear zones were conduits for fluid flow, and that therefore fluid played a major role in the Laxfordian event (Beach, 1976).

In the Central Region, pyroxene granulites (a term for pyroxene-bearing gneisses that had been metamorphosed at granulite-facies which was fashionable around this time) were preserved from amphibolite-facies retrogression as they were a sufficient distance away from the shear zones and their fluids (Beach, 1974). Gneisses pervasively deformed in the Laxfordian have, without fail, undergone hydrous retrogression (Beach, 1974). Cresswell and Park (1973) related metamorphic features to the three main tectonothermal events (Badcallian, Inverian and Laxfordian) by correlating them with structures that could be tied to each event. They found that original mineral segregation banding and some migmatisation occurred in the Badcallian, formation of amphibolite-facies mineralogy and further migmatisation occurred in the Inverian, and further amphibolite-facies metamorphism, late greenschist-facies retrogression and alkali metasomatism occurred in the Laxfordian (Cresswell and Park, 1973).

Tarney (1973) investigated Scourie dykes with a picritic composition in Assynt and interpreted three stages of metamorphism affecting these dykes (and therefore the host gneisses too). First, they underwent amphibolitisation and metasomatism with little or no associated deformation. Discrete Laxfordian shearing brought about deformation and recrystallisation at amphibolite-facies where the dykes were affected. Evidence for this second phase can be seen in mineral alteration textures from anthophyllite to talc, and the presence of other lower temperature minerals such as tremolite (Tarney, 1973). Late serpentinisation, possibly Caledonian in age, was found in brittle, fracturable dykes, especially close to the Moine Thrust (Tarney, 1973). Tarney (1973) interpreted that hornblende in picritic dykes was magmatic, suggesting that the dykes were intruded into hot, deep country rock and that metamorphism was not standard prograde regional metamorphism as the first event was at amphibolite-facies (Tarney, 1973).

Detailed geochemical analyses of rock samples also led to new and more detailed interpretations of the origin and evolution of the Lewisian. Sheraton et al. (1973a)

conducted extensive sampling of all lithologies in areas at Drumbeg and Rhiconich to compare the geochemistry of Scourian and Laxfordian gneisses respectively. There is little or no difference between the geochemistry of samples from Drumbeg, whether at granulite-facies (Badcallian) or amphibolite-facies (Inverian) (Sheraton et al., 1973a) suggesting the latter was a reworked equivalent of the former. This suggested that the geochemical system has remained closed since this time (Sheraton et al., 1973a). The minor element geochemistry of the Laxfordian gneisses at Rhiconich was considered to be too different to be a reworked equivalent of the those at Drumbeg and Rhiconich and so was suggested to be a fairly typical segment of upper crust subsequently juxtaposed with the lower crustal Assynt gneisses (Sheraton et al., 1973a). The Drumbeg (Assynt) gneisses in general were found to be slightly enriched (relative to Rhiconich and other areas including Lewis and Greenland) in Ca, Mg, Fe, Cr and Ni (reflecting their predominantly more mafic chemistry) while being very strongly depleted in K_2O, Rb, Th and U (Sheraton et al., 1973a). They were found to have high K/Rb and Ba/Rb ratios and very low Rb/Sr, K/Sr and K/Rb ratios while being slightly depleted in Ce, La and Pb (Sheraton et al., 1973a). The relative depletion of these elements is to be expected as their host minerals plagioclase and aluminous hornblende are not stable at granulite-facies (Sheraton et al., 1973a). They suggest that the Assynt pyroxene granulite gneisses are fairly standard lower crust rocks that tend to be depleted in the aforementioned elements, but they suggest a permeable aqueous phase could be the reason for the extreme depletion seen (Sheraton et al., 1973a).

In a previous paper, (Sheraton, 1970) suggested that, based on geochemistry, the Assynt gneisses were originally a potash-poor basalt-andesite-dacite-rhyolite sequence with intercalated sediments. Sheraton et al. (1973a) give some rather unconvincing evidence to support this theory. Holland and Lambert (1973) examined the geochemical evidence for possible origins for the Assynt gneisses (their 'Scourie Assemblage'). They disregarded the origin as being sedimentary or a volcanic sequence (Sheraton et al., 1973a) due to the K/Pb

ratio and Sr and Pb levels (Holland and Lambert, 1973). Instead they favoured a plutonic origin, drawn directly from the mantle with multiple fractionation events leading to depletion of granitic constituents (Holland and Lambert, 1973).

In this paper, Holland and Lambert (1973) also conducted an extensive geochemical survey of the entire mainland Lewisian and divided it into 'assemblages' on petrological and geochemical grounds. They agreed with Sheraton et al (1973a) that the Laxfordian rocks cannot be reworked Scourian equivalents (Holland and Lambert, 1973). They suggested Gruinard and Scourie are cogenetic based on broadly similar geochemical signatures, although they have slightly differing silica and alkali levels (Holland and Lambert, 1973). Tarney (1973) made some geochemical measurements of the Scourie Dykes in Assynt and divided them into several groups based on petrography and geochemistry. Olivine gabbros are enriched in Fe and S while bronzite-picrites are enriched in Cr and Ni (Tarney, 1973). These more mafic types are found mainly in the Assynt area while the more common quartz-dolerite dykes are found throughout the complex, metamorphosed to amphibolites in varying degrees.

Rollinson and Windley (1980) investigated the geochemistry of a variety of gneisses from the Scourie/Badcall area of the Central Region. Major element data suggested that the mafic granulites were tholeiitic in composition and the tonalite, trondhjemite and granite gneisses were calc-alkaline (Rollinson and Windley, 1980). As deformation is minimal in this area, they argued that these chemistries were primary magmatic and not caused by retrogression (Rollinson and Windley, 1980). Major and minor element geochemistry indicated that the mafic gneiss could not be a residue after fractionation of the tonalite from the same source, hence they are unrelated and the source of the dominant tonalites was unknown (Rollinson and Windley, 1980). Quartz/feldspar relationships and chemistries suggested that the tonalite was parental to the trondhjemite and the trondhjemite parental to the granite, both via fractional crystallisation, while rare earth element (REEs)

concentrations indicate that the trondhjemite was strongly fractionated compared to the tonalite (Rollinson and Windley, 1980). These interpretations were backed up by field relationships (Rollinson and Windley, 1980).

The granites show a variation between samples of Ce and Y which cannot be explained by partial melting of the tonalite, hence Rollinson and Windley (1980) proposed they formed from fractional crystallisation of the trondhjemite. Evidence for this included a smooth quartz-feldspar compositional trend between the two and the gradation of one to the other in the same sheet (Rollinson and Windley, 1980). This model would require a plagioclase-rich residue and, in support, an anorthosite sheet is found at Scourie; Ce and Y preferentially partition into a granitic melt rather than plagioclase explaining their relative enrichment in the granites (Rollinson and Windley, 1980). It had previously been suggested that the trondhjemites were derived by partial melting of the tonalites but Rollinson and Windley (1980) argued that sharp cross-cutting field relationships between the two and a lack of evidence of melting textures in the tonalites precluded this idea and that fractional crystallisation was the method involved. Rollinson and Windley (1980) suggested that hornblende and plagioclase were the main phases fractionating from the tonalite, which indicated a depth of >45km, >10% H_2O and dehydration in subsequent granulite-facies metamorphism. They do not seem to have considered the possibility of magma mixing in their investigations.

Tarney and Weaver (1987) found much the same geochemistry in their measurements of Scourian granulites as Rollinson and Windley (1980) did, and agreed with the suggestion that the depletion in U, Th and Rb was a primary magmatic feature. They suggested a model where hydrothermal fluids removed the relevant elements from a subducting ocean slab and because Archaean subduction is believed to be shallow, there was no mantle wedge to re-enrich the subsequent plutonic material (Tarney and Weaver, 1987). They suggested that slight enrichment of REEs in the mafic granulites indicated an

undepleted mantle source, such as oceanic crust, hence agreeing with their model (Tarney and Weaver, 1987). They also found that intermediate granulites were enriched in light REEs relative to tonalitic granulites, which were also more depleted in heavy REEs, and trondhjemitic granulites were relatively depleted in all but the lightest REEs, while amphibolite-facies gneisses showed similar concentrations for all REEs. They used this to argue for depletion as a magmatic feature as opposed to via granulite-facies metamorphism (Tarney and Weaver, 1987).

Unlike some previous workers (e.g. Holland and Lambert, 1973; Sheraton et al., 1973a) who sampled widely and tried to come up with an origin and evolution for the whole of the complex, Rollinson and Fowler (1987) focused on one specific area and combined detailed field mapping with geochemistry to try and understand the Scourian rocks. They investigated Gruinard, at the southern tip of the Central Region, and field mapping showed agmatite trains with amphibolitic, ultramafic and tonalitic gneiss enclaves enclosed in later widespread trondhjemitic and granitic gneiss, all of of which were subsequently metamorphosed at hornblende-granulite-facies and later retrogressed (Rollinson and Fowler, 1987). Geochemical analyses of the amphibolites revealed variations in immobile elements like Zr and Ni and high Ti/Zr ratios that indicated a variety of compositions for their magmatic source; the amphibolites were therefore interpreted not to be a simple comagmatic suite though still derived from a similar mantle source region (Rollinson and Fowler, 1987). REE measurements, however, suggest a heterogeneous mantle source; this could be due to crustal contamination though the authors thought this was unlikely. Generally, the amphibolites were thought to have a MORB-like source, based on their geochemistry, but uncertainty of Archaean tectonic processes means further interpretation is difficult (Rollinson and Fowler, 1987). The authors used these geochemical data to model conditions of magma generation: the tonalites were interpreted to have formed from a wet partial melt (30% melting) of a basaltic source, leaving a

garnetiferous residue; the trondhjemite was modelled to have formed by partial (20-30%) melting of a geochemically evolved basaltic source, possibly the amphibolites, followed by fractional crystallisation of hornblende; the granitic gneiss was interpreted to also be formed by partial (10%) melting but under drier conditions and with addition of light REEs (Rollinson and Fowler, 1987). The tonalite and trondhjemite could both therefore have formed from the amphibolites but the granite was not derived from either (Rollinson and Fowler, 1987). The tonalite and trondhjemite both require melting under wet conditions so Rollinson and Fowler (1987) suggested a shallow-dipping subducting slab, agreeing with Tarney and Weaver (1987) and Rollinson and Windley (1980) who suggested this for the Scourie area.

As well as trying to understand how the protolith LGC rocks formed, various wokers have investigated how the protoliths evolved and gave rise to new bodies of rock. Castro (2004) showed that partial melting of the dominate tonalite gneiss in the Central Region could only form small amounts of granitic melt. The granite sheets in this area are K-rich and there is not enough K in the tonalites to generate them. He suggested mafic ferrodiorite sheets in the Northern Region may have contributed K and other elements in partial melting to form the granite sheets around the Laxford Shear Zone. Watkins et al. (2007) experimentally melted samples of typical amphibolite-facies biotite tonalite and hornblende tonalite from the region of the Laxford Shear Zone which were interpreted to berepresentative of the tonalites at the time of potassic granite formation. They also found that the potassic granite sheets from here could not have formed from partial melting of the tonalites.

Johnson et al. (2012) showed that the Central Region gneisses partially melted during the Badcallian tectonothermal event. They found evidence for this partial melting from the field relationships, petrography and geochemistry of large layered mafic-ultramafic bodies. Felsic sheets and quartz-feldspar pegmatites with coarse peritectic

clinopyroxene record are records of migmatisation of the metagabbroic rocks as they cross-cut layering in the mafic bodies. Whole-rock geochemistry linked these felsic melts with the source metagabbros and with the ultra-high temperature conditions in the Badcallian event, the partial melting of large volumes of TTG and mafic gneiss was inevitable. Field and petrographic evidence for this migmatisation in the TTG gneisses has been obscured by later reworking but the dry refractory nature of the large mafic-ultramafic bodies prevented them from being extensively reworked and enabled the preservation of the relationships of the felsic sheets and clinopyroxene-pegmatites to their host metagabbros.

Advances in understanding of metamorphic reactions and mineral stability fields and experimental work to create geothermometry and geobarometry systems allowed for estimates of pressures (P) and temperatures (T) of metamorphism in the Lewisian Gneiss Complex. Much work has been done to establish PT conditions in the Lewisian (e.g. Rollinson, 1979; Savage and Sills, 1980) using a variety of geothermometers and geobarometers (Wood and Banno, 1973; Wells, 1977; Lindsley, 1983) but only a few will be described here. Barnicoat (1983) deduced granulite-facies metamorphism in the Scourian rocks exceeded 1000°C and 8.5kbar from garnet-clinopyroxene ion-exchange thermometry, although he warned of problems with incomplete re-equilibration of thermometer minerals such as garnet, orthopyroxene and clinopyroxene as a result of very slow cooling after peak metamorphism. O'Hara and Yarwood (1978) found that PT conditions yielded by geothermobarometry were not necessarily peak metamorphic temperatures but reflected conditions at which diffusion stopped.

Sills and Rollinson (1987) used a variety of geothermometers and geobarometers on various lithologies to try and get PT estimates for Scourian metamorphism. Dependent on the calibration, the two-pyroxene geothermometer gave temperatures of 700-900°C for ultramafic granulites and 600-825°C for tonalitic granulites (Sills and Rollinson, 1987). Again, different calibrations gave a range of temperatures on the garnet-pyroxene

thermometer in ultramafic granulites while mineral textures were important here too: mineral grain cores gave temperatures of 700-900°C while symplectic overgrowths were around 600°C (Sills and Rollinson, 1987). Garnet-pyroxene can also be used as a geobarometer but requires quartz so Sills and Rollinson (1987) applied it to structurally related metasediments near Scourie and obtained pressures of 6.8-8.5kbar. Pressure estimates for the ultramafic granulites using less reliable geobarometers yielded a wide range of pressures from 1.8-12.2kbar; the authors suggest a range of 7.7-8.5kbar may be about right (Sills and Rollinson, 1987). Textural and geothermobarometric evidence suggested that the garnet-pyroxene system was 'frozen' at 750-800°C and 7-8kbar so the peak metamorphic conditions would have been slightly higher than this (Sills and Rollinson, 1987). They also investigated cogenetic Scourian tonalites and trondhjemites: ilmenite-magnetite oxygen thermometry indicated a magmatic temperature of 890-1030°C while hypersolvus feldspars gave a temperature of 1000°C (Sills and Rollinson, 1987). Cartwright and Barnicoat (1987) estimated granulite-facies metamorphism at Stoer in the Central Region from metasediments as having peak temperatures of 925-990°C and peak pressure of >11kbar.

Most of the PT estimate work has concentrated on the Scourian granulite-facies metamorphic event while relatively little has been done on later metamorphic events. Sills and Rollinson (1987) suggested Inverian retrogression occurred at ~600°C and tentatively estimated >500°C for Laxfordian metamorphism from muscovites in shear zones. Droop et al. (1999) used metasediments and other rocks from the Loch Maree Group to estimate Laxfordian PT conditions more precisely. They estimated 630°C and 6.5kbar from metapelites and 530°C from other rocks (Droop et al., 1999). Baba (1998) estimated PT conditions in the Proterozoic granulite-facies rocks of South Harris. From mineral textures he determined a metamorphic history of: prograde metamorphism with temperature increase the dominant factor; prograde metamorphism with pressure increase the

dominant factor; decompression retrogression; retrogression with shearing (Baba, 1998). He estimated peak metamorphic conditions of 800°C and 13-14kbar from metasediments (Baba, 1998). Baba (1999) subsequently found sillimanite inclusions in orthopyroxene indicating a peak temperature of 950°C.

Barnicoat (1987) proposed a new model for the cause of Scourian high-grade metamorphism – enhanced heat flow in the base of the crust from radionuclide decay together with tectonic crustal thickening. This went against previous suggestions that high-grade metamorphism is caused by enhanced mantle heat flow and an increase in magmatism (e.g. Oxburgh and Turcotte, 1974; Schuiling and Kreulen, 1979). In the Lewisian, it was previously suggested that intrusion of the tonalitic magmas were the cause of high-grade metamorphism but Barnicoat (1987) disagrees as he argues that the time elapsed between major magmatic activity and peak metamorphism (~200Ma) was too long. It should be noted though that this assumption is based on old Sm-Nd geochronology that may be incorrectly interpreted. His thermal models suggest a slow cooling rate as does the extent of re-equilibration of Scourian granulites (Barnicoat, 1987). He also argues against the alternative idea that mantle-derived CO_2 degassing was the cause of metamorphism as he calculated that the amount of CO_2 necessary would completely dehydrate the rocks and make stable isotope ratios homogeneous, neither of which is seen (Barnicoat, 1987). He pointed to the repeated sequence of metasediments and ultramafics mapped by Davies (1976) as evidence for the thrusting which caused tectonic thickening (Barnicoat, 1987). The model suggests a peak metamorphic temperature of 750-1075°C at 35km depth, dependent on the amount of radiogenic heat flow and that the Scourian rocks could have remained at a temperature of >900°C for more than 100Ma with a slow cooling rate of 1-2°C/Ma (Barnicoat, 1987).

The most recent (at time of thesis submission) attempts to constrain PT conditions in the LGC have involved using mineral equilibria modelling. Johnson and White

(2011) constructed pseudosections in THERMOCALC (Holland and Powell, 1998) for the bulk composition of a metagabbro and a metapyroxenite from near Scourie. Both have granulite-facies metamorphic assemblages so the calculated PT estimates are interpreted to reflect peak Badcallian conditions. They calculated conditions of 8.5-11.5kbar and 875-975°C. Furthermore, they interpreted near-isothermal decompression to pressures of 7-9kbar from the metamorphic peak as garnet in the metagabbro had decompression rims of plagioclase, orthopyroxene and magnetite. Their Badcallian PT estimates broadly agree with previous work. Zirkler et al. (2012) followed a similar approach in combining mineral equilibria modelling with petrographic observation to determine peak Badcallian conditions of >900°C and 13-16kbar from metasedimentary gneisses at Stoer, from the same suite of rocks analysed by Cartwright and Barnicoat (1987). The pressures are relatively high compared to the peak Badcallian pressure estimates of Johnson and White (2011) from metabasic rocks at Scourie, indicating that further work is required to properly constrain peak Badcallian PT condition. Petrographic characterisation of the metasediments by Zirkler et al. (2012) showed that there was hydrous retrogression of the peak granulite-facies assemblage, evidenced by retrograde growth of hornblende, biotite and other hydrous minerals. This retrogressive assemblage indicated PT conditions of 5-6.5kbar and 520-550°C; this was interpreted to reflect the Inverian event.

Geochronology

Another side of continued research into the Lewisian Gneiss Complex, which largely superceded geochemical and metamorphic investigations from the 1990s onwards, was isotope geochronology. The first geochronological investigation into the Lewisian Gneiss Complex was by Giletti (1959) who dated Laxfordian TTG gneiss and pegmatite from Laxford Bridge, yielding ages of ~1300-1500Ma, and a Scourian pegmatite from south of Scourie at ~2670-2770Ma, both by Rb-Sr dating. Giletti et al (1961) followed this up by using Rb-Sr and K-Ar decay systems to obtain dates of >2460Ma and ~1600Ma for a

Scourian pegmatite and Laxfordian rocks respectively. We now know that ages generated by these methods must be viewed with care: Ar is easily lost from the crystal lattice; Rb-Sr systems generally record cooling ages, which can of course vary widely with the ambient conditions, as well as being lost very easily from the crystal lattice (e.g. Wheeler et al., 2010); and Rb-Sr isochrons must also be constructed from undisturbed comagmatic rocks, not easily determinable in the Lewisian. For these reasons, these decay systems have largely fallen out of favour in studies of the Lewisian due to its polymetamorphic history, although some workers have subsequently tried it as a check for other systems (e.g. Chamberlain et al., 1986; Waters et al., 1990; Cliff et al., 1998). Pidgeon and Bowes (1972) made one of the earliest attempts at dating zircons using the U-Pb decay system, which was advantageous due to its high closure temperature and the robust nature of zircon. They obtained an age of 2700±20Ma for granulite-facies rocks from the Central Region (Pidgeon and Bowes, 1972). This technique was to come to the forefront in later decades.

The 1980s brought on a fresh pulse of dating work as isotopic systems became better understood and it was Sm-Nd that was at the forefront. Sm-Nd analysis can be performed on single minerals (if there is a spread in Sm/Nd ratios) or whole-rock analyses so it is relatively easy to carry out (Whitehouse et al., 1996). Hamilton et al. (1979) were the first to apply the Sm-Nd decay system to the Lewisian. They measured isotopic ratios in mafic and felsic gneisses from the Northern and Central regions and constructed a regression line to give an age of 2920±50Ma, which was interpreted as a protolith age. Humphries and Cliff (1982) also obtained an age of 2920±50Ma although this was solely from Scourian granulites. The Sm-Nd isotopes also gave an age of 2490±30Ma for the breakdown of garnet, interpreted as a cooling age, which suggests the isotopic system was still open and therefore liable to be affected, yielding isochrons of dubious importance (Whitehouse et al., 1996).

Sm-Nd dating led to detailed interpretations of crustal differentiation and growth, for example Burton et al. (1994) obtained mineral ages of ~3300Ma for hornblendite and ~2490Ma for trondhjemite at Gruinard. Whitehouse et al. (1996) later showed that many of the ages previously obtained from Sm-Nd dating (e.g. Waters et al., 1990; Cohen et al., 1991; Whitehouse, 1993; Burton et al., 1994; Whitehouse and Robertson, 1995) were of dubious importance due to the effects of later metamorphism, very large uncertainties and construction of spurious isochrons ('errorchrons') from non-cogenetic rocks. An important factor in dating magmatic protolith formation by single mineral dating is that the mineral must be in equilibrium with the parent magma but in the Lewisian, most minerals are in disequilibrium due to subsequent polyphase tectonothermal activity (Whitehouse et al., 1996). Rollinson and Gravestock (2012) investigated rare earth element (REE) patterns (including Sm and Nd) in clinopyroxenes from LGC mafic rocks and showed that they had been variably altered during the Badcallian granulite-facies metamorphism. This showed the potential unreliability of Sm-Nd dating of protolith formation and offered an explanation for the scattered pattern of whole rock isochron ages.

Whitehouse et al. (1996) constructed whole-rock isochrons from mafic gneisses and trondhjemites from Gruinard that they believed to be cogenetic from field evidence and obtained ages of 2943±91Ma and 2795±28Ma respectively. They interpreted that their whole-rock isochrons represented magmatic crystallisation while the mineral isochrons of previous workers either represented cooling ages or were affected by subsequent reopening of the Sm-Nd system by later tectonothermal activity (Whitehouse et al., 1996). Cliff et al. (1998) measured Sm-Nd ratios from the Outer Hebrides but they too encountered problems: in some samples, mineral data did not plot on an isochron with the whole-rock data and the authors acknowledged ambiguity in the closure behaviour of the Sm-Nd system.

As described above, the Sm-Nd dating technique is not without its problems. Dating using lead isotopes became the main approach to dating events in the Lewisian from the late 1980s onwards. At first it was used for comparison with Sm-Nd ages (Whitehouse, 1993; Whitehouse and Robertson, 1995; Whitehouse et al., 1997b). All early U-Pb dating work and much of the more up-to-date work was done by the thermal ionisation mass spectrometry (TIMS) technique, which involves extracting a particular part of a zircon and ionising it before mass spectrometry analysis (Parrish and Noble, 2003). By the late 1980s, however, the secondary ionisation mass spectrometry (SIMS) technique had been developed and was starting to be used for dating the Lewisian. This technique involves analysing isotopic composition using an ion microprobe (Ireland and Williams, 2003). SIMS has a good spatial resolution (~30μm) allowing it to analyse tiny parts of a zircon grain but the precision of dates obtained is not as good as TIMS which can achieve very small uncertainties although it does not have the spatial resolution of SIMS (Ireland and Williams, 2003).

SIMS made it possible to date individual chemical domains within zircons (e.g. cores, overgrowths), identified using cathodoluminescence imaging. Technological advances meant that this could be done by TIMS too though, by abrading or micro-milling out the relevant parts of the zircon (e.g. Krogh, 1982; Mattinson, 2005). Corfu et al. (1994) dated zircons from the Central Region by TIMS. They yielded ages of >2710Ma, interpreted as the timing of the granulite-facies event, and ~2480-2490Ma, interpreted to be the pre-dyke Inverian event (Corfu et al., 1994). Field evidence had suggested that the Inverian event was amphibolite-facies but Corfu et al. (1994) suggested it may have been granulite-facies to have caused the significant zircon U-Pb resetting. The authors also suggest that an influx of fluid in the Inverian event (field evidence from abundant pegmatites) may have aided zircon recrystallisation at upper amphibolite facies (Corfu et al., 1994). Field evidence suggested that the post-dyke Laxfordian event was amphibolite-facies and as zircon was

not believed to be affected at such pressure-temperature conditions, Corfu et al. (1994) used titanite and rutile to date this event, again by the U-Pb system. Granite sheets on the boundary of the Northern and Central Regions yielded titanite ages of >1754Ma while rutile and titanite from banded gneiss deformed in the Laxfordian produced an age of ~1670-1690Ma (Corfu et al., 1994). These minerals contained unusually high levels of uranium, thorium and lead which led the authors to conclude that metasomatism played a large part in the Laxfordian event (Corfu et al., 1994).

Whitehouse et al. (1997b) used the U-Pb system to try and resolve the controversy arising from the variance in Sm-Nd ages obtained from Gruinard (Burton et al., 1994; Whitehouse et al., 1996). SIMS Pb isotope data yielded an age cluster of ~2850-2750Ma reflecting a high-grade tectonothermal event that broadly correlated with the Sm-Nd work of Whitehouse et al. (1996). Corfu et al. (1998) also dated (using TIMS) rocks at Gruinard, which was interpreted to be at the southern limit of the Central Region based on the presence of a few patches of granulite-facies pyroxene-bearing gneisses. They suggested a granulite-facies event dated at ~2730Ma while the U-Pb data yielded no significant age to match the Inverian previously dated in the Scourie area of the Central Region (Corfu et al., 1998). The correlation of high-grade event dates led them to affirm the presence of Gruinard in the Central Region while they explained the lack of a date for the Inverian event at Gruinard as down to shielding from the amphibolite-facies rehydrating fluids (Corfu et al., 1998).

Another mineral that has been used for dating with the U-Pb system is monazite. Zhu et al. (1997) obtained monazite crystals that were trapped as inclusions inside large metamorphic garnets from a metasediment near Scourie. They argued that the garnet acted as a buffer, protecting the monazite from later amphibolite-facies reworking (i.e. the Laxfordian) and would date granulite-facies metamorphism (Zhu et al., 1997). SIMS dating of monazites yielded two age clusters at ~2740Ma and ~2400-2500Ma, which were

interpreted as two granulite-facies events (Zhu et al., 1997). Monazites that were not protected by garnet yielded Laxfordian ages of ~1750Ma (Zhu et al., 1997).

U-Pb dating was used by Heaman and Tarney (1989) on baddeleyite to date the intrusion of the Scourie Dykes. This dating by TIMS yielded age clusters of 2418+7/-4Ma for norites and bronzite picrites and 1992+3/-2Ma for olivine gabbros and Fe-rich dolerites (Heaman and Tarney, 1989). The reliability of these ages is uncertain as the behaviour of baddeleyite in complex geological environments is poorly understood. Furthermore, field evidence shows that the 2418Ma picrite dykes actually cross-cut the 1992Ma Fe-dolerite dykes (Tarney, 1973).

As more and more isotope dating work was carried out, the traditional three-region model with granulite-facies Badcallian and amphibolite-facies Inverian pre-dyke events and the post-dyke amphibolite-facies Laxfordian was beginning to be questioned. This mainly stemmed from U-Pb ion microprobe (SIMS) dating from the mid-1990s onwards (Friend and Kinny, 1995; Kinny and Friend, 1997; Friend and Kinny, 2001; Love et al., 2004; Kinny et al., 2005; Love et al., 2010). Kinny and Friend (1997) suggested that the Lewisian Gneiss Complex was composed of distinct crustal blocks and redefined them as disparate terranes separated by crustal-scale shear zones (Friend and Kinny, 2001). Their work initially focussed on the Northern and Central Regions and their boundary at the Laxford Shear Zone (LSZ) (Kinny and Friend, 1997). They obtained protolith ages of ~2680-2840Ma from the north and ~2960-3030Ma from the south (Kinny and Friend, 1997); granulite-facies metamorphism was dated to the south of the LSZ at ~2490Ma, while the Northern Region was never believed to have reacged granulite-facies metamorphic conditions (Friend and Kinny, 2001).

Kinny and Friend (1997) suggested that the first common dateable event from either side of the LSZ was the Laxfordian at ~1750Ma. They used this to argue against the previously-held view that the Northern Region rocks were the same as the Central Region

but had suffered pervasive Laxfordian reworking (Kinny and Friend, 1997). Assuming that metabasic sheets seen in the Northern Region were transposed equivalents of the Scourie Dykes, they suggested that the two crustal blocks docked some time between the Inverian event (no geochronological evidence for it in the Northern Region) and the intrusion of the Scourie Dykes (Kinny and Friend, 1997). Friend and Kinny (2001) subsequently proposed that the terrane docking event was what caused Laxfordian metamorphism and deformation. This was based on isotopic ages of 1854±13Ma for granite sheets that they believed occurred only on the north side of the LSZ.

Friend and Kinny (2001) interpreted that two terranes amalgamated during the Laxfordian tectonothermal event. Goodenough et al. (2010) later showed that the granite sheets dated by Friend and Kinny (2001) actually occur south of the LSZ as well and the shear zone itself showed two generations of structures interpreted to be Inverian and Laxfordian. This led to the suggestion that the blocks amalgamated in the Inverian with some reactivation in the Laxfordian (Goodenough et al., 2010). Friend & Kinny (2001) tested U-Pb zircon isotope data to see if correlations could be made between the mainland and the Lewisian of the Outer Hebrides. They obtained an age of 1672±8Ma for granite sheets in North Harris and suggested that they therefore should not be correlated with those of the Northern Region on the mainland, which were dated at 1854±13Ma (Friend and Kinny, 2001). They suggested that the ~1740Ma Laxfordian event occurred in much of the Outer Hebrides but that South Harris (interpreted to be a separate terrane due to granulite-facies metamorphism at ~1880Ma) accreted some time after ~1675Ma, the age for one of its bounding shear zones (Friend and Kinny, 2001).

Love et al. (2004), using the same ion microprobe technique, dated rocks from Gruinard to try and prove if the Lewisian rocks there could be correlated with the rest of the Central Region. They obtained a protolith age from Gruinard of ~2820-2850Ma with high-grade metamorphism at ~2730Ma and no isotopic evidence for an event around

~2490Ma (Love et al., 2004). From Badcall Bay in the northern part of the Central Region, they struggled to obtain any clear dates as isotopic disturbance was extreme at ~2480Ga interpreted to be due to a granulite-facies tectonothermal event (Love et al., 2004). This led them to interpret that Badcall and Gruinard were from different terranes with the boundary being the Strathan Line, a 15m-wide shear zone just south of Lochinver (Love et al., 2004). They dated rocks from either side of this structure and interpreted the isotopic data to show that this was indeed the boundary. The rocks to the south of the Strathan Line correlate with Gruinard while those to the north appear to correlate with Badcall (Love et al., 2004). The authors suggest that terrane accretion between Gruinard and Assynt was the Inverian event despite the fact that there was no isotopic signature at such a time from Badcall or Gruinard (Love et al., 2004) and one would expect terrane docking to generate deformation and metamorphism which would be recorded in the isotopic systems. Furthermore, the Inverian event is believed to be more widespread than the Lochinver area, with Inverian fabrics recognised at Torridon in the Southern Region (e.g. Cresswell, 1972; Wheeler et al., 1987) and the Laxford Shear Zone between the Northern and Central Regions (Goodenough et al., 2010).

Commenting on Love et al. (2004), Corfu (2007) suggests that the isotope regression lines for Badcall indicate that there must be a tectonothermal event at ~2800-2600Ma if the ~2480Ma event identified by Love et al. (2004) is a 'real' event. Corfu et al. (1994) specifically suggested this was at ~2720Ma. He also points to the monazite data of Zhu et al. (1997) as further evidence of a granulite-facies metamorphism around this time (Corfu, 2007). As for Gruinard, Corfu (2007) suggests that Love et al. (2004) have misinterpreted both field evidence and zircon morphology and emphasises the complexity of zoning and poorly understood nature of zircon, and the problem of linking zircon data directly to field relationships. In reply, Friend et al. (2007) defend their interpretation (Love et al., 2004) of no inheritance in the zircons from Gruinard as the trondhjemites in which

they are found are undersaturated in zirconium so any inherited zircons would recrystallise as new magmatic zircons and inheritance is therefore unlikely. Corfu (2007) argues that SIMS cannot validate the precise ages obtained by TIMS while Friend et al. (2007) contend that TIMS can yield mixed ages as it cannot always distinguish between distinct zircon zones.

Following all this ion microprobe dating work (Friend and Kinny, 1995; Kinny and Friend, 1997; Friend and Kinny, 2001; Love et al., 2004), Kinny et al. (2005) formalised a model where the Lewisian Gneiss Complex is composed of disparate terranes with different formation and metamorphic histories which amalgamated during a common tectonothermal event. In this paper they offered revised definitions of some existing nomenclature while suggesting the abandonment of many other names that had become obsolete, were essentially duplicates or did not fit their new model (Kinny et al., 2005). They presented a map (Fig. 2.7) showing all their different terranes and essential dates related to each as well as brief descriptions of each terrane and their sutures (Kinny et al., 2005).

Park (2005), in commenting on this model, lauded the authors for attempting to rationalize the terminology associated with the Lewisian but disagreed with their suggestion that the term 'Laxfordian' should be applied only to a ~1740Ma metamorphic event and instead preferred its traditional use as covering all events following the Scourie Dyke intrusion. He also prefers to use the term 'block' as opposed to 'terrane' as used by Kinny et al. (2005) as 'terrane' implies great amounts of translational movement for which there is no evidence (Park et al., 2005). In the discussion, Park (2005) tentatively suggests a two-plate model with subduction in the Palaeoproterozoic (evidenced by arc material e.g. the ~2000Ma Loch Maree Group (Whitehouse et al., 1997a)) with rearrangement into crustal blocks during the Laxfordian event. He suggests that the present geochronological

data fail to show any major distinction between different parts of the Lewisian Gneiss Complex with the exception of Assynt (Park et al., 2005).

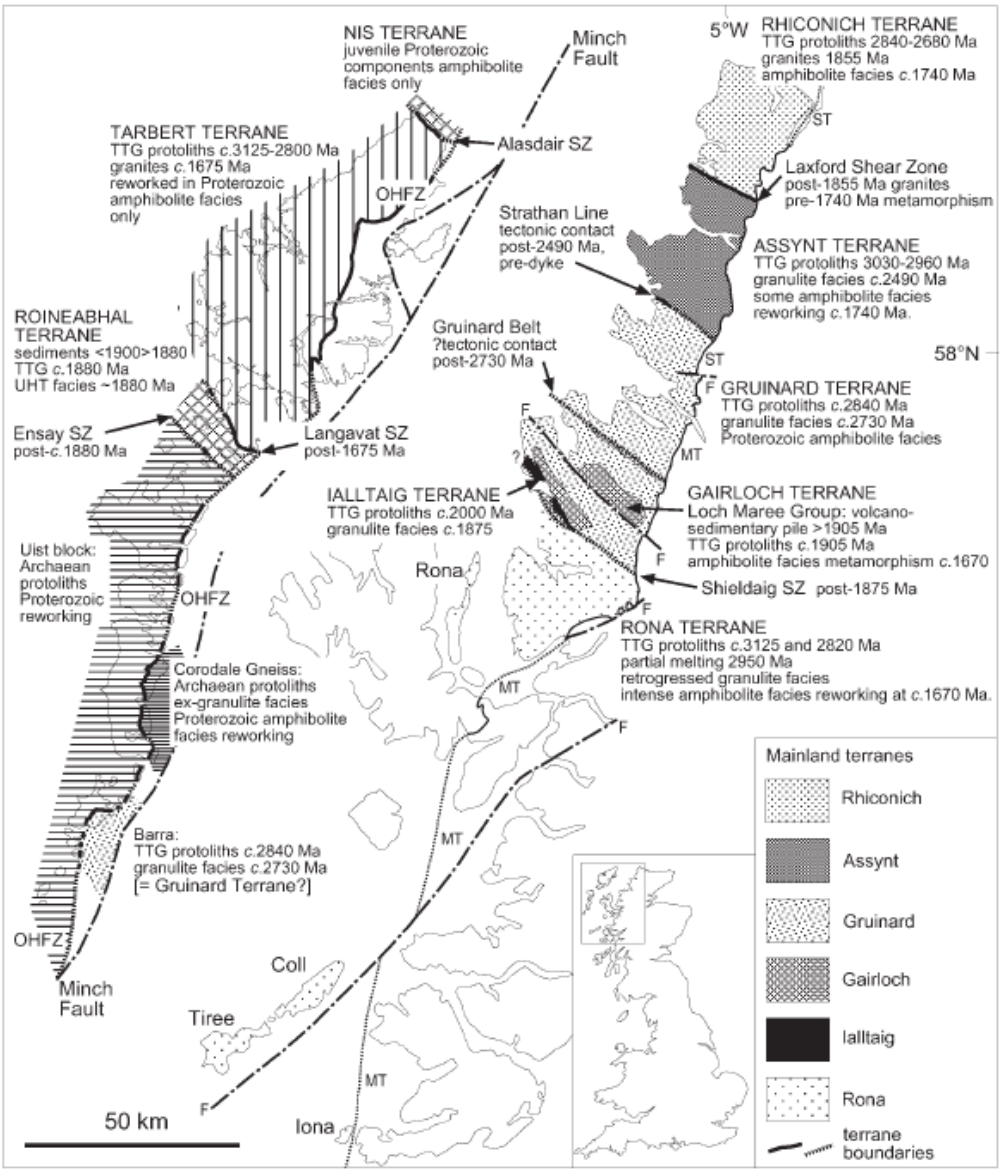

Fig. 2.7 Terrane model for the Lewisian suggested by Kinny et al. (2005).

In reply, Kinny et al. (2005) defended their redefinition of the term 'Laxfordian' and maintained that its blanket use for anything postdating the dykes can lead to confusion of wholly separate events and features. They argue that the lack of Palaeoproterozoic plutonic rocks precludes the idea that the Lewisian Gneiss Complex was involved directly in subduction (Park et al., 2005). They instead suggest that the 'terranes' of the Lewisian were somewhere outboard of the subduction zone and the arc is no longer visible, analogous the

Cordilleras of North America (Park et al., 2005). As for the two-plate model, Kinny et al. (2005) point to a lack of granulite-facies gneisses in possible lower-plate areas as a problem with that model, as well as Sm-Nd isotope data suggesting crustal differentiation at different times in different parts of the Lewisian (e.g. Whitehouse, 1989).

Park (2005) subsequently expanded on his two-plate model by assigning the terranes of Kinny et al. (2005) to either an upper or lower plate or as Palaeoproterozoic arc complexes (Fig. 2.8). He defined upper plate blocks as being characterised by retrogressed granulite-facies Archaean rocks with localised Laxfordian deformation while the lower plate blocks were amphibolite-facies, originating at a higher crustal level. The upper plate blocks are Gruinard, Ruadh-mheallan, Tiree-Coll and East Uist while Assynt (which yielded older protolith ages than elsewhere) was interpreted to have joined them in the Inverian event. The lower plate blocks are Rhiconich, Carnmore-Tollie, Rona, West Uist and Tarbert (Fig. 2.9). SIMS dating by Kelly et al. (2008) supports correlation within the Lewisian and less in the way of disparate terranes but they suggest Tarbert may be correlated with Gruinard as the share a tectonothermal event at ~2730Ma. Kinny et al. (2005) thought Tarbert and Rhiconich could not be correlated due to different ages of the granite sheets in each terrane although Park (2005) suggests that the differing ages may be caused by different melt phases. In terms of the Palaeoproterozoic arc rocks, the structure of the Roineabhal terrane is synformal so the Tarbert and West Uist blocks are interpreted to be contiguous, backed up by U-Pb isotope TIMS dating by Mason et al. (2004) who, despite some ambiguities in the isotopic data, suggested protolith ages for both as being ~2800Ma. The Nis terrane also has a synformal structure so may be contiguous with the Roineabhal terrane (Fig. 2.10). Park (2005) also interpreted that the Loch Maree Group could also have been part of the same block with later disruption by the Outer Hebrides and Minch faults. The synformal structures may have been caused by late Laxfordian folding. Park (2005) suggests that one terrane may have multiple TTG protolith ages from multiple intrusive

events, as well as effects on ages from magmatic assimilation & fractionation, something not considered by Kinny et al. (2005). Furthermore, care must be taken when using tectonothermal events for correlation as lithology, strain variation and amount of fluid may be heterogeneous but could all influence interpretation.

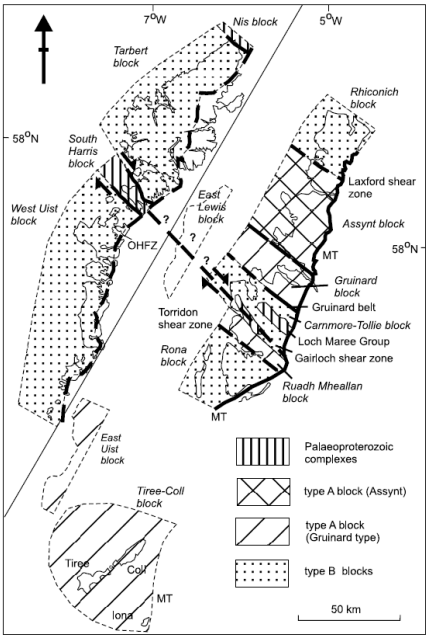

Fig. 2.8 Revised terrane model from Park (2005) showing upper plate (type A), lower plate (type B) and Palaeoproterozoic arc complex areas.

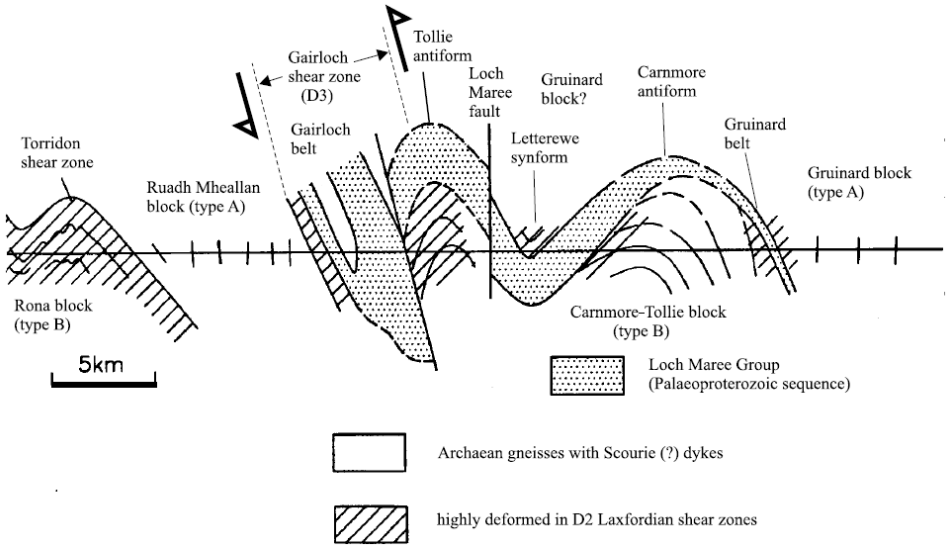

Fig. 2.9 Structural relationships between upper plate (type A) and lower plate (type B) blocks in the Southern mainlaind Lewisian, from Park (2005).

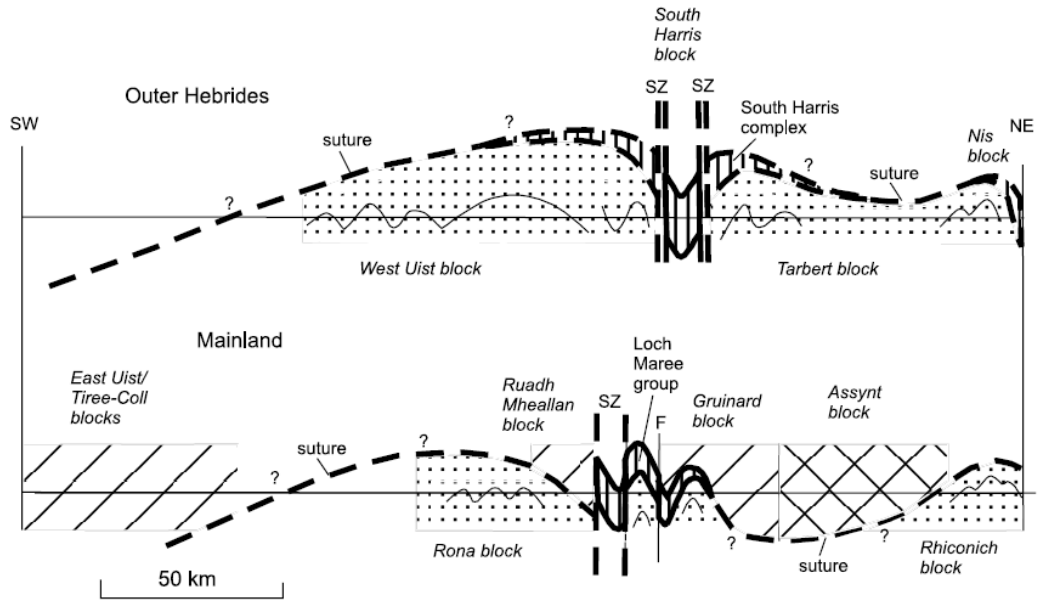

Fig. 2.10 Wider structure of the mainland and Outer Hebrides Lewisian and possible correlation, from Park (2005).

Another aspect of research into the Lewisian Gneiss Complex has been looking for comparisons with other similar geological areas. This was recognised in the title and content of the proceedings of the 2nd Lewisian conference of 1972. In this volume are several articles on Precambrian rocks in Greenland and attempts were made to correlate them with the Scottish Lewisian Gneiss Complex. The geology of southern Greenland is composed of a central Archaean block, which was last affected by regional metamorphism at ~2500-2700Ma, flanked to the north by the Nagssugtoqidian mobile belt and to the south by the Ketilidian mobile belt, both of which were most recently deformed at ~1700-1900Ma (Andrews et al., 1973). All three are composed of polymetamorphic TTG gneisses and have a dolerite dyke suite that separates early and late regional metamorphism (Andrews et al., 1973). Individual rock types of the Angmagssalik area of southeast Greenland are very similar to equivalents in the Lewisian such as folded supracrustals correlating with South Harris or the Loch Maree Group (Wright et al., 1973). The Archaean gneisses at Angmagssalik belong to the Nagssugtoqidian, which is petrologically and geochronologically (Andrews et al., 1973) similar to the Laxfordian gneisses of the Lewisian (Wright et al., 1973). Andrews et al. (1973) considered the gneisses around Frederikshab in

southwest Greenland, part of the Archaean block, to be very similar to the Central Region of the mainland Lewisian.

The 3rd Lewisian conference of 1985 brought about further insights into correlations with Greenland and further afield. Myers (1987) correlated the Lewisian with the Nagssugtoqidian mobile belt of Greenland as they share a similar history, deduced from field relationships and recorded in isotopic ages. The Nagssugtoqidian formed around ~2900-2700Ma with metamorphism and deformation around ~2600-2300Ma, followed by intrusion of a mafic dyke suite and then further regional metamorphism at ~1900-1700Ma which reflects the evolution of the Lewisian fairly closely (Myers, 1987; Kalsbeek et al., 1993). Korstgard et al. (1987) appear to correlate the central Archaean block of Greenland with the Lewisian on a map in their paper, despite not making any specific references to the Lewisian Gneiss Complex. The Lewisian and southern Greenland were also correlated with the Nain Province of Labrador in Canada (Korstgard et al., 1987). Park (1994) looked for wider correlations in the North Atlantic region. He found that many of the Precambrian shield regions in this area shared metamorphic and deformation histories or were in tectonically-related settings. All recorded an orogenic event at ~1900-1600Ma, which was interpreted to have been caused by the collision of the Malin block with Laurentia and Baltica (Fig. 2.11).

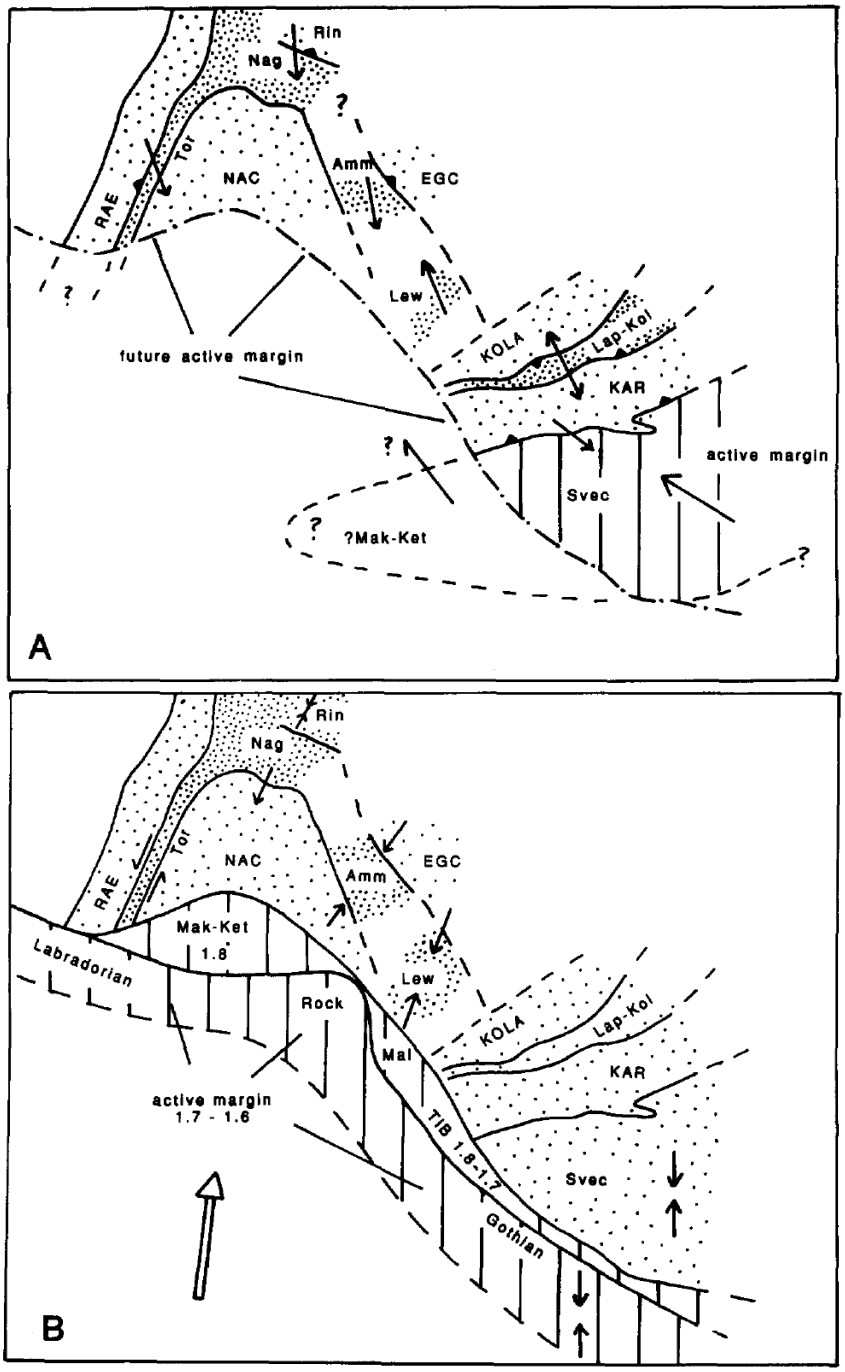

Fig. 2.11 Speculative plate kinematic models for the periods 2000-1800Ma (A) and 1800-1600Ma (B), after Park (1994). Abbreviations: *EGC=E* Greenland craton; KAR=Karelia craton; *Lap-Kol=Lapland-Kola* belt; *Rin=Rinkian* terrain; *Tor=* Torngat belt; *Mal=* Matin block; *NAC= N* Atlantic craton; *Mak= Makkovik; Ket= Ketilidian; Nag= Nagssugtoqidian; Amm=Ammassalik; Lew=* Lewisian; Svec= Svecofennian; *TIB=* Trans-Scandinavian igneous belt; *GGF=* Great Glen fault; *HBF=* Highland Boundary fault; B= BABEL deep seismic reflection line. At 1900-1800Ma: cratons, open stipple; tectonically active intracontinental belts, close stipple; magmatic arc terrain at the active continental margin, oblique ruling. Arrows represent main directions of upward tectonic transport within the Early Proterozoic belts; black triangles indicate inferred dip of margins of continental blocks. (B) At 1800-1600Ma: cratons and active intracontinental belts ornamented as in (A).

In his reinterpretation of the Kinny et al. (2005) terrane model, Park (2005) offered some further suggestions on wider North Atlantic correlations and palaeogeography (Fig. 2.12). In his upper- and lower-plate model, he suggests that the two plates that collided were the Central Greenland Craton and North Atlantic Craton and that the Lewisian is equivalent to Nagssugtoquidian of Greenland, which were both caught up in this orogeny, which caused the Laxfordian event in the Lewisian. He put forward the following sequence of events:- 1) the Palaeoproterozoic arc rocks (Roineabhal & Nis terranes, Loch Maree Group) accreted to upper plate at ~1900Ma; 2) Plate collision and subduction at ~1870Ma generating the calc-alkaline plutonic rocks of Roineabhal, Nis and Loch Maree with early Laxfordian metamorphism; 3) Malin arc collides with Lewisian at ~1740Ma generating widespread metamorphism and deformation, causing disruption of plates and rearrangement into present situation along major shear zones.

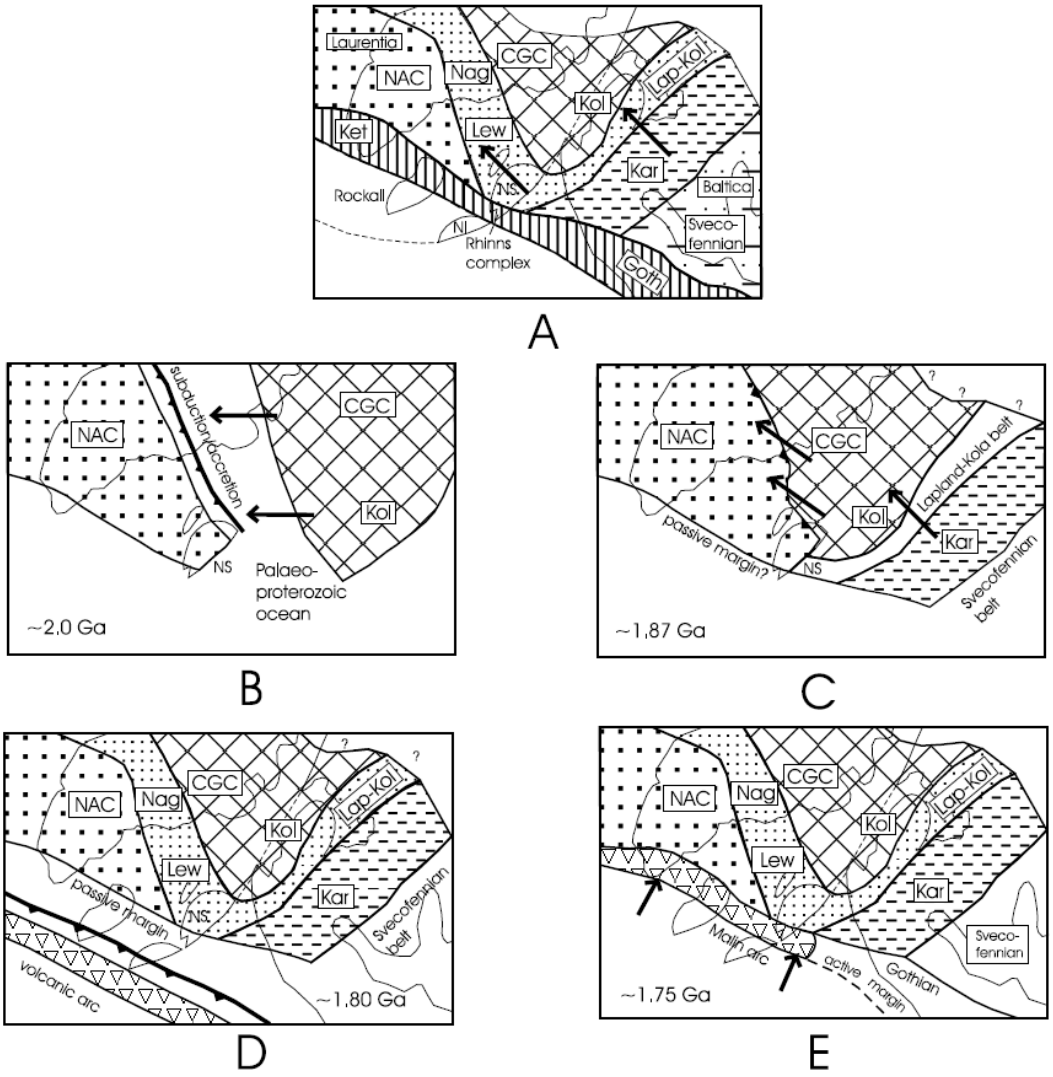

Fig. 2.12 The Lewisian in its wider Precambrian context, from Park (2005). CGC, central Greenland craton; Goth, Gothian belt; Kar, Karelia craton; Ket, Ketilidian belt; Kol, Kola craton; Lap-Kol, Lapland–Kola belt; Lew, Lewisian; NAC, North Atlantic craton; Nag, Nagssugtoqidian belt; NI, north Ireland; NS, north Scotland. (A) Distribution of cratons and orogenic belts during the Mesoproterozoic. (B) At 2000Ma: subduction and creation of a volcanic arc in oceanic crust between two continental plates (NAC and CGC/Kol) followed by accretion of oceanic/arc elements along the leading edge of the NAC. (C) At 1870Ma: collision of the two continents followed by underthrusting of the CGC/Kol craton beneath the NAC, causing the early Laxfordian deformation and metamorphism. At the same time, collision occurs in the Lapland/Kola belt to the SE caused by collision with the Karelia craton. Note the NW–SE movement direction. (D) At 1800Ma: development of a volcanic arc in oceanic crust SW of the amalgamated continent created in B. (E) At 1750Ma: collision between the 'Malin arc' and the continent, causing late Laxfordian deformation, metamorphism and granitic melt formation in the Lewisian complex.

3. Methodology

A variety of analytical techniques were used during the PhD work and all are fully described in this chapter. These range from basic geological mapping through to chemical microanalysis. The provisional workflow at the commencement of the project was: mapping, sampling, optical/SEM petrography, EBSD, ion microprobe analysis. Other analytical techniques have subsequently been used and the workflow has not been a step-by-step process – multiple techniques were often used concurrently as different samples were at different stages of the workflow. Each analytical technique is described in the following sections.

Mapping

Field mapping was an essential part of the project as the general geology and field relationships must be understood so as to give further analysis a clear context. Lithology, mineral assemblages, mineral fabrics and other structures build up a picture of the geological history of the rock; once this is known, the results of geochemical and microstructural analysis can be linked to the mapped rocks to show how zircons responds under different geological conditions.

Mapping was generally of relatively small areas, between ~1km^2 and 35m^2. Some mapped localities were sites described in the literature while others were identified as suitable for this study by ground reconnaissance of large areas. The criterion for choosing localities to map was unambiguously-displayed field relationships between lithologies and structures of different age, where the relative ages were clear.

Mapping was carried out either by traditional means, using a paper base-map and GPS, or using the SigmaMobile software from the British Geological Survey on an iXplore tablet computer. The tablet computer enables mapping at a variety of scales on the same base-map, which is very useful for detailed maps of very small areas while also making a

larger context map for that detail map. Multiple base-maps can be used and all can be geo-referenced, which, along with the built-in GPS system, means that the position of the user, and hence their map, is always known. The GPS system is precise to 1m and accuracy was consistently checked by comparison of the GPS location marker to the topographical surroundings of the user's position. For some of the very detailed small-scale maps, a measuring tape and graph paper were used as the detail was beyond the resolution of the GPS and any base-map.

Sampling

As well as recording the geological history of each locality, detailed field mapping also provided a framework for strategic sampling for further analysis. Samples were taken mainly from the rocks that were most likely to contain zircons: felsic-intermediate meta-igneous gneisses and metasediments. Occasionally samples were taken from mafic lithologies if their identity was unclear in the field and required petrological investigation.

Once a rock had been selected for sampling, a suitable part of the outcrop was sought. Every effort was made to collect samples of similar sizes and homogeneous composition but this was difficult, again due to the hard and often isotropic nature of the rocks. Samples were ~1000-2000cm^3 in size. Before the sample was broken off, an orientation mark was marked on a surface of the sample in black marker pen. The dip and strike of this mark was measured and noted. This enabled future analysis where a kinematic reference frame was required.

Sample Preparation

It was desired that zircons would be analysed in-situ where possible to give a petrographic context to to the isotopic and trace element data acquired from the zircons. This required preparation of thin and thick sections. Samples were cut using a rock-saw with a slow diamond grinding blade at the University of Liverpool. Thin-section sized pieces

of the samples were sent to be made into standard 30µm-thick polished thin sections at the University of Birmingham or University of Keele. Comparable pieces were also made into polished thick sections at University of Liverpool; these were manually polished with carborundum powder at 400-1200 grade then with 1-6µm Buehler Metadi Diamond Suspension on a Kent 3 Automatic Lapping and Polishing Unit. Thin and thick sections which were subject to electron backscatter diffraction (EBSD, see below) analysis were also polished with 0.25µm Syton™ colloidal silica solution.

Petrography

Thin sections were analysed with a Vickers polarising transmitted light optical polarising microscope for petrographic textures in order to build up a history of the sample. Photomicrographs of important mineral textures were taken using a Nikon Coolpix 4500 digital camera attached to a Zeiss polarising transmitted light optical microscope.

Mechanical zircon separation

In order to augment analysis of in-situ zircons, samples were also crushed and zircons separated from them at Trinity College Dublin. Samples were broken using a hydraulic rock splitter followed by a jaw crusher which reduced them to sand grade. The sand was the sieved to <500µm size and saturated with water; this was then run across a vibrating Wilfley water table to separate heavy and light grains. Following overnight drying in the oven, the heavy fractions were passed through methylene iodide separating grains heavier (such as zircon) and lighter than a specific gravity of 3.3. The heavy fraction was caught in filter paper, allowing the methylene iodide to pass through and be recycled; it was then thoroughly washed in acetone to remove any that may have remained attached to the grains. Magnetically susceptible grains such as magnetite were removed with a hand magnet and the remaining fraction was passed through a Frantz isodynamic separator which separated titanite and any quartz, feldspar and apatite grains that got through the

separation process. Zircon grains were then hand-picked out of the separates for analysis under a Leica DMLP reflected light microscope at the University of Edinburgh; large, fracture- and inclusion-free translucent grains were selected. These grains were mounted in Epothin epoxy resin in a one-inch diameter aluminium holder. This grain mount was then polished with 400-1200 grade Struers Silicon Carbide grinding paper, Buehler Metadi Diamond Suspension at 1-6µm and 0.25µm Syton colloidal silica solution.

Scanning Electron Microscope Analysis

Before analysis, samples were coated with a very thin layer of graphite and earthed using colloidal graphite paint. Samples were analysed using a Philips XL30 Scanning Electron Microscope (SEM) at the University of Liverpool. The Philips SEM is a 'conventional' SEM that has a vertical column and horizontal stage, which can be tilted if necessary thus making it versatile for a number of different types of imaging. The electron beam is generated from a tungsten filament, which passes electrons through a condenser lens, an objective lens, and between the scan coils before passing through the final aperture and the pole piece into the chamber. Each lens focuses the beam magnetically and the aperture reduces the intensity of the beam. The scan coils of the microscope alter the angle of the beam in a systematic fashion; this enables the software to reconstruct an image based on where the beam was pointing and what intensity was detected at any given point in time. The interaction of the electron beam with the near surface of the minerals in the specimen produces a suite of electrons and other radiation that can be used to characterise the sample (e.g. Lloyd and Hall, 1981; Prior et al., 1999). A different volume of the sample – the activation volume – is responsible for the generation of each type of radiation and each type can be 'imaged' using different detectors. Backscattered electrons and cathodoluminescence are two types of interactions that were used to image samples in this project.

BSE Imaging

In-situ zircons were located using backscattered electron (BSE) imaging. Backscattered electrons have a high energy and therefore travel in straight lines from the sample surface. They are generated by scattering of the electron beam by a single large interaction or several smaller interactions within the sample but retain most of their energy and are able to exit the specimen (Lloyd and Hall, 1981). Solid-state detectors are mounted on either side of the pole piece and enable imaging of electrons scattered directly back from the sample. Atoms with a larger atomic number (proton number) have more electrons so there are more electrons to scatter those from the beam making heavier elements appear brighter. Since the unit cell of the material in the sample surface is usually smaller than the diameter of the electron beam and the activation volume, the brightness of the response is averaged over all the different types of atom in the sample producing images of mean atomic number (Z-contrast). As a result, minerals containing elements with a high atomic number appear brighter than those without; for example, zircon with its high concentration of element 40, zirconium, appears much brighter than plagioclase where the heaviest formula element is element 20, calcium. In most samples, the presence of zirconium meant that zircons were the brightest mineral in the sample and could therefore be located easily. Photo images were taken at a working distance of ~22mm, accelerating voltage of 20kV and an emission current of ~3nA. BSE imaging was also used to show major-phase mineral textures, which elucidated the textural history of the sample.

Cathodoluminescence Imaging

All zircons were imaged using cathodoluminescence (CL). When the SEM electron beam hits the sample surface, as well as scattering electrons, electromagnetic radiation is produced. When electrons in the outer shell of an atom are displaced, photons of visible light – cathodoluminescence – are produced. CL emmittance can be 'quenched' by the presence of Fe^{2+} so ferromagnesian minerals do not luminesce. The activation of CL in other

minerals is variably understood. In zircon, it is thought to arise from lattice defects and vibration of the uranyl ion but mainly from trivalent rare earth elements, particularly Dy^{3+} (Corfu et al., 2003). CL is traditionally used to show internal chemical zoning in zircon – the brighter and darker CL responses due to varying levels of REEs are interpreted to represent different growth or recrystallization domains. This zoning is used as a guide for ion microprobe analysis (see below) – analytical ablation spots should not overlap different zones so that the data gathered represent a single event. CL images were taken at a working distance of 21-23mm, accelerating voltage of 10kV and spot size of and an emission current of ~3nA.

Energy Dispersive X-Ray Spectroscopy

Another SEM-hosted technique used was Energy Dispersive X-Ray Spectroscopy (EDS). X-ray radiation is emitted when the incident electron beam hits the sample; the spectrum of energies of the X-rays emitted is characteristic of the elements present and the number emitted for given conditions is proportional to the concentration of each element. Measurement can be qualitative or quantitative if calibrated against known standards. EDS records the energy of the X-rays produced from a point using a Li-doped Si crystal. Electron holes are created in this semi-conducting crystal when an x-ray hits it; the number of holes is proportional to the energy of the X-rays. Applying a potential allows a current to flow that is proportional to the number of holes, thereby measuring the energy of the last X-ray to strike the crystal. After counting X-rays for a given time the spectrum is analysed for peaks. Once the peaks are identified the size of each peak is measured against the standard calibration to calculate the concentration of each element. All the X-rays are measured on the same spectrometer so one analysis records all elements.

EDS was carried out using the Philips XL30 SEM at the University of Liverpool. Qualitative analysis was widely used for confirming whether bright crystals imaged in BSE were in fact zircons. Semi-quantitative EDS was conducted on major phases in various

samples to determine the major element chemistry and provide further information about the sample history. Repeat analyses of a cobalt standard were conducted throughout the analytical session to ensure beam conditions were stable. Measured spectra were compared to standards to determine element abundances. Detection limits for the major elements measured were ~0.5wt%. Analytical precision was generally <10% (95% confidence levels) for concentrations >1wt% but higher for concentrations <1wt%.

EBSD

Electron backscatter diffraction (EBSD) analysis was carried out in a CamScan X500 Crystal Probe SEM at the University of Liverpool. The CamScan SEM varies from the aforementioned Philips SEM as it uses a field emission gun to generate the electron beam and the column is angled at 70° to the sample surface. This layout is not very flexible for different types of analysis but is instead optimised for EBSD. When the incident electron beam interacts with the activation volume, cones of electrons are diffracted off the lattice planes and onto a phosphor screen detector. The pattern of bands (Kikuchi bands) generated by electrons hitting the phosphor screen are referred to as electron backscatter patterns (EBSPs). These patterns are then digitally indexed by software to determine the phase and crystallographic orientation quantitatively. EBSPs were acquired with Flamenco software which processes the EBSPs with a series of algorithms and compares them to a database of match units to identify the phase. Each crystal or area of sample was acquired individually using the automatic mapping function in Flamenco software where the beam rasters across a specified area. Acquisition parameters including binning, Hough space and V/H ratio were refined for each map; match units for mineral phases were taken from the American Mineralogist library preloaded in the Flamenco program. The spatial resolution of the Camscan SEM is ~0.5µm for zircon while the precision in measuring the crystallographic angles is ±0.5° and accuracy is ±2°.

Once acquired, raw data files were processed in CHANNEL5 software, mainly using the Tango module. This allows a map of the data of the acquisition area to be constructed showing different datasets: band contrast – the pattern quality of the Kikuchi bands for each pixel; all-euler angles – the crystallographic angles of each pixel; and Texture Component – a plot of crystallographic orientation relative to a reference point. The Texture Component function was particularly useful in highlighting intracrystal lattice misorientation. Tango allows the dataset to be cleaned-up – pixels of poor pattern quality can be removed, single pixels of misindexed data can be removed and interpolation between good data points can be used to improve coverage and subsequent interpretation.

X-Ray Fluorescence Analysis

X-Ray Fluorescence (XRF) analysis was carried out at the University of Edinburgh in order to determine the bulk chemistry of the rocks from which analysed zircons were taken. Samples were taken adjacent to those that had already been processed for zircon analysis. The XRF methodology largely follows that of Fitton et al. (1998) and is described below. The samples were cut into small pieces with a diamond-tipped saw, saw marks were ground away on a diamond wheel, and the fragments were rinsed in clean water. They were then dried before being ground to a fine powder in an agate Tema barrel. Agate was used in preference to tungsten carbide to avoid contamination with Ta and Co. Major-element concentrations were determined after fusion with a lithium borate flux containing La_2O_3 as a heavy absorber, similar to Fitton et al. (1998).

The rock powder was dried at 110°C for at least one hour, and a nominal but precisely weighed 1g aliquot was ignited at 1100°C so as to determine loss on ignition (LOI). The residue was then mixed with Johnson Matthey Spectroflux 105 in a sample-to-flux ratio of 1:5, based on the unignited sample mass, and fused at 1100°C in a muffle furnace in a Pt5%Au crucible. After the initial fusion, the crucible was reweighed and any flux weight loss was made up with extra flux. After a second fusion over a Meker burner, the molten

mixture was swirled several times to ensure homogeneity, cast onto a graphite mould, and flattened with an aluminium plunger into a thin disk. The mould and plunger were maintained at a temperature of 220°C on a hotplate. Trace-element concentrations were determined on pressed-powder samples. Six grams of rock powder were mixed thoroughly with four drops of a 2% aqueous solution of polyvinyl alcohol. The mixture was formed into a 38-mm disc on a 40-mm diameter polished tungsten carbide disc, backed and surrounded by aluminium, and compressed in a hydraulic press at 0.6 tons/cm^2.

The fused and pressed samples were analyzed using a Philips PW2404 automatic X-ray fluorescence spectrometer with a Rh-anode X-ray tube. Corrections for matrix effects on the intensities of major-element lines were made using theoretical alpha coefficients calculated online using the Philips software. The coefficients were calculated to allow for the amount of extra flux replacing volatile components in the sample so that analytical totals should be 100%, less the measured LOI. Intensities of the longer-wavelength trace-element lines (La, Ce, Nd, Cu, Ni, Co, Cr, V, Ba, and Sc) were corrected for matrix effects using alpha coefficients based on major-element concentrations measured at the same time on the powder samples. Matrix corrections were applied to the intensities of the other trace-element lines by using the count rate from the Rh Kα Compton scatter line as an internal standard (Fitton et al., 1998). Line-overlap corrections were applied using synthetic standards.

The analytical reproducibility and precision of major elements (Si, Al, Fe, Mg, Ca, Na, Ti, Mn, K, P) were tested against the BHVO-1 standard by comparing measured values to those of Govindaraju (1994) (Table 3.1) while trace elements (U, Th, Pb, Zr, Y, Nb, Sr, Rb, Zn, Cu, Ni, Cr, V, Ba, Sc, La, Ce, Nd) were tested against the BCR, BEN, BHVO-1 and BIR standards (Table 3.2). Analytical error was generally <2% (95% confidence levels) for major elements although it was <10% for Na and P; precision was generally better than 5% (95% confidence levels) but Na (22%) and P (11%) were higher. For trace elements, analytical

error was generally <10% (95% confidence levels) but varied between the different standards used. Detection limits are given in Table 3.3 and were 0.2wt% or lower for major elements and 10ppm or lower for trace elements.

EMPA

Electron microprobe analyses (EMPA) were carried out at the University of Manchester using a Cameca SX100 electron microprobe. EMPA is a quantitative version of EDS analysis. Carbon coated thin section and 1" rounds were bridged to the sample holder with silver paint. Beam conditions of ~20nA current and an acceleration voltage of 15kV produced a spot size of ~1µm. There are five wavelength dispersive detectors, each equipped with a choice of diffracting crystals, allowing simultaneous quantitative analyses of up to five different elements at chosen points across the sample. Transects of points were set up and stored so that analysis could be done in automated mode. A range of standards were used to calibrate peaks in the Kα line including: fayalite for Fe; periclase for Mg; wollastonite for Ca and Si; rutile for Ti; chromite for Cr; corundum for Al; jadeite for Na; tephroite for Mn; and potassium feldspar for K. Detection limits for the major elements measured were <0.1wt%. Analytical precision was better than 1% (95% confidence levels) for concentrations of >10wt% and better than 20% (95% confidence levels) for concentrations of <10wt%.

	BHVO-1				
Element	Ave. (n=136)	2σ	Precision (% at 2σ)	Std. value	Reproducibility (% at 2σ)
SiO2	50.23	0.81	1.61	49.94	0.58
Al2O3	13.69	0.33	2.44	13.80	0.78
Fe2O3	12.37	0.12	0.98	12.23	1.12
MgO	7.18	0.18	2.53	7.23	0.68
CaO	11.45	0.21	1.86	11.40	0.40
Na2O	2.47	0.53	21.54	2.26	8.39
K2O	0.527	0.01	2.42	0.520	1.38
TiO2	2.726	0.04	1.54	2.710	0.60
MnO	0.170	0.01	3.82	0.168	1.03
P2O5	0.292	0.03	11.20	0.273	6.65

Table 2.1 Precision and accuracy of XRF spectrometer for major elements during analytical session; reproducibility calculated from comparison of measured values of BHVO-1 standard with those of Govindaraja (1994) (Std. value column).

	BCR				
Element	Ave. (n=3)	2σ	Precision (% at 2σ)	Std. value	Reproducibility (% at 2σ)
U	1.93	0.34	17.58	1.75	9.48
Th	6.67	0.50	7.48	5.98	10.30
Pb	14.13	0.47	3.34	13.60	3.77
Nb	12.74	0.24	1.88	14.00	9.00
Zr	191.34	2.23	1.17	190.00	0.70
Y	38.16	0.60	1.58	38.00	0.42
Sr	333.19	5.75	1.73	330.00	0.96
Rb	47.73	0.69	1.44	47.20	1.11
Zn	124.47	0.81	0.65	129.50	3.89
Cu	19.63	0.09	0.48	19.00	3.23
Ni	10.00	1.57	15.75	13.00	23.08
Cr	10.30	1.32	12.81	16.00	35.63
V	404.47	2.64	0.65	407.00	0.62
Ba	667.00	4.01	0.60	681.00	2.06
Sc	33.17	0.84	2.53	32.60	1.71
La	24.63	0.90	3.65	24.90	1.07
Ce	55.13	2.74	4.98	53.70	2.60
Nd	30.10	0.59	1.96	28.80	4.32

(continued)

BEN

Element	Ave. (n=3)	2σ	Precision (% at 2σ)	Std. value	Reproducibility (% at 2σ)
U	3.07	0.34	11.08	2.40	21.74
Th	12.10	0.28	2.34	10.40	14.05
Pb	4.17	0.41	9.86	4.00	4.00
Nb	117.05	0.68	0.58	105.00	10.29
Zr	271.52	2.09	0.77	260.00	4.24
Y	29.80	0.31	1.04	30.00	0.67
Sr	1384.40	9.31	0.67	1370.00	1.04
Rb	47.77	0.44	0.92	47.00	1.61
Zn	130.03	1.06	0.82	120.00	7.72
Cu	74.50	1.02	1.37	72.00	3.36
Ni	271.23	1.47	0.54	267.00	1.56
Cr	370.93	0.50	0.13	360.00	2.95
V	236.80	4.75	2.01	235.00	0.76
Ba	1031.20	10.38	1.01	1025.00	0.60
Sc	22.50	1.02	4.53	22.00	2.22
La	89.30	0.16	0.18	82.00	8.17
Ce	157.10	1.42	0.91	152.00	3.25
Nd	70.07	1.84	2.62	67.00	4.38

(continued)

BHVO-1

Element	Ave. (n=3)	2σ	Precision (% at 2σ)	Std. value	Reproducibility (% at 2σ)
U	0.80	0.33	40.82	0.42	47.50
Th	0.13	0.62	463.68	1.08	87.65
Pb	2.23	0.09	4.22	2.60	14.10
Nb	19.34	0.13	0.69	19.00	1.76
Zr	174.53	1.20	0.69	179.00	2.50
Y	27.43	0.42	1.53	27.60	0.62
Sr	390.86	1.68	0.43	403.00	3.01
Rb	9.49	0.29	3.05	11.00	13.73
Zn	105.53	1.18	1.12	105.00	0.51
Cu	134.83	0.75	0.56	136.00	0.86
Ni	117.17	0.50	0.43	121.00	3.17
Cr	289.60	2.24	0.78	289.00	0.21
V	309.10	2.21	0.71	317.00	2.49
Ba	141.97	2.96	2.09	139.00	2.09
Sc	33.67	1.32	3.92	31.80	5.54
La	12.43	0.74	5.92	15.80	21.31
Ce	39.70	1.45	3.66	39.00	1.76
Nd	26.47	0.19	0.71	25.20	4.79

(continued)

				BIR	
Element	Ave. (n=3)	2σ	Precision (% at 2σ)	Std. value	Reproducibility (% at 2σ)
U	0.13	0.19	141.42	0.01	92.50
Th	-1.03	0.82	-79.54	0.03	102.90
Pb	3.33	0.25	7.48	3.00	10.00
Nb	0.63	0.09	14.89	0.60	5.26
Zr	17.47	1.02	5.86	15.50	11.26
Y	16.62	0.39	2.32	16.00	3.74
Sr	109.02	0.58	0.53	108.00	0.94
Rb	0.50	0.16	32.66	0.25	50.00
Zn	66.33	0.34	0.51	71.00	6.57
Cu	125.00	0.99	0.79	126.00	0.79
Ni	150.47	0.25	0.17	166.00	9.36
Cr	368.63	1.18	0.32	382.00	3.50
V	325.27	2.22	0.68	313.00	3.77
Ba	11.07	1.09	9.83	7.00	36.75
Sc	41.87	1.05	2.51	44.00	4.85
La	1.43	1.64	114.12	0.62	56.74
Ce	2.03	3.77	185.64	1.95	4.10
Nd	2.90	1.07	36.93	2.50	13.79

Table 2.2 Precision and accuracy of XRF spectrometer for trace elements during analytical session; reproducibility calculated from comparison of measured values of BCR, BEN, BHVO-1 and BIR standards with those of Govindaraja (1994) (Std. value column). Analyses marked in red have high analytical error (2σ), analyses marked in blue are below detection limits of machine.

Major	Si	Al	Fe	Mg	Ca	Na	K	Ti	Mn	P
wt%	0.20	0.10	0.06	0.10	0.06	0.10	0.01	0.01	0.01	0.01
Trace	Rb	Ba	Th	U	Pb	Nb	La	Ce	Sr	Nd
ppm	0.6	10.0	0.8	0.8	0.8	0.2	2.0	3.0	1.0	2.0
Trace	Zr	Y	Zn	Cu	Ni	Sc	Cr	V		
ppm	0.8	0.8	1.0	1.0	2.0	1.0	2.0	4.0		

Table 2.3 Detection limits for major and trace element on the XRF spectrometer.

Ion Microprobe Analysis

For ion microprobe analysis, samples had to be prepared in one inch rounds to fit the sample holder. The epoxy grain mount was already in this format but thin and thick sections had to be cut to size. Small chips of thin section were cut using a steel rule and Stanley knife and edges were ground down to smooth off corners. These chips were then

attached to a one inch diameter glass round with Epothin epoxy resin. They were then re-polished to ensure the top surface was completely level and sputter-coated with pure gold to avoid electrostatic charging.

Ion microprobe analysis was conducted at the Edinburgh Ion Microprobe Facility at the University of Edinburgh. Analyses were carried out on two different ion microprobes. U-Pb isotope analysis was conducted using a Cameca IMS 1270 ion microprobe. The 1270 has a ~4nA O_2^- primary ion source with 22.5 keV net impact energy; the beam is focussed using Köhler illumination, which ensures uniform beam density. The primary beam is mass analysed to ensure a pure beam of O_2^- ions and eliminate any O_2H^- from the duoplasmatron source. An additional lens immediately after the ion source enables a constant beam density and current to be maintained despite changes in the source over long timescales. The primary beam alignment gives ellipsoidal analysis pits (~25 µm max. dimension) with sharp edges and flat bottoms. Clean analysis pits are considered essential to reduce peripheral contamination and allow even sputtering over the entire analysed area. Further effects of peripheral contamination are minimised by a field aperture that restricts the secondary ion signal to a ~15µm square at the centre of the analysis pit.

The Plesovice (Slama et al., 2008) zircon standard was used for calibration of U/Pb ratios. During the analytical session, the standard yielded a mean $^{206}Pb/^{238}U$ ratio of 0.05359±0.00023 (MSWD = 2.4; 95% conf.; Fig. 3.1; 340.5±4.8Ma; *n = 62*). Calculation and calibration of ratios and data reduction were conducted using in-house software developed by Richard Hinton at the University of Edinburgh. The detection limits for individual isotopes were typically <0.15ppb. A common Pb correction was also applied in-house. A common Pb contribution to analyses is believed to be derived from either surface contamination of the sample (i.e. from preparation) or from within the zircon lattice itself. Common Pb surface contamination was reduced by rastering the sample with the ion microprobe beam immediately prior to isotope measurement and by production of flat-

bottom analysis pits through carefully tuned beam conditions. Correction for in-situ common Pb was made using measured ^{204}Pb counts above that of the detector background (typically ~0.2 to 1.5ppb). In the analyses for this project, measured common Pb was generally <5ppb, although occasionally analyses were much higher than this, likely the result of contamination on the sample surface and in exposed cracks.

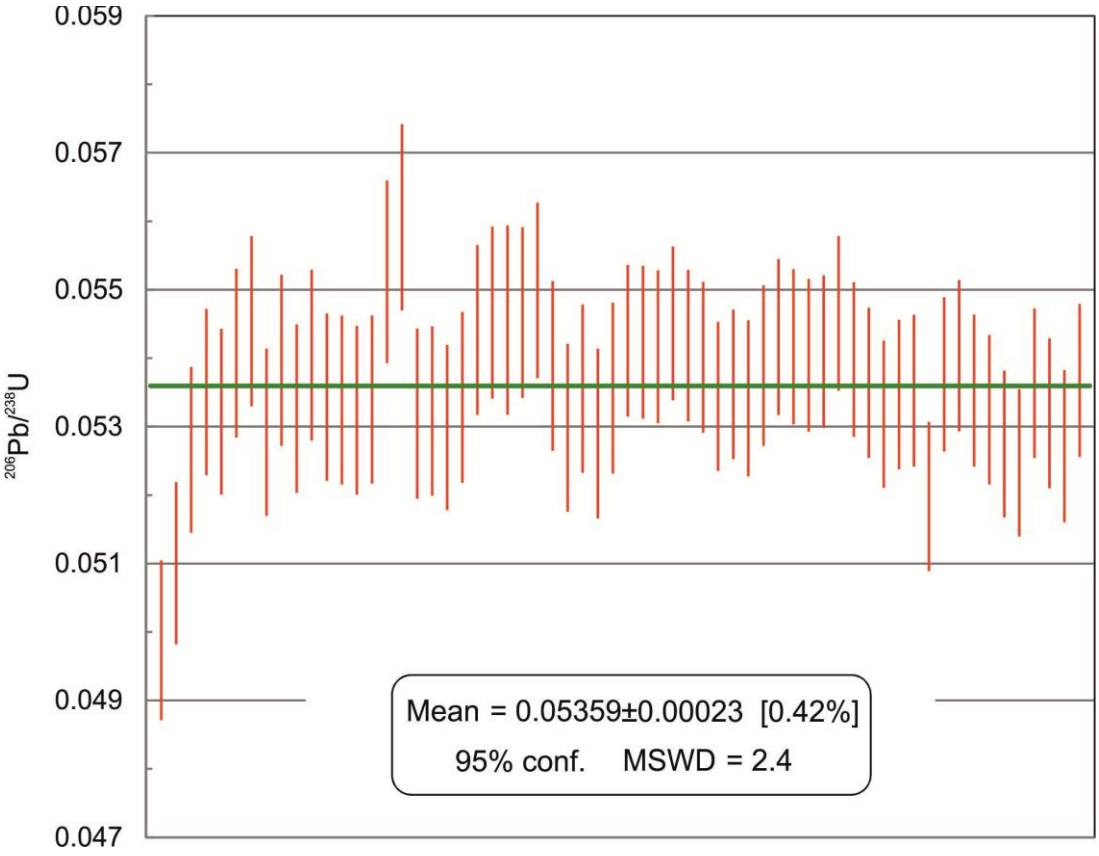

Fig. 2.13 Weighted average plot of ^{206}Pb/^{238}U in the Plesovice standard zircon, illustrating analytical reproducibility during the analytical session.

Total element abundances (REEs, Ti, Hf, Ba, Zr, Y) were measured with a Cameca 4f ion microprobe. The 4f has a duoplasmatron O_2^- ion source with 14.5 keV net impact energy; detection limits for the different elements are given in Table 3.4. The 91500 zircon standard and NIST SRM610 glass standard were used to calibrate trace element concentrations between analyses of unknowns. The analyses from the 91500 zircon show an expected, smooth increase in chondrite-normalised values of trivalent REEs as ionic

radius decreases from La to Lu, together with large positive Ce anomaly and small negative Eu anomaly (Fig. 3.2). Good agreement is obtained between the SIMS measurements for zircon 91500 presented here and those of Whitehouse and Platt (2003) and Hoskin (1998). There is some variation in REE concentrations in the analyses of 91500 (Table 3.5), also encountered by Hoskin (1998). For most REEs (particularly the heavier ones), the average analytical error is <10% (2σ) but for some for the lighter REEs which have lower concentrations, it can be significantly higher. This interpreted to be partly due a lack of reproducibility from the spectrometer but also from heterogeneity in the 91500 standard as noted above. Errors on Hf, Ti, Y and Zr are ~4-14% (2σ) while Ba is much higher (±49%) due to its low concentration. Analytical reproducibility against the NIST SRM610 glass standard was better than 7% (2σ) for elements analysed (Table 3.5). Raw data was reduced using the JCION6 software written by John Craven at the University of Edinburgh. REE data was chondrite-normalised against the values of McDonough and Sun (1995).

Element	Detection limit (ppm)	
Ti	0.12	
Y	0.01	
Zr	0.12	
Hf	0.17	
Ba	0.03	
La	0.02	*0.08*
Ce	0.03	*0.05*
Pr	0.02	*0.22*
Nd	0.19	*0.42*
Sm	0.16	*1.08*
Eu	0.04	*0.71*
Gd	0.07	*0.35*
Tb	0.03	*0.83*
Dy	0.12	*0.49*
Ho	0.03	*0.55*
Er	0.1	*0.63*
Tm	0.03	*1.21*
Yb	0.18	*1.12*
Lu	0.03	*1.22*

Table 2.4 Detection limits for trace elements measured on the 4f ion microprobe; numbers in italics denote chondrite-normalised detection limits (ppm) for rare earth elements, presented here as chondrite-normlaised values are given in data tables in chapters 5-7.

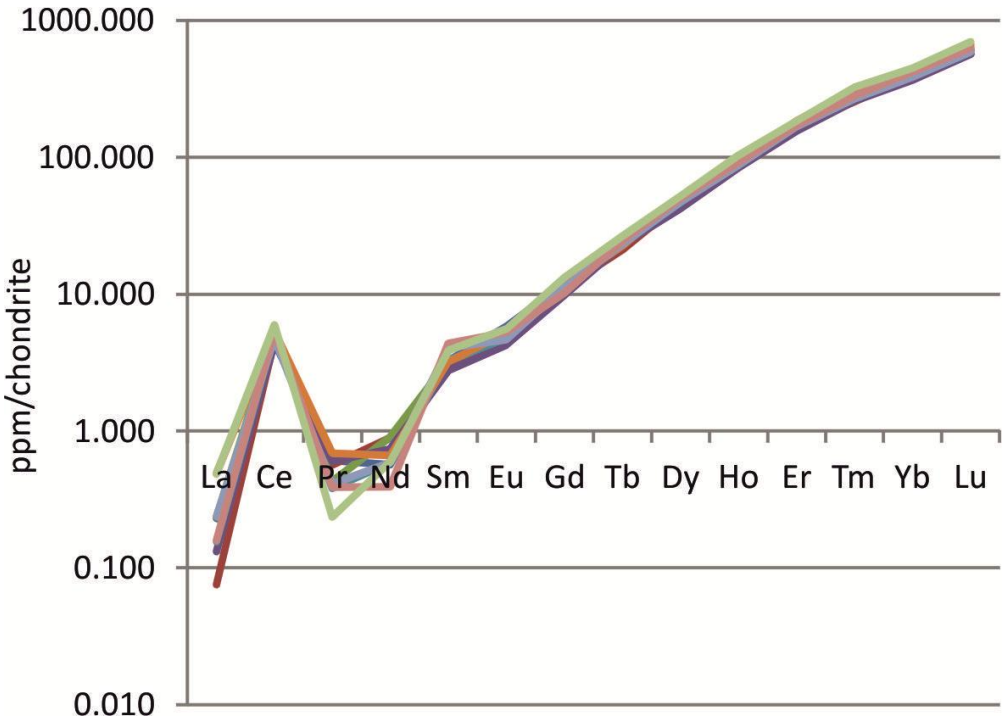

Fig. 2.14 Chondrite-normalised REE values for analyses of Geostandards 91500 zircon standard showing analytical reproducibility during analytical session.

NIST SRM610

Analysis ID	1	2	3	27	54	85	102	126	Average	Error (%, 2σ)
Si	327210	327210	327210	327210	327210	327210	327210	327210	327210	0
Y	414	415	403	414	414	414	414	414	412.9	1.0
Zr	500	454	436	500	500	500	500	500	486.4	5.4
Ba	500	455	427	500	522	500	500	500	488.2	6.3
Hf	500	463	422	500	522	500	500	500	488.5	6.4
Ti	437	412	403	437	442	437	437	437	430.5	3.3
La	510	489	471	510	520	510	510	510	503.9	3.2
Ce	524	505	487	524	532	524	524	524	518.1	2.9
Pr	501	490	470	501	512	501	501	501	496.8	2.5
Nd	532	535	515	532	545	532	532	532	531.8	1.5
Sm	516	528	511	516	529	516	516	516	518.4	1.2
Eu	518	517	504	518	528	518	518	518	517.3	1.3
Gd	506	565	559	506	510	506	475	506	516.5	5.9
Tb	500	509	493	500	509	500	506	500	502.4	1.1
Dy	500	501	496	500	507	500	500	500	500.6	0.6
Ho	500	517	497	500	510	500	500	500	503.1	1.3
Er	500	518	500	500	515	500	500	500	504.4	1.5
Tm	500	509	493	500	513	500	500	500	502.0	1.2
Yb	500	510	490	500	503	500	500	500	500.6	1.1
Lu	500	506	486	500	508	500	500	500	500.2	1.3

(continued)

Geostandards 91500

Analysis ID	5	15	29	48	56	69	87	128	185	Average	Error (%, 2σ)
Si	149577	149580	149580	149580	149580	149580	149580	149580	149580	149579.7	0.0
Y	133	133	140	132	139	142	135	138	150	138.1	4.1
Zr	480494	488830	562520	537750	558310	569400	554279	557890	570100	542174.8	6.3
Ba	0.609	0.446	0.289	0.320	0.096	0.434	0.758	0.298	0.326	0.397	48.915
Hf	5065	4963	6148	5533	6033	6252	5624	6043	7828	5943.0	14.2
Ti	5.16	4.41	5.42	5.14	5.72	4.49	4.82	4.90	5.74	5.09	9.48
La	0.055	0.018	0.056	0.031	0.037	0.116	0.057	0.038	0.115	0.058	60.454
Ce	3.06	2.83	3.18	2.70	3.14	3.26	2.89	3.29	3.65	3.11	9.15
Pr	0.057	0.052	0.040	0.055	0.035	0.064	0.038	0.036	0.022	0.044	30.238
Nd	0.259	0.406	0.413	0.338	0.269	0.303	0.268	0.179	0.273	0.301	24.807
Sm	0.481	0.457	0.479	0.408	0.485	0.476	0.602	0.646	0.570	0.512	15.040
Eu	0.326	0.279	0.265	0.239	0.267	0.294	0.262	0.295	0.313	0.282	9.753
Gd	2.37	2.22	2.29	1.95	2.55	2.32	2.24	2.03	2.65	2.29	9.70
Tb	0.835	0.763	0.821	0.830	0.853	0.812	0.835	0.884	0.953	0.843	6.209
Dy	12.1	11.4	12.0	10.3	11.4	12.5	11.5	12.2	12.7	11.8	6.2
Ho	4.88	4.77	5.08	4.56	5.02	5.00	4.72	4.96	5.59	4.95	5.88
Er	27.7	27.0	29.1	24.6	27.6	29.2	26.6	27.0	29.3	27.6	5.5
Tm	6.82	6.26	6.96	6.35	7.49	7.61	6.60	6.93	7.95	7.00	8.28
Yb	69.1	65.4	66.9	58.7	65.0	65.0	61.7	67.3	71.9	65.7	5.9
Lu	14.8	14.0	15.4	13.9	14.9	16.2	14.4	15.3	17.0	15.1	6.7

Table 2.5 Measured values of REEs in 91500 zircon standard and NIST SRM610 glass standard during analytical session showing analytical error.

4. Sample Characterisation

Zircons from many samples from the Lewisian Gneiss Complex (LGC) of Northwest Scotland have been analysed as part of this study. Findings from the zircons are reported in chapters 5-7. This chapter will give a comprehensive characterisation of the samples from which zircons have been analysed. Data from samples which are not discussed in chapters 5-7 are provided in the Thesis Appendix.

4a: Field Relationships and Sample Petrography

In this section, the field relationships of lithologies, structures and mineral assemblages at the sample localities, and the petrography of the samples, are described and interpreted in the context of the existing understanding of the tectonothermal evolution of the LGC (reviewed in chapter 2b). The samples were all collected from the Assynt terrane/Central Region of the LGC, mostly in the vicinity of Scourie village (Fig. 4.1). Samples were collected from five localities: Badcall Point, Duartmore Point, Sithean Mor, Geisgeil and Scourie Mor (Fig. 4.1).

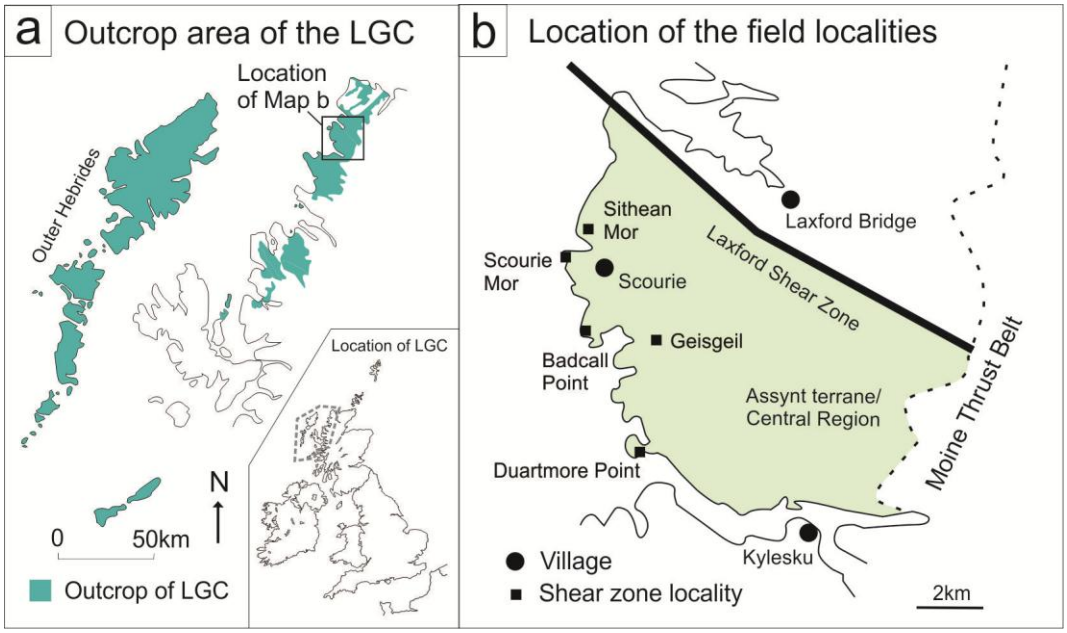

Fig. 4.1 a Map showing the outcrop area of the LGC and location of map **b**, inset shows location within British Isles; **b** Map showing location of field localities and nearby settlements.

Badcall Point

Field Relationships

The Badcall Point field area is located at UK grid reference NC146414, ~ 3km SSW of Scourie village. Exposure is excellent and is above the high tide line (Fig. 4.2a). The major rock type here is a variably-deformed grey TTG gneiss, typical of the Assynt terrane/Central Region (e.g. Sutton and Watson, 1951; Tarney and Weaver, 1987). The oldest recognised structure is a gneissic layering fabric (Fig. 4.2b) with ~5-20mm wide layers of mafic and felsic minerals. A sample (JM09/BP02) of this was taken at NC 14562 41558. Field inspection suggests the pale white-grey felsic layers are composed of quartz and feldspar while the dark-grey mafic layers are amphibole or pyroxene. No mineral lineations were observed. The gneissic layering generally dips to the southwest but there are tight to open folds of <10m wavelength present (Fig. 4.2b). Occasional pods of 2cm-5m long mafic rock are wrapped by the gneissic layering. As the oldest recognised structure, the gneissic layering is interpreted to have formed in the Badcallian tectonothermal event; the gneissic layering is attributed to the Badcallian elsewhere in the Assynt terrane/Central Region (e.g. Park, 1970; Friend and Kinny, 1995; Whitehouse and Kemp, 2010).

At NC 14564 41555, the Badcallian gneissic layering is cross-cut by a 20cm-wide zone of another fabric (Fig. 4.2c&d). It is similar in appearance to the Badcallian gneissic layering and again no lineations were observed. Sample JM09/BP01 was taken from here. Both this fabric and the Badcallian gneissic layering are cross-cut by a member of the Scourie Dyke Swarm (Fig. 4.2b). This means that the fabric in sample JM09/BP01 pre-dates Scourie dyke intrusion but post-dates the Badcallian gneissic layering, therefore it is interpreted that it formed during the Inverian tectonothermal event. In the Assynt terrane/Central Region, the Inverian is normally characterised by shear zones yp to several kilometres wide such, as the Canisp Shear Zone (e.g. Evans, 1965; Evans and Lambert, 1974; Jensen, 1984; Attfield, 1987), so this 20cm-wide zone would be an unusual structural

feature to develop in the Inverian. However, the relative chronology of the field relationships suggests it is likely to be Inverian in age.

A ~20m-wide northwest-trending discrete shear zone cross-cuts the Scourie dyke and the earlier fabrics in the grey TTG gneiss (Fig. 4.2b). As it post-dates the Scourie dyke, this shear zone will have formed during the Laxfordian tectonothermal event. This size of shear zone is a typical structural feature of Laxfordian deformation in the Assynt terrane/Central Region (Wynn, 1995). Compositional layering of mafic and felsic minerals in the grey TTG gneiss are still present but are narrower (~3mm wide) than in the Badcallian gneissic layering; mineral aggregate lineations of hornblende or plagioclase were observed. Sample JM09/BP06 was taken from this shear zone at NC 14565 41561. The Laxfordian shear zone cuts across the Scourie dyke at a low angle and follows the contact between the dyke and the grey TTG gneiss for ~100m (Fig. 4.2b). Where the dyke is deformed by the shear zone, a composite L-S tectonite fabric is developed with elongate hornblende mineral aggregates clearly visible. Garnets with what appears to be sigmoid plagioclase tails are visible at NC 14565 41560 (Fig. 4.2e) and indicate sinistral movement on the shear zone. There is a ~10m wavelength reclined fold in the Laxfordian shear zone at NC 14566 41566; sample JM09/BP04 was taken from here. The fold post-dates the shear zone as the south- to southwest-plunging mineral lineation of the shear zone is rotated to plunge southeast on the fold limb (Fig. 4.2c). The fold is therefore interpreted to be late-Laxfordian in age. The latest structure in the relative chronology of the Badcall Point locality is a ~30-50cm wide pegmatitic granite vein which cross-cuts all earlier structures (Fig. 4.2c), therefore it is also interpreted to be late-Laxfordian in age.

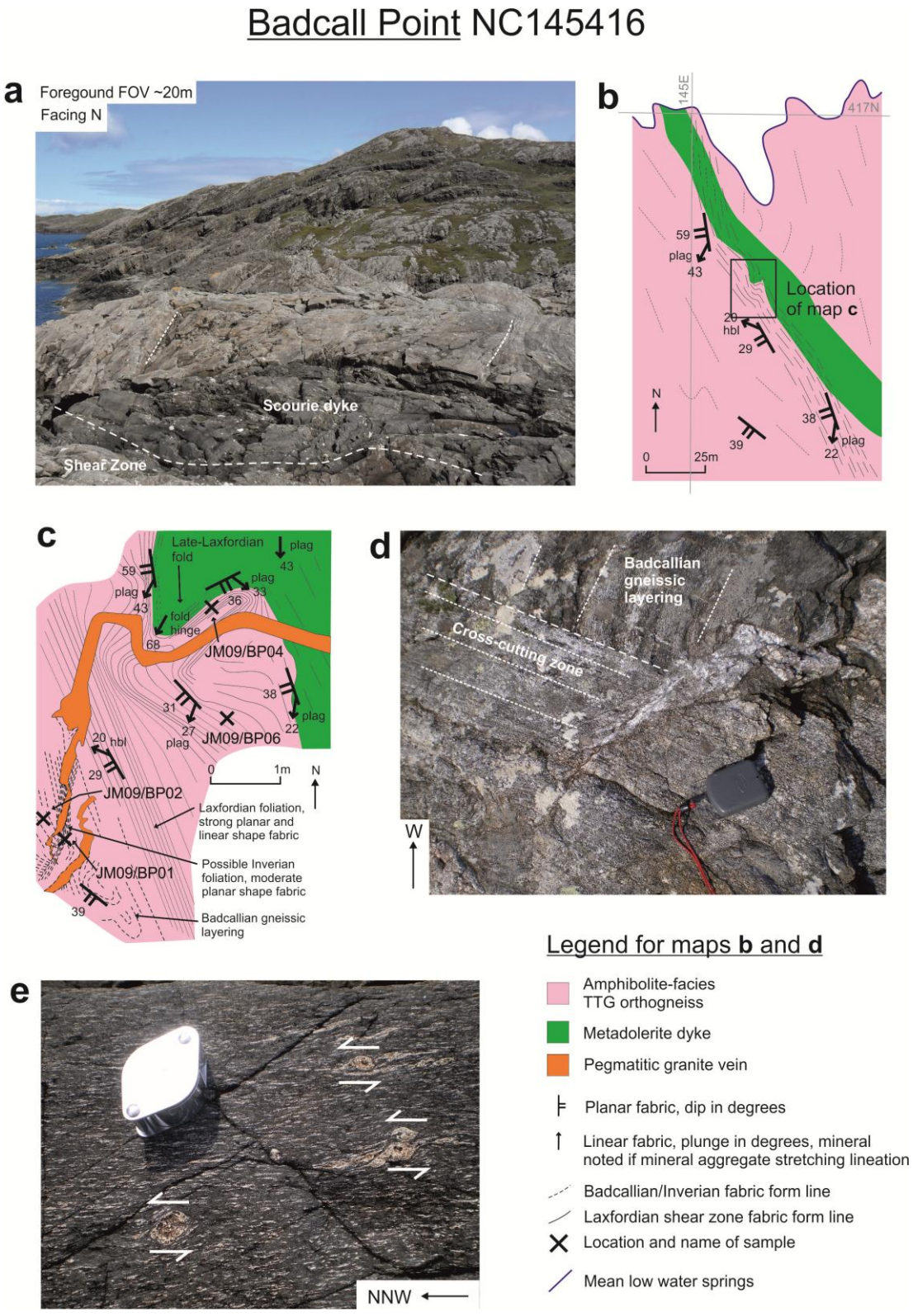

Fig. 4.2 a Photograph of the Badcall Point locality; **b** Field map of main lithologies and structures at the locality; **c** Detailed field map showing all generations of structures with sample locations marked; **d** Photograph showing the zone of possible Inverian fabric cross-cutting the Badcallian gneissic layering, compass clinometer is 10cm long; **e** Photograph of garnets with apparent sigmoid tails indicating sinistral shear sense, handlens is 3cm long. Numbered pale grey lines on field maps denote UK Ordnance Survey grid lines.

Sample Petrography

Four samples from Badcall Point are used in chapters 5-7 of this thesis: JM09/BP02, JM09/BP01, JM09/BP06 and JM09/BP04. Thin sections (Figs. 4.3,6,10&12) of each sample was made so that the petrography could be well-constrained by optical- and scanning electron-microscopy. Detailed petrographic descriptions are given in tables 4.1-4 and images of key mineral textures from each sample are shown in figures 4.4-5,7-9,11&13.

Sample JM09/BP02

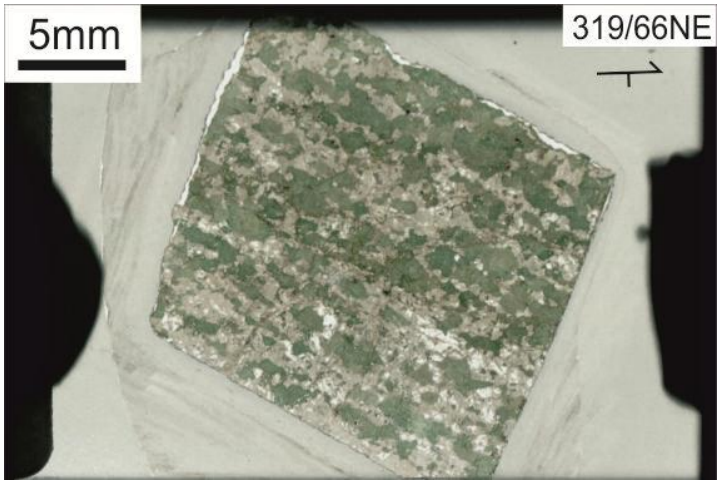

Fig. 4.3 PPL scan of the thin section from sample JM09/BP02.

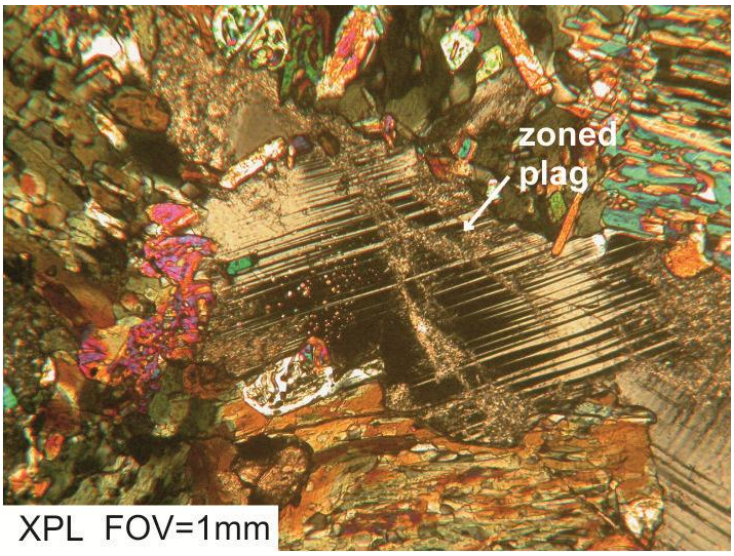

Fig. 4.4 Photomicrograph of plagioclase with zoned extinction in sample JM09/BP02 (plag = plagioclase).

Modal Mineralogy

- ~50% plagioclase
- ~40% hornblende
- ~10% quartz
- Minor minerals:
    - sub-mm equant epidotes, very high relief and birefringence with straight extinction
    - high-relief speckly-brown sub-mm equant titanites

~50% plagioclase

- Irregular xenomorphic ~2mm crystals
- Widespread sericitisation to varying degrees, lamellar twinning usually still visible, sometimes in what appears to be albite-pericline twinning
- Zoned extinction common, sometimes sub-concentric (Fig. 4.4)

~40% hornblende

- Occurs in a sieve texture with quartz as pseudomorphs after pyroxene (Fig. 4.5)
- Aggregates of sub-mm equant crystals
- Crystals within a single pseudomorph undergo pleochroic colour change from green to colourless at the same microscope stage rotation angle but this is not the case between different pseudomorphs
- Aggregated with sub-mm equant quartz crystals in the middle of the pseudomorphs but only hornblende around the edge

~10% quartz

- Occurs in a sieve texture with hornblende as pseudomorphs after pyroxene
- Sub-mm equant crystals
- Present in the centre of the pseudomorphs, not at the edge
- Rare xenomorphic ~2mm crystals not associated with sieve texture

General Comments

- Weakly-developed banding of mafic and felsic minerals visible at the thin section scale, no mineral lineations

Interpretation Comments

- Although Badcallian gneissic layering is the structural feature in this sample, sieve-textured hornblende and quartz shows that the Badcallian granulite-facies assemblage has been statically retrogressed to amphibolite-facies.
- The sericitisation of plagioclase may be linked to the retrogression of pyroxene but it may also have been caused by fluids associated with the late-Laxfordian pegmatitic granite vein which is located <1m from this sample, although other samples further from the vein (as well as samples from other localities without a pegmatitic granite vein) also have sericitised plagioclase.

Table 4.1 Petrographic description of sample JM09/BP02.

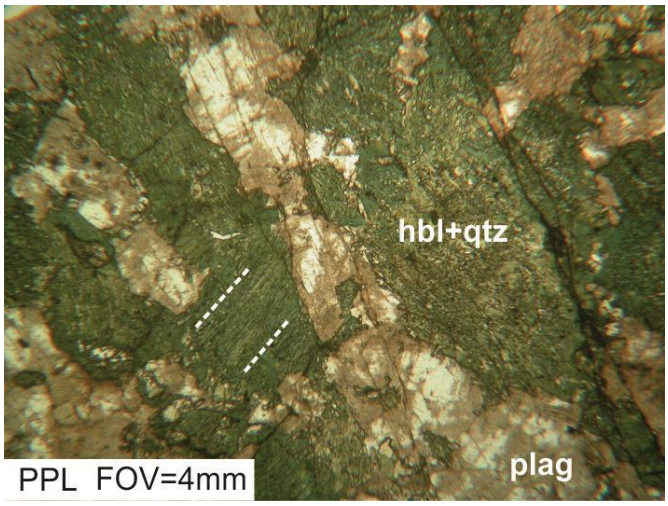

Fig. 4.5 Photomicrograph of sieve-textured hornblende and quartz in a pseudomorph after pyroxene in sample JM09/BP02, dashed line denotes the trace of a pyroxene cleavage preserved in the pseudomorph (plag = plagioclase, hbl = hornblende, qtz = quartz).

Sample JM09/BP01

Fig. 4.6 PPL scan of the thin section from sample JM09/BP01.

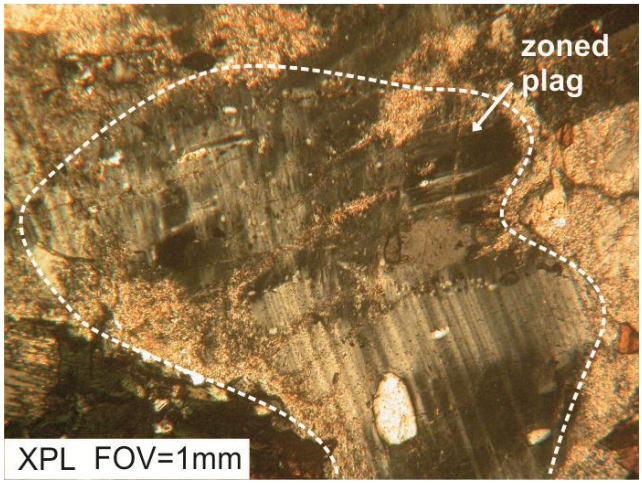

Fig. 4.7 Photomicrograph of plagioclase with zoned extinction in sample JM09/BP01, dashed white line denotes crystal boundary (plag = plagioclase).

Modal Mineralogy • ~45% plagioclase • ~40% quartz • ~10% hornblende • ~5% chloritised biotite
~45% plagioclase • 1-3mm stubby xenomorphic crystals • Patchy sericitisation to varying degrees, lamellar twinning sometimes well-preserved, often possible albite-pericline twinning (Fig. 4.7) • Zoned extinction common, sometimes vaguely sub-concentric
~40% quartz • Sub-2mm stubby xenomorphic crystals in matrix, larger ones occasionally have undulose extinction • Occurs in a sieve texture with hornblende as pseudomorphs after pyroxene, sub-mm equant crystals present in the centre of the pseudomorphs but not at the edge
~10% hornblende • Aggregates of sub-mm equant crystals with sub-mm equant quartz crystals in a typical sieve texture as pseudomorphs after pyroxene, where quartz and hornblende are in the middle of the pseudomorphs but only hornblende around the edge (Fig. 4.8) • Crystals within a single pseudomorph undergo pleochroic colour change from green to colourless at the same microscope stage rotation angle but this is not the case between different pseudomorphs • Also occasionally occurs in the matrix as xenomorphic-subidiomorphic 1-2mm crystals
~5% chloritised biotite • Clusters of laths/prisms at various orientations, individual crystals up to 1mm long • Straight extinction and one strong edge-parallel cleavage • Slightly pleochroic pale yellow-green in PPL but first-ordder dark blue-grey birefringence indicates chloritisation of original biotite (Fig. 4.9)
General Comments • Gneissic layering not obvious at the thin section-scale
Interpretation Comments • Sieve-textured hornblende and quartz indicates static retrogression of (Badcallian) pyroxene; this may have occurred in the Inverian tectonothermal event which would agree with the observation that the planar fabric visible in the field formed between the Badcallian and intrusion of the Scourie dykes. • The sericitisation of plagioclase may be linked to the retrogression of pyroxene but it may also have been caused by fluids associated with the late-Laxfordian pegmatitic granite vein which is located <1m from this sample, although other samples further from the vein (as well as samples from other localities without a pegmatitic granite vein) also have sericitised plagioclase.

Table 4.2 Petrographic description of sample JM09/BP01.

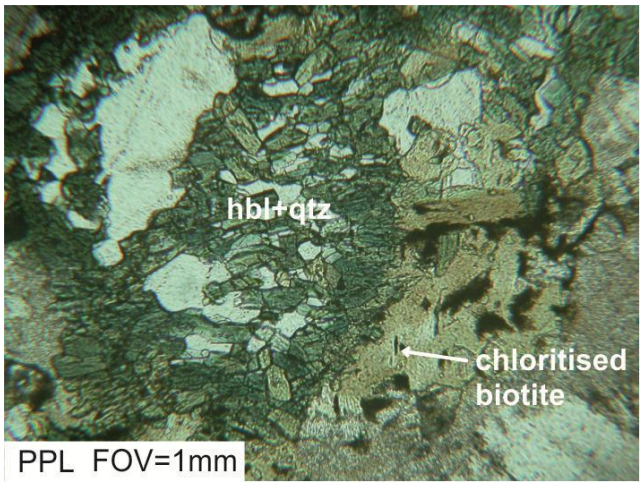

Fig. 4.8 Photomicrograph of sieve-textured hornblende and quartz in a pseudomorph after pyroxene in sample JM09/BP01, chloritised biotite also shown (hbl = hornblende, qtz = quartz).

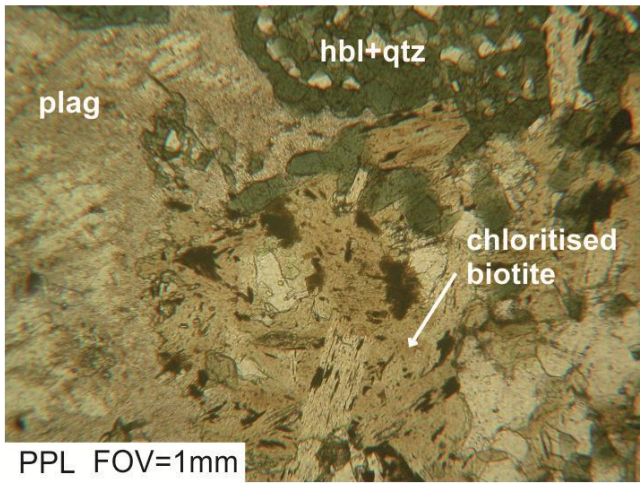

Fig. 4.9 Photomicrograph of laths of chloritised biotite in sample JM09/BP01 with sieve-textured hornblende and quartz after pyroxene also shown (hbl = hornblende, qtz = quartz).

Sample JM09/BP06

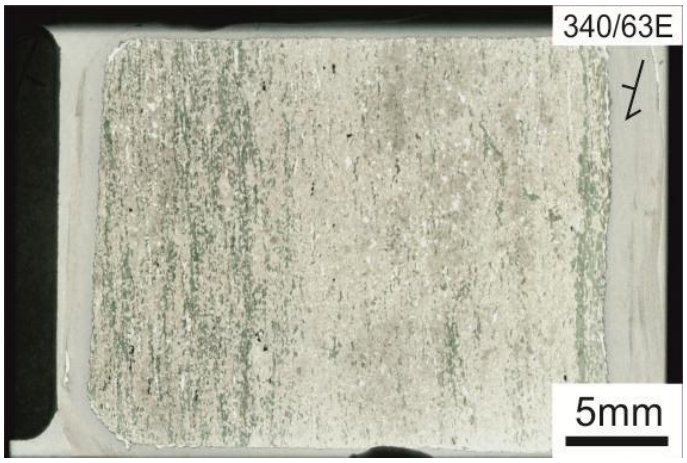

Fig. 4.10 PPL scan of the thin section from sample JM09/BP06.

Modal Mineralogy
• ~75% plagioclase
• ~20% hornblende
• ~5% quartz
• Minor minerals:
  ○ sub-mm equant epidotes, very high relief and birefringence with straight extinction
  ○ generally xenomorphic opaques

~75% plagioclase • Pervasively sericitised (Fig. 4.12) • Sub-2mm subidiomorphic crystals • Some larger crystals remain unsericitised in the centre and have zoned extinction
~20% hornblende • Elongate but rather xenomorphic stubby crystals, sub-mm and often aggregated • Different crystals undergo pleochroic colour change from green to colourless at the same microscope stage rotation angle • 1-2 cleavages occasionally visible
~5% quartz • Slightly elongated subidiomorphic crystals up to 1mm long • Simple extinction
General Comments • Coarse cm-scale banding of felsic and mafic minerals • Moderately well-developed hornblende and plagioclase aggregate mineral stretching lineations
Interpretation Comments • The presence of planar and linear fabrics with an amphibolite-facies mineralogy is in agreement with the interpretation from field relationships that this is a Laxfordian shear zone. • The sericitisation of plagioclase is likely caused by fluids flowing along the shear zone. It is possible that it may be associated with the late-Laxfordian pegmatitic granite vein which is located ~1m from this sample, although samples from other localities without a pegmatitic granite vein also have sericitised plagioclase.

Table 4.3 Petrographic description of sample JM09/BP06.

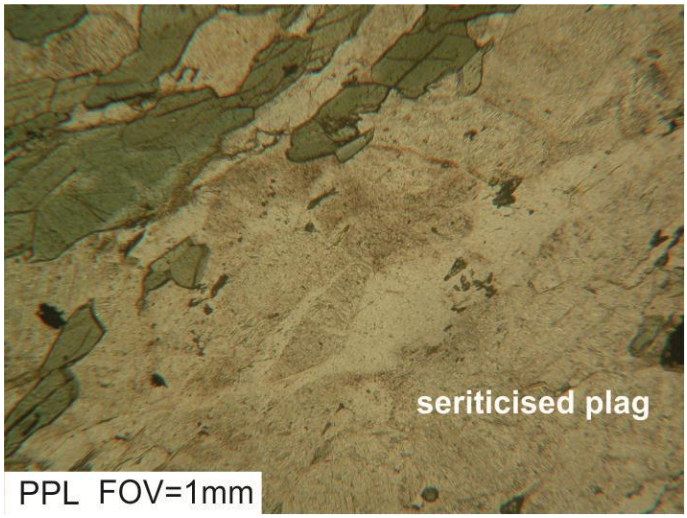

Fig. 4.11 Photomicrograph of sericitised plagioclase (plag = plagioclase) in sample JM09/BP06, the speckly pale-brown patches.

Sample JM09/BP04

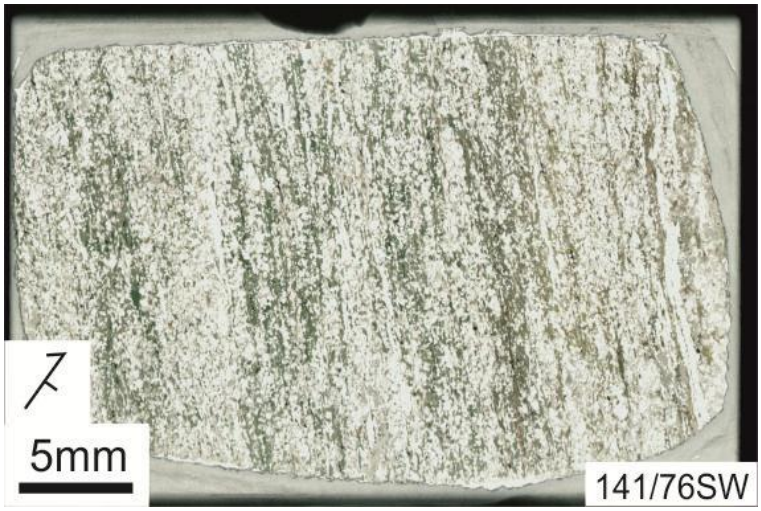

Fig. 4.12 PPL scan of the thin section from sample JM09/BP04.

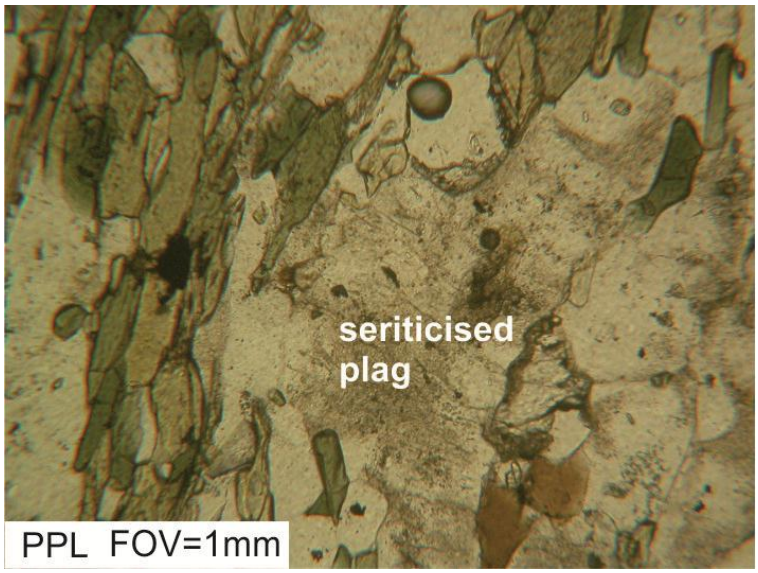

Fig. 4.13 Photomicrograph of sericitised plagioclase (plag = plagioclase) in sample JM09/BP04, the speckly pale-brown patches.

Modal Mineralogy • ~55% quartz • ~20% plagioclase • ~20% hornblende • ~5% biotite • Minor minerals: ○ sub-mm xenomorphic elongate epidotes, very high relief, grey-yellow birefringence, straight extinction
~55% quartz • Sub-2mm grains, often aggregated, larger crystals have undulose extinction
~20% plagioclase • Widespread sericitisation (Fig. 4.13) • Lamellar twinning rarely still visible and concentric zoned extinction sometimes visible through sericitisation • Sub-1mm stubby xenomorphic crystals
~20% hornblende • Sub-2mm elongate xenomorphic crystals, often aggregated • Different crystals undergo pleochroic colour change from green to colourless at the same microscope stage rotation angle
~5% biotite • Elongate brown laths to 1mm, occasionally aggregated • Laths strongly aligned with very consistent pleochroism
General Comments • Poorly-developed cm-scale banding of felsic and mafic minerals • Moderately well-developed hornblende and biotite aggregate mineral stretching lineations
Interpretation Comments • The presence of planar and linear fabrics with an amphibolite-facies mineralogy is in agreement with the interpretation from field relationships that this is a Laxfordian shear zone. • The sericitisation of plagioclase may be linked to the retrogression of pyroxene but it may also have been caused by fluids associated with the late-Laxfordian pegmatitic granite vein which is located <1m from this sample, although other samples further from the vein (as well as samples from other localities without a pegmatitic granite vein) also have sericitised plagioclase. • Although field evidence suggested that this sample is a folded equivalent of sample JM09/BP06, the modal mineralogy of the sample is quite different. This is interpreted to reflect compositional heterogeneity in the rocks over distances a few metres.

Table 4.4 Petrographic description of sample JM09/BP04.

Duartmore Point

Field Relationships

The Duartmore Point field area is located on an isolated coastal headland at NC178359, ~5km WNW of Kylesku village. The mapped area is on a wave-washed rock platform so there is almost 100% exposure (Fig. 4.14a). As at Badcall Point, the major rock type here is the typical Assynt terrane/Central Region variably-deformed grey TTG gneiss. The oldest recognised structure at this locality is a gneissic layering fabric (Fig. 4.14b) with ~5-20mm wide layers of mafic or felsic minerals. A sample (JM09/DP03) of this was taken at NC 17881 35957. Field inspection suggests the pale white-grey felsic layers are composed of quartz and feldspar while the dark-grey mafic layers are amphibole or pyroxene. In some places, the mafic minerals have a brownish colour suggesting the presence of orthopyroxene and therefore a granulite-facies metamorphic assemblage. No mineral lineations were observed. The gneissic layering generally dips gently to the north but on the southern tip of the headland it dips gently to the southwest (Fig. 4.14b). As the oldest recognised structure, the gneissic layering is interpreted to have formed in the Badcallian tectonothermal event, the same as that found at the Badcall Point locality.

On the southeast edge of the headland, a ~5m-wide northwest-trending Scourie dyke cross-cuts the Badcallian gneissic layering. This is cross-cut by a west-trending ~10m-wide shear zone. The dyke is deflected from its northwesterly orientation into a westerly orientation (Fig. 4.14b); it is strongly deformed and narrows to an indistinguishable compositional layer in the core of the shear zone. The shear zone clearly post-dates the dyke and is therefore Laxfordian in age. The Laxfordian shear zone has a closely spaced (~2-5mm) planar shear zone fabric with a well-developed plagioclase mineral aggregate stretching lineation. The orientation of the shear zone planar fabric and the gneissic layering on the north side of the shear zone is the same but on the south side of the shear zone, the southwest-dipping gneissic layering can clearly be seen to bend back on itself into

the shear zone (Fig. 4.14a&b), indicating a sinistral movement sense. A sample (JM09/DP02) of the grey TTG gneiss from the Laxfordian shear zone was taken at NC 17923 35972. On either side of the shear zone, there is a ~5-10m wide zone where the brown orthopyroxene of visible elsewhere in the gneissic layering is not seen; the mafic mineral is amphibole. It is interpreted that fluids flowing along the shear zone percolated into the granulite-facies gneiss and retrogressed it to amphibolite-facies. A sample (JM09/DP01) from this zone was taken at NC 17907 35965.

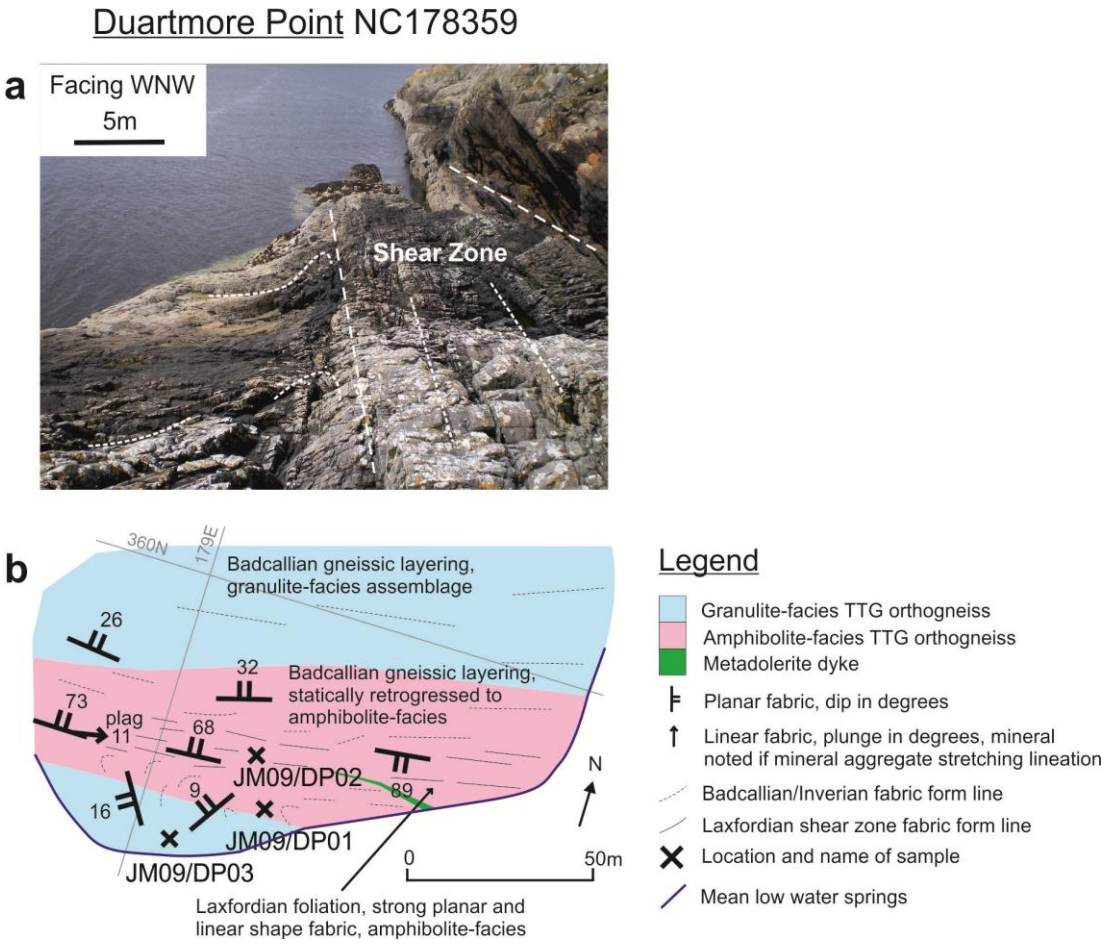

Fig. 4.14 a Photograph of the Duartmore Point locality showing the Laxfordian shear zone and the Badcallian gneissic layering deflected into the shear zone; **b** Detailed field map showing structures and metamorphic assemblages with sample locations marked. Numbered pale grey lines on field maps denote UK Ordnance Survey grid lines.

Sample Petrography

Three samples from Duartmore Point are used in chapters 5-7 of this thesis: JM09/DP03, JM09/DP01 and JM09/DP02. Thin sections (Figs. 4.15,18&21) of each sample was made so that the petrography could be well-constrained by optical- and scanning electron-

microscopy. Detailed petrographic descriptions are given in tables 4.5-7 and images of key mineral textures from each sample are shown in figures 4.16-17,19-20&22.

Sample JM09/DP03

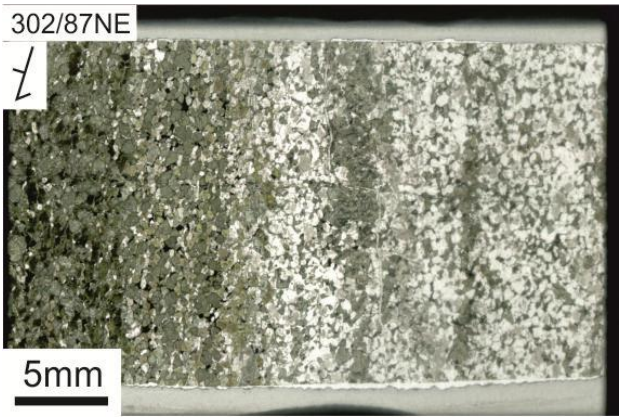

Fig. 4.15 PPL scan of the thin section from sample JM09/DP03.

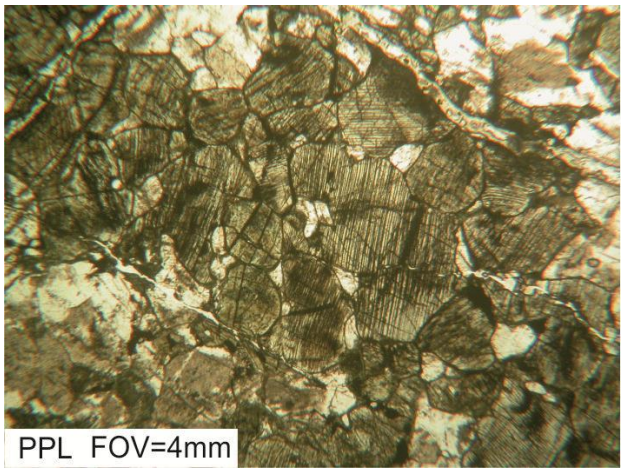

Fig. 4.16 Photomicrograph of pale-green clinopyroxene in sample JM09/DP03.

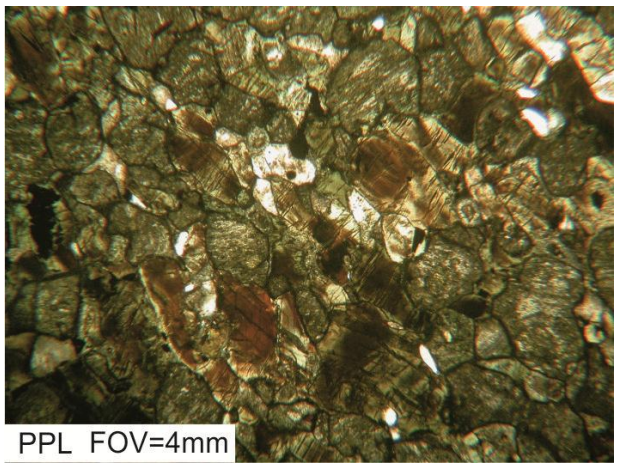

Fig. 4.17 Photomicrograph of altered pyroxene in sample JM09/DP03 with distinctive brown staining.

Modal Mineralogy

- ~60% pyroxene and alteration products
- ~30% plagioclase
- ~10% quartz
- Minor minerals:
    - Xenomorphic opaques in mafic band

~60% pyroxene and alteration products

- In the more felsic band on this slide, there are many sub-2mm subidiomorphic equant pale green clinopyroxenes (Fig. 4.16), often showing one good cleavage and with first-order pink-blue birefringence. There are similar crystals here which are browner in colour and have lower birefringence, interpreted to be orthopyroxene. Some of the pyroxenes have narrow hornblende rims
- In the more mafic band on the slide, crystals are 1-3mm subidiomorphic equant; there are four types:
    - Highly fractured, green-colourless pleochroism, first-order blue birefringence, distinctive brown staining in PPL (Fig. 4.17) – possibly hornblende replacing pyroxene
    - Colourless and speckly, remnant of one cleavage, speckly first-oreder blue-grey birefringence
    - Pale green and speckly, remnant of one cleavage, speckly first-order grey birefringence, occurs at boundary between mafic and felsic bands
    - Pale muddy yellow colour, often one strong cleavage, extinction parallel to cleavage, first-order grey-yellow birefringence – probably epidote replacing pyroxene

~30% plagioclase

- Subidiomorphic 1-2mm crystals
- Patchy sericitisation
- Zoned extinction common, often vaguely sub-concentric
- Lamellar twinning common, possible albite-pericline twinning common

~10% quartz

- 1-2mm subidiomorphic crystals with undulose extinction

General Comments

- Weakly-developed cm-scale banding of mafic and felsic minerals visible at the thin section scale, no mineral lineations

Interpretation Comments

- The patchy/partial retrogression of pyroxenes in the mafic band on this slide suggests an influx of fluid as the retrogression products (interpreted as hornblende and epidote) are hydrous phases. Field relationships suggested this sample was collected from an area with a granulite-facies assemblage, beyond the reach of fluids from the Laxfordian shear zone but thin section petrography suggests perhaps some of this fluid did indeed reach, and react, with this sample.
- The occasional sericitisation of plagioclase may be linked with the fluid which caused partial retrogression of pyroxene.

Table 4.5 Petrographic description of sample JM09/DP03.

Sample JM09/DP01

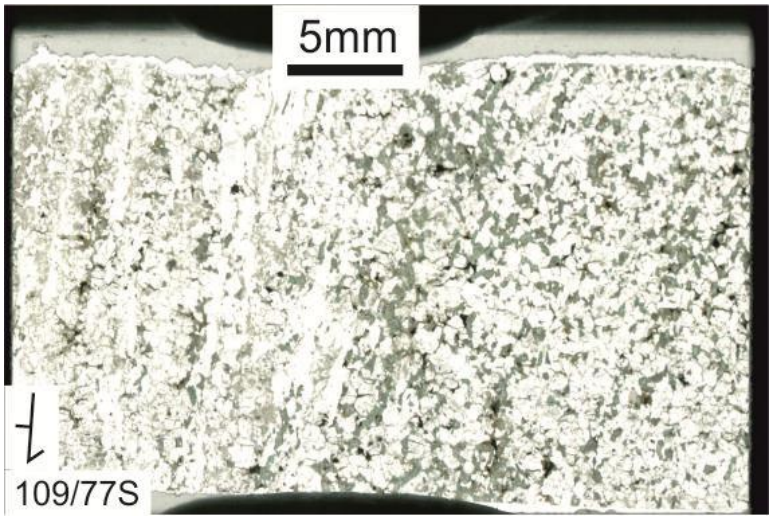

Fig. 4.18 PPL scan of the thin section from sample JM09/DP01.

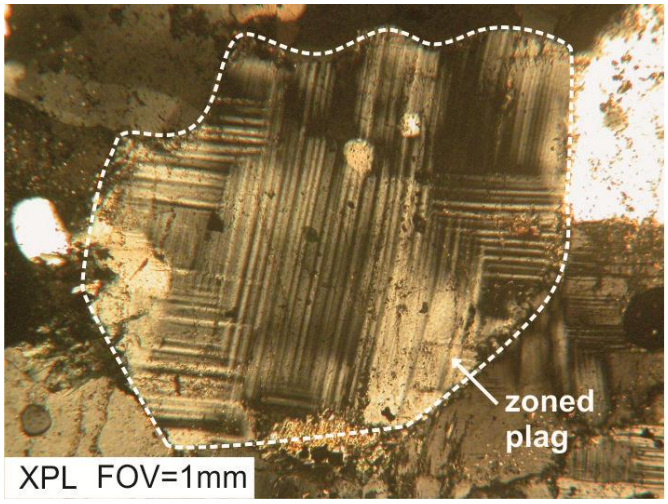

Fig. 4.19 Photomicrograph of plagioclase with zoned extinction in sample JM09/DP01, dashed white line denotes crystal boundary (plag = plagioclase).

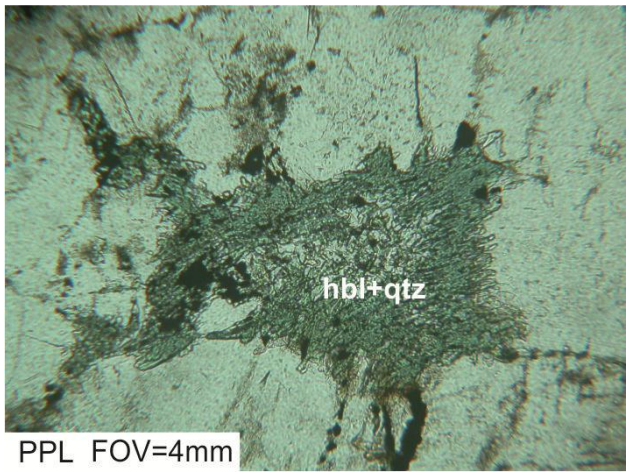

Fig. 4.20 Photomicrograph of sieve-textured hornblende and quartz in a pseudomorph after pyroxene in sample JM09/DP01 (hbl = hornblende, qtz = quartz).

Modal Mineralogy

- ~40% plagioclase
- ~40% quartz
- ~20% hornblende
- Minor minerals:
    - Biotite laths and xenomorphic opaques associated with sieve texture

~40% plagioclase

- 1-2mm stubby xenomorphic crystals
- Occasionally weakly sericitised
- Occasional lamellar twinning, possible albite-pericline twinning common (Fig. 4.19)
- Zoned extinction common, often sub-concentric

~40% quartz

- 1-2mm equant subidiomorphic crystals
- Undulose extinction common

~20% hornblende

- Aggregates of sub-mm equant crystals with sub-mm equant quartz crystals in a typical sieve texture as pseudomorphs after pyroxene, where quartz and hornblende are in the middle of the pseudomorphs but only hornblende around the edge (Fig. 4.20)
- Crystals within a single pseudomorph undergo pleochroic colour change from green to colourless at the same microscope stage rotation angle but this is not the case between different pseudomorphs
- Rare sub-mm biotites and opaques occur throughout the pseudomorph with rare remnant pyroxene in the centre. The pyroxene is colourless in PPL with blue birefringence. Variably-oriented biotite laths undergo a pleochroic colour change from brown to colourless but at different microscope stage rotation angles.

General Comments

- Weakly-developed banding of mafic and felsic minerals visible at the thin section scale, no mineral lineations

Interpretation Comments

- Although Badcallian gneissic layering is the structural feature in this sample, sieve-textured hornblende and quartz shows that the Badcallian granulite-facies assemblage has been statically retrogressed to amphibolite-facies. This agrees with the interpretation based on field relationships that there is a zone of static retrogression on either side of the Laxfordian shear zone.
- The sericitisation of plagioclase may be linked to the retrogression of pyroxene but it is not widely developed suggesting that any fluid escaping from the adjacent shear zone may have reacted with pyroxene first and that there was not enough to sericitise much of the plagioclase.

Table 4.6 Petrographic description of sample JM09/DP01.

Sample JM09/DP02

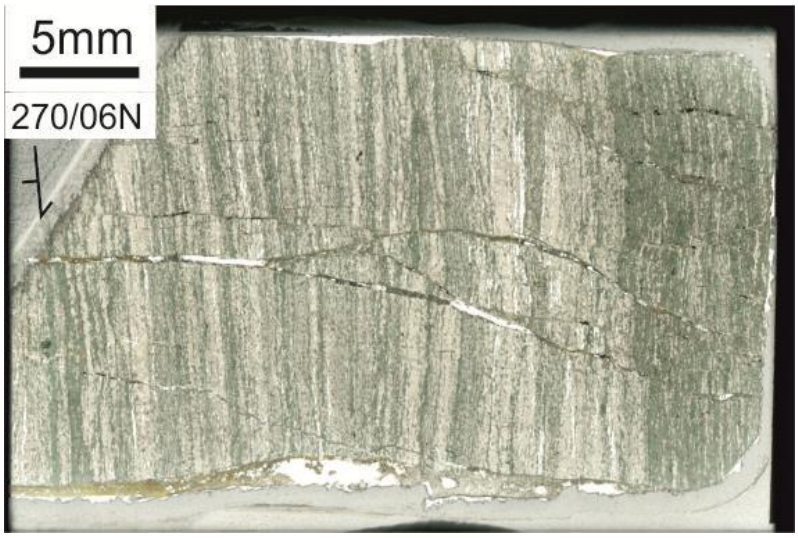

Fig. 4.21 PPL scan of the thin section from sample JM09/DP02.

Modal Mineralogy • ~50% hornblende • ~45% plagioclase • ~5% quartz • Minor minerals: ○ generally xenomorphic opaques
~50% hornblende • Sub-1mm crystals, laths or subidiomorphic rhombs, often aggregated and a bit ragged • Different crystals undergo pleochroic colour change from green to colourless at the same microscope stage rotation angle
~45% plagioclase • Considerable and widespread sericitisation (Fig. 4.22) • Stubby xenomorphic sub-mm crystals • Occasional sub-concentric zoned extinction • Rare faint remnant of lamellar twinning
~5% quartz • Elongate aggregates of xenomorphic sub-mm crystals • Usually simple extinction, rarely undulose
General Comments • Coarse cm-scale banding of felsic and mafic minerals • Well-developed hornblende and plagioclase aggregate mineral stretching lineations
Interpretation Comments • The presence of planar and linear fabrics with an amphibolite-facies mineralogy is in agreement with the interpretation from field relationships that this is a Laxfordian shear zone. • The sericitisation of plagioclase is likely caused by fluids flowing along the shear zone.

Table 4.7 Petrographic description of sample JM09/DP02.

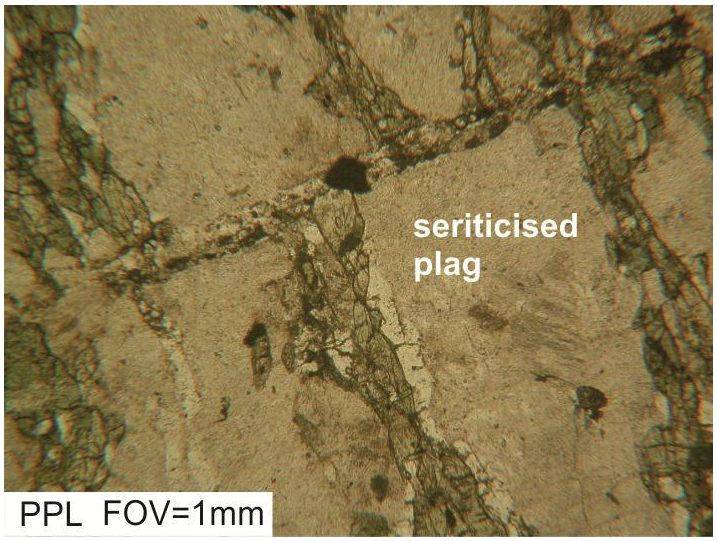

Fig. 4.22 Photomicrograph of sericitised plagioclase (plag = plagioclase) in sample JM09/BP04, the speckly pale-brown patches.

Sithean Mor

Field Relationships

The Sithean Mor field area is located at NC149461, ~1.5km NW of Scourie village. The locality is on moorland 80-100m above sea-level with patchy rock exposures. At this locality is an assemblage of generally flaggy, friable schistose rocks enclosed in the typical Assynt terrane/Central Region grey TTG gneisses described from Badcall Point and Duartmore Point (Fig. 4.23). These schistose rocks have been described by Beach (1973), Okeke et al. (1983) Barnicoat et al. (1987) and Zhu et al. (1997) and are interpreted to be metasediments. The metasediment assemblage is heterogeneous in appearance, with some parts having a brownish colour and very friable texture, suggesting the presence of a large percentage of biotite; other parts are less friable and have a white-grey colour suggesting they are quartz-rich. There is a variably developed planar fabric, most notable as compositional layering in the more biotite-rich schistose parts; no lineations were observed. The contact between the metasediments and the grey TTG gneiss is not exposed anywhere at this locality but the trend of the planar fabric in the metasediments suggests it would cross-cut the lithological contact (Fig. 4.23). In the grey TTG gneiss, there is a gneissic layering fabric (Fig. 4.23) with ~5-20mm wide layers of mafic and felsic minerals. Field inspection suggests the pale white-grey felsic layers are composed of quartz and feldspar while the dark-grey mafic layers are amphibole or pyroxene. No mineral lineations were observed. The strike of both the gneissic layering and the planar schistose fabric in the metasediments is highly variable. An undeformed northwest-trending Scourie dyke passes ~20m to the northeast of the metasediment outcrop. The fact that the Scourie dyke is undeformed indicates that the fabric in the surrounding grey TTG gneiss is older, either Badcallian or Inverian. In the Assynt terrane/Central Region, Inverian deformation is generally characterised by kilometre-wide shear zones such as the Canisp Shear Zone (e.g. Evans, 1965; Evans and Lambert, 1974; Jensen, 1984; Attfield, 1987), unlike the variably

oriented gneissic layering at this locality. This, in conjunction with the similarity of the gneissic layering here to that at Badcall Point and Duartmore Point, suggests that the fabric in the TTG gneiss is Badcallian in age. As the fabrics in the grey TTG gneiss and metasediment outcrop both appear to cross-cut the lithological contact, they are interpreted to be the same age and therefore the fabric in the metasediment is also Badcallian in age (Fig. 4.23).

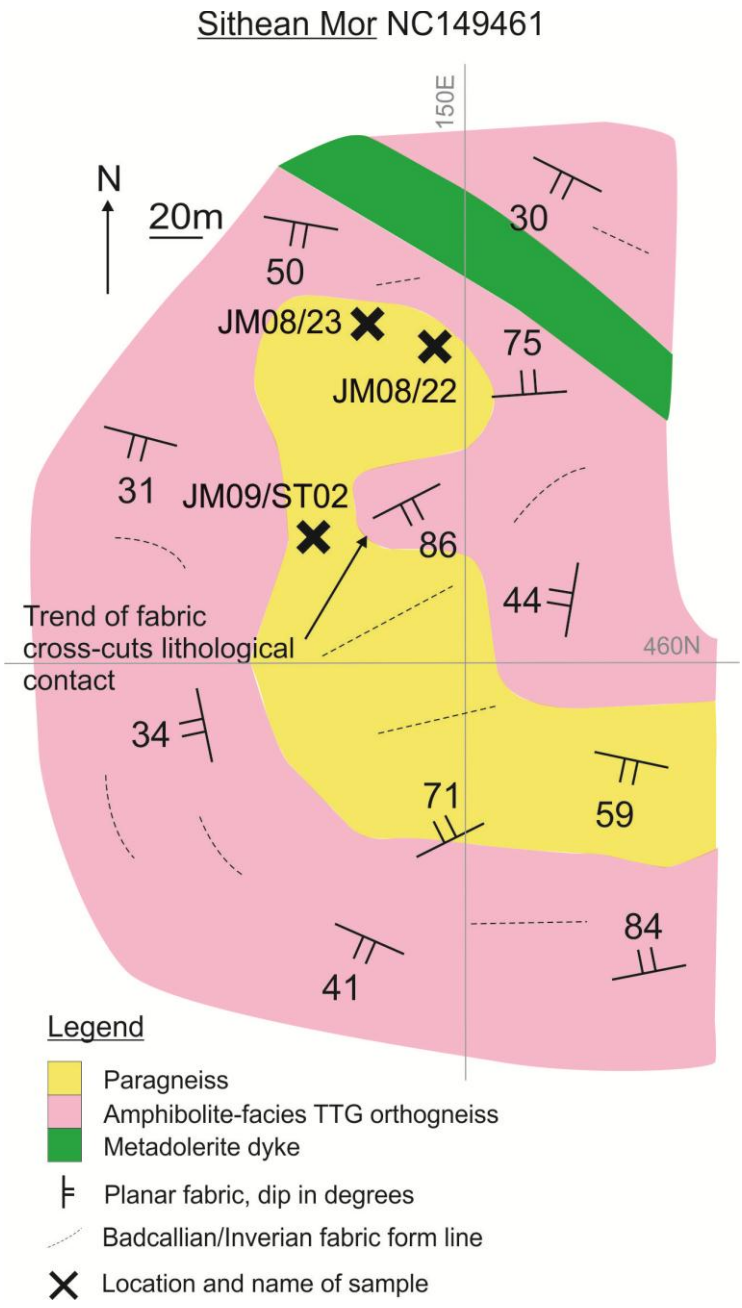

Fig. 4.23 Field map of structures and lithologies at the Sithean Mor locality with sample locations marked. Numbered pale grey lines on field maps denote UK Ordnance Survey grid lines.

Sample Petrography

Three samples from Sithean Mor are used in chapters 5-7 of this thesis: JM08/22, JM08/23 and JM09/ST02. Thin sections (Figs. 4.24,27&29) of each sample was made so that the petrography could be well-constrained by optical- and scanning electron-microscopy. Detailed petrographic descriptions are given in tables 4.8-10 and images of key mineral textures from each sample are shown in figures 4.25-26,28&30.

Sample JM08/22

Fig. 4.24 PPL scan of the thin section from sample JM08/22.

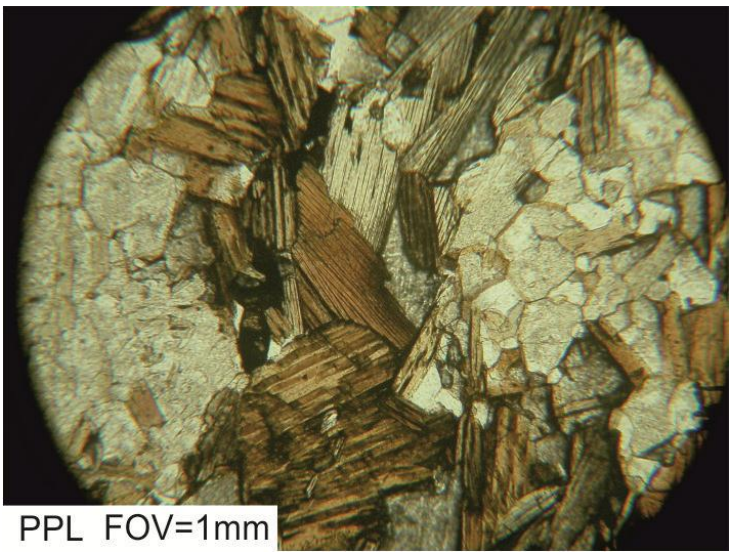

Fig. 4.25 Variably-oriented laths of pleochroic brown-colourless biotite in sample JM08/22.

Modal Mineralogy • ~60% plagioclase • ~25% biotite • ~10% quartz • ~5% garnet
~60 plagioclase • Sub-1mm subidiomorphic equant crystals • Widespread partial sericitisation • Poorly-preserved lamellar twinning and concentric zoned extinction in rare larger crystals
~25% biotite • Laths and stubby crystals, 0.5-1mm • No obvious lineation defined by laths (Fig. 4.25) • Different crystals undergo pleochroic colour change from brown to colourless at different microscope stage rotation angle
~10% quartz • Fairly idiomorphic equant, sub-1mm • Undulose extinction common
~5% garnet • Relict porphyroblasts up to 3mm • Now broken into fragments which are themselves heavily fractured (Fig. 4.26) • Quartz and biotite grow among fragments of garnet but do not define an obvious reaction texture like a rim
General Comments • Weakly-developed compositional layering, no mineral stretching lineations
Interpretation Comments • Garnets are interpreted to reflect an early metamorphic event but have been fractured and partially altered in a subsequent metamorphic event. The general lack of fabrics indicates that metamorphism was static. • The weakly-developed compositional banding may have formed in an early tectonothermal, analogous to the formation of gneissic layering in the surrounding grey TTG gneisses.

Table 4.8 Petrographic description of sample JM08/22.

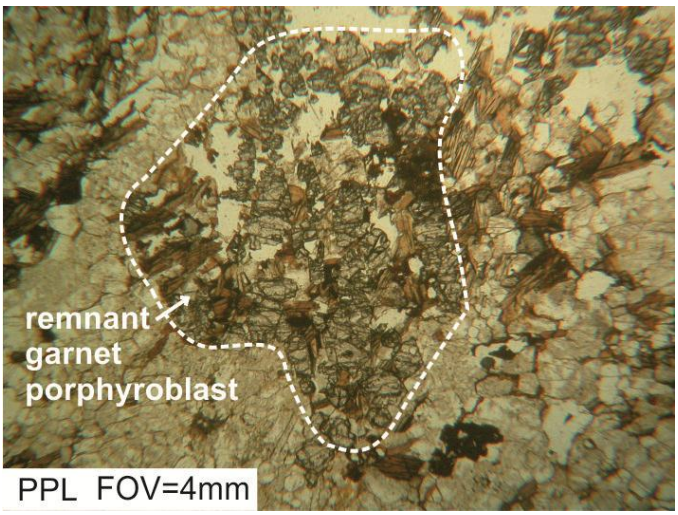

Fig. 4.26 Broken up and heavily-fractured garnet porphyroblast in sample JM08/22, dashed white line denotes crystal boundary.

Sample JM08/23

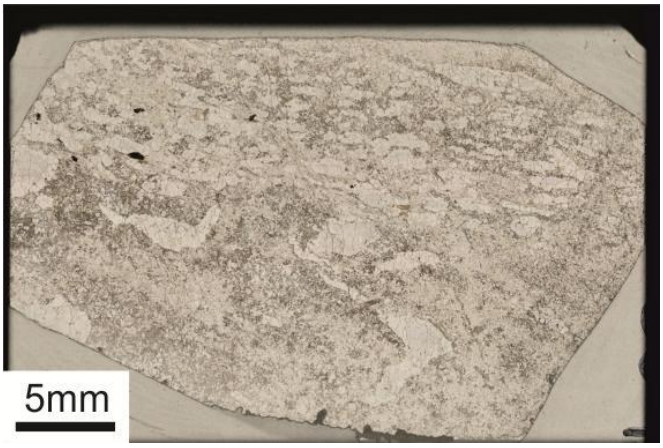

Fig. 4.27 PPL scan of the thin section from sample JM08/23.

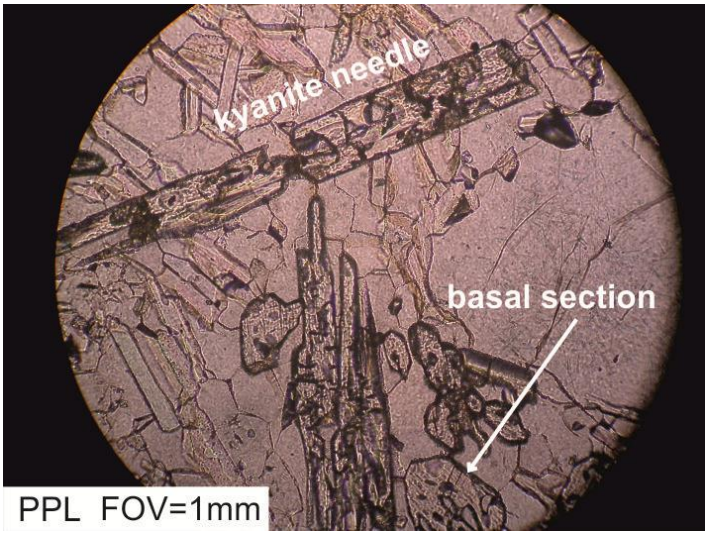

Fig. 4.28 High-relief kyanite crystals in sample JM08/23.

Modal Mineralogy • ~40% quartz (in fine groundmass and aggregates) • ~25% feldspar (in fine groundmass and as large individual crystals) • ~20% muscovite (in fine groundmass) • ~15% aluminosilicates • Minor minerals: ○ Xenomorphic opaques
~55% fine groundmass • ~0.1-0.2mm equant quartz crystals • ~0.2-0.5mm feldspars, often partially sericitised and occasionally zoned • muscovite needles ~0.5mm long which form a weak planar fabric and bend around larger crystals, first-order pink to blue interference colours
~20% Quartz aggregates • Aggregates have fairly irregular shapes, occasionally lensoid or arcuate, ~2x5mm • Constituent crystals are fairly equant, ~0.5mm in diameter
~15% kyanite • generally sub-idiomorphic equant crystals, ~0.2-1mm in diameter, occasionally show one faint cleavage, rarely another possible one at right angles, first-order yellow to orange-brown interference colours, usually have overgrowths and inclusions of quartz. Also occurs as idiomorphic needles, 0.5-1.2mm long with straight extinction and first-order brown interference colours (Fig. 4.28)
~10% large feldspar crystals • Fairly equant, ~0.5-2mm in diameter • Occasional partial sericitisation, often invaded by other crystals round edges • Lamellar twinning prominent, often as possible albite-pericline twins, indicating plagioclase
General Comments • Weakly-developed planar fabric defined by muscovite needles
Interpretation Comments • The quartz aggregates could be recrystallized porphyroclasts. • Generally an unusual rock and difficult to interpret.

Table 4.9 Petrographic description of sample JM08/23.

Sample JM09/ST02

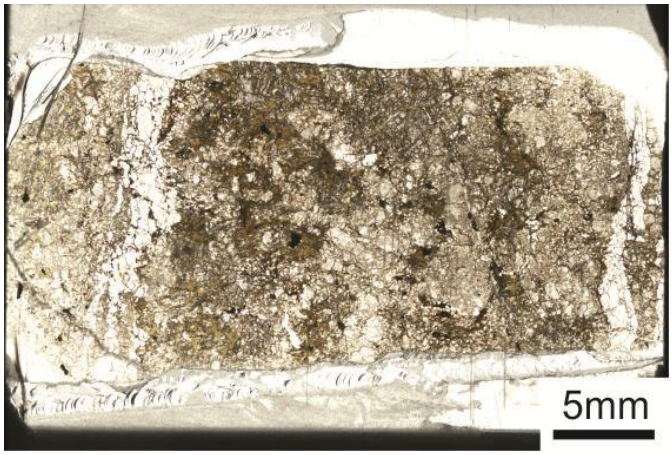

Fig. 4.29 PPL scan of the thin section from sample JM09/ST02.

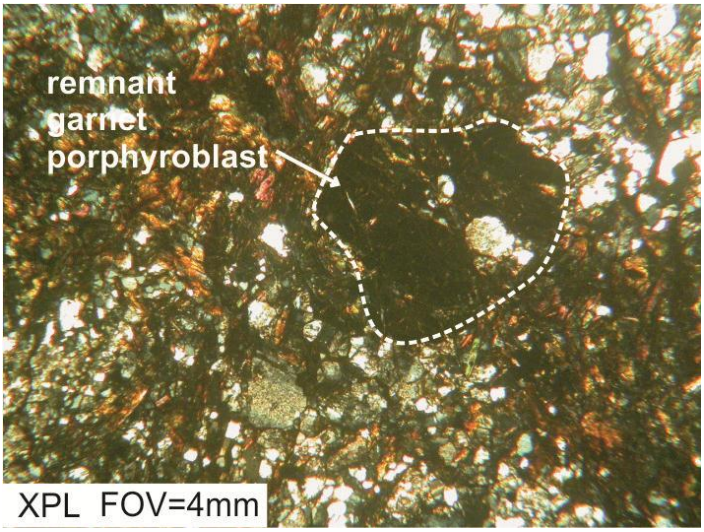

Fig. 4.30 Broken up and heavily-fractured garnet porphyroblast in sample JM09/ST02, dashed white line denotes crystal boundary.

Modal Mineralogy • ~30% plagioclase • ~30% quartz • ~30% biotite • ~10% garnet
~30% plagioclase • Sub-2mm equant xenomorphic crystals • Usually well-sericitised but some remnant lamellar twinning • Zoned extinction common • Smallest crystals aggregate with quartz in a ~2-5mm ovoid shape, giving the appearance of a porphyroclast
~30% quartz • Equant xenomorphic crystals, sub-2mm • Undulose extinction common, but no consistent orientation • Occurs in aggregates with plagioclase (porphyroclast?)
~30% biotite • Laths or xenomorphic crystals, to 1mm • Weakly-developed fabric defined by laths • Pleochroic colour change from brown to colourless; different crystals undergo pleochroic colour change at different microscope stage rotation angles • Usually associated with garnet
~10% garnet • Relict porphyroblasts up to 3mm (Fig. 4.30) • High relief, isotropic • Now broken into sub-mm fragments which are themselves heavily fractured • Quartz and biotite grow among fragments of garnet but do not define an obvious reaction texture like a rim
General Comments • Weakly-developed compositional layering, no mineral stretching lineations
Interpretation Comments • Garnets are interpreted to reflect an early metamorphic event but have been fractured and partially altered in a subsequent metamorphic event. The general lack of fabrics indicates that metamorphism was static. • The weakly-developed compositional banding may have formed in an early tectonothermal, analogous to the formation of gneissic layering in the surrounding grey TTG gneisses.

Table 4.10 Petrographic description of sample JM09/ST02.

Geisgeil

Field Relationships

The Geisgeil field area is located at UK grid reference NC179410, ~ 3km SE of Scourie village. The locality is on moorland 60-120m above sea-level with patchy rock exposures (Fig. 4.31a). As at Badcall Point and Duartmore Point, the major rock type here is the typical Assynt terrane/Central Region variably-deformed grey TTG gneiss. The oldest recognised structure is a gneissic layering fabric (Fig. 4.31b) with ~5-20mm wide layers of mafic and felsic minerals. A sample (JM08/GG09) of this was taken at NC 17947 41005. Field inspection suggests the pale white-grey felsic layers are composed of quartz and feldspar while the dark-grey mafic layers are amphibole or pyroxene. No mineral lineations were observed. The strike of the gneissic layering is highly variable (Fig. 4.31b). As the oldest recognised structure, the gneissic layering is interpreted to have formed in the Badcallian tectonothermal event, the same as that found at the Badcall Point and Duartmore Point localities.

A 5-10m wide member of the Scourie Dyke Swarm cuts the Badcallian gneissic layering (Fig. 4.31b&c). This dyke is then cut by a ~20m-wide west-trending discrete shear zone (Fig. 4.31b). As it post-dates the Scourie dyke, this shear zone will have formed during the Laxfordian tectonothermal event. This size of shear zone is a typical structural feature of Laxfordian deformation in the Assynt terrane/Central Region (Wynn, 1995). Compositional layering of mafic and felsic minerals in the grey TTG gneiss are still present but are narrower (~3mm wide) than in the Badcallian gneissic layering; mineral aggregate stretching lineations of quartz were observed. The dyke is deflected from its northwesterly orientation into a westerly orientation (Fig. 4.31b); it is strongly deformed and narrows to an indistinguishable compositional layer in the core of the shear zone. Following the shear zone to the east for ~150m from the point where the dyke enters the shear zone, a Scourie dyke exits the shear zone on its south side; if this is the same dyke, the displacement on the

shear zone would be constrained to ~150m. The geometry of the dyke deflection indicates a sinistral movement on the shear zone.

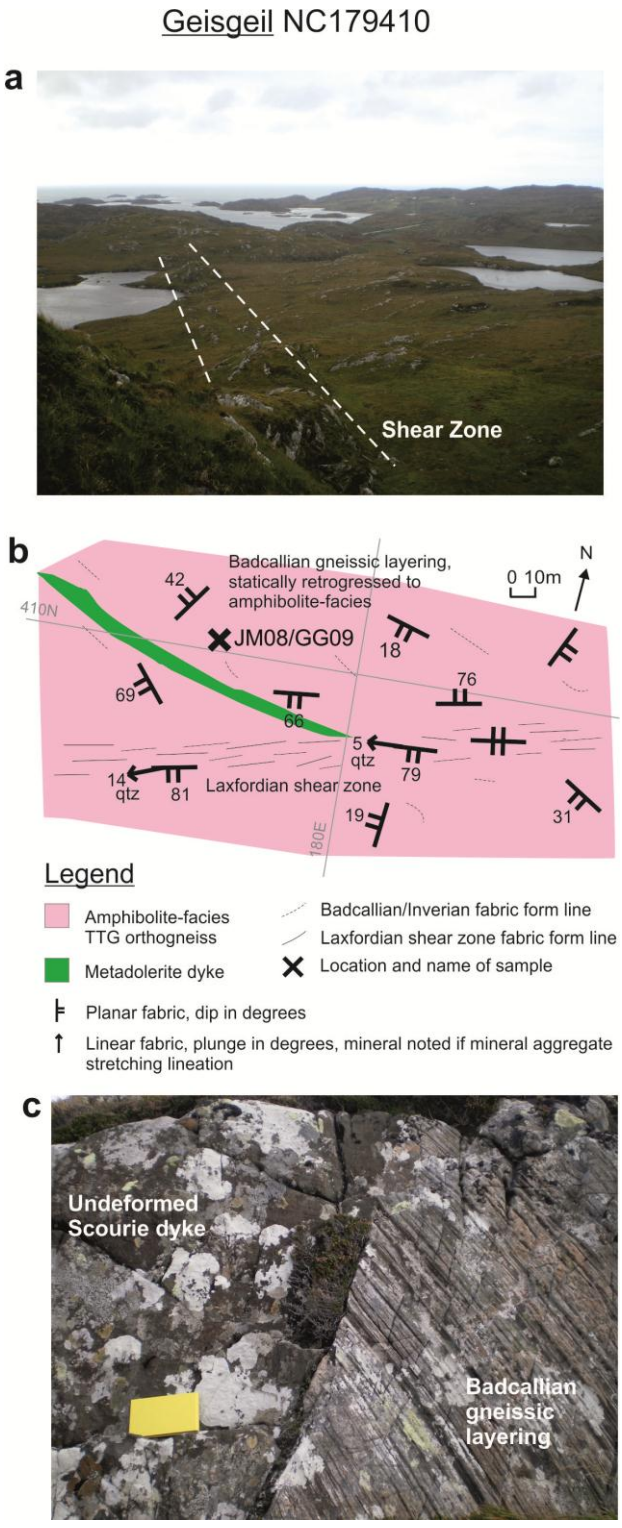

Fig. 4.31 a Photograph of the Geisgeil locality with the Laxfordian shear zone marked by dashed white line; **b** Field map of lithologies and structures at the locality with sample location marked. Numbered pale grey lines on field maps denote UK Ordnance Survey grid lines; **c** Photograph showing the undeformed Scourie dyke cross-cutting Badcallian gneissic layering in the grey TTG gneiss, notebook is 21cm long.

Sample Petrography

One sample from Geisgeil (JM08/GG09) is used in chapter 5 of this thesis. A thin section (Fig. 4.32) of this sample was made so that the petrography could be well-constrained by optical- and scanning electron-microscopy. A detailed petrographic description is given in table 4.11 and images of key mineral textures are shown in figure 4.33.

Sample JM08/GG09

Fig. 4.32 PPL scan of the thin section from sample JM08/GG09.

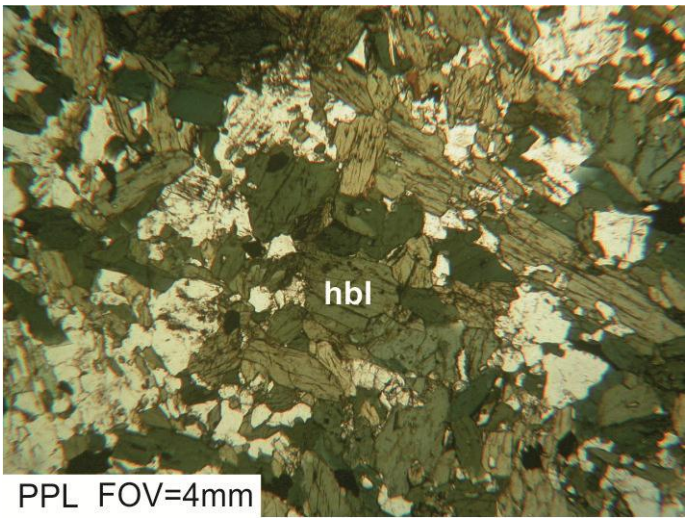

Fig. 4.33 Photomicrograph showing hornblende (hbl = hornblende) in sample GG09.

Modal Mineralogy • ~40% hornblende • ~30% plagioclase • ~30% quartz • Minor minerals: ○ Biotite laths and xenomorphic opaques generally associated with hornblende
~40% hornblende • Prismatic crystals ~0.5-1mm, often quite idiomorphic but do not define a shape fabric, aggregated into irregularly-shaped clumps (Fig. 4.33) • 2 cleavages at 120° occasionally visible • Different crystals undergo pleochroic colour change from green to colourless at different microscope stage rotation angles
~30% plagioclase • Fairly equant crystals ~0.2-0.6mm • Lamellar twinning often well preserved • Occasional concentric zoned extinction • Occasional partly sericitised crystal
~30% quartz • Equant ~0.1mm
General Comments • Gneissic layering of mafic and felsic minerals not visible at the thin section scale, no mineral lineations
Interpretation Comments • Although Badcallian gneissic layering is the structural feature in this sample, the presence of hornblende but not pyroxene suggests that the Badcallian granulite-facies assemblage has been statically retrogressed to amphibolite-facies.

Table 4.11 Petrographic description of sample JM08/GG09.

Scourie Mor

Field Relationships

The Scourie Mor field area is located at UK grid reference NC141442, ~ 1km W of Scourie village. Exposure is generally wave-washed platforms in the intertidal zone and some above the high tide line with occasional isolated inland crags and pavements. As at Badcall Point and Duartmore Point, the major rock type here is the typical Assynt terrane/Central Region variably-deformed grey TTG gneiss. The oldest recognised structure is a gneissic layering fabric (Fig. 4.34) with ~5-20mm wide layers of mafic and felsic minerals. A sample (JM09/SM09) of this was taken at NC 14146 44175. Field inspection suggests the pale white-grey felsic layers are composed of quartz and feldspar while the dark-grey mafic layers are amphibole or pyroxene. No mineral lineations were observed. The gneissic layering generally dips moderately steeply to the WSW (Fig. 4.34). As the oldest recognised structure, the gneissic layering is interpreted to have formed in the Badcallian tectonothermal event, the same as that found at the Badcall Point, Duartmore Point and Geisgeil localities.

Two northwest-trending <1m-wide members of the Scourie Dyke Swarm cut the Badcallian gneissic layering (Fig. 4.34). They join up and into one body which is deflected into a southwesterly orientation by a ~5m-wide discrete shear zone (Fig. 4.34). The dyke is strongly deformed and narrows to an indistinguishable compositional layer in the core of the shear zone. As it post-dates the Scourie dyke, this shear zone will have formed during the Laxfordian tectonothermal event. This size of shear zone is a typical structural feature of Laxfordian deformation in the Assynt terrane/Central Region (Wynn, 1995). Compositional layering of mafic and felsic minerals in the grey TTG gneiss are still present but are narrower (~3mm wide) than in the Badcallian gneissic layering and the shear zone fabric is flaggy; mineral aggregate stretching lineations of plagioclase and quartz were observed. Various other lithologies are present at this locality, including mafic and

ultramafic gneiss, a schistose calc-silicate gneiss and an Inverian pegmatitic granite vein. These other lithologies have been described previously (Cohen et al., 1991; Corfu et al., 1994).

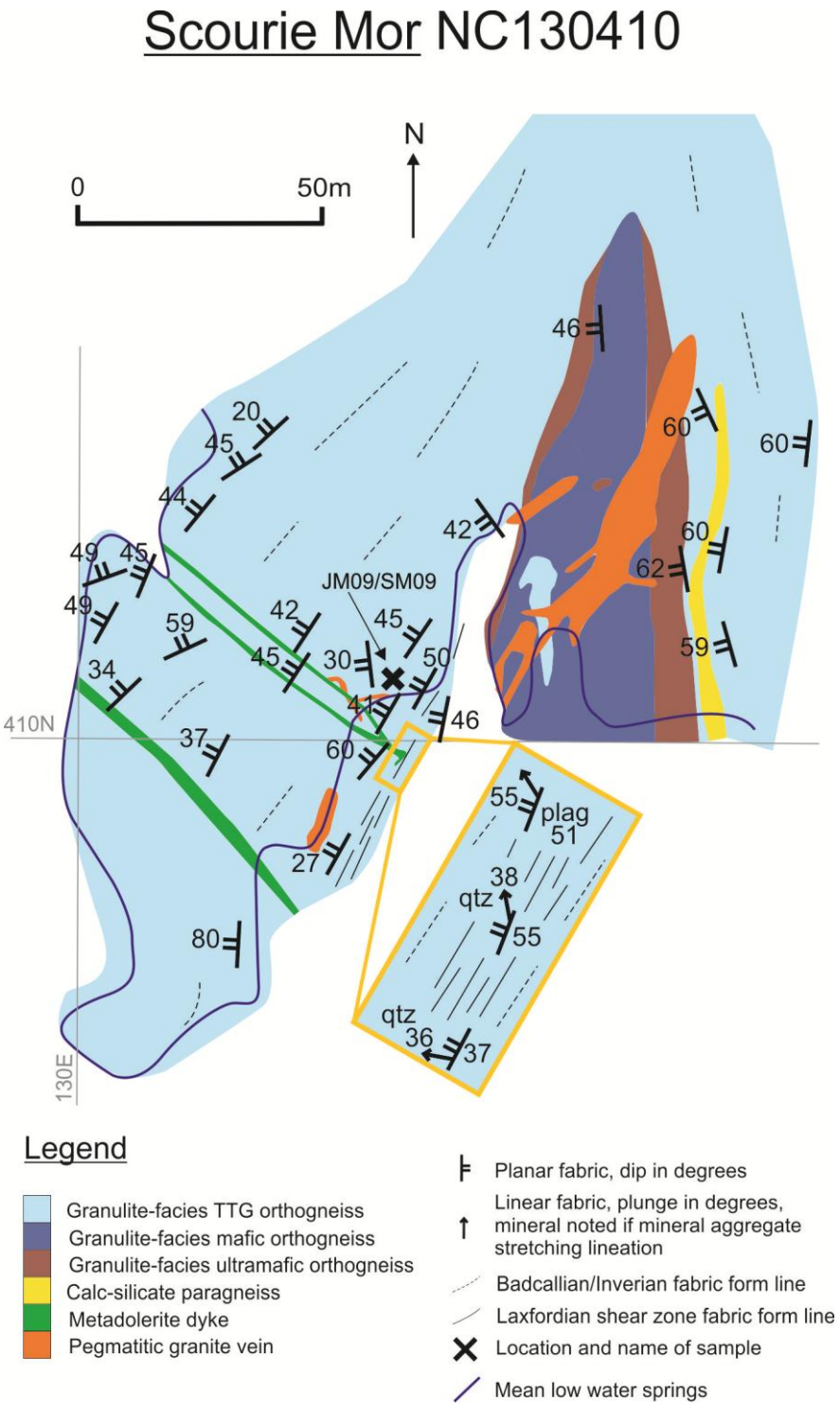

Fig. 4.34 Field map of structures and lithologies at the Sithean Mor locality with sample location marked. Numbered pale grey lines on field maps denote UK Ordnance Survey grid lines.

Sample Petrography

One sample from Scourie Mor (JM09/SM09) is used in chapters 5-7 of this thesis. A thin section (Fig. 4.35) of this sample was made so that the petrography could be well-constrained by optical- and scanning electron-microscopy. A detailed petrographic description is given in table 4.12 and images of key mineral textures are shown in figure 4.36.

Sample JM09/SM09

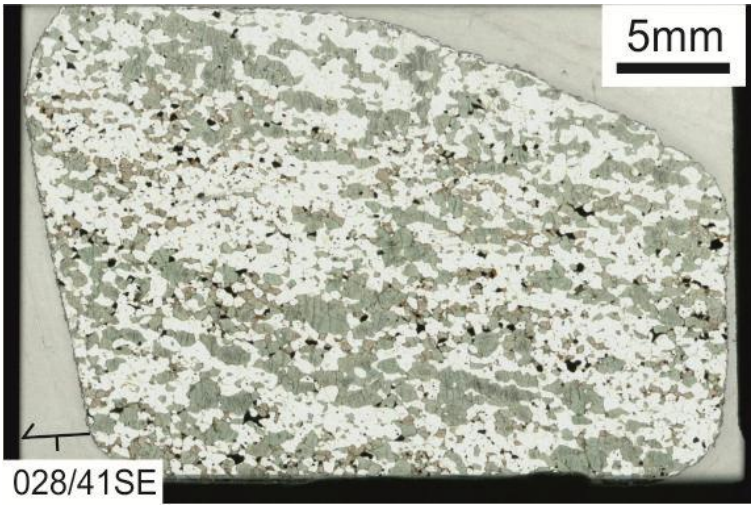

Fig. 4.35 PPL scan of the thin section from sample JM09/SM09.

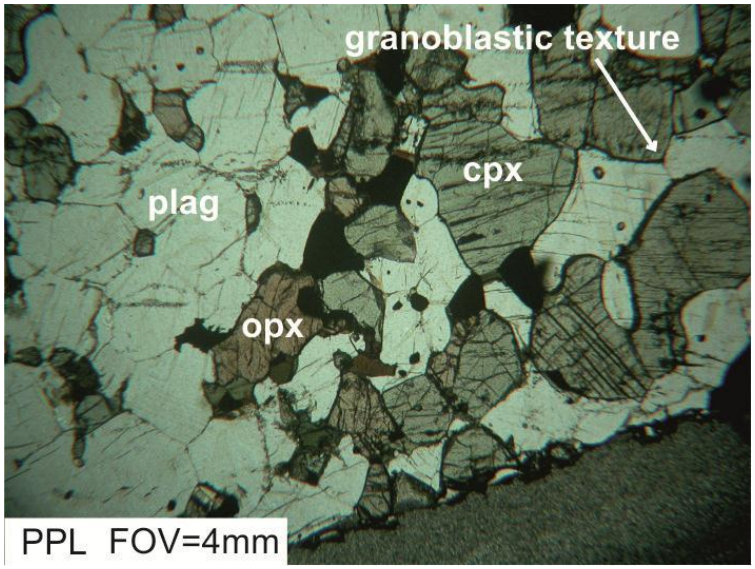

Fig. 4.36 Photomicrograph showing pale green clinopyroxene, reddish-brown orthopyroxene and granoblastic to sub-granoblastic texture in sample JM09/SM09 (cpx = clinopyroxene, opx = orthopyroxene, plag = plagioclase).

Modal Mineralogy • ~55% plagioclase • ~30% clinopyroxene • ~10% quartz • ~5% orthopyroxene • Minor minerals: ○ Subidiomorphic equant opaques
~55% plagioclase • Stubby subidiomorphic 1-4mm crystals • Lamellar twinning always well-preserved • Zoned extinction common, linear or sub-concentric
~30% clinopyroxene • Stubby crystals 1-3mm • Non-pleochroic, pale green (Fig. 4.36) • Often fractured • First-order yellow birefringence, oblique extinction
~10% quartz • Stubby subidiomorphic crystals, sub-2mm • Occasional undulose extinction
~5% orthopyroxene • Stubby ~1mm crystals • High relief, often fractured • Pale red in colour (Fig. 4.36) with weak pleochroism to pale green • First-order yellow-blue birefringence, straightish extinction
General Comments • Weakly-developed gneissic layering of mafic and felsic minerals visible at the thin section scale, no mineral lineations • Granoblastic to sub-granoblastic texture (Fig. 4.36)
Interpretation Comments • 2 pyroxene-plagioclase-quartz assemblage with granoblastic texture – classic pristine Badcallian assemblage (e.g. Sutton and Watson, 1951).

Table 4.12 Petrographic description of sample JM09/SM09.

4b: Sample Geochemistry

Further insight into the nature of the samples was gained from geochemical analysis of the sample whole-rock composition and mineral chemistry.

Sample Whole Rock Composition

Major and trace element composition of 10 of the 12 samples was determined by X-ray fluorescence analysis (see Chapter 3 for a description of analytical methods) and the results are shown in Table 4.13. Major element contents of samples from the grey TTG gneiss were used to calculate CIPW norms and a name was derived for each sample using the Streckeisen (1974) classification for plutonic rocks (Table 4.14, Fig. 4.37). The CIPW norm is used with caution only to ascribe a name to the interpreted parent magmatic rock and assumes that the parent rock was anhydrous. Most of the samples now contain hornblende and some other hydrous minerals which have formed through metamorphic reactions involving water through the Inverian and Laxfordian tectonothermal events. The fact that some samples record up to three metamorphic events since the protolith would suggest that they will have undergone at least some bulk chemical change and therefore the names ascribed using the QAP classification may be inaccurate. Primitive mantle-normalised (Hofmann, 1988) whole rock trace element contents of the grey TTG gneiss are plotted against the range and average of late-Archaean (3.4-2.5Ga) high-Al TTG samples compiled by Condie (2005) (Fig. 4.38).

Majors (Wt.%)	JM09/ BP02	JM09/ BP01	JM09/ BP06	JM09/ BP04	JM09/ DP03	JM09/ DP01	JM09/ DP02	JM09/ SM09	JM08/ 22	JM08/ 23
SiO_2	46.87	60.30	64.38	62.33	49.55	53.69	62.54	51.33	61.14	56.04
$Al2O_3$	15.69	16.56	15.67	16.57	16.45	14.36	14.99	14.46	18.04	19.28
FeO_T	11.14	6.01	5.22	5.28	9.45	8.40	6.44	11.66	8.07	10.71
MgO	7.06	3.46	2.64	2.56	6.90	7.35	3.80	6.78	2.11	2.55
CaO	10.56	5.75	4.64	5.14	9.98	8.62	5.04	10.93	1.35	3.23
Na_2O	2.51	4.61	4.72	4.94	3.30	3.61	4.18	3.03	2.15	3.25
K_2O	1.32	0.91	0.73	0.62	1.15	0.68	0.78	0.45	2.43	1.21
TiO_2	1.14	0.62	0.51	0.62	1.02	0.40	0.53	0.85	0.77	1.09
MnO	0.16	0.10	0.08	0.07	0.12	0.11	0.11	0.21	0.06	0.20
P_2O_5	0.96	0.23	0.12	0.19	0.53	0.27	0.13	0.08	0.03	0.03
LOI	2.01	1.19	1.00	1.09	1.18	2.05	1.16	0.16	3.56	2.21
Total	99.41	99.74	99.70	99.41	99.63	99.54	99.70	99.94	99.72	99.79
Traces (ppm)										
Rb	36.7	21.7	8.7	5.4	4.5	3	9	3.7	36.9	12.9
Ba	542.1	263.5	290.7	151.9	313.8	149.7	221	213.4	923.9	836.6
Th	11.4	bd	bd	bd	3.6	bd	bd	bd	bd	bd
U	bd	bd	bd	bd	bd	bd	bd	bd	bd	bd
Pb	6.3	10.1	6.6	2.6	4.9	6.4	8.3	4.5	14.8	19.6
Nb	7.6	5	3.3	3.4	7.2	1.4	4.2	3	11.5	12
La	135.2	25.6	17.4	15.2	60.2	22.8	23.5	14.4	14.4	30.5
Ce	270.2	55	35.7	36.4	127.6	60.6	49.7	36.5	25.4	48.2
Sr	540.9	517.3	597.2	452.8	560	421.8	448.9	268.9	236.4	505.3
Nd	133.1	24.1	15.3	19.8	71.2	42.3	20.9	20.1	6.9	10.3
Zr	215.1	125.7	87.7	118.9	233.4	182	125.9	62.3	118.1	607.4
Y	38.5	12.3	9.1	12.8	23.4	22.4	10.7	26.6	9.8	23.1
Zn	133.3	88.8	54	74.5	122	156.3	63.7	97.4	74.3	128.1
Cu	44.7	35.9	48.4	35.5	15.4	26.2	38.6	57.9	138.8	145.1
Ni	161.5	75.7	51.1	62.8	89.6	121.1	56.5	272.4	23.9	34.1
Sc	38.6	15.8	16.1	21.6	30.6	34.6	13.1	41	20.4	28.5
Cr	200.1	92.5	78.6	182.8	305	709	42.8	243.4	233.4	426.6
V	246	114	102.6	119.1	204.9	122.2	106	279.7	218.5	280.6

Table 4.13 Whole rock major and trace element composition for samples described in Chapter 4a; bd denotes below detection limits; FeO_T denotes total iron oxide concentration.

Volume %	JM09/ BP02	JM09/ BP01	JM09/ BP06	JM09/ BP04	JM09/ DP03	JM09/ DP01	JM09/ DP02	JM09/ SM09
Quartz	0.00	12.63	20.11	16.48	0.00	2.27	18.65	0.00
Anorthite	30.50	22.41	19.67	21.66	28.75	22.85	20.47	26.82
Albite	24.88	42.44	42.87	45.12	31.88	35.18	38.59	29.62
Orthoclase	9.87	6.23	4.98	4.21	8.28	4.91	5.31	3.32
Diopside	14.14	3.83	2.15	2.26	14.39	14.91	3.17	21.73
Hypersthene	4.87	9.67	8.03	7.75	2.91	16.36	11.20	13.91
Olivine	8.98	0.00	0.00	0.00	8.73	0.00	0.00	0.07
Ilmenite	1.40	0.71	0.57	0.70	1.22	0.48	0.61	1.03
Magnetite	3.17	1.59	1.36	1.39	2.63	2.36	1.71	3.28
Apatite	2.13	0.47	0.24	0.39	1.15	0.59	0.27	0.18
Zircon	0.03	0.02	0.01	0.02	0.03	0.02	0.02	0.01
Chromite	0.03	0.01	0.01	0.02	0.03	0.09	0.01	0.04
Total	99.99	100.01	100.00	100.00	100.00	100.02	100.01	100.01
Normalised QAP								
M	27.99	13.50	10.18	10.01	26.03	31.27	14.37	35.71
Q	0.00	15.09	22.95	18.84	0.00	3.48	22.46	0.00
A	15.13	7.44	5.68	4.81	12.02	7.53	6.40	5.56
P	84.87	77.47	71.37	76.35	87.98	88.99	71.14	94.44
Total	100.00	100.00	100.00	100.00	100.00	100.00	100.00	100.00
QAP Field	9	10*	5	10*	9	10	5	10

Sample	QAP Field	Rock Name
BP02	9	hypersthene monzodiorite
BP01	10*	hypersthene diorite
BP06	5	hypersthene tonalite
BP04	10*	hypersthene diorite
DP03	9	hypersthene monzodiorite
DP01	10	hypersthene diorite
DP02	5	hypersthene tonalite
SM09	10	hypersthene diorite

Table 4.14 CIPW normative mineralogy and name for parent rocks of the grey TTG gneiss samples. The CIPW normative mineralogies of the samples all contained hypersthene, therefore the names are from the charnockite classification.

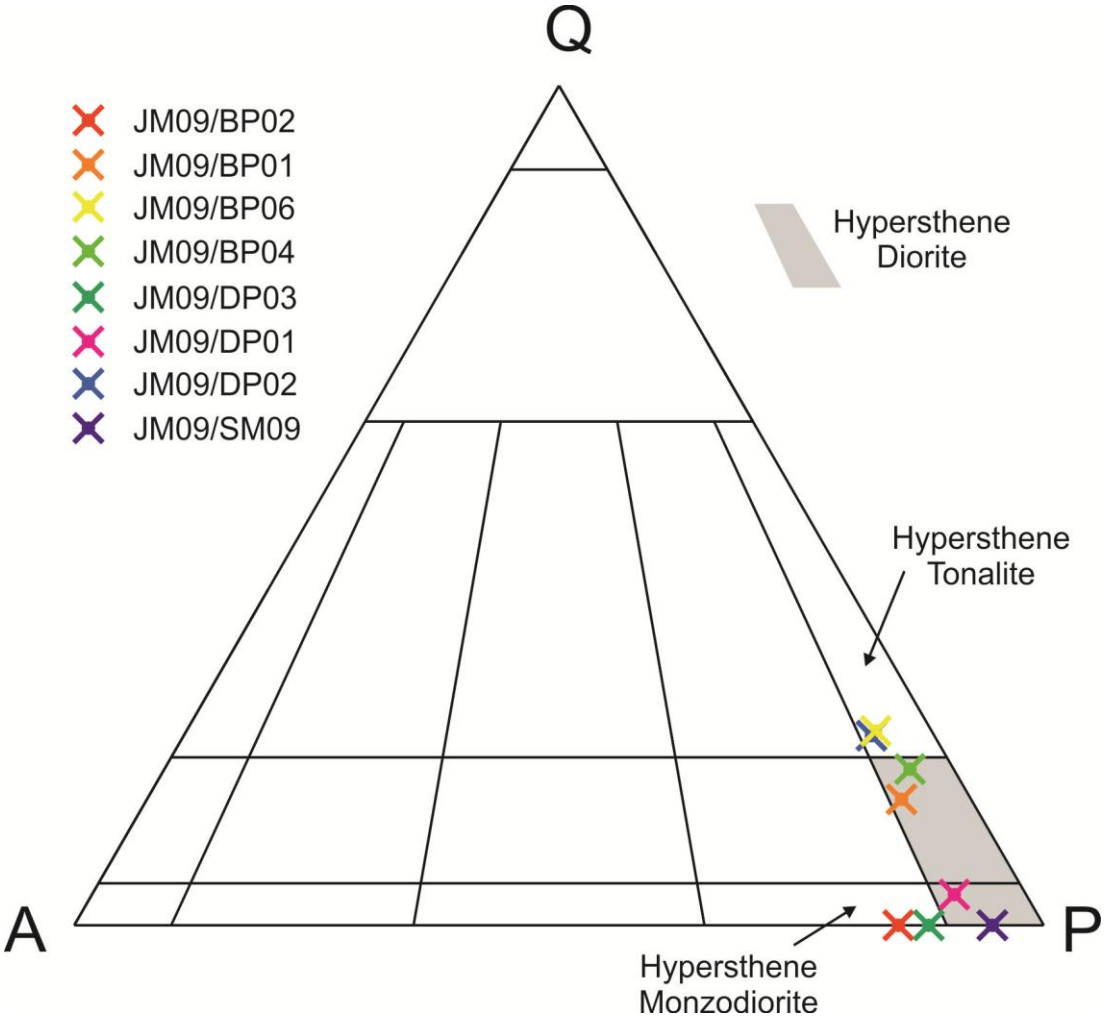

Fig. 4.37 QAP ternary diagram with fields named after the classification of Streckeisen (1974). The CIPW normative mineralogies of the grey TTG gneiss samples all contained hypersthene, therefore the names are from the charnockite classification.

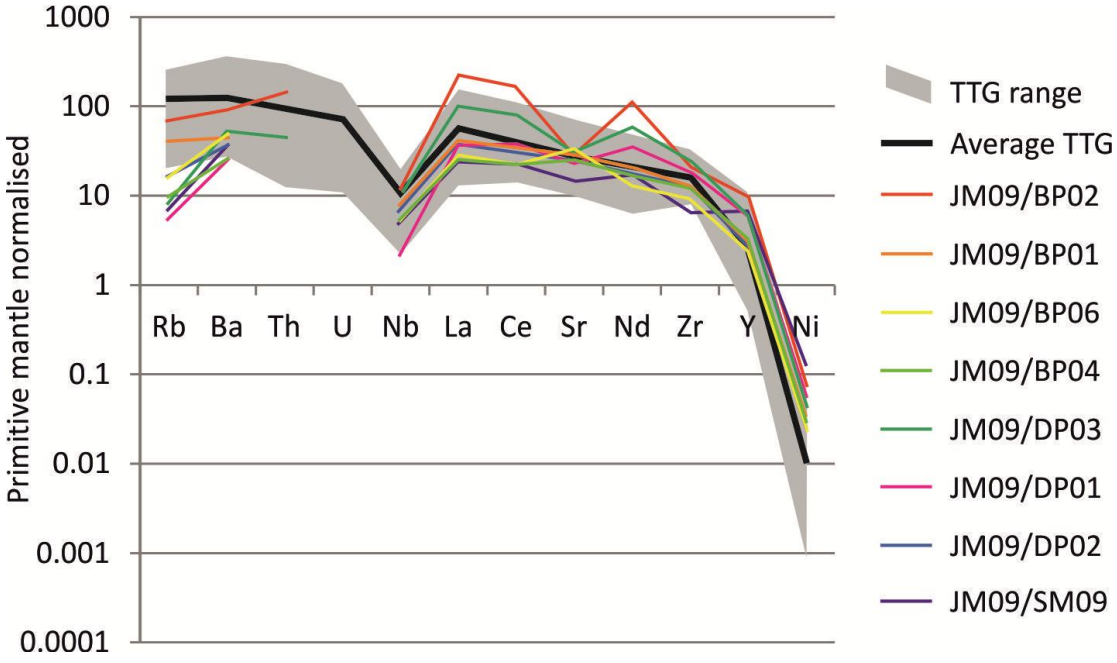

Fig. 4.38 Spider diagram of trace element concentrations of the grey TTG gneiss samples; TTG range and Average TTG values from the compilation of late-Archaean (3.4-2.5Ga) high-Al TTG samples in Condie (2005); all values normalised to the primitive mantle values of Hofmann (1988).

Mineral Chemistry

Further characterisation of the chemistry of the samples was gained from SEM-EDS and EMPA (see Chapter 3 for a description of analytical methods) analysis of major and some minor minerals. Semi-quantitative single analyses of minerals in each sample were made by SEM-EDS; the results are shown in Tables 4.15-4.19. Oxide weight per cent totals for some analyses are high, likely due to a lack of beam stability or instrument precision. However, the cation counts calculated from these analyses make up stoichiometric mineral formulae so these analyses have still been included.

Sample	JM09/BP02		JM09/BP01		JM09/BP06		JM09/BP04	
Mineral	Hbl	Plag	Hbl	Plag	Hbl	Plag	Hbl	Plag
SiO_2	46.93	60.61	42.55	66.13	49.00	68.37	36.07	62.34
TiO_2	0.59	bd	0.67	bd	0.55	bd	1.50	bd
Al_2O_3	9.12	26.37	12.96	23.15	9.32	20.43	17.50	25.91
FeO_T	13.31	bd	19.43	bd	14.46	bd	21.37	bd
MnO	bd	bd	bd	bd	bd	bd	bd	bd
MgO	14.10	bd	10.43	bd	14.28	bd	14.71	bd
CaO	11.89	6.87	11.81	1.34	12.09	0.25	bd	6.23
Na_2O	1.25	8.53	1.71	9.57	1.53	11.60	bd	8.44
K_2O	0.51	bd	1.13	1.66	0.54	0.28	5.14	bd
Total	97.70	102.38	100.69	101.85	101.77	100.93	96.29	102.92
No. of oxygens	23	8	23	8	23	8	23	8
Si	6.86	2.64	6.28	2.86	6.89	2.96	5.59	2.69
Ti	0.06	0.00	0.07	0.00	0.06	0.00	0.17	0.00
Al	1.57	1.36	2.25	1.18	1.55	1.04	3.20	1.32
Fe	1.63	0.00	2.40	0.00	1.70	0.00	2.77	0.00
Mn	0.00	0.00	0.00	0.00	0.00	0.00	0.00	0.00
Mg	3.07	0.00	2.29	0.00	3.00	0.00	3.40	0.00
Ca	1.86	0.32	1.87	0.06	1.82	0.01	0.00	0.29
Na	0.35	0.72	0.49	0.80	0.42	0.97	0.00	0.71
K	0.10	0.00	0.21	0.09	0.10	0.02	1.02	0.00
Total	15.51	5.04	15.87	5.00	15.53	5.01	16.15	5.00
X_{Mg}	0.65		0.49		0.64		0.55	
X_{An}		0.31		0.07		0.01		0.29

Table 4.15 EDS analyses of major phases in samples from the Badcall Point locality; FeO_T denotes total iron oxide content; bd denotes below detection limits; Hbl = hornblende, Plag = plagioclase.

Sample	JM09/DP03			JM09/DP01		JM09/DP02	
Mineral	Hbl	Plag	Cpx	Hbl	Plag	Hbl	Plag
SiO_2	38.97	61.69	57.86	48.14	58.84	44.05	65.08
TiO_2	bd	bd	bd	bd	bd	bd	bd
Al_2O_3	23.28	28.25	3.07	11.70	25.86	14.36	24.11
FeO_T	12.71	1.26	10.39	13.68	bd	17.43	bd
MnO	bd	bd	bd	bd	bd	bd	bd
MgO	5.42	bd	14.61	13.88	bd	11.06	bd
CaO	20.75	3.49	25.54	12.80	7.71	12.48	0.81
Na_2O	bd	6.55	0.91	1.36	7.44	1.74	8.64
K_2O	bd	4.33	bd	0.52	bd	0.65	2.41
Total	101.13	105.57	112.38	102.08	99.85	101.77	101.05
	23	8	6	23	8	23	8
Si	5.60	2.64	1.93	6.73	2.63	6.33	2.84
Ti	0.00	0.00	0.00	0.00	0.00	0.00	0.00
Al	3.94	1.42	0.12	1.93	1.36	2.43	1.24
Fe	1.53	0.05	0.29	1.60	0.00	2.10	0.00
Mn	0.00	0.00	0.00	0.00	0.00	0.00	0.00
Mg	1.16	0.00	0.73	2.89	0.00	2.37	0.00
Ca	3.20	0.16	0.91	1.92	0.37	1.92	0.04
Na	0.00	0.54	0.06	0.37	0.65	0.48	0.73
K	0.00	0.24	0.00	0.09	0.00	0.12	0.13
Total	15.43	5.04	4.04	15.53	5.01	15.75	4.98
X_{Mg}	0.43		0.71	0.64		0.53	
X_{An}		0.23			0.36		0.05

Table 4.16 EDS analyses of major phases in samples from the Duartmore Point locality; FeO_T denotes total iron oxide content; bd denotes below detection limits; Hbl = hornblende, Plag = plagioclase.

Sample	JM08/22				JM08/23		JM09/ST02		
Mineral	Grt	Bt	Plag	Msc	Ky (needle)	Ky (basal)	Grt	Bt	Plag
SiO_2	38.33	38.45	64.61	50.49	38.91	37.91	42.29	40.37	65.02
TiO_2	bd	2.20	bd	2.50	bd	bd	bd	2.29	bd
Al_2O_3	21.99	19.96	25.73	38.40	65.29	64.97	23.94	20.60	27.55
FeO_T	30.39	14.76	bd	3.05	bd	bd	38.33	19.62	0.99
MnO	5.52	bd	bd	bd	bd	bd	2.95	bd	bd
MgO	4.50	13.75	bd	0.72	bd	bd	4.75	13.64	bd
CaO	2.71	bd	3.60	bd	bd	bd	2.86	bd	1.16
Na_2O	bd	bd	8.84	1.21	bd	bd	bd	bd	7.52
K_2O	bd	9.23	1.63	10.66	bd	bd	bd	7.34	4.31
Total	103.44	98.35	104.41	107.03	104.20	102.88	115.12	103.86	106.55
No. of oxygens	12	22	8	22	5	5	12	22	8
Si	2.96	5.47	2.75	6.03	1.00	0.99	2.96	5.48	2.73
Ti	0.00	0.24	0.00	0.22	0.00	0.00	0.00	0.23	0.00
Al	2.00	3.35	1.29	5.40	1.99	2.01	1.97	3.30	1.36
Fe	1.96	1.76	0.00	0.30	0.01	0.00	2.24	2.23	0.03
Mn	0.36	0.00	0.00	0.00	0.00	0.00	0.17	0.00	0.00
Mg	0.52	2.92	0.00	0.13	0.00	0.00	0.50	2.76	0.00
Ca	0.22	0.00	0.16	0.00	0.00	0.00	0.21	0.00	0.05
Na	0.00	0.13	0.73	0.28	0.00	0.00	0.00	0.00	0.61
K	0.00	1.67	0.09	1.62	0.00	0.00	0.00	1.27	0.23
Total	8.04	15.53	5.02	14.00	3.00	3.00	8.06	15.27	5.01
X_{An}			0.18						0.08
X_{Alm}	0.64						0.72		
X_{Pyr}	0.17						0.16		
X_{Grs}	0.07						0.07		
X_{Sps}	0.12						0.06		

Table 4.17 EDS analyses of major phases in samples from the Sithean Mor locality; FeO_T denotes total iron oxide content; bd denotes below detection limits; Grt = garnet, Bt = biotite, Plag = plagioclase, Msc = muscovite, Ky = kyanite.

Sample	JM09/GG09	
Mineral	Hbl	Plag
SiO_2	49.37	68.01
TiO_2	0.68	bd
Al_2O_3	14.13	29.81
FeO_T	21.54	bd
MnO	bd	bd
MgO	10.96	bd
CaO	13.79	8.29
Na_2O	1.42	8.56
K_2O	0.43	bd
Total	112.32	114.67
No. of oxygens	23	8
Si	6.47	2.64
Ti	0.07	0.00
Al	2.18	1.37
Fe	2.36	0.00
Mn	0.00	0.00
Mg	2.14	0.00
Ca	1.94	0.35
Na	0.36	0.64
K	0.07	0.00
Total	15.59	5.00
X_{Mg}	0.48	
X_{An}		0.35

Table 4.18 EDS analyses of major phases in samples from the Geisgeil locality; FeO_T denotes total iron oxide content; bd denotes below detection limits; Hbl = hornblende, Plag = plagioclase.

Sample	JM09/SM09			
Mineral	Opx	Cpx	Ilm	Plag
SiO_2	53.85	54.70	bd	61.79
TiO_2	bd	bd	57.32	bd
Al_2O_3	2.13	3.54	bd	28.98
FeO_T	27.14	10.93	47.59	bd
MnO	0.79	bd	bd	bd
MgO	22.22	14.00	bd	bd
CaO	0.53	24.39	bd	10.03
Na_2O	bd	bd	bd	6.62
K_2O	bd	bd	bd	0.31
Total	106.66	107.56	104.91	107.73
No. of oxygens	6	6	3	8
Si	1.92	1.90	0.00	2.57
Ti	0.00	0.00	1.03	0.00
Al	0.09	0.15	0.00	1.42
Fe	0.81	0.32	0.95	0.00
Mn	0.02	0.00	0.00	0.00
Mg	1.18	0.73	0.00	0.00
Ca	0.02	0.91	0.00	0.45
Na	0.00	0.04	0.00	0.53
K	0.00	0.00	0.00	0.02
Total	4.04	4.04	1.97	4.99
X_{Mg}	0.59	0.70		
X_{An}				0.46

Table 4.19 EDS analyses of major phases in samples from the Scourie Mor locality; FeO_T denotes total iron oxide content; bd denotes below detection limits; Hbl = hornblende, Plag = plagioclase, Cpx = clinopyroxene.

At Badcall Point, hornblende has a variable composition between samples. X_{Mg} ranges from 0.49-0.65 with 8-9 Si p.f.u. The hornblende in sample JM09/BP04 is relatively Si-poor (5.59 p.f.u.) and Al-rich (3.2 p.f.u) but K-rich (1.02) with no Na or Ca. Plagioclase from the Badcall Point samples are generally albitic with X_{An} ranging from 0.31 down to 0.01 in sample JM09/BP06. There is also variability in hornblende composition between samples from Duartmore Point with X_{Mg} ranging from 0.43 to 0.64. Hornblende from sample JM09/DP03 (statically retrogressed Badcallian gneissic layering) is relatively Ca-rich (3.20 p.f.u.) while hornblendes from JM09/DP01 (shear zone margin) and JM09/DP02 (the Laxfordian shear zone) are Mg-rich (2.89 and 2.37 p.f.u. respectively). Like at Badcall Point, plagioclase is albitic with X_{An} ranging from 0.36 to 0.05. Clinopyroxene in the Badcallian assemblage in JM09/DP03 is diopsidic with 0.91 p.f.u. Ca and X_{Mg} of 0.71.

Almandine is the main component in garnets from the garnet- and biotite-bearing metasediments from Sithean Mor (samples JM08/22 and JM09/ST02; 0.64 and 0.72 p.f.u. respectively). Plagioclase from these two samples is albitic with X_{An} of 0.18 and 0.08 respectively. Hornblende from sample JM09/GG09 from Geisgeil has similar concentrations of Fe, Mg and Ca (2.36, 2.14 and 1.94 p.f.u. respectively). Plagioclase in this sample has an X_{An} of 0.35. Plagioclase from sample JM09/SM09 (granulite-facies Badcallian assemblage) from Scourie Mor has the highest anorthite component in plagioclase of any of the samples analysed by EDS (X_{An} of 0.46). Clinopyroxene in this sample is diopsidic with 0.91 p.f.u. Ca and X_{Mg} of 0.70; orthopyroxene is enstatitic (X_{Mg} of 0.59).

In order to determine if there was significant intracrystal geochemical variability, EMPA compositional traverses were made of major minerals in selected samples – JM09/SM09, JM09/BP01, JM09/DP01 and JM09/DP02 (transect locations on the thin sections are shown in Fig. 4.39). These samples were chosen as they were interpreted to reflect typical examples of the Badcallian granulite-facies metamorphic assemblage (JM09/SM09), possible Inverian deformation (JM09/BP01), a Laxfordian shear zone

(JM09/DP02) and statically retrogressed granulites (JM09/DP01). Plagioclase, orthopyroxene, clinopyroxene and hornblende were analysed (Tables 4.20-4.23). In the case of hornblende from JM09/DP01 and JM09/BP01, where hornblende is associated with quartz in a sieve texture, some analytical spots were discarded where they had clearly sampled quartz or a mixture of hornblende and quartz. Plots of X_{An} for plagioclase and X_{Mg} for hornblende, orthopyroxene and clinopyroxene show little or no chemical zoning within the minerals (Fig. 4.40); average compositions for each transect is given in Tables 4.24-4.27.

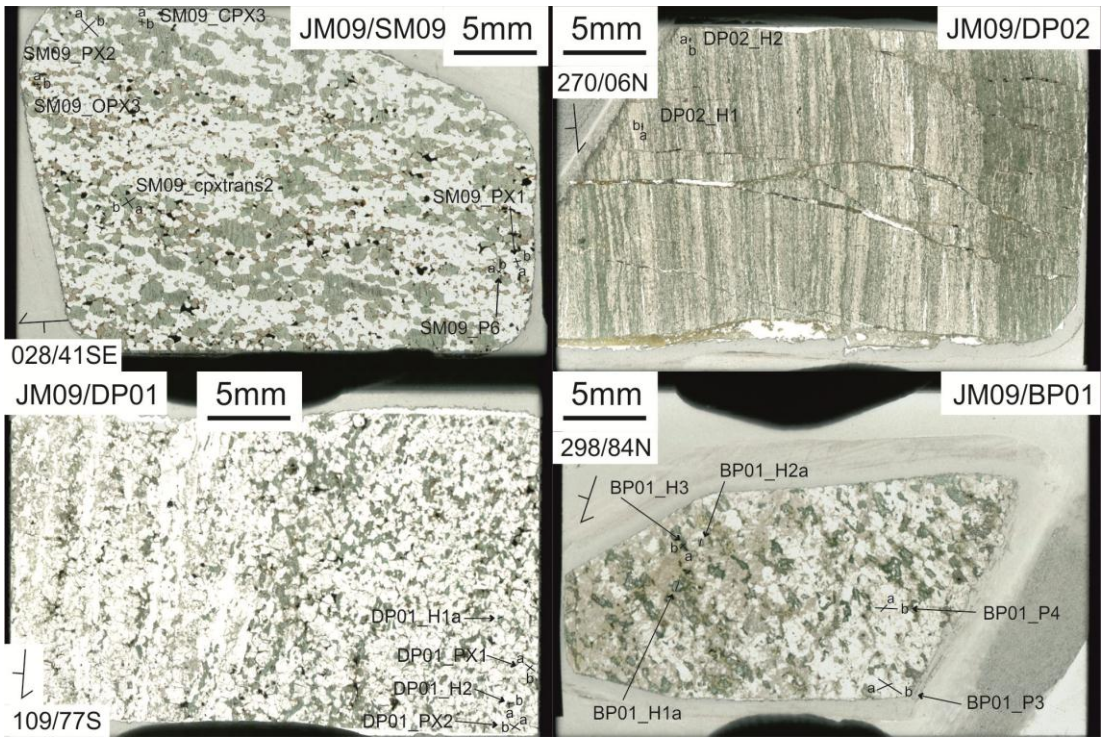

Fig. 4.39 Location of EMPA compositional transects on PPL scans of thin sections. Black lines denote transect lines, a or b denote a transect name suffix where more than one transect was made of single crystal.

Crystal: SM09_PX1a

	Transect data points											
SiO_2	56.35	56.11	55.66	56.77	55.95	56.69	56.62	55.79	56.98	56.13	56.44	55.19
Al_2O_3	26.54	26.29	26.25	26.18	26.45	26.13	26.35	26.54	26.49	26.46	26.44	27.19
CaO	8.71	8.34	8.50	8.56	8.34	8.34	8.36	8.62	8.35	8.54	8.70	9.32
FeO_T	0.08	0.06	0.06	bd	0.06	0.08	0.06	bd	0.08	0.06	0.08	0.14
Na_2O	6.67	6.80	6.72	6.79	6.83	6.84	6.77	6.64	6.81	6.78	6.65	6.42
K_2O	0.32	0.30	0.30	0.32	0.32	0.33	0.36	0.35	0.30	0.31	0.26	0.21
Total	98.67	97.91	97.49	98.62	97.94	98.41	98.52	97.95	99.02	98.27	98.56	98.47
Cations p.f.u. for 8 oxygens												
Si	2.57	2.57	2.57	2.58	2.57	2.59	2.58	2.56	2.58	2.57	2.57	2.52
Al	1.42	1.42	1.43	1.40	1.43	1.40	1.41	1.43	1.41	1.43	1.42	1.47
Ca	0.42	0.41	0.42	0.42	0.41	0.41	0.41	0.42	0.41	0.42	0.42	0.46
Fe	0.00	0.00	0.00	0.00	0.00	0.00	0.00	0.00	0.00	0.00	0.00	0.01
Na	0.59	0.60	0.60	0.60	0.61	0.60	0.60	0.59	0.60	0.60	0.59	0.57
K	0.02	0.02	0.02	0.02	0.02	0.02	0.02	0.02	0.02	0.02	0.02	0.01
Total	5.03	5.03	5.03	5.02	5.03	5.02	5.02	5.03	5.02	5.03	5.02	5.03
X_{An}	0.42	0.40	0.41	0.41	0.40	0.40	0.41	0.42	0.40	0.41	0.42	0.45

(continued)

Crystal: SM09_PX1b

	Transect data points							
SiO_2	56.07	55.71	55.62	56.48	56.82	56.62	56.91	55.44
Al_2O_3	26.36	26.34	26.35	26.27	26.47	26.35	26.23	26.28
CaO	8.60	8.32	8.45	8.26	8.43	8.36	8.48	8.71
FeO_T	0.09	0.07	0.08	0.08	0.07	0.08	0.09	0.13
Na_2O	6.65	6.79	6.65	6.80	6.67	6.65	6.79	6.69
K_2O	0.38	0.36	0.31	0.31	0.34	0.33	0.31	0.30
Total	98.15	97.58	97.46	98.20	98.80	98.38	98.81	97.56
Cations p.f.u. for 8 oxygens								
Si	2.57	2.57	2.56	2.58	2.58	2.58	2.58	2.56
Al	1.42	1.43	1.43	1.41	1.42	1.42	1.40	1.43
Ca	0.42	0.41	0.42	0.40	0.41	0.41	0.41	0.43
Fe	0.00	0.00	0.00	0.00	0.00	0.00	0.00	0.01
Na	0.59	0.61	0.59	0.60	0.59	0.59	0.60	0.60
K	0.02	0.02	0.02	0.02	0.02	0.02	0.02	0.02
Total	5.03	5.03	5.03	5.02	5.02	5.01	5.02	5.04
X_{An}	0.42	0.40	0.41	0.40	0.41	0.41	0.41	0.42

(continued)

Crystal: SM09_PX2a

	Transect data points														
SiO_2	57.68	58.11	58.01	57.83	57.95	58.47	59.08	58.39	57.30	58.62	59.22	58.17	58.62	59.15	58.90
Al_2O_3	26.65	26.32	26.51	26.55	26.18	26.35	26.06	26.12	27.13	26.50	25.97	26.14	25.95	26.11	26.21
CaO	8.32	7.83	8.06	8.18	7.71	8.15	7.57	7.70	8.96	7.92	7.76	7.89	7.76	7.73	7.88
FeO_T	bd	0.07	0.06	0.07	bd	0.06	bd	0.07	0.07	0.23	0.15	0.12	bd	0.07	0.07
Na_2O	6.85	7.20	7.10	7.13	7.19	7.05	7.36	7.47	6.64	7.19	7.29	7.23	7.12	7.25	7.17
K_2O	bd	0.33	0.29	0.27	0.35	0.29	0.35	0.35	0.29	0.33	0.35	0.34	0.37	0.38	0.35
Total	99.50	99.86	100.02	100.02	99.38	100.36	100.43	100.11	100.39	100.79	100.74	99.89	99.82	100.69	100.58
Cations p.f.u. for 8 oxygens															
Si	2.59	2.61	2.60	2.59	2.61	2.61	2.63	2.61	2.56	2.61	2.63	2.61	2.63	2.63	2.62
Al	1.41	1.39	1.40	1.40	1.39	1.39	1.37	1.38	1.43	1.39	1.36	1.38	1.37	1.37	1.37
Ca	0.40	0.38	0.39	0.39	0.37	0.39	0.36	0.37	0.43	0.38	0.37	0.38	0.37	0.37	0.38
Fe	0.00	0.00	0.00	0.00	0.00	0.00	0.00	0.00	0.00	0.01	0.01	0.00	0.00	0.00	0.00
Na	0.60	0.63	0.62	0.62	0.63	0.61	0.64	0.65	0.58	0.62	0.63	0.63	0.62	0.62	0.62
K	0.00	0.02	0.02	0.02	0.02	0.02	0.02	0.02	0.02	0.02	0.02	0.02	0.02	0.02	0.02
Total	5.00	5.02	5.02	5.02	5.02	5.01	5.01	5.03	5.02	5.02	5.01	5.02	5.01	5.01	5.01
X_{An}	0.40	0.38	0.39	0.39	0.37	0.39	0.36	0.36	0.43	0.38	0.37	0.38	0.38	0.37	0.38

(continued)

Crystal: SM09_PX2b

	Transect data points															
SiO_2	57.67	58.75	57.70	59.24	58.20	58.69	58.76	59.02	58.84	59.35	59.03	58.89	58.84	58.31	58.46	58.45
Al_2O_3	26.67	26.17	26.98	25.98	26.22	26.01	26.37	26.13	26.14	25.81	25.83	25.44	25.96	26.13	25.95	26.56
CaO	8.49	7.99	8.75	7.70	7.88	7.63	8.15	7.97	7.74	7.59	7.67	7.43	7.49	7.79	7.62	8.12
FeO_T	0.11	0.07	0.07	0.08	0.08	0.10	bd	0.06	0.06	0.06	0.06	0.07	0.06	0.10	0.07	0.17
Na_2O	6.89	7.23	6.76	7.34	7.24	7.37	7.05	6.97	7.27	7.24	7.27	7.23	7.11	7.26	7.16	7.15
K_2O	0.33	0.37	0.31	0.34	0.37	0.38	0.30	0.69	0.32	0.43	0.41	0.41	0.37	0.38	0.37	0.38
Total	100.15	100.57	100.56	100.69	99.98	100.18	100.63	100.84	100.37	100.48	100.28	99.47	99.82	99.97	99.63	100.83
Cations p.f.u. for 8 oxygens																
Si	2.58	2.62	2.57	2.63	2.61	2.62	2.61	2.62	2.62	2.64	2.63	2.65	2.63	2.61	2.62	2.60
Al	1.41	1.37	1.42	1.36	1.38	1.37	1.38	1.37	1.37	1.35	1.36	1.35	1.37	1.38	1.37	1.39
Ca	0.41	0.38	0.42	0.37	0.38	0.37	0.39	0.38	0.37	0.36	0.37	0.36	0.36	0.37	0.37	0.39
Fe	0.00	0.00	0.00	0.00	0.00	0.00	0.00	0.00	0.00	0.00	0.00	0.00	0.00	0.00	0.00	0.01
Na	0.60	0.62	0.58	0.63	0.63	0.64	0.61	0.60	0.63	0.62	0.63	0.63	0.62	0.63	0.62	0.62
K	0.02	0.02	0.02	0.02	0.02	0.02	0.02	0.04	0.02	0.02	0.02	0.02	0.02	0.02	0.02	0.02
Total	5.02	5.02	5.02	5.01	5.02	5.02	5.01	5.01	5.01	5.01	5.01	5.01	5.00	5.02	5.01	5.02
X_{An}	0.41	0.38	0.42	0.37	0.38	0.36	0.39	0.39	0.37	0.37	0.37	0.36	0.37	0.37	0.37	0.39

(continued)

Crystal: SM09_P6a

	Transect data points									
SiO_2	57.31	56.64	56.56	57.27	56.97	56.16	56.01	55.82	56.49	55.10
Al_2O_3	26.79	26.70	26.82	26.63	26.78	26.63	26.75	26.43	26.32	26.57
CaO	8.53	8.50	8.38	8.60	8.54	8.56	8.57	8.44	8.46	8.59
FeO_T	0.12	0.10	0.07	0.07	0.07	bd	0.07	0.10	0.10	0.15
Na_2O	6.77	6.75	6.73	6.84	6.88	6.69	6.81	6.65	6.84	6.66
K_2O	0.29	0.29	0.29	0.29	0.27	0.26	0.27	0.27	0.27	0.26
Total	99.81	98.97	98.85	99.69	99.51	98.30	98.47	97.69	98.49	97.32
Cations p.f.u. for 8 oxygens										
Si	2.58	2.57	2.57	2.58	2.57	2.56	2.56	2.56	2.58	2.55
Al	1.42	1.43	1.43	1.41	1.42	1.43	1.44	1.43	1.41	1.45
Ca	0.41	0.41	0.41	0.41	0.41	0.42	0.42	0.42	0.41	0.43
Fe	0.00	0.00	0.00	0.00	0.00	0.00	0.00	0.00	0.00	0.01
Na	0.59	0.59	0.59	0.60	0.60	0.59	0.60	0.59	0.60	0.60
K	0.02	0.02	0.02	0.02	0.02	0.02	0.02	0.02	0.02	0.02
Total	5.02	5.02	5.02	5.02	5.03	5.02	5.03	5.02	5.03	5.04
X_{An}	0.41	0.41	0.41	0.41	0.41	0.41	0.41	0.41	0.41	0.42

(continued)

Crystal: SM09_P6b

	Transect data points				
SiO_2	56.28	55.20	55.92	55.97	56.21
Al_2O_3	26.30	26.54	26.36	26.54	26.17
CaO	8.44	8.50	8.46	8.66	8.63
FeO_T	0.11	0.07	bd	0.10	0.08
Na_2O	6.63	6.73	6.67	6.92	6.78
K_2O	0.28	0.30	0.29	0.30	0.30
Total	98.04	97.34	97.70	98.50	98.15
Cations p.f.u. for 8 oxygens					
Si	2.58	2.55	2.57	2.56	2.57
Al	1.42	1.44	1.43	1.43	1.41
Ca	0.41	0.42	0.42	0.42	0.42
Fe	0.00	0.00	0.00	0.00	0.00
Na	0.59	0.60	0.59	0.61	0.60
K	0.02	0.02	0.02	0.02	0.02
Total	5.02	5.04	5.02	5.04	5.03
X_{An}	0.41	0.41	0.41	0.41	0.41

(continued)

Crystal: BP01_P3a

	Transect data points																	
SiO_2	58.14	57.77	58.63	58.86	59.50	58.02	57.97	58.68	59.53	59.49	61.68	60.65	59.39	58.73	59.13	59.96	59.34	60.02
Al_2O_3	25.45	25.34	25.38	25.24	25.40	25.02	24.86	25.18	24.92	25.17	23.79	24.34	25.00	25.46	25.07	25.06	25.28	25.23
CaO	6.50	6.86	7.10	6.71	6.43	6.58	6.66	6.59	6.48	6.66	6.15	6.23	6.57	6.69	6.57	6.57	6.80	6.67
FeO_T	bd	bd	bd	bd	bd	bd	bd	bd	bd	bd	0.07	bd	0.06	bd	bd	bd	bd	bd
Na_2O	7.42	7.76	7.59	7.76	7.89	7.76	7.96	8.18	7.95	8.06	7.48	7.85	8.08	7.94	8.08	8.08	8.17	7.99
K_2O	0.18	0.18	0.15	0.17	0.18	0.17	0.17	0.18	0.19	0.18	0.20	0.18	0.22	0.18	0.19	0.20	0.19	0.16
Total	97.68	97.91	98.86	98.74	99.39	97.54	97.62	98.81	99.05	99.56	99.36	99.25	99.31	98.99	99.04	99.87	99.78	100.08
Cations p.f.u. for 8 oxygens																		
Si	2.65	2.64	2.65	2.66	2.67	2.65	2.65	2.65	2.68	2.67	2.75	2.71	2.67	2.65	2.66	2.68	2.66	2.67
Al	1.37	1.36	1.35	1.34	1.34	1.35	1.34	1.34	1.32	1.33	1.25	1.28	1.32	1.35	1.33	1.32	1.33	1.32
Ca	0.32	0.34	0.34	0.32	0.31	0.32	0.33	0.32	0.31	0.32	0.29	0.30	0.32	0.32	0.32	0.31	0.33	0.32
Fe	0.00	0.00	0.00	0.00	0.00	0.00	0.00	0.00	0.00	0.00	0.00	0.00	0.00	0.00	0.00	0.00	0.00	0.00
Na	0.66	0.69	0.66	0.68	0.69	0.69	0.71	0.72	0.69	0.70	0.65	0.68	0.70	0.69	0.71	0.70	0.71	0.69
K	0.01	0.01	0.01	0.01	0.01	0.01	0.01	0.01	0.01	0.01	0.01	0.01	0.01	0.01	0.01	0.01	0.01	0.01
Total	5.00	5.03	5.01	5.01	5.01	5.02	5.04	5.04	5.01	5.02	4.95	4.99	5.03	5.03	5.03	5.02	5.04	5.01
X_{An}	0.33	0.33	0.34	0.32	0.31	0.32	0.32	0.31	0.31	0.31	0.31	0.30	0.31	0.32	0.31	0.31	0.31	0.32

(continued)

Crystal: BP01_P3b

	Transect data points												
SiO_2	59.16	59.46	59.81	59.18	59.89	60.71	61.04	60.93	61.36	61.40	61.03	59.77	59.96
Al_2O_3	25.33	25.31	24.83	25.47	24.67	24.70	24.64	24.30	24.26	24.31	24.39	25.09	25.07
CaO	6.51	6.44	6.46	6.85	6.43	6.54	6.44	6.37	6.41	6.37	6.40	6.50	6.56
FeO_T	bd	bd	bd	0.06	bd	0.07	bd	bd	bd	bd	bd	bd	bd
Na_2O	8.05	7.92	8.11	7.53	8.08	7.90	7.71	7.64	7.80	7.75	7.66	8.13	8.01
K_2O	0.16	0.17	0.18	0.21	0.18	0.14	0.17	0.16	0.13	0.12	0.16	0.21	0.17
Total	99.21	99.31	99.40	99.28	99.26	100.05	100.00	99.40	99.96	99.95	99.64	99.70	99.76
Cations p.f.u. for 8 oxygens													
Si	2.66	2.67	2.68	2.66	2.69	2.70	2.71	2.72	2.73	2.73	2.72	2.67	2.68
Al	1.34	1.34	1.31	1.35	1.31	1.29	1.29	1.28	1.27	1.27	1.28	1.32	1.32
Ca	0.31	0.31	0.31	0.33	0.31	0.31	0.31	0.30	0.30	0.30	0.31	0.31	0.31
Fe	0.00	0.00	0.00	0.00	0.00	0.00	0.00	0.00	0.00	0.00	0.00	0.00	0.00
Na	0.70	0.69	0.71	0.66	0.70	0.68	0.66	0.66	0.67	0.67	0.66	0.70	0.69
K	0.01	0.01	0.01	0.01	0.01	0.01	0.01	0.01	0.01	0.01	0.01	0.01	0.01
Total	5.03	5.01	5.02	5.00	5.02	5.00	4.98	4.97	4.98	4.97	4.98	5.02	5.01
X_{An}	0.31	0.31	0.31	0.33	0.31	0.31	0.32	0.32	0.31	0.31	0.32	0.31	0.31

(continued)

Crystal: BP01_P4a

	Transect data points																			
SiO_2	59.11	58.84	59.76	59.79	58.34	58.60	58.77	59.18	59.27	59.54	58.93	59.20	59.34	58.27	59.12	59.86	59.91	59.96	58.75	59.65
Al_2O_3	25.00	25.13	24.89	25.15	24.72	24.90	24.81	25.11	24.97	24.94	24.97	24.92	24.96	25.10	24.93	25.11	24.45	24.81	25.28	24.89
CaO	6.38	6.42	6.54	6.32	6.63	6.40	6.47	6.39	6.47	6.41	6.62	6.53	6.65	6.49	6.57	6.69	6.36	6.28	6.58	6.06
FeO_T	bd	bd	bd	0.06	0.06	bd	bd	bd	0.06	bd	bd	bd	bd	bd	bd	0.06	bd	bd	bd	0.07
Na_2O	7.95	7.95	8.00	8.02	8.07	7.91	8.15	7.98	7.94	7.85	7.89	7.86	7.99	7.96	7.81	7.98	7.89	7.85	7.94	7.97
K_2O	0.15	0.18	0.19	0.18	0.17	0.17	0.18	0.11	0.18	0.18	0.18	0.17	0.17	0.18	0.19	0.18	0.17	0.16	0.16	0.24
Total	98.60	98.52	99.37	99.52	97.98	97.98	98.37	98.76	98.87	98.91	98.58	98.68	99.12	98.00	98.62	99.87	98.78	99.06	98.71	98.88
Cations p.f.u. for 8 oxygens																				
Si	2.67	2.66	2.68	2.68	2.66	2.67	2.67	2.67	2.67	2.68	2.67	2.67	2.67	2.65	2.67	2.67	2.70	2.69	2.65	2.68
Al	1.33	1.34	1.32	1.33	1.33	1.34	1.33	1.33	1.33	1.32	1.33	1.33	1.32	1.35	1.33	1.32	1.30	1.31	1.35	1.32
Ca	0.31	0.31	0.31	0.30	0.32	0.31	0.31	0.31	0.31	0.31	0.32	0.32	0.32	0.32	0.32	0.32	0.31	0.30	0.32	0.29
Fe	0.00	0.00	0.00	0.00	0.00	0.00	0.00	0.00	0.00	0.00	0.00	0.00	0.00	0.00	0.00	0.00	0.00	0.00	0.00	0.00
Na	0.70	0.70	0.70	0.70	0.71	0.70	0.72	0.70	0.69	0.68	0.69	0.69	0.70	0.70	0.68	0.69	0.69	0.68	0.70	0.70
K	0.01	0.01	0.01	0.01	0.01	0.01	0.01	0.01	0.01	0.01	0.01	0.01	0.01	0.01	0.01	0.01	0.01	0.01	0.01	0.01
Total	5.02	5.02	5.02	5.01	5.04	5.02	5.03	5.02	5.02	5.01	5.02	5.01	5.02	5.03	5.01	5.02	5.00	5.00	5.02	5.01
X_{An}	0.31	0.31	0.31	0.30	0.31	0.31	0.30	0.31	0.31	0.31	0.32	0.31	0.32	0.31	0.32	0.32	0.31	0.31	0.31	0.30

(continued)

Crystal: BP01_P4b

	Transect data points								
SiO_2	58.87	59.13	59.16	58.51	58.74	59.46	59.70	58.79	59.11
Al_2O_3	24.96	24.79	25.39	25.02	24.91	24.94	25.51	25.05	25.22
CaO	6.48	6.47	6.55	6.57	6.64	6.53	6.23	6.58	6.45
FeO_T	bd	bd	0.00	bd	bd	bd	bd	bd	bd
Na_2O	7.88	7.93	7.87	7.94	7.93	8.08	7.88	7.99	7.94
K_2O	0.18	0.17	0.19	0.18	0.19	0.17	0.27	0.17	0.20
Total	98.37	98.48	99.15	98.22	98.41	99.17	99.58	98.57	98.91
Cations p.f.u. for 8 oxygens									
Si	2.67	2.68	2.66	2.66	2.66	2.67	2.67	2.66	2.66
Al	1.33	1.32	1.35	1.34	1.33	1.32	1.34	1.34	1.34
Ca	0.31	0.31	0.32	0.32	0.32	0.31	0.30	0.32	0.31
Fe	0.00	0.00	0.00	0.00	0.00	0.00	0.00	0.00	0.00
Na	0.69	0.70	0.69	0.70	0.70	0.70	0.68	0.70	0.69
K	0.01	0.01	0.01	0.01	0.01	0.01	0.02	0.01	0.01
Total	5.02	5.02	5.02	5.03	5.03	5.02	5.01	5.03	5.02
X_{An}	0.31	0.31	0.32	0.31	0.32	0.31	0.30	0.31	0.31

(continued)

Crystal: DP01_PX1a

	Transect data points														
SiO_2	60.02	59.88	60.24	60.18	60.44	60.89	62.15	62.22	60.58	60.65	60.34	60.28	61.01	60.67	60.17
Al_2O_3	26.24	26.25	26.17	26.12	25.94	26.03	25.32	25.24	25.84	26.18	26.15	26.24	26.24	26.35	26.12
CaO	7.49	7.31	6.97	7.10	7.13	7.31	6.05	6.15	7.17	7.18	7.14	7.25	7.15	7.47	7.40
FeO_T	0.10	bd	bd	bd	bd	bd	bd	bd	bd	0.06	bd	bd	bd	bd	0.08
Na_2O	7.60	7.60	7.86	7.71	7.89	7.93	8.38	8.61	7.71	7.91	7.83	7.80	7.81	7.82	7.70
K_2O	0.14	0.17	0.18	0.17	0.16	0.16	0.17	0.18	0.17	0.16	0.17	0.17	0.15	0.16	0.13
Total	101.60	101.21	101.42	101.29	101.55	102.32	102.06	102.40	101.47	102.14	101.63	101.74	102.35	102.47	101.60
Cations p.f.u. for 8 oxygens															
Si	2.64	2.64	2.65	2.65	2.66	2.66	2.71	2.70	2.66	2.65	2.65	2.64	2.66	2.64	2.64
Al	1.36	1.36	1.36	1.36	1.34	1.34	1.30	1.29	1.34	1.35	1.35	1.36	1.35	1.35	1.35
Ca	0.35	0.35	0.33	0.33	0.34	0.34	0.28	0.29	0.34	0.34	0.34	0.34	0.33	0.35	0.35
Fe	0.00	0.00	0.00	0.00	0.00	0.00	0.00	0.00	0.00	0.00	0.00	0.00	0.00	0.00	0.00
Na	0.65	0.65	0.67	0.66	0.67	0.67	0.71	0.73	0.66	0.67	0.67	0.66	0.66	0.66	0.66
K	0.01	0.01	0.01	0.01	0.01	0.01	0.01	0.01	0.01	0.01	0.01	0.01	0.01	0.01	0.01
Total	5.01	5.01	5.01	5.01	5.01	5.02	5.00	5.02	5.00	5.02	5.01	5.01	5.00	5.01	5.01
X_{An}	0.35	0.35	0.33	0.34	0.33	0.34	0.29	0.28	0.34	0.33	0.34	0.34	0.34	0.35	0.35

(continued)

Crystal: DP01_PX1b

	Transect data points															
SiO_2	59.68	58.29	59.64	59.42	59.41	59.25	61.19	59.78	59.45	59.41	58.96	61.39	59.04	59.01	59.48	59.82
Al_2O_3	26.08	26.15	26.09	26.03	26.35	25.66	25.00	26.02	26.18	25.98	26.13	24.36	26.05	26.52	26.29	26.51
CaO	7.38	7.27	7.24	7.19	7.32	6.63	5.82	7.21	7.30	7.25	7.29	4.62	7.18	7.28	7.33	7.58
FeO_T	0.18	bd	bd	bd	bd	0.06	bd	bd	bd	bd	bd	bd	bd	bd	bd	bd
Na_2O	7.71	7.77	7.72	7.61	7.65	8.19	8.55	7.93	7.73	7.74	7.77	9.23	7.96	7.68	7.56	7.60
K_2O	0.13	0.13	0.14	0.14	0.14	0.17	0.18	0.16	0.17	0.14	0.15	0.09	0.18	0.16	0.18	0.14
Total	101.15	99.60	100.81	100.38	100.88	99.95	100.73	101.10	100.82	100.52	100.30	99.68	100.40	100.65	100.84	101.64
Cations p.f.u. for 8 oxygens																
Si	2.64	2.62	2.64	2.64	2.63	2.65	2.70	2.64	2.63	2.64	2.63	2.73	2.63	2.62	2.63	2.63
Al	1.36	1.38	1.36	1.36	1.37	1.35	1.30	1.35	1.37	1.36	1.37	1.28	1.37	1.39	1.37	1.37
Ca	0.35	0.35	0.34	0.34	0.35	0.32	0.28	0.34	0.35	0.35	0.35	0.22	0.34	0.35	0.35	0.36
Fe	0.01	0.00	0.00	0.00	0.00	0.00	0.00	0.00	0.00	0.00	0.00	0.00	0.00	0.00	0.00	0.00
Na	0.66	0.68	0.66	0.66	0.66	0.71	0.73	0.68	0.66	0.67	0.67	0.80	0.69	0.66	0.65	0.65
K	0.01	0.01	0.01	0.01	0.01	0.01	0.01	0.01	0.01	0.01	0.01	0.01	0.01	0.01	0.01	0.01
Total	5.02	5.03	5.01	5.01	5.02	5.04	5.02	5.03	5.02	5.02	5.03	5.03	5.04	5.02	5.01	5.01
X_{An}	0.35	0.34	0.34	0.34	0.35	0.31	0.27	0.33	0.34	0.34	0.34	0.22	0.33	0.34	0.35	0.36

(continued)

Crystal: DP01_PX2a

	Transect data points									
SiO_2	59.83	60.90	59.76	60.53	60.68	60.85	60.44	60.51	60.36	60.68
Al_2O_3	26.91	26.13	26.38	26.33	26.39	26.45	26.29	26.33	26.17	26.08
CaO	7.79	7.29	7.44	7.33	7.25	7.50	7.26	7.38	7.23	7.29
FeO_T	bd	bd	bd	0.07	bd	bd	bd	bd	bd	bd
Na_2O	7.45	7.65	7.67	7.72	7.90	7.88	7.88	7.74	7.86	7.84
K_2O	0.16	0.21	0.17	0.19	0.18	0.18	0.20	0.21	0.20	0.17
Total	102.13	102.17	101.41	102.17	102.40	102.85	102.07	102.17	101.82	102.04
Cations p.f.u. for 8 oxygens										
Si	2.62	2.66	2.63	2.64	2.64	2.64	2.64	2.64	2.65	2.65
Al	1.39	1.34	1.37	1.36	1.36	1.35	1.36	1.36	1.35	1.34
Ca	0.37	0.34	0.35	0.34	0.34	0.35	0.34	0.35	0.34	0.34
Fe	0.00	0.00	0.00	0.00	0.00	0.00	0.00	0.00	0.00	0.00
Na	0.63	0.65	0.65	0.65	0.67	0.66	0.67	0.66	0.67	0.66
K	0.01	0.01	0.01	0.01	0.01	0.01	0.01	0.01	0.01	0.01
Total	5.01	5.00	5.02	5.01	5.02	5.02	5.02	5.01	5.02	5.01
X_{An}	0.37	0.34	0.35	0.34	0.34	0.34	0.34	0.35	0.34	0.34

(continued)

Crystal: DP01_PX2b

	Transect data points								
SiO_2	59.98	60.76	69.98	60.18	60.20	60.06	59.69	59.21	58.14
Al_2O_3	26.52	26.25	20.98	25.86	26.22	26.20	26.38	26.04	27.27
CaO	7.49	7.13	0.15	7.09	7.34	7.28	7.27	7.14	7.34
FeO_T	bd	0.07	bd	bd	bd	0.06	bd	bd	0.07
Na_2O	7.69	8.03	11.30	7.80	7.69	7.78	7.86	7.83	6.98
K_2O	0.16	0.21	0.20	0.17	0.21	0.18	0.14	0.19	0.62
Total	101.83	102.44	102.62	101.10	101.66	101.56	101.34	100.42	100.42
Cations p.f.u. for 8 oxygens									
Si	2.63	2.65	2.97	2.65	2.64	2.64	2.63	2.63	2.59
Al	1.37	1.35	1.05	1.34	1.36	1.36	1.37	1.37	1.43
Ca	0.35	0.33	0.01	0.34	0.35	0.34	0.34	0.34	0.35
Fe	0.00	0.00	0.00	0.00	0.00	0.00	0.00	0.00	0.00
Na	0.65	0.68	0.93	0.67	0.65	0.66	0.67	0.68	0.60
K	0.01	0.01	0.01	0.01	0.01	0.01	0.01	0.01	0.04
Total	5.02	5.02	4.97	5.01	5.01	5.02	5.02	5.03	5.01
X_{An}	0.35	0.33	0.01	0.33	0.35	0.34	0.34	0.34	0.37

Table 4.20 Compositional transects (EMPA) of plagioclase from samples JM09/SM09, JM09/BP01 and JM09/DP01; bd denotes below detection limits.

Crystal: SM09_OPX3a							Crystal: SM09_OPX3b				
	Transect data points						Transect data points				
SiO_2	51.44	50.41	51.33	51.35	51.45	51.53	51.65	51.88	51.59	51.62	51.98
TiO_2	0.04	0.06	bd	bd	bd	bd	bd	bd	bd	0.14	bd
Al_2O_3	1.82	2.58	1.99	2.06	2.04	1.84	1.86	1.96	2.01	2.03	2.07
Cr_2O_3	0.04	bd	bd	bd	bd	0.04	0.04	bd	bd	bd	bd
MgO	21.32	21.21	21.20	21.04	21.03	20.90	21.10	21.00	20.99	21.05	21.29
CaO	0.35	0.42	0.50	0.60	0.40	0.36	0.44	0.49	0.46	0.55	0.53
MnO	0.61	0.63	0.67	0.69	0.72	0.68	0.64	0.65	0.69	0.69	0.71
FeO_T	24.37	24.61	24.70	24.87	24.96	24.84	24.88	25.09	24.94	24.76	24.67
Na_2O	bd	0.05	0.10	bd	bd	bd	bd	bd	0.07	bd	bd
Total	99.99	99.97	100.49	100.60	100.61	100.19	100.60	101.06	100.75	100.83	101.24
Cations p.f.u. for 6 oxygens											
Si	1.94	1.91	1.93	1.93	1.93	1.94	1.94	1.94	1.93	1.93	1.94
Ti	0.00	0.00	0.00	0.00	0.00	0.00	0.00	0.00	0.00	0.00	0.00
Al	0.08	0.12	0.09	0.09	0.09	0.08	0.08	0.09	0.09	0.09	0.09
Cr	0.00	0.00	0.00	0.00	0.00	0.00	0.00	0.00	0.00	0.00	0.00
Mg	1.20	1.20	1.19	1.18	1.18	1.17	1.18	1.17	1.17	1.17	1.18
Ca	0.01	0.02	0.02	0.02	0.02	0.01	0.02	0.02	0.02	0.02	0.02
Mn	0.02	0.02	0.02	0.02	0.02	0.02	0.02	0.02	0.02	0.02	0.02
Fe	0.77	0.78	0.78	0.78	0.78	0.78	0.78	0.78	0.78	0.78	0.77
Na	0.00	0.00	0.01	0.00	0.00	0.00	0.00	0.00	0.00	0.00	0.00
Total	4.02	4.04	4.03	4.03	4.02	4.02	4.02	4.02	4.02	4.02	4.02
X_{Mg}	0.61	0.61	0.60	0.60	0.60	0.60	0.60	0.60	0.60	0.60	0.61

Table 4.21 Compositional transects (EMPA) of orthopyroxene from sample JM09/SM09; bd denotes below detection limits.

Crystal: SM09_cpx_trans2a

	Transect data points											
SiO_2	51.54	51.29	52.29	52.55	50.78	50.82	50.33	50.31	48.61	50.29	50.17	50.36
TiO_2	0.25	0.31	0.08	0.10	0.43	0.41	0.42	0.41	2.82	0.47	0.41	0.38
Al_2O_3	3.05	2.95	1.61	1.76	3.50	3.48	3.68	3.67	3.10	3.70	3.74	3.69
Cr_2O_3	0.04	0.04	0.04	0.04	0.05	bd	0.06	0.05	0.05	0.04	0.06	0.05
MgO	13.93	13.22	14.28	14.32	12.68	12.41	12.37	12.14	12.38	12.26	12.12	12.35
CaO	22.07	22.79	22.90	23.09	22.43	21.09	21.78	22.11	18.51	21.51	21.89	21.01
MnO	0.29	0.30	0.27	0.27	0.31	0.38	0.33	0.29	0.38	0.35	0.32	0.35
FeO_T	8.37	8.41	7.70	7.36	9.16	10.41	9.92	9.51	13.94	10.21	9.88	10.46
Na_2O	0.62	0.69	0.51	0.50	0.83	0.78	0.77	0.79	0.74	0.79	0.79	0.75
Total	100.16	100.01	99.67	99.99	100.18	99.78	99.64	99.25	100.51	99.62	99.38	99.40
Cations p.f.u. for 6 oxygens												
Si	1.92	1.92	1.95	1.95	1.90	1.91	1.90	1.90	1.85	1.90	1.90	1.91
Ti	0.01	0.01	0.00	0.00	0.01	0.01	0.01	0.01	0.08	0.01	0.01	0.01
Al	0.13	0.13	0.07	0.08	0.15	0.15	0.16	0.16	0.14	0.16	0.17	0.16
Cr	0.00	0.00	0.00	0.00	0.00	0.00	0.00	0.00	0.00	0.00	0.00	0.00
Mg	0.77	0.74	0.80	0.79	0.71	0.70	0.70	0.68	0.70	0.69	0.68	0.70
Ca	0.88	0.91	0.92	0.92	0.90	0.85	0.88	0.90	0.75	0.87	0.89	0.85
Mn	0.01	0.01	0.01	0.01	0.01	0.01	0.01	0.01	0.01	0.01	0.01	0.01
Fe	0.26	0.26	0.24	0.23	0.29	0.33	0.31	0.30	0.44	0.32	0.31	0.33
Na	0.04	0.05	0.04	0.04	0.06	0.06	0.06	0.06	0.05	0.06	0.06	0.06
Total	4.03	4.03	4.03	4.02	4.04	4.03	4.03	4.03	4.03	4.03	4.03	4.03
X_{Mg}	0.75	0.74	0.77	0.78	0.71	0.68	0.69	0.69	0.61	0.68	0.69	0.68

(continued)

Crystal: SM09_cpx_trans2a (continued)

	Transect data points												
SiO_2	50.82	50.06	50.39	50.30	50.29	50.33	50.43	49.92	50.15	50.75	50.37	51.40	51.13
TiO_2	0.46	0.42	0.42	0.48	0.44	0.47	0.43	0.42	0.43	0.41	0.39	0.35	0.34
Al_2O_3	3.77	3.66	3.70	3.70	3.73	3.67	3.69	3.59	3.51	3.52	3.26	3.35	3.23
Cr_2O_3	0.05	0.05	0.05	0.06	0.04	0.05	0.05	bd	0.06	0.04	0.04	0.05	bd
MgO	12.52	12.27	12.28	12.35	12.28	12.35	12.11	12.28	12.18	12.41	12.45	12.63	12.62
CaO	21.43	21.21	21.50	21.58	21.93	21.39	21.77	21.14	21.87	21.30	20.83	21.68	22.16
MnO	0.32	0.33	0.35	0.34	0.32	0.35	0.33	0.33	0.32	0.33	0.32	0.32	0.31
FeO_T	10.35	10.27	9.85	10.26	9.70	10.53	9.66	10.17	9.77	10.52	10.52	10.26	9.27
Na_2O	0.81	0.76	0.86	0.77	0.79	0.81	0.84	0.86	0.78	0.85	0.71	0.73	0.78
Total	100.52	99.02	99.40	99.85	99.50	99.95	99.30	98.70	99.06	100.13	98.89	100.76	99.82
Cations p.f.u. for 6 oxygens													
Si	1.90	1.90	1.90	1.90	1.90	1.90	1.91	1.90	1.90	1.91	1.92	1.92	1.92
Ti	0.01	0.01	0.01	0.01	0.01	0.01	0.01	0.01	0.01	0.01	0.01	0.01	0.01
Al	0.17	0.16	0.16	0.16	0.17	0.16	0.16	0.16	0.16	0.16	0.15	0.15	0.14
Cr	0.00	0.00	0.00	0.00	0.00	0.00	0.00	0.00	0.00	0.00	0.00	0.00	0.00
Mg	0.70	0.70	0.69	0.69	0.69	0.69	0.68	0.70	0.69	0.70	0.71	0.70	0.71
Ca	0.86	0.86	0.87	0.87	0.89	0.86	0.88	0.86	0.89	0.86	0.85	0.87	0.89
Mn	0.01	0.01	0.01	0.01	0.01	0.01	0.01	0.01	0.01	0.01	0.01	0.01	0.01
Fe	0.32	0.33	0.31	0.32	0.31	0.33	0.31	0.32	0.31	0.33	0.33	0.32	0.29
Na	0.06	0.06	0.06	0.06	0.06	0.06	0.06	0.06	0.06	0.06	0.05	0.05	0.06
Total	4.03	4.03	4.03	4.03	4.03	4.04	4.03	4.04	4.03	4.03	4.03	4.03	4.03
X_{Mg}	0.68	0.68	0.69	0.68	0.69	0.68	0.69	0.68	0.69	0.68	0.68	0.69	0.71

(continued)

Crystal: SM09_cpx_trans2b

	Transect data points											
SiO_2	51.04	50.85	50.87	51.22	50.91	50.52	50.51	50.60	50.65	50.28	50.67	50.23
TiO_2	0.27	0.32	0.38	0.37	0.39	0.42	0.44	0.44	0.25	0.45	0.39	0.44
Al_2O_3	2.89	3.26	3.63	3.75	3.42	3.64	3.69	3.63	3.09	3.73	3.55	3.45
Cr_2O_3	bd	0.05	0.06	0.04	0.04	bd	0.05	0.05	bd	0.04	0.04	bd
MgO	12.75	12.78	12.55	11.58	13.07	12.30	12.37	12.26	15.69	12.27	12.33	12.94
CaO	21.43	20.89	21.57	20.19	19.85	21.58	21.61	21.69	10.88	21.83	22.10	18.51
MnO	0.32	0.36	0.31	0.38	0.41	0.33	0.32	0.31	0.63	0.33	0.34	0.42
FeO_T	9.78	10.37	10.08	11.47	11.54	9.95	9.86	9.96	18.67	9.76	9.51	12.87
Na_2O	0.80	0.75	0.83	0.63	0.70	0.85	0.84	0.77	0.40	0.82	0.81	0.68
Total	99.27	99.63	100.27	99.63	100.33	99.60	99.68	99.71	100.25	99.51	99.75	99.53
Cations p.f.u. for 6 oxygens												
Si	1.93	1.92	1.91	1.93	1.91	1.91	1.90	1.91	1.91	1.90	1.91	1.91
Ti	0.01	0.01	0.01	0.01	0.01	0.01	0.01	0.01	0.01	0.01	0.01	0.01
Al	0.13	0.14	0.16	0.17	0.15	0.16	0.16	0.16	0.14	0.17	0.16	0.15
Cr	0.00	0.00	0.00	0.00	0.00	0.00	0.00	0.00	0.00	0.00	0.00	0.00
Mg	0.72	0.72	0.70	0.65	0.73	0.69	0.69	0.69	0.88	0.69	0.69	0.73
Ca	0.87	0.84	0.87	0.82	0.80	0.87	0.87	0.88	0.44	0.88	0.89	0.75
Mn	0.01	0.01	0.01	0.01	0.01	0.01	0.01	0.01	0.02	0.01	0.01	0.01
Fe	0.31	0.33	0.32	0.36	0.36	0.31	0.31	0.31	0.59	0.31	0.30	0.41
Na	0.06	0.06	0.06	0.05	0.05	0.06	0.06	0.06	0.03	0.06	0.06	0.05
Total	4.03	4.03	4.03	4.00	4.03	4.03	4.03	4.03	4.02	4.03	4.03	4.03
X_{Mg}	0.70	0.69	0.69	0.64	0.67	0.69	0.69	0.69	0.60	0.69	0.70	0.64

(continued)

Crystal: SM09_cpx_trans2b (continued)

	Transect data points										
SiO_2	50.60	49.51	50.51	50.90	50.77	50.41	50.68	50.13	50.59	50.65	51.33
TiO_2	0.42	0.42	0.47	0.46	0.46	0.46	0.44	0.44	0.40	0.40	0.31
Al_2O_3	3.72	4.21	3.78	3.72	3.67	3.62	3.58	3.56	3.48	3.41	3.09
Cr_2O_3	0.05	0.05	0.05	0.04	bd	bd	0.05	bd	bd	bd	bd
MgO	12.38	12.47	12.25	12.26	12.14	12.34	12.39	12.59	12.34	12.50	12.72
CaO	21.85	20.82	21.76	22.06	22.16	21.33	21.62	20.52	22.11	22.03	21.76
MnO	0.32	0.35	0.35	0.31	0.33	0.31	0.32	0.30	0.34	0.34	0.31
FeO_T	9.71	10.76	10.12	10.04	9.73	10.24	10.12	10.72	9.92	9.80	9.68
Na_2O	0.83	0.81	0.79	0.78	0.80	0.83	0.84	0.76	0.85	0.76	0.77
Total	99.88	99.40	100.06	100.58	100.05	99.54	100.04	98.99	100.03	99.87	99.97
Cations p.f.u. for 6 oxygens											
Si	1.90	1.88	1.90	1.90	1.91	1.90	1.91	1.90	1.90	1.91	1.93
Ti	0.01	0.01	0.01	0.01	0.01	0.01	0.01	0.01	0.01	0.01	0.01
Al	0.16	0.19	0.17	0.16	0.16	0.16	0.16	0.16	0.15	0.15	0.14
Cr	0.00	0.00	0.00	0.00	0.00	0.00	0.00	0.00	0.00	0.00	0.00
Mg	0.69	0.71	0.69	0.68	0.68	0.70	0.69	0.71	0.69	0.70	0.71
Ca	0.88	0.85	0.88	0.88	0.89	0.86	0.87	0.84	0.89	0.89	0.87
Mn	0.01	0.01	0.01	0.01	0.01	0.01	0.01	0.01	0.01	0.01	0.01
Fe	0.31	0.34	0.32	0.31	0.31	0.32	0.32	0.34	0.31	0.31	0.30
Na	0.06	0.06	0.06	0.06	0.06	0.06	0.06	0.06	0.06	0.06	0.06
Total	4.03	4.04	4.03	4.03	4.03	4.03	4.03	4.03	4.04	4.03	4.03
X_{Mg}	0.69	0.67	0.68	0.69	0.69	0.68	0.69	0.68	0.69	0.69	0.70

(continued)

Crystal: SM09CPX3a

	Transect data points							
SiO_2	51.94	51.20	51.71	49.96	51.40	51.42	51.00	51.32
TiO_2	0.25	0.29	0.30	0.38	0.32	0.29	0.31	0.25
Al_2O_3	2.79	2.85	2.95	3.02	2.85	2.98	2.93	2.82
Cr_2O_3	bd	bd	bd	bd	bd	bd	bd	bd
MgO	13.02	12.58	12.59	12.71	12.73	12.67	12.52	13.01
CaO	21.31	22.50	21.95	21.32	21.58	21.93	21.71	20.72
MnO	0.34	0.34	0.36	0.32	0.36	0.31	0.30	0.36
FeO_T	10.95	10.01	10.42	9.50	11.38	10.63	10.13	11.13
Na_2O	0.71	0.77	0.83	0.80	0.72	0.79	0.76	0.71
Total	101.31	100.53	101.12	98.01	101.32	101.02	99.67	100.33
Cations p.f.u. for 6 oxygens								
Si	1.93	1.92	1.92	1.91	1.92	1.92	1.92	1.93
Ti	0.01	0.01	0.01	0.01	0.01	0.01	0.01	0.01
Al	0.12	0.13	0.13	0.14	0.13	0.13	0.13	0.12
Cr	0.00	0.00	0.00	0.00	0.00	0.00	0.00	0.00
Mg	0.72	0.70	0.70	0.73	0.71	0.70	0.70	0.73
Ca	0.85	0.90	0.88	0.88	0.86	0.88	0.88	0.83
Mn	0.01	0.01	0.01	0.01	0.01	0.01	0.01	0.01
Fe	0.34	0.31	0.32	0.30	0.35	0.33	0.32	0.35
Na	0.05	0.06	0.06	0.06	0.05	0.06	0.06	0.05
Total	4.03	4.04	4.03	4.04	4.04	4.04	4.03	4.03
X_{Mg}	0.68	0.69	0.68	0.70	0.67	0.68	0.69	0.68

(continued)

Crystal: SM09CPX3b

	Transect data points						
SiO_2	51.36	51.32	51.28	51.59	51.19	51.46	51.27
TiO_2	0.28	0.26	0.31	0.34	0.34	0.30	0.33
Al_2O_3	2.79	2.87	2.94	2.85	2.91	2.88	2.83
Cr_2O_3	bd	bd	bd	bd	bd	bd	bd
MgO	12.60	12.59	12.73	12.69	12.85	12.77	12.97
CaO	22.11	22.23	21.35	22.03	20.75	21.70	22.11
MnO	0.34	0.31	0.34	0.37	0.35	0.38	0.33
FeO_T	10.24	10.24	10.94	10.12	11.16	10.80	10.61
Na_2O	0.72	0.75	0.83	0.70	0.68	0.75	0.75
Total	100.42	100.55	100.70	100.69	100.24	101.03	101.20
Cations p.f.u. for 6 oxygens							
Si	1.93	1.92	1.92	1.93	1.92	1.92	1.91
Ti	0.01	0.01	0.01	0.01	0.01	0.01	0.01
Al	0.12	0.13	0.13	0.13	0.13	0.13	0.12
Cr	0.00	0.00	0.00	0.00	0.00	0.00	0.00
Mg	0.70	0.70	0.71	0.71	0.72	0.71	0.72
Ca	0.89	0.89	0.86	0.88	0.84	0.87	0.88
Mn	0.01	0.01	0.01	0.01	0.01	0.01	0.01
Fe	0.32	0.32	0.34	0.32	0.35	0.34	0.33
Na	0.05	0.05	0.06	0.05	0.05	0.05	0.05
Total	4.03	4.03	4.04	4.03	4.03	4.04	4.04
X_{Mg}	0.69	0.69	0.67	0.69	0.67	0.68	0.69

Table 4.22 Compositional transects (EMPA) of clinopyroxene from sample JM09/SM09; bd denotes below detection limits.

Crystal: BP01_H1a1											Crystal: BP01_H2a1	
	Transect data points										Transect data points	
SiO_2	39.84	40.32	41.05	40.44	39.72	39.11	40.19	39.43	41.76	40.05	39.36	40.10
TiO_2	0.49	0.51	0.51	0.55	0.51	0.44	0.54	0.57	0.49	0.56	0.51	0.52
Al_2O_3	12.26	12.30	12.18	13.18	12.86	12.95	12.98	13.01	10.99	13.19	13.11	12.65
Cr_2O_3	0.00	0.00	0.00	0.00	0.00	0.00	0.00	0.00	0.00	0.00	0.00	0.00
MgO	9.51	9.88	9.52	9.55	9.50	9.37	9.50	9.69	9.71	9.47	9.60	9.73
CaO	11.65	11.41	11.34	11.54	11.59	11.54	11.54	11.69	11.28	11.62	11.48	11.38
MnO	0.31	0.33	0.29	0.32	0.30	0.33	0.26	0.29	0.31	0.30	0.35	0.33
FeO_T	17.97	18.04	18.16	17.60	18.30	18.02	18.02	17.72	18.45	18.11	17.96	17.74
Na_2O	1.55	1.59	1.47	1.56	1.52	1.57	1.57	1.42	1.59	1.44	1.58	1.45
K_2O	1.14	1.06	1.18	1.25	1.31	1.26	1.23	1.29	1.09	1.28	1.26	1.19
Total	94.71	95.44	95.71	95.98	95.61	94.58	95.83	95.11	95.66	96.03	95.21	95.08
Cations p.f.u. for 23 oxygens												
Si	6.26	6.28	6.36	6.25	6.20	6.17	6.24	6.17	6.48	6.21	6.16	6.26
Ti	0.06	0.06	0.06	0.06	0.06	0.05	0.06	0.07	0.06	0.07	0.06	0.06
Al	2.27	2.26	2.23	2.40	2.36	2.41	2.37	2.40	2.01	2.41	2.42	2.33
Cr	0.00	0.00	0.00	0.00	0.00	0.00	0.00	0.00	0.00	0.00	0.00	0.00
Mg	2.23	2.29	2.20	2.20	2.21	2.20	2.20	2.26	2.25	2.19	2.24	2.26
Ca	1.96	1.90	1.88	1.91	1.94	1.95	1.92	1.96	1.88	1.93	1.93	1.90
Mn	0.04	0.04	0.04	0.04	0.04	0.04	0.03	0.04	0.04	0.04	0.05	0.04
Fe	2.36	2.35	2.35	2.27	2.39	2.38	2.34	2.32	2.39	2.35	2.35	2.32
Na	0.47	0.48	0.44	0.47	0.46	0.48	0.47	0.43	0.48	0.43	0.48	0.44
K	0.23	0.21	0.23	0.25	0.26	0.25	0.24	0.26	0.22	0.25	0.25	0.24
Total	15.89	15.88	15.80	15.85	15.92	15.94	15.87	15.91	15.80	15.87	15.93	15.85
X_{Mg}	0.49	0.49	0.48	0.49	0.48	0.48	0.48	0.49	0.48	0.48	0.49	0.49

(continued)

	Crystal: BP01_H3a									Crystal: BP01_H3b					
	Transect data points									Transect data points					
SiO_2	39.89	40.48	39.38	39.67	40.87	39.39	40.02	39.78	40.13	40.63	41.62	39.63	40.38	42.96	40.83
TiO_2	0.57	0.53	0.56	0.50	0.52	0.63	0.59	0.65	0.69	0.53	0.37	0.58	0.52	0.44	0.54
Al_2O_3	12.54	11.71	11.82	12.33	11.52	12.36	12.73	12.92	12.93	12.27	8.91	12.71	11.93	9.96	12.68
Cr_2O_3	0.00	0.00	0.00	0.00	0.00	0.00	0.00	0.00	0.00	0.00	0.00	0.00	0.00	0.00	0.00
MgO	9.57	9.57	9.65	9.43	9.82	9.66	9.35	9.32	9.47	9.82	11.61	9.43	9.75	10.03	9.72
CaO	11.33	11.25	11.40	11.37	11.19	11.33	11.46	11.56	11.49	11.33	10.91	11.41	11.28	11.06	11.55
MnO	0.36	0.29	0.30	0.31	0.32	0.29	0.28	0.35	0.34	0.36	0.27	0.30	0.29	0.30	0.33
FeO_T	18.20	18.37	18.16	18.02	18.22	18.27	17.84	17.84	17.77	17.56	17.94	18.12	18.24	18.26	17.60
Na_2O	1.66	1.60	1.72	1.53	1.37	1.65	1.60	1.65	1.62	1.72	1.39	1.70	1.63	1.58	1.72
K_2O	1.13	1.06	1.06	1.14	1.11	1.20	1.22	1.22	1.16	1.05	0.96	1.13	1.07	0.84	1.06
Total	95.25	94.86	94.06	94.30	94.93	94.77	95.09	95.29	95.59	95.27	93.98	95.02	95.09	95.43	96.05
Cations p.f.u. for 23 oxygens															
Si	6.24	6.35	6.25	6.26	6.39	6.21	6.26	6.21	6.24	6.32	6.57	6.21	6.32	6.65	6.30
Ti	0.07	0.06	0.07	0.06	0.06	0.07	0.07	0.08	0.08	0.06	0.04	0.07	0.06	0.05	0.06
Al	2.31	2.17	2.21	2.29	2.12	2.30	2.35	2.38	2.37	2.25	1.66	2.35	2.20	1.82	2.30
Cr	0.00	0.00	0.00	0.00	0.00	0.00	0.00	0.00	0.00	0.00	0.00	0.00	0.00	0.00	0.00
Mg	2.23	2.24	2.28	2.22	2.29	2.27	2.18	2.17	2.19	2.28	2.73	2.20	2.27	2.31	2.24
Ca	1.90	1.89	1.94	1.92	1.88	1.91	1.92	1.94	1.91	1.89	1.85	1.92	1.89	1.83	1.91
Mn	0.05	0.04	0.04	0.04	0.04	0.04	0.04	0.05	0.05	0.05	0.04	0.04	0.04	0.04	0.04
Fe	2.38	2.41	2.41	2.38	2.38	2.41	2.33	2.33	2.31	2.28	2.37	2.38	2.39	2.36	2.27
Na	0.50	0.49	0.53	0.47	0.41	0.50	0.49	0.50	0.49	0.52	0.42	0.52	0.49	0.48	0.52
K	0.22	0.21	0.22	0.23	0.22	0.24	0.24	0.24	0.23	0.21	0.19	0.23	0.21	0.17	0.21
Total	15.90	15.85	15.95	15.88	15.80	15.95	15.87	15.89	15.86	15.86	15.87	15.91	15.88	15.71	15.85
X_{Mg}	0.48	0.48	0.49	0.48	0.49	0.49	0.48	0.48	0.49	0.50	0.54	0.48	0.49	0.49	0.50

(continued)

Crystal: DP01_H1_a1							Crystal: DP01_H2a				
	Transect data points						Transect data points				
SiO_2	45.88	44.59	45.12	52.41	46.20	47.42	54.33	54.12	54.12	52.00	51.03
TiO_2	0.46	0.41	0.27	0.00	0.00	0.00	0.27	0.35	0.26	0.34	0.17
Al_2O_3	10.76	11.94	11.70	8.57	9.01	9.23	5.30	4.75	4.38	5.70	5.62
Cr_2O_3	0.00	0.00	0.00	0.00	0.00	0.00	0.06	0.04	0.05	0.05	0.00
MgO	14.51	13.91	13.70	14.23	16.07	15.69	15.38	17.79	18.14	17.20	18.43
CaO	11.80	11.79	11.62	10.94	10.44	11.73	11.69	12.25	12.02	12.20	10.50
MnO	0.33	0.29	0.30	0.34	0.30	0.34	0.28	0.30	0.30	0.25	0.27
FeO_T	12.64	12.86	12.57	11.53	12.03	10.90	9.89	9.43	9.45	10.88	10.36
Na_2O	1.13	1.37	1.24	0.95	0.88	0.93	0.57	0.48	0.41	0.62	0.44
K_2O	0.56	0.53	0.55	0.27	0.26	0.36	0.20	0.14	0.13	0.19	0.15
Total	98.07	97.68	97.07	99.22	95.19	96.59	97.97	99.65	99.25	99.43	96.97
Cations p.f.u. for 23 oxygens											
Si	6.68	6.54	6.63	7.35	6.86	6.92	7.66	7.52	7.54	7.32	7.32
Ti	0.05	0.04	0.03	0.00	0.00	0.00	0.03	0.04	0.03	0.04	0.02
Al	1.84	2.06	2.03	1.42	1.58	1.59	0.88	0.78	0.72	0.95	0.95
Cr	0.00	0.00	0.00	0.00	0.00	0.00	0.01	0.00	0.01	0.01	0.00
Mg	3.15	3.04	3.00	2.98	3.56	3.41	3.23	3.68	3.77	3.61	3.94
Ca	1.84	1.85	1.83	1.64	1.66	1.83	1.77	1.82	1.79	1.84	1.61
Mn	0.04	0.04	0.04	0.04	0.04	0.04	0.03	0.04	0.04	0.03	0.03
Fe	1.54	1.58	1.54	1.35	1.49	1.33	1.17	1.10	1.10	1.28	1.24
Na	0.32	0.39	0.35	0.26	0.25	0.26	0.16	0.13	0.11	0.17	0.12
K	0.10	0.10	0.10	0.05	0.05	0.07	0.04	0.02	0.02	0.03	0.03
Total	15.56	15.63	15.55	15.09	15.50	15.45	14.96	15.13	15.13	15.27	15.26
X_{Mg}	0.67	0.66	0.66	0.69	0.70	0.72	0.73	0.77	0.77	0.74	0.76

(continued)

Crystal: DP01_H2b										Crystal: DP02_H1a								
	Transect data points									Transect data points								
SiO_2	51.64	58.69	53.08	52.34	53.21	52.87	52.75	50.50	56.49	42.60	42.35	42.15	46.89	43.21	43.22	43.65	42.64	43.80
TiO_2	0.16	0.21	0.29	0.26	0.21	0.25	0.23	0.24	0.23	0.37	0.53	0.45	0.45	0.45	0.46	0.50	0.54	0.63
Al_2O_3	5.88	4.65	4.98	5.14	4.75	5.22	4.77	6.80	6.53	10.33	13.91	14.05	12.16	14.07	14.01	13.50	13.63	13.90
Cr_2O_3	0.00	0.05	0.06	0.05	0.05	0.04	0.05	0.04	0.06	0.00	0.00	0.00	0.00	0.00	0.00	0.00	0.00	0.00
MgO	17.12	15.48	18.02	17.81	18.22	17.42	17.69	16.45	14.04	12.43	10.54	10.38	10.26	10.75	10.55	11.21	10.60	10.73
CaO	11.95	10.91	12.04	12.03	12.02	11.89	11.95	10.26	10.71	8.47	11.51	11.37	10.38	11.93	11.60	11.83	11.62	11.66
MnO	0.24	0.26	0.25	0.28	0.27	0.32	0.25	0.30	0.29	0.46	0.27	0.25	0.26	0.29	0.24	0.24	0.23	0.27
FeO_T	10.49	8.88	9.82	9.94	9.69	9.85	10.10	12.20	10.11	18.95	16.62	16.52	15.84	15.72	15.68	15.51	16.34	15.11
Na_2O	0.63	0.47	0.51	0.53	0.45	0.49	0.67	0.53	0.68	1.15	1.61	1.56	1.87	1.24	1.13	1.40	1.54	1.35
K_2O	0.21	0.16	0.15	0.16	0.13	0.17	0.14	0.20	0.27	0.32	0.47	0.46	0.45	0.48	0.49	0.48	0.46	0.51
Total	98.33	99.75	99.17	98.53	99.00	98.51	98.60	97.51	99.41	95.07	97.81	97.18	98.55	98.14	97.38	98.31	97.60	97.96
Cations p.f.u. for 23 oxygens																		
Si	7.33	7.99	7.43	7.39	7.46	7.45	7.45	7.26	7.79	6.57	6.32	6.32	6.83	6.38	6.42	6.43	6.37	6.45
Ti	0.02	0.02	0.03	0.03	0.02	0.03	0.02	0.03	0.02	0.04	0.06	0.05	0.05	0.05	0.05	0.06	0.06	0.07
Al	0.98	0.75	0.82	0.85	0.79	0.87	0.79	1.15	1.06	1.88	2.45	2.48	2.09	2.45	2.45	2.34	2.40	2.41
Cr	0.00	0.00	0.01	0.01	0.00	0.00	0.01	0.00	0.01	0.00	0.00	0.00	0.00	0.00	0.00	0.00	0.00	0.00
Mg	3.62	3.14	3.76	3.75	3.81	3.66	3.72	3.52	2.88	2.86	2.35	2.32	2.23	2.37	2.34	2.46	2.36	2.36
Ca	1.82	1.59	1.81	1.82	1.80	1.80	1.81	1.58	1.58	1.40	1.84	1.83	1.62	1.89	1.85	1.87	1.86	1.84
Mn	0.03	0.03	0.03	0.03	0.03	0.04	0.03	0.04	0.03	0.06	0.03	0.03	0.03	0.04	0.03	0.03	0.03	0.03
Fe	1.25	1.01	1.15	1.17	1.14	1.16	1.19	1.47	1.17	2.44	2.07	2.07	1.93	1.94	1.95	1.91	2.04	1.86
Na	0.17	0.12	0.14	0.15	0.12	0.13	0.18	0.15	0.18	0.34	0.46	0.45	0.53	0.35	0.33	0.40	0.44	0.38
K	0.04	0.03	0.03	0.03	0.02	0.03	0.03	0.04	0.05	0.06	0.09	0.09	0.08	0.09	0.09	0.09	0.09	0.10
Total	15.26	14.69	15.20	15.24	15.20	15.17	15.23	15.23	14.77	15.65	15.67	15.65	15.38	15.56	15.51	15.59	15.64	15.51
X_{Mg}	0.74	0.76	0.77	0.76	0.77	0.76	0.76	0.71	0.71	0.54	0.53	0.53	0.54	0.55	0.55	0.56	0.54	0.56

(continued)

Crystal: DP02_H1b						Crystal: DP02_H2a		Crystal: DP02_H2b				
	Transect data points					Transect data points		Transect data points				
SiO_2	42.78	42.46	42.92	44.99	42.59	44.09	49.19	42.85	43.10	44.21	51.34	43.48
TiO_2	0.59	0.49	0.50	0.51	0.65	0.55	0.18	0.58	0.51	0.57	0.13	0.52
Al_2O_3	13.08	13.81	14.13	13.70	13.43	12.52	5.86	13.02	13.61	13.27	2.62	12.90
Cr_2O_3	0.04	0.00	0.00	0.00	0.00	0.06	0.05	0.05	0.06	0.07	0.06	0.08
MgO	10.99	10.63	10.52	10.41	10.64	11.44	11.69	11.31	11.34	10.78	11.36	11.12
CaO	11.68	11.40	11.41	11.07	11.37	11.24	11.38	11.30	11.61	11.41	11.96	11.46
MnO	0.24	0.23	0.27	0.21	0.26	0.24	0.79	0.24	0.26	0.24	1.21	0.26
FeO_T	16.25	16.35	16.56	16.67	16.35	14.71	17.21	15.99	14.48	16.03	18.52	15.56
Na_2O	1.40	1.38	1.45	1.53	1.51	1.20	1.03	1.41	1.31	1.20	0.53	1.25
K_2O	0.53	0.44	0.47	0.46	0.56	0.46	0.16	0.50	0.46	0.50	0.08	0.51
Total	97.57	97.18	98.22	99.55	97.35	96.51	97.53	97.23	96.74	98.27	97.80	97.13
Cations p.f.u. for 23 oxygens												
Si	6.39	6.36	6.36	6.54	6.37	6.57	7.31	6.41	6.42	6.51	7.65	6.48
Ti	0.07	0.06	0.06	0.06	0.07	0.06	0.02	0.06	0.06	0.06	0.01	0.06
Al	2.30	2.44	2.47	2.35	2.37	2.20	1.03	2.29	2.39	2.30	0.46	2.27
Cr	0.00	0.00	0.00	0.00	0.00	0.01	0.01	0.01	0.01	0.01	0.01	0.01
Mg	2.45	2.37	2.32	2.26	2.37	2.54	2.59	2.52	2.52	2.37	2.52	2.47
Ca	1.87	1.83	1.81	1.72	1.82	1.79	1.81	1.81	1.85	1.80	1.91	1.83
Mn	0.03	0.03	0.03	0.03	0.03	0.03	0.10	0.03	0.03	0.03	0.15	0.03
Fe	2.03	2.05	2.05	2.03	2.05	1.83	2.14	2.00	1.80	1.97	2.31	1.94
Na	0.41	0.40	0.42	0.43	0.44	0.35	0.30	0.41	0.38	0.34	0.15	0.36
K	0.10	0.08	0.09	0.09	0.11	0.09	0.03	0.10	0.09	0.09	0.02	0.10
Total	15.64	15.61	15.61	15.49	15.64	15.48	15.32	15.63	15.55	15.49	15.19	15.55
X_{Mg}	0.55	0.54	0.53	0.53	0.54	0.58	0.55	0.56	0.58	0.55	0.52	0.56

Table 4.23 Compositional transects (EMPA) of hornblende from samples JM09/BP01, JM09/DP01 and JM09/DP02; bd denotes below detection limits.

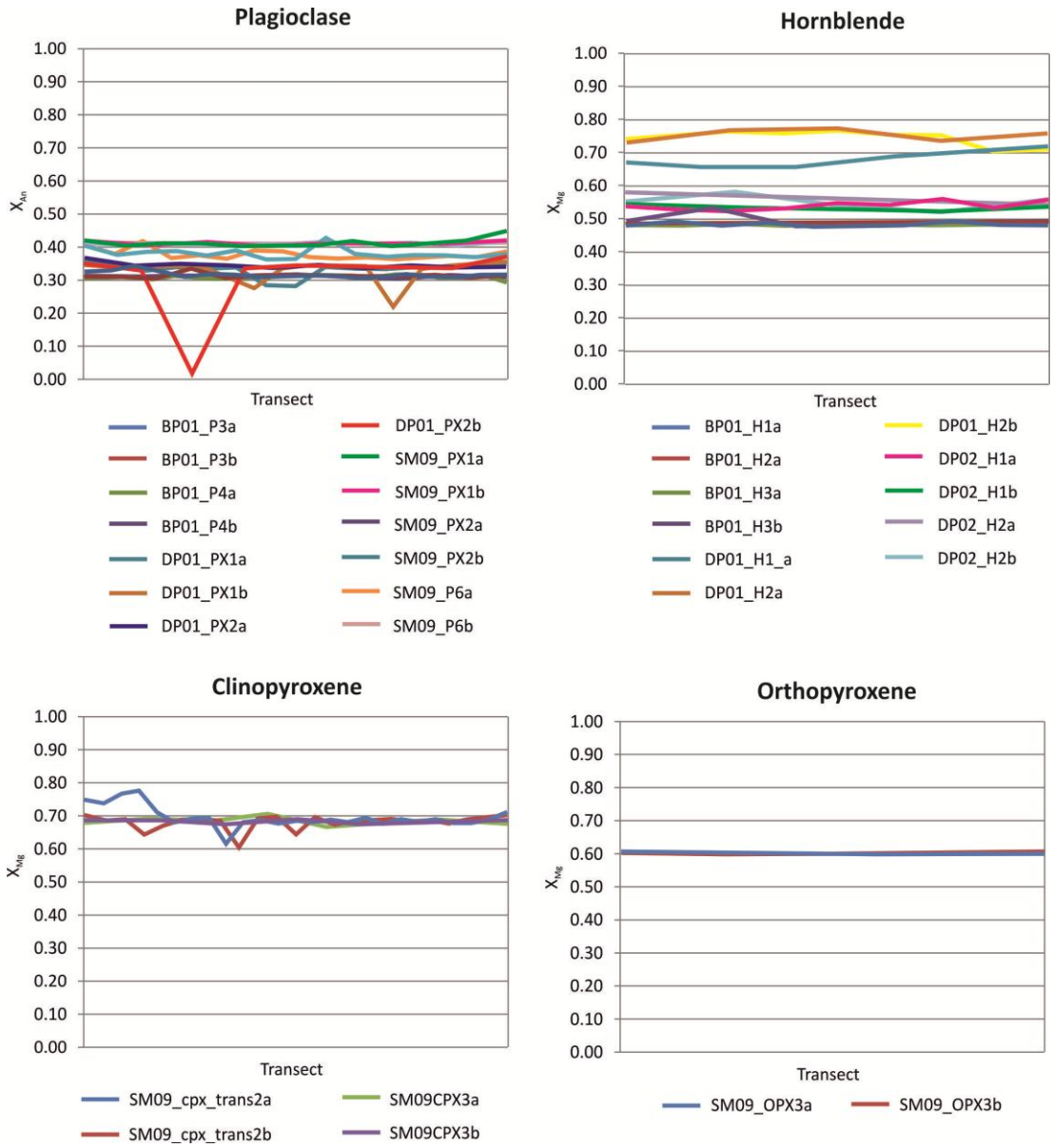

Fig. 4.40 X_{An} and X_{Mg} from EMPA compositional traverses of major minerals in samples JM09/SM09, JM09/BP01, JM09/DP01 and JM09/DP02.

Plagioclase

Sample	JM09/SM09											
Crystal	SM09_PX1a		SM09_PX1b		SM09_PX2a		SM09_PX2b		SM09_P6a		SM09_P6b	
n=	12		8		15		16		10		5	
SiO_2	56.22	*0.52*	56.21	*0.57*	58.37	*0.57*	58.64	*0.49*	56.43	*0.69*	55.91	*0.43*
Al_2O_3	26.44	*0.27*	26.33	*0.07*	26.32	*0.31*	26.15	*0.37*	26.64	*0.16*	26.38	*0.16*
CaO	8.56	*0.28*	8.45	*0.15*	7.96	*0.34*	7.88	*0.36*	8.52	*0.07*	8.54	*0.10*
FeO_T	0.06	*0.04*	0.09	*0.02*	0.07	*0.06*	0.08	*0.04*	0.08	*0.04*	0.07	*0.04*
Na_2O	6.73	*0.12*	6.71	*0.07*	7.15	*0.20*	7.16	*0.17*	6.76	*0.08*	6.75	*0.11*
K_2O	0.31	*0.04*	0.33	*0.03*	0.31	*0.09*	0.38	*0.09*	0.28	*0.01*	0.30	*0.01*
Total	98.32		98.12		100.17		100.28		98.71		97.95	
Cations p.f.u. for 8 oxygens												
Si	2.57	*0.02*	2.57	*0.01*	2.61	*0.02*	2.62	*0.02*	2.57	*0.01*	2.56	*0.01*
Al	1.42	*0.02*	1.42	*0.01*	1.39	*0.02*	1.38	*0.02*	1.43	*0.01*	1.43	*0.01*
Ca	0.42	*0.01*	0.41	*0.01*	0.38	*0.02*	0.38	*0.02*	0.42	*0.00*	0.42	*0.00*
Fe	0.00	*0.00*	0.00	*0.00*	0.00	*0.00*	0.00	*0.00*	0.00	*0.00*	0.00	*0.00*
Na	0.60	*0.01*	0.60	*0.01*	0.62	*0.02*	0.62	*0.01*	0.60	*0.01*	0.60	*0.01*
K	0.02	*0.00*	0.02	*0.00*	0.02	*0.01*	0.02	*0.01*	0.02	*0.00*	0.02	*0.00*
Total	5.03		5.02		5.02		5.01		5.03		5.03	
X_{An}	0.41		0.41		0.38		0.38		0.41		0.41	

(continued)

Plagioclase

Sample	JM09/BP01								Sample	JM09/DP01							
Crystal	BP01_P3a		BP01_P3b		BP01_P4a		BP01_P4b		Crystal	DP01_PX1a		DP01_PX1b		DP01_PX2a		DP01_PX2b	
n=	18		13		20		9		n=	15		16		10		9	
SiO_2	59.19	*1.00*	60.28	*0.82*	59.21	*0.52*	59.05	*0.37*	SiO_2	60.65	*0.70*	59.57	*0.77*	60.45	*0.39*	60.91	*3.48*
Al_2O_3	25.06	*0.42*	24.80	*0.42*	24.95	*0.18*	25.09	*0.24*	Al_2O_3	26.03	*0.33*	25.96	*0.56*	26.35	*0.23*	25.75	*1.83*
CaO	6.60	*0.22*	6.48	*0.12*	6.46	*0.15*	6.50	*0.12*	CaO	7.08	*0.42*	6.99	*0.75*	7.38	*0.17*	6.47	*2.37*
FeO_T	0.01	*0.02*	0.01	*0.02*	0.02	*0.03*	0.00	*0.00*	FeO_T	0.02	*0.03*	0.01	*0.05*	0.01	*0.02*	0.02	*0.03*
Na_2O	7.89	*0.22*	7.87	*0.20*	7.95	*0.08*	7.94	*0.06*	Na_2O	7.88	*0.27*	7.90	*0.43*	7.76	*0.14*	8.11	*1.23*
K_2O	0.18	*0.01*	0.17	*0.03*	0.17	*0.02*	0.19	*0.03*	K_2O	0.16	*0.01*	0.15	*0.02*	0.19	*0.02*	0.23	*0.15*
Total	98.94		99.61		98.76		98.76		Total	101.81		100.59		102.12		101.49	
Cations p.f.u. for 8 oxygens									Cations p.f.u. for 8 oxygens								
Si	2.67	*0.03*	2.69	*0.03*	2.67	*0.01*	2.67	*0.01*	Si	2.66	*0.02*	2.64	*0.03*	2.64	*0.01*	2.67	*0.11*
Al	1.33	*0.03*	1.31	*0.03*	1.33	*0.01*	1.33	*0.01*	Al	1.34	*0.02*	1.36	*0.03*	1.36	*0.01*	1.33	*0.11*
Ca	0.32	*0.01*	0.31	*0.01*	0.31	*0.01*	0.31	*0.01*	Ca	0.33	*0.02*	0.33	*0.04*	0.35	*0.01*	0.31	*0.11*
Fe	0.00	*0.00*	0.00	*0.00*	0.00	*0.00*	0.00	*0.00*	Fe	0.00	*0.00*	0.00	*0.00*	0.00	*0.00*	0.00	*0.00*
Na	0.69	*0.02*	0.68	*0.02*	0.70	*0.01*	0.69	*0.01*	Na	0.67	*0.02*	0.68	*0.04*	0.66	*0.01*	0.69	*0.09*
K	0.01	*0.00*	0.01	*0.00*	0.01	*0.00*	0.01	*0.00*	K	0.01	*0.00*	0.01	*0.00*	0.01	*0.00*	0.01	*0.01*
Total	5.02		5.00		5.02		5.02		Total	5.01		5.02		5.01		5.01	
X_{An}	0.32		0.31		0.31		0.31		X_{An}	0.33		0.33		0.34		0.31	

Table 4.24 Average composition of plagioclase crystals analysed by EMPA traverses from samples JM09/SM09, JM09/BP01 and JM09/DP01; values in italics denote 1 standard deviation on the average values to their left.

Orthopyroxene

Sample	JM09/SM09			
Crystal	SM09_OPX3a		SM09_OPX3b	
n=	6		5	
SiO_2	51.25	*0.42*	51.74	*0.17*
TiO_2	0.02	*0.03*	0.03	*0.06*
Al_2O_3	2.06	*0.28*	1.98	*0.08*
Cr_2O_3	0.01	*0.02*	0.01	*0.02*
MgO	21.12	*0.15*	21.08	*0.12*
CaO	0.44	*0.10*	0.49	*0.04*
MnO	0.67	*0.04*	0.68	*0.03*
FeO_T	24.72	*0.21*	24.87	*0.16*
Na_2O	0.02	*0.04*	0.01	*0.03*
Total	100.31		100.89	
Cations p.f.u. for 6 oxygens				
Si	1.93	*0.01*	1.94	*0.00*
Ti	0.00	*0.00*	0.00	*0.00*
Al	0.09	*0.01*	0.09	*0.00*
Cr	0.00	*0.00*	0.00	*0.00*
Mg	1.19	*0.01*	1.18	*0.01*
Ca	0.02	*0.00*	0.02	*0.00*
Mn	0.02	*0.00*	0.02	*0.00*
Fe	0.78	*0.01*	0.78	*0.01*
Na	0.00	*0.00*	0.00	*0.00*
Total	4.03		4.02	
X_{Mg}	0.60		0.60	

Table 4.25 Average composition of orthopyroxene crystals analysed by EMPA traverses from sample JM09/SM09; values in italics denote 1 standard deviation on the average values to their left.

Clinopyroxene

Sample	JM09/SM09							
Crystal	SM09_cpxtrans2a		SM09_cpxtrans2b		SM09CPX3a		SM09CPX3b	
n=	25		23		8		7	
SiO_2	50.63	*0.79*	50.63	*0.38*	51.24	*0.59*	51.35	*0.13*
TiO_2	0.48	*0.50*	0.40	*0.06*	0.30	*0.04*	0.31	*0.03*
Al_2O_3	3.37	*0.56*	3.55	*0.28*	2.90	*0.08*	2.87	*0.05*
Cr_2O_3	0.04	*0.02*	0.03	*0.02*	bd		bd	
MgO	12.61	*0.64*	12.58	*0.74*	12.73	*0.19*	12.74	*0.14*
CaO	21.64	*0.88*	20.87	*2.35*	21.63	*0.53*	21.75	*0.54*
MnO	0.32	*0.03*	0.35	*0.07*	0.34	*0.02*	0.34	*0.02*
FeO_T	9.86	*1.22*	10.64	*1.91*	10.52	*0.63*	10.59	*0.40*
Na_2O	0.76	*0.09*	0.77	*0.10*	0.76	*0.05*	0.74	*0.05*
Total	99.70		99.81		100.41		100.69	
Cations p.f.u. for 6 oxygens								
Si	1.91	*0.02*	1.91	*0.01*	1.92	*0.01*	1.92	*0.00*
Ti	0.01	*0.01*	0.01	*0.00*	0.01	*0.00*	0.01	*0.00*
Al	0.15	*0.03*	0.16	*0.01*	0.13	*0.00*	0.13	*0.00*
Cr	0.00	*0.00*	0.00	*0.00*	0.00	*0.00*	0.00	*0.00*
Mg	0.71	*0.03*	0.71	*0.04*	0.71	*0.01*	0.71	*0.01*
Ca	0.87	*0.03*	0.84	*0.09*	0.87	*0.02*	0.87	*0.02*
Mn	0.01	*0.00*	0.01	*0.00*	0.01	*0.00*	0.01	*0.00*
Fe	0.31	*0.04*	0.34	*0.06*	0.33	*0.02*	0.33	*0.01*
Na	0.06	*0.01*	0.06	*0.01*	0.06	*0.00*	0.05	*0.00*
Total	4.03		4.03		4.03		4.03	
X_{Mg}	0.69		0.68		0.68		0.68	

Table 4.26 Average composition of clinopyroxene crystals analysed by EMPA traverses from sample JM09/SM09; values in italics denote 1 standard deviation on the average values to their left; bd denotes below detection limits.

Hornblende

Sample	JM09/BP01								JM09/DP01					
Crystal	BP01_H1a1		BP01_H2a1		BP01_H3a		BP01_H3b		DP01_H1_a1		DP01_H2a		DP01_H2b	
n=	10		2		9		6		6		5		9	
SiO_2	40.19	*0.77*	39.73	*0.52*	39.96	*0.49*	41.01	*1.15*	46.93	*2.85*	53.12	*1.51*	53.51	*2.52*
TiO_2	0.52	*0.04*	0.51	*0.01*	0.58	*0.06*	0.50	*0.08*	0.19	*0.22*	0.28	*0.07*	0.23	*0.03*
Al_2O_3	12.59	*0.68*	12.88	*0.32*	12.32	*0.53*	11.41	*1.59*	10.20	*1.46*	5.15	*0.57*	5.41	*0.80*
Cr_2O_3	0.00	*0.00*	0.00	*0.00*	0.00	*0.00*	0.00	*0.00*	0.00	*0.00*	0.04	*0.02*	0.04	*0.02*
MgO	9.57	*0.15*	9.66	*0.09*	9.54	*0.16*	10.06	*0.78*	14.69	*0.97*	17.39	*1.21*	16.92	*1.38*
CaO	11.52	*0.14*	11.43	*0.07*	11.38	*0.12*	11.26	*0.23*	11.39	*0.57*	11.73	*0.72*	11.53	*0.70*
MnO	0.30	*0.02*	0.34	*0.01*	0.32	*0.03*	0.31	*0.03*	0.31	*0.02*	0.28	*0.02*	0.27	*0.02*
FeO_T	18.04	*0.25*	17.85	*0.16*	18.08	*0.22*	17.95	*0.31*	12.09	*0.76*	10.00	*0.62*	10.12	*0.90*
Na_2O	1.53	*0.06*	1.51	*0.09*	1.60	*0.10*	1.62	*0.13*	1.08	*0.20*	0.50	*0.09*	0.55	*0.09*
K_2O	1.21	*0.09*	1.23	*0.05*	1.14	*0.06*	1.02	*0.10*	0.42	*0.14*	0.16	*0.03*	0.18	*0.04*
Total	95.47		95.15		94.91		95.14		97.30		98.65		98.76	
Cations p.f.u. for 23 oxygens														
Si	6.26	*0.10*	6.21	*0.07*	6.27	*0.06*	6.39	*0.17*	6.83	*0.29*	7.47	*0.15*	7.51	*0.23*
Ti	0.06	*0.00*	0.06	*0.00*	0.07	*0.01*	0.06	*0.01*	0.02	*0.02*	0.03	*0.01*	0.02	*0.00*
Al	2.31	*0.13*	2.37	*0.06*	2.28	*0.09*	2.10	*0.29*	1.75	*0.26*	0.85	*0.10*	0.90	*0.14*
Cr	0.00	*0.00*	0.00	*0.00*	0.00	*0.00*	0.00	*0.00*	0.00	*0.00*	0.00	*0.00*	0.00	*0.00*
Mg	2.22	*0.03*	2.25	*0.02*	2.23	*0.04*	2.34	*0.20*	3.19	*0.24*	3.65	*0.26*	3.54	*0.32*
Ca	1.92	*0.03*	1.92	*0.02*	1.91	*0.02*	1.88	*0.03*	1.78	*0.10*	1.77	*0.09*	1.73	*0.11*
Mn	0.04	*0.00*	0.04	*0.00*	0.04	*0.00*	0.04	*0.00*	0.04	*0.00*	0.03	*0.00*	0.03	*0.00*
Fe	2.35	*0.04*	2.33	*0.03*	2.37	*0.04*	2.34	*0.05*	1.47	*0.11*	1.18	*0.08*	1.19	*0.12*
Na	0.46	*0.02*	0.46	*0.03*	0.49	*0.03*	0.49	*0.04*	0.31	*0.06*	0.14	*0.02*	0.15	*0.02*
K	0.24	*0.02*	0.25	*0.01*	0.23	*0.01*	0.20	*0.02*	0.08	*0.03*	0.03	*0.01*	0.03	*0.01*
Total	15.87		15.89		15.88		15.85		15.47		15.15		15.11	
X_{Mg}	0.49		0.49		0.48		0.50		0.68		0.76		0.75	

(continued)

Hornblende

Sample	JM09/DP02							
Crystal	DP02_H1a		DP02_H1b		DP02_H2a		DP02_H2b	
n=	9		5		4		3	
SiO_2	43.39	*1.43*	43.14	*1.04*	44.81	*2.97*	46.34	*4.35*
TiO_2	0.49	*0.07*	0.55	*0.07*	0.45	*0.19*	0.40	*0.24*
Al_2O_3	13.28	*1.26*	13.63	*0.40*	11.25	*3.62*	9.60	*6.04*
Cr_2O_3	0.00	*0.00*	0.01	*0.02*	0.05	*0.01*	0.07	*0.01*
MgO	10.83	*0.66*	10.64	*0.22*	11.44	*0.17*	11.09	*0.29*
CaO	11.15	*1.10*	11.39	*0.22*	11.38	*0.16*	11.61	*0.30*
MnO	0.28	*0.07*	0.24	*0.02*	0.38	*0.27*	0.57	*0.55*
FeO_T	16.25	*1.12*	16.44	*0.17*	15.60	*1.26*	16.70	*1.59*
Na_2O	1.43	*0.24*	1.46	*0.06*	1.24	*0.16*	0.99	*0.40*
K_2O	0.46	*0.06*	0.49	*0.05*	0.40	*0.16*	0.36	*0.24*
Total	97.55		97.98		97.00		97.74	
Cations p.f.u. for 23 oxygens								
Si	6.46	*0.16*	6.40	*0.08*	6.68	*0.43*	6.88	*0.67*
Ti	0.05	*0.01*	0.06	*0.01*	0.05	*0.02*	0.05	*0.03*
Al	2.33	*0.21*	2.38	*0.07*	1.98	*0.64*	1.68	*1.05*
Cr	0.00	*0.00*	0.00	*0.00*	0.01	*0.00*	0.01	*0.00*
Mg	2.40	*0.18*	2.35	*0.07*	2.54	*0.03*	2.45	*0.08*
Ca	1.78	*0.16*	1.81	*0.05*	1.82	*0.03*	1.85	*0.06*
Mn	0.04	*0.01*	0.03	*0.00*	0.05	*0.03*	0.07	*0.07*
Fe	2.02	*0.17*	2.04	*0.01*	1.94	*0.16*	2.07	*0.20*
Na	0.41	*0.07*	0.42	*0.02*	0.36	*0.05*	0.29	*0.12*
K	0.09	*0.01*	0.09	*0.01*	0.08	*0.03*	0.07	*0.05*
Total	15.58		15.60		15.50		15.41	
X_{Mg}	0.54		0.54		0.57		0.54	

Table 4.27 Average composition of hornblende crystals analysed by EMPA traverses from samples JM09/BP01, JM09/DP01 and JM09/DP02; values in italics denote 1 standard deviation on the average values to their left.

4c: Representativeness of the Samples

This PhD initially set out to investigate how U-Pb isotopic ages are affected by metamorphic and deformational overprinting in a typical Precambrian tonalite-trondhjemite-granodiorite (TTG) complex. Zircon trace element chemistry, whole rock composition and mineral chemistry were analysed to enable links to be made between zircons and the rocks they were in. In particular, comparison of zircons from inside and outside Laxfordian shear zones was to illustrate the effects of shear zone formation on zircon chemistry and microstructure. However, subsequent sample characterisation (chapters 4a and 4b) indicate the compositional heterogeneity of the samples collected here. Field observation shows that the samples are compositionally heterogeneous at the hand specimen scale due to gneissic layering or compositional layering in shear zone rocks. This is the case throughout the Lewisian Gneiss Complex (LGC) and other TTG complexes across the world (Windley and Bridgwater, 1971; Martin, 1994). The whole rock composition of the 8 grey TTG gneiss samples analysed is variable. SiO_2 contents range from 47wt% in JM09/BP02 (statically retrogressed Badcallian gneissic layering) to 65wt% in JM09/BP06 (Laxfordian shear zone) while Na is higher in the more felsic samples and Ca, Fe and Mg higher is the more mafic samples.

Several suites of whole rock analyses of TTG gneisses from the Central Region/Assynt Terrane have been conducted previously (Holland and Lambert, 1973; Sheraton et al., 1973a; Beach, 1976; Rollinson and Windley, 1980) and are correlated in Table 4.28 and Fig. 4.41. Sample JM09/SM09 (the granulite-facies Badcallian assemblage from Scourie Mor) has 10wt% less SiO_2 than average value of the equivalent pyroxene granulite of Holland and Lambert (1973) and has higher CaO, MgO and FeO_T contents than this and the average pyroxene granulite of Sheraton et al. (1973a). Beach (1976) analysed typical TTG gneisses from inside and outside shear zones in the Scourie area; his data show a 21wt% range in SiO_2 content of samples from outside shear zones and a 22wt% range

inside shear zones (Table 4.28). This further illustrates the compositional heterogeneity of the TTG gneisses of the LGC at small scales. Taking the grey TTG gneiss samples of this study as a whole, they plot within the wide compositional ranges for most major elements although K_2O is lower than many previously published analyses (Fig. 4.41).

CIPW normative mineralogy shows that the possible protoliths to the TTG gneisses of (Holland and Lambert, 1973; Sheraton et al., 1973a; Beach, 1976; Rollinson and Windley, 1980) plot in a range of fields (Table 4.29, Fig. 4.42). The presence of hypersthene in the normative mineralogy of all samples indicates charnockitic protoliths. The average pyroxene granulite of Holland and Lambert (1973) is a hypersthene tonalite while the average pyroxene granulite of Sheraton et al. (1973a) is a hypersthene diorite, as is sample JM09/SM09 so even prior to hydrous retrogression, there was heterogeneity in rock chemistry, likely inherited from the protolith. The average retrogressed TTG gneiss of Sheraton et al. (1973a) is a hypersthene tonalite while the analogous TTG gneisses from outside Laxfordian shear zones of Beach (1976) have a range of compositions from hypersthene-diorite, -granodiorite and -monzodiorite. Analogous samples in this study are JM09/BP02 (hypersthene monzodiorite) and JM09/DP01 (hypersthene diorite). Three of the four 'tonalites' analysed by Rollinson and Windley (1980) are in fact tonalites but the fourth is a hypersthene diorite.

The average TTG gneiss from Laxfordian shear zones of Sheraton et al. (1973a) is a hypersthene diorite while those of Beach (1976) range from hypersthene-monzodiorite and -granodiorite to hypersthene-monzonite and -syenite, relatively alkalic compositions. The Laxfordian shear zone samples in this study (JM09/DP02, JM09/BP06 and JM09/BP04) are all hypersthene tonalites. The CIPW normative mineralogy of many of the samples in this study is closer to "P" in a QAP triangle than samples from previous studies. The range in normative mineralogies shown by the samples in this study and those of (Holland and Lambert, 1973; Sheraton et al., 1973a; Beach, 1976; Rollinson and Windley, 1980) may be

partly due to heterogeneity in the composition of the protolith rocks but also partly due to metasomatic changes in rocks which have undergone hydrous retrogression (Beach, 1973; Beach, 1974; Beach, 1976). CIPW normative mineralogy calculations do not account for the presence of hydrous minerals but it is possible that there was igneous hornblende in these rocks. This may explain some of the heterogeneity in normative modal mineralogies.

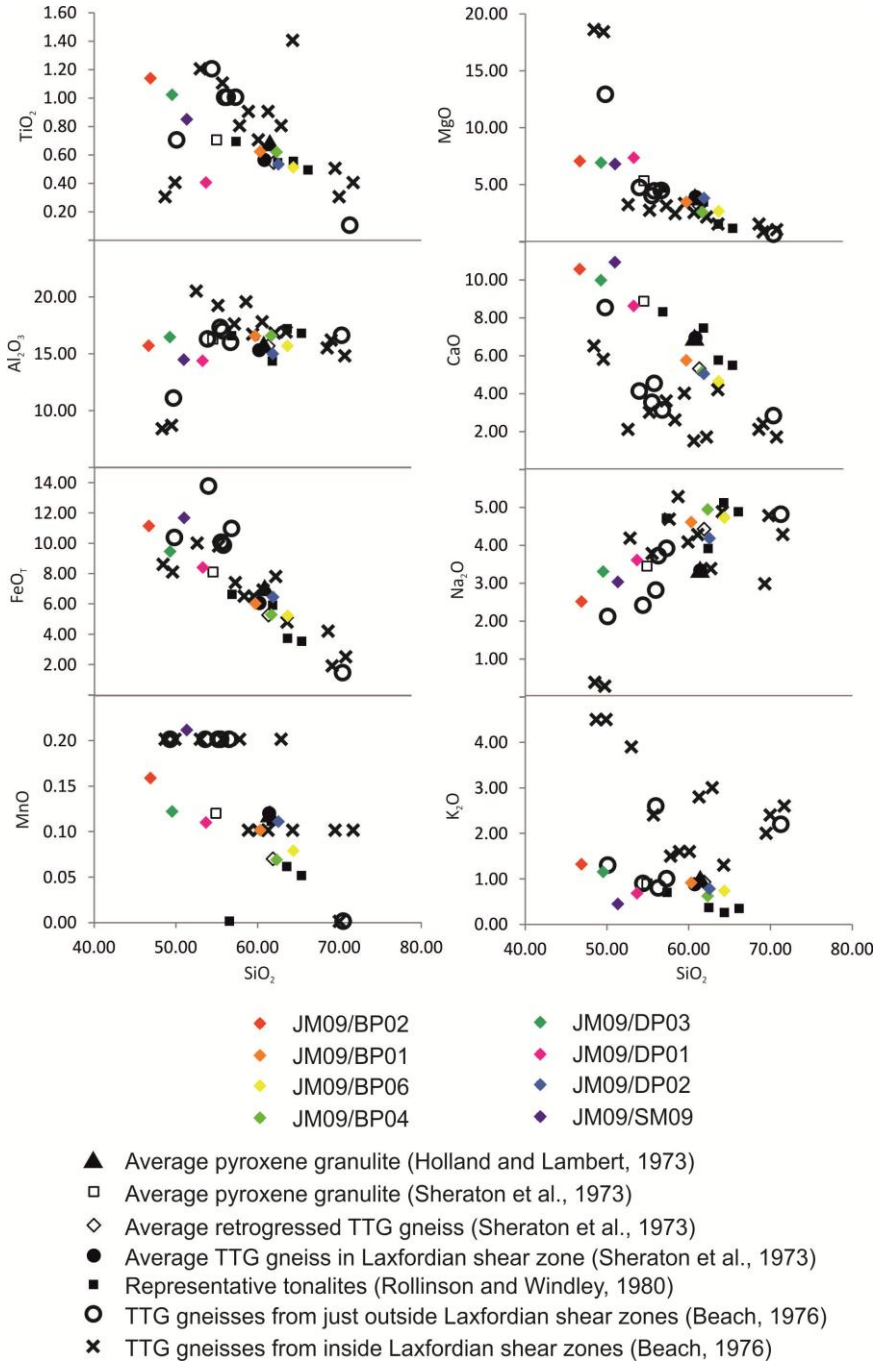

Fig. 4.41 Harker plots of major element oxide whole rock compositions against silica of various frey TTG gneisses from the Central Region/Assynt Terrane; data from this study, Holland and Lambert (1973), Sheraton et al. (1973a), Rollinson and Windley (1980) and Beach (1976); values are in wt%.

Sample/Source	Tectonothermal Setting in LGC	SiO_2	TiO_2	Al_2O_3	FeO_T	MnO	MgO	CaO	Na_2O	K_2O	P_2O_5	LOI	Total
JM09/BP02	Just outside Laxfordian shear zone	46.87	1.14	15.69	11.14	0.16	7.06	10.56	2.51	1.32	0.96	2.01	99.41
JM09/BP01	Possible Inverian structure	60.30	0.62	16.56	6.01	0.10	3.46	5.75	4.61	0.91	0.23	1.19	99.74
JM09/BP06	Laxfordian shear zone	64.38	0.51	15.67	5.22	0.08	2.64	4.64	4.72	0.73	0.12	1.00	99.70
JM09/BP04	Laxfordian shear zone	62.33	0.62	16.57	5.28	0.07	2.56	5.14	4.94	0.62	0.19	1.09	99.41
JM09/DP03	Badcallian assemblage	49.55	1.02	16.45	9.45	0.12	6.90	9.98	3.30	1.15	0.53	1.18	99.63
JM09/DP01	Just outside Laxfordian shear zone	53.69	0.40	14.36	8.40	0.11	7.35	8.62	3.61	0.68	0.27	2.05	99.54
JM09/DP02	Laxfordian shear zone	62.54	0.53	14.99	6.44	0.11	3.80	5.04	4.18	0.78	0.13	1.16	99.70
JM09/SM09	Badcallian assemblage	51.33	0.85	14.46	11.66	0.21	6.78	10.93	3.03	0.45	0.08	0.16	99.94
Holland and Lambert (1973)	Badcallian assemblage	61.40	0.68	15.80	7.10	0.12	3.90	6.90	3.30	1.00	na	na	100.20
Sheraton et al. (1973)	Badcallian assemblage	54.89	0.69	16.27	8.10	0.12	5.31	8.83	3.41	0.89	0.13	1.59	100.23
Sheraton et al. (1973)	Statically retrogressed Badcallian	61.89	0.53	15.68	5.26	0.07	3.09	5.27	4.39	0.93	0.20	1.93	99.24
Sheraton et al. (1973)	Laxfordian shear zone	60.75	0.55	15.29	6.04	0.08	3.45	5.27	4.64	0.88	0.18	1.85	98.98
Rollinson and Windley (1980)	Badcallian assemblage	62.38	0.53	14.47	5.96	0.11	3.33	7.42	3.84	0.37	0.19	na	98.60
Rollinson and Windley (1980)	Badcallian assemblage	66.07	0.48	16.90	3.57	0.05	1.01	5.45	4.81	0.35	0.10	na	98.79
Rollinson and Windley (1980)	Badcallian assemblage	64.27	0.54	17.30	3.77	0.06	1.39	5.73	5.05	0.26	0.10	na	98.47
Rollinson and Windley (1980)	Badcallian assemblage	57.27	0.68	16.69	6.67	nd	4.55	8.28	4.64	0.70	0.15	na	99.63
Beach (1976) U6973	Just outside Laxfordian shear zone	54.30	1.20	16.30	13.90	0.20	4.60	4.10	2.40	0.90	0.10	1.40	99.40
Beach (1976) U6994	Just outside Laxfordian shear zone	57.20	1.00	16.00	11.10	0.20	4.30	3.10	3.90	1.00	0.10	1.30	99.20
Beach (1976) U7159	Just outside Laxfordian shear zone	55.90	1.00	17.30	10.20	0.20	3.90	3.50	2.80	2.60	0.20	2.60	100.20
Beach (1976) U6856	Just outside Laxfordian shear zone	56.20	1.00	17.00	10.00	0.20	4.30	4.50	3.70	0.80	0.10	1.50	99.30
Beach (1976) U7156	Just outside Laxfordian shear zone	71.20	0.10	16.60	1.60	nd	0.50	2.80	4.80	2.20	nd	0.50	100.30
Beach (1976) U7308	Just outside Laxfordian shear zone	50.00	0.70	11.10	10.50	0.20	12.80	8.50	2.10	1.30	0.10	1.80	99.10

(continued)

Sample/Source	Tectonothermal Setting in LGC	SiO_2	TiO_2	Al_2O_3	FeO_T	MnO	MgO	CaO	Na_2O	K_2O	P_2O_5	LOI	Total
Beach (1976) S6854	Laxfordian shear zone	52.90	1.20	20.50	10.00	0.20	3.10	2.00	4.20	3.90	0.10	2.00	100.10
Beach (1976) SS7165	Laxfordian shear zone	62.80	0.80	16.80	7.80	0.20	2.00	1.60	3.40	3.00	nd	2.20	100.60
Beach (1976) SS7164	Laxfordian shear zone	61.20	0.90	17.80	6.90	0.10	2.40	1.40	4.30	2.80	0.10	1.50	99.40
Beach (1976) SS7166	Laxfordian shear zone	58.80	0.90	19.30	6.50	0.10	2.30	2.50	5.30	1.60	0.20	1.80	99.30
Beach (1976) SS7155	Laxfordian shear zone	69.90	0.30	16.20	1.90	nd	0.70	2.30	4.80	2.40	0.10	0.80	99.40
Beach (1976) SS7309	Laxfordian shear zone	48.60	0.30	8.40	8.60	0.20	18.50	6.40	0.40	4.50	0.10	4.90	100.90
Beach (1976) SS7168	Laxfordian shear zone	64.20	1.40	16.90	4.80	0.10	1.40	4.10	4.90	1.30	0.30	0.70	100.10
Beach (1976) SSS7157	Laxfordian shear zone	69.40	0.50	15.50	4.20	0.10	1.40	2.00	3.00	2.00	0.30	1.10	99.50
Beach (1976) SSS7158	Laxfordian shear zone	55.60	1.10	19.20	9.80	0.20	2.60	2.90	3.80	2.40	0.10	1.60	99.30
Beach (1976) SSS7154	Laxfordian shear zone	71.60	0.40	14.80	2.50	0.10	0.90	1.60	4.30	2.60	0.10	1.30	100.20
Beach (1976) SSS7310	Laxfordian shear zone	49.80	0.40	8.70	8.10	0.20	18.30	5.70	0.30	4.50	0.10	2.00	98.10
Beach (1976) SSS7170	Laxfordian shear zone	60.00	0.70	16.70	6.50	0.10	3.20	3.90	4.10	1.60	0.30	2.00	99.10
Beach (1976) SSS7171	Laxfordian shear zone	57.70	0.80	17.60	7.40	0.20	3.00	3.50	4.70	1.50	0.20	2.70	99.30

Table 4.28 Major element oxide whole rock compositions of various grey TTG gneisses from the Central Region/Assynt Terrane; data from this study, Holland and Lambert (1973), Sheraton et al. (1973a), Rollinson and Windley (1980) and Beach (1976); values are in wt%; na denotes not available, nd denotes none detected.

Sample/Source	Qtz	An	Ab	Or	Dio	Hyp	Olv	Ilm	Mag	Apt	Total	Q	A	P	QAP Field	Name
JM09/BP02	0.00	30.50	24.88	9.87	14.14	4.87	8.98	1.40	3.17	2.13	99.93	0	15	85	9	Hypersthene Monzodiorite
JM09/BP01	12.63	22.41	42.44	6.23	3.83	9.67	0.00	0.71	1.59	0.47	99.98	15	7	77	5	Hypersthene Tonalite
JM09/BP06	20.11	19.67	42.87	4.98	2.15	8.03	0.00	0.57	1.36	0.24	99.98	23	6	71	5	Hypersthene Tonalite
JM09/BP04	16.48	21.66	45.12	4.21	2.26	7.75	0.00	0.70	1.39	0.39	99.96	19	5	76	5	Hypersthene Tonalite
JM09/DP03	0.00	28.75	31.88	8.28	14.39	2.91	8.73	1.22	2.63	1.15	99.94	0	12	88	9	Hypersthene Monzodiorite
JM09/DP01	2.27	22.85	35.18	4.91	14.91	16.36	0.00	0.48	2.36	0.59	99.91	3	8	89	10*	Hypersthene Diorite
JM09/DP02	18.65	20.47	38.59	5.31	3.17	11.20	0.00	0.61	1.71	0.27	99.98	22	6	71	5	Hypersthene Tonalite
JM09/SM09	0.00	26.82	29.62	3.32	21.73	13.91	0.07	1.03	3.28	0.18	99.96	0	6	94	10*	Hypersthene Diorite
Holland and Lambert (1973)	17.90	25.99	30.25	6.71	6.32	10.16	0.00	0.77	1.88	0.00	99.98	22	8	70	5	Hypersthene Tonalite
Sheraton et al. (1973)	5.89	28.15	32.43	6.22	12.03	11.94	0.00	0.81	2.22	0.28	99.98	8	9	83	10*	Hypersthene Diorite
Sheraton et al. (1973)	17.56	21.05	40.66	6.32	3.31	8.66	0.00	0.61	1.40	0.42	99.99	21	7	72	5	Hypersthene Tonalite
Sheraton et al. (1973)	14.56	19.10	43.36	6.04	4.87	9.40	0.00	0.64	1.62	0.38	99.97	18	7	75	10*	Hypersthene Diorite
Rollinson and Windley (1980)	20.43	21.93	35.62	2.62	10.28	6.50	0.00	0.61	1.59	0.40	99.98	25	3	71	5	Hypersthene Tonalite
Rollinson and Windley (1980)	24.06	23.50	43.03	2.39	2.11	3.23	0.00	0.53	0.92	0.20	99.97	26	3	72	5	Hypersthene Tonalite
Rollinson and Windley (1980)	20.20	23.96	45.51	1.83	2.88	3.81	0.00	0.60	0.98	0.20	99.96	22	2	76	5	Hypersthene Tonalite
Rollinson and Windley (1980)	4.96	23.48	43.03	4.80	12.39	8.44	0.00	0.78	1.78	0.31	99.97	7	6	87	10*	Hypersthene Diorite
Beach (1976) U6973	18.17	22.03	23.77	6.55	0.00	20.65	0.00	1.47	3.96	0.22	96.82	26	9	65	4	Hypersthene Granodiorite
Beach (1976) U6994	14.90	16.08	37.63	7.07	0.00	17.52	0.00	1.19	3.08	0.22	97.69	20	9	71	9*	Hypersthene Monzodiorite
Beach (1976) U7159	14.21	17.49	26.96	18.06	0.00	15.87	0.00	1.19	2.83	0.43	97.04	19	24	58	9*	Hypersthene Monzodiorite
Beach (1976) U6856	13.06	23.47	35.51	5.66	0.00	16.59	0.00	1.19	2.76	0.22	98.46	17	7	76	10*	Hypersthene Diorite
Beach (1976) U7156	27.63	13.64	41.61	13.78	0.00	2.04	0.00	0.11	0.40	0.00	99.20	29	14	57	4	Hypersthene Granodiorite
Beach (1976) U7308	0.00	19.29	21.30	9.60	18.89	18.56	8.16	0.88	3.07	0.23	99.98	0	19	81	9	Hypersthene Monzodiorite

(continued)

Sample/Source	Qtz	An	Ab	Or	Dio	Hyp	Olv	Ilm	Mag	Apt	Total	Q	A	P	QAP Field	Name
Beach (1976) S6854	0.97	10.05	40.01	26.72	0.00	13.47	0.00	1.42	2.74	0.21	95.59	1	34	64	8	Hypersthene Monzonite
Beach (1976) SS7165	23.69	8.42	31.61	20.10	0.00	9.54	0.00	0.92	2.09	0.00	96.38	28	24	48	4	Hypersthene Granodiorite
Beach (1976) SS7164	17.88	6.72	40.07	18.81	0.00	9.54	0.00	1.04	1.85	0.21	96.12	21	23	56	4	Hypersthene Granodiorite
Beach (1976) SS7166	12.08	11.78	49.56	10.86	0.00	9.05	0.00	1.04	1.75	0.42	96.55	14	13	73	9*	Hypersthene Monzodiorite
Beach (1976) SS7155	27.04	10.76	42.27	15.26	0.00	2.48	0.00	0.33	0.48	0.20	98.82	28	16	56	4	Hypersthene Granodiorite
Beach (1976) SS7309	0.00	8.88	4.08	32.99	18.01	7.44	25.44	0.38	2.53	0.23	99.98	0	72	28	7	Hypersthene Syenite
Beach (1976) SS7168	20.19	18.61	43.91	8.48	0.00	4.94	0.00	1.55	1.24	0.60	99.53	22	9	69	4	Hypersthene Granodiorite
Beach (1976) SSS7157	39.37	8.28	27.35	13.19	0.00	5.66	0.00	0.56	1.10	0.61	96.13	45	15	40	4	Hypersthene Granodiorite
Beach (1976) SSS7158	11.71	14.88	36.35	16.58	0.00	12.34	0.00	1.30	2.70	0.21	96.07	15	21	64	9*	Hypersthene Monzodiorite
Beach (1976) SSS7154	32.01	7.35	37.96	16.56	0.00	3.34	0.00	0.44	0.63	0.20	98.48	34	18	48	4	Hypersthene Granodiorite
Beach (1976) SSS7310	0.00	10.30	3.05	32.89	14.32	17.57	18.74	0.50	2.37	0.23	99.97	0	71	29	7	Hypersthene Syenite
Beach (1976) SSS7170	16.44	18.41	38.41	10.88	0.00	11.34	0.00	0.81	1.75	0.63	98.67	20	13	68	9*	Hypersthene Monzodiorite
Beach (1976) SSS7171	11.14	17.21	44.53	10.32	0.00	11.70	0.00	0.94	2.02	0.42	98.27	13	12	74	9*	Hypersthene Monzodiorite

Table 4.29 Normative mineralogy (CIPW) of whole rock compositions of various grey TTG gneisses from the Central Region/Assynt Terrane; data from this study, Holland and Lambert (1973), Sheraton et al. (1973a), Rollinson and Windley (1980) and Beach (1976); values are in %; QAP field and rock name are determined using the classification of Streckeisen (1974); Qtz = quartz, An = anorthite, Ab = albite, Or = orthoclase, Dio = diopside, Hyp = hypersthene, Olv = olivine, Ilm = ilmenite, Mag = magnetite, Apt = apatite.

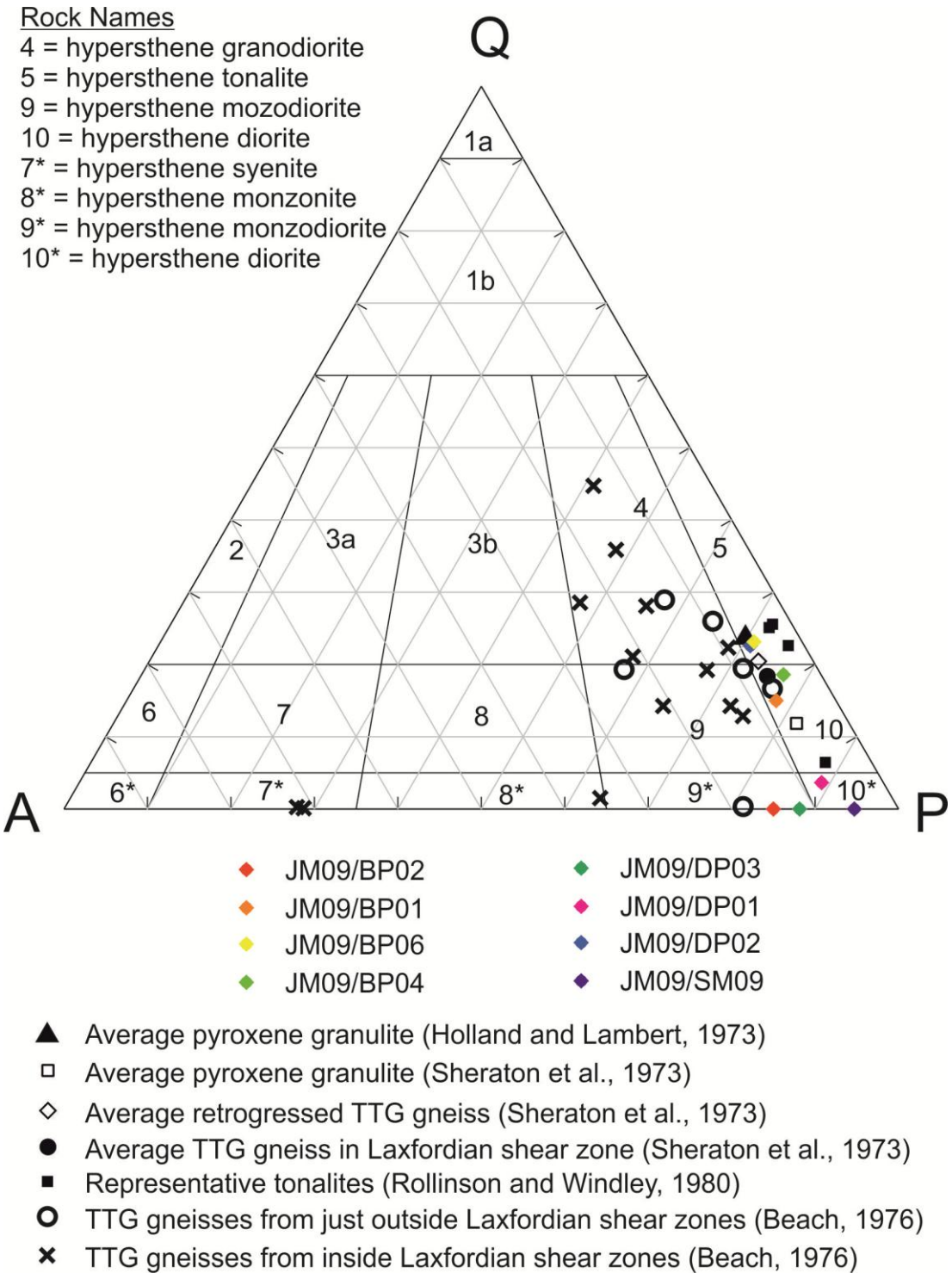

Fig. 4.42 QAP diagram of normative mineralogy (CIPW) of whole rock compositions of various grey TTG gneisses from the Central Region/Assynt Terrane; QAP field and rock name are determined using the classification of Streckeisen (1974).

As well as variation in normative mineralogy, there is also heterogeneity in the current modal mineralogy of the samples. Quartz content ranges from ~5% to ~55% while plagioclase ranges from ~20% to ~75%. Beach (1973) recorded plagioclase content as low as

10% from a Laxfordian shear zone, also from the Scourie area. His shear zone samples generally have a greater percentage of biotite with less hornblende than the equivalent samples described in chapter 4a (Table 4.30). Those from just outside shear zones are within range of equivalent samples in this study but are still variable in modal mineralogy. The chemistry of the modal minerals is also variable between samples, even over small distances although the compositional transects presented in chapter 4b indicated there was minimal intracrystal chemical variability. At Badcall Point, where the four samples were located within a few metres of each other, hornblende and plagioclase in each sample can have quite different compositions (Table 4.15). A similar scenario occurs at Duartmore Point (Table 4.16). Beach (1973) also records variable composition between hornblende, plagioclase and biotite between samples.

While every effort was made to collect homogeneous samples, the compositional heterogeneity of the rocks meant that the part of the sample that went to make the thin section could have a different composition to the part that went for whole rock XRF analysis. For example, the modal percentage of quartz, estimated from the thin section, in sample JM09/BP06 is ~5% but the XRF analysis measured 64.38wt% SiO_2. Similarly, JM09/DP02 also has ~5% quartz in the modal mineralogy estimated from the thin section but 62.54wt% SiO_2. Again this illustrates the heterogeneity of the rocks, even at the hand specimen scale. In summary, this makes achieving the initial aim of this PhD – understanding how tectonothermal overprinting affects zircon ages and chemistry by analysing samples inside and outside shear zones – rather difficult as the geochemical framework (i.e. the host rock) is different for different zircons/samples. As a result, the project has evolved and the manuscripts in the chapters 5-7 reflect investigations into the effects of tectonothermal overprinting in zircon which are not so heavily tied to the sample geochemistry.

		Identifier	Hornblende	Plagioclase	Quartz	Biotite	Clinopyroxene	Epidote	K-feldspar	Muscovite
Shear zones	This Study	JM09/BP06	20	75	5			minor		
		JM09/BP04	20	20	55	5		minor		
		JM09/DP02	50	45	5					
	Beach 1973 Table 1	6824	9.5	52.8	24.2	13.3				
		7001	15.7	54.0	19.4	8.0				
		6964	2.2	48.6	15.6	23.5		5.0		
		6995	50.5	9.9	8.8	26.3				
		6923	45.2	38.8	7.1					
		6819		52.8	28.6	8.4			4.0	6.1
Adjacent to shear zones	This Study	JM09/BP02	40	50	10			minor		
		JM09/DP01	20	40	40	minor				
		JM09/GG09	40	30	30	minor				
	Beach 1973 Table 1	6825	21.3	51.1	17.5		7.5			
		7000	33.1	40.3	25.2					
		6818		55.0	32.0	6.0			6.9	

Table 4.30 Comparison between modal mineralogies of equivalent grey TTG gneisses of the Central Region/Assynt Terrane between this study and Beach (1973); the range in modal mineralogy between equivalent samples indicates the heterogeneity of the rocks.

5. The Effects of Crystal Lattice Distortion on Trace Element Mobility and U-Th-Pb Isotope Systematics in Zircon: Examples from the Lewisian Gneiss Complex, Northwest Scotland

Formatted for submission to *Contributions to Mineralogy and Petrology*

The Effects of Crystal Lattice Distortion on Trace Element Mobility and U-Th-Pb Isotope Systematics in Zircon: Examples from the Lewisian Gneiss Complex, Northwest Scotland

John M. MacDonald[1], John Wheeler[1], Simon L. Harley[2], Elisabetta Mariani[1], Kathryn M. Goodenough[3], Quentin Crowley[4], Daniel Tatham[1]

[1] School of Environmental Sciences, Jane Herdman Laboratories, University of Liverpool, L69 3GP, UK

[2] School of GeoSciences, Grant Institute, The King's Buildings, West Mains Road, Edinburgh, EH9 3JW, UK

[3] British Geological Survey, Murchison House, West Mains Road, Edinburgh, EH9 3LA, UK

[4] Dept. Geology, School of Natural Sciences, Trinity College, Dublin 2, Ireland, IE

Corresponding author: John M. MacDonald

Postal: School of Environmental Sciences, University of Liverpool, L69 3GP, UK.

Email: jmacd@liv.ac.uk

Telephone: 01517945201

Abstract Zircon is a key mineral in geochemical and geochronological studies in a range of geological settings as it is mechanically and chemically robust. However, distortion of its crystal lattice can change the abundance and distribution of key elements such as U and Pb. Our Electron Backscatter Diffraction (EBSD) analysis of ninety-nine zircons from the Lewisian Gneiss Complex (LGC) of northwest Scotland has revealed five zircons with lattice distortion. The distortion can take the form of gradual bending of the lattice or division of the crystal into subgrains. Weighted Burgers Vectors analysis of EBSD data lends support to

the observation that the zircon lattices have been distorted either by post-crystallisation plastic distortion or possibly as a growth microstructure. Three of the five distorted zircons, along with many of the undistorted zircons in the population, were analysed by ion microprobe to measure U and Pb isotopes, Ti and REEs. Comparison of Th/U ratio, $^{207}Pb/^{206}Pb$ age, REE pattern and concentration, and Ti abundance between zircons with and without lattice distortion indicates that the distortion heterogeneously affects these elements and isotopes within single crystals, within samples and between localities. Th/U ratios in distorted zircons ranges from 0.3-3.2 while REE patterns vary heterogeneously, sometimes depleted in heavy REEs or lacking a Eu anomaly. Ti-thermometry records temperatures that were either low (~700°C) or high (~900°C) relative to undistorted zircons. One distorted zircon records apparent $^{207}Pb/^{206}Pb$ isotopic ages (-3.0% to +0.3% discordance) in the range of 2420-2450Ma but this does not correlate with any previously dated tectonothermal event in the LGC. Two other distorted zircons give discordant ages of 2331±22Ma and 2266±0Ma, defining a discordia lower intercept within error of a late amphibolite-facies tectonothermal event. This illustrates that Pb may be mobilised in distorted zircons at lower metamorphic grade than in undistorted zircons. These findings show the advantages in testing for lattice distortion by EBSD prior to micro-beam analysis so as to avoid making false geological interpretations based on such grains, and also that distorted lattices record information on otherwise cryptic events.

Keywords – zircon, lattice distortion, trace elements & isotopes, EBSD

Introduction

Zircon is a common accessory mineral in a wide range of sedimentary, igneous and metamorphic rocks. It has a high volume diffusion closure temperature of typically >900°C for radiogenic Pb (Cherniak and Watson, 2003) and is regarded as a mechanically and

chemically robust mineral (Finch and Hanchar, 2003), suitable for geochemical investigation of Precambrian geological events. The primary incorporation of uranium but not lead makes it ideal for radiometric dating; it also contains other elements such as hafnium, titanium and the rare earth elements (REE), which allow a range of geological interpretations to be made.

Populations of zircons are routinely analysed to determine the tectonothermal evolution of rocks throughout the world, generally involving U-Pb isotopic measurements. Recent research, however, has indicated that some of this isotopic and trace element analysis could be compromised by plastic deformation of the zircon crystal lattice (Reddy et al., 2006; Timms et al., 2006a; Timms et al., 2006b; Timms et al., 2011). Plastic deformation occurs when forces applied to a grain cause the crystal lattice to bend and distort through movement of lattice dislocations; crystals may also grow with defects and therefore have a distorted lattice from the time of their initial formation. High spatial resolution zircon analysis has conventionally been guided by backscattered electron (BSE) and cathodoluminescence (CL) imaging in a scanning electron microscope. CL reveals internal chemical zoning, xenocrysts, overgrowths, inclusions and metamictisation while BSE imaging highlights fractures. Fractures are generally avoided in subsequent analysis as they may contain contamination or may have lost or gained key elements, which would result in data giving meaningless geological interpretations. While BSE and CL can show brittle deformation (fracturing) of the crystal lattice, they do not show plastic lattice distortion.

The technique required to reveal lattice distortion is electron backscatter diffraction (EBSD) (Prior et al., 1999; Prior et al., 2009). EBSD mapping is conducted inside a scanning electron microscope. The electron beam rasters across the sample surface and at each point a Kikuchi (diffraction) pattern is obtained. EBSD software automatically indexes prominent lattice planes from the diffraction pattern, which are controlled by the crystal lattice orientation (Prior et al., 1999). If there is variation in the crystallographic orientation

across a crystal (lattice distortion), this will be shown by an EBSD map. Reddy et al. (2006) first showed that lattice distortion, in the form of low-angle boundaries from the plastic deformation of zircon, acted as enhanced diffusion pathways for trace elements. CL imaging of a single zircon megacryst from an Indian Ocean gabbro revealed narrow lines of reduced CL emittance, corresponding with the low-angle boundaries revealed by EBSD. Ion microprobe analysis of REEs indicated that in the part of the megacryst that had been plastically deformed, REE abundance had been modified from that in the undeformed part; REE patterns showed a relative enrichment in middle REEs and depletion in heavy REEs. Timms et al. (2006b) investigated the effects of lattice distortion formed by plastic deformation on the U-Th-Pb system in a zircon megacryst from the Lewisian Gneiss Complex (LGC) of Northwest Scotland (the same host rocks as the zircon population in this study). They found that, as with REEs, low-angle boundaries within the zircon megacryst acted as enhanced diffusion pathways for U and Th; the highest measured concentrations and Th/U ratios were found to be in these microstructures. $^{207}Pb/^{206}Pb$ ages were uniform across the megacryst, which led the authors to infer that plastic deformation had occurred shortly after crystallisation. Timms et al. (2011) examined another zircon megacryst, this time from a Siberian xenolith. As with the zircons from the LGC and Indian Ocean, this megacryst contained subgrains separated by low-angle boundaries. They determined that Ti is also affected by lattice distortion, as with REE and U-Th-Pb in their previous studies. The low-angle boundaries were depleted in Ti relative to the subgrains and this could not be explained by volume diffusion alone – the low-angle boundaries were acting as fast diffusion pathways.

The previous work documented examples of plastic deformation in single zircon megacrysts several millimetres in diameter; in this contribution we investigate the frequency, effects and causes of plastic deformation across a large population of zircons of more normal size (<200µm length) of the type routinely used for U-Pb dating and other

geochemical analyses. Our multigrain study comprises fifty-five zircons located on thin sections and rock chips and forty-four mechanically separated grain-mounted zircons, all of which we have analysed by EBSD; a subset of zircons with and without lattice distortion were analysed by ion microprobe for U-Th-Pb, REE and Ti and we document the effect of the lattice distortion on the mobility of these elements and isotopes. These were chosen based on whether they were large enough for subsequent ion microprobe analysis to measure the effects of lattice distortion. Our aim is to understand the frequency, effects and causes of lattice distortion in a zircon population, in the context of the tectonothermal evolution of the LGC. We highlight the advantages of conducting EBSD analysis prior to ion microprobe analysis – it allows the identification of zircons with lattice distortion, which may yield different trace element and isotope data to undeformed zircons and therefore record different aspects of the formation and tectonothermal evolution of their host rocks.

Geological Setting

Rocks from the Lewisian Gneiss Complex (LGC) of northwest Scotland were chosen for this study. The LGC crops out along the coastal strip of the northwest mainland as well as most of the Outer Hebrides (Fig. 5.1a). The LGC is composed dominantly of tonalite-trondhjemite-granodiorite (TTG) gneisses with subordinate mafic and metasedimentary units, cross-cut by the mafic Scourie Dyke Swarm and minor granite and pegmatite sheets (e.g. Peach et al., 1907; Tarney and Weaver, 1987). Sutton and Watson (1951) distinguished two tectonothermal events, one before and one after intrusion of the Scourie Dykes; the later of these two events, the Laxfordian, comprised static and dynamic amphibolite-facies retrogression and heterogeneous deformation across the LGC. Sutton and Watson named the pre-Scourie dyke event the 'Scourian' but it has since been subdivided into the Badcallian (Park, 1970) and the Inverian (Evans, 1965). Both the Badcallian and Inverian are heterogeneously overprinted by the Laxfordian and are only preserved in certain areas of

the complex, most notably the 'Central Region' of Sutton and Watson (1951), the area around Scourie (Fig. 5.1b). Field mapping and petrography showed that the Inverian assemblage is also amphibolite-facies, whilst the earlier Badcallian is granulite-facies.

U-Pb dating of zircon has been widely applied to the LGC. Different workers have recorded a range of ages from different parts of the LGC (e.g. Corfu et al., 1994; Corfu et al., 1998; Whitehouse and Bridgwater, 2001; Kelly et al., 2008; Whitehouse and Kemp, 2010) but it has proved difficult to match zircon ages confidently to the field geology. It has also been suggested that the LGC is composed of discrete terranes based on U-Pb zircon ages (Friend and Kinny, 1995; Kinny and Friend, 1997; Friend and Kinny, 2001; Love et al., 2004; Kinny et al., 2005; Love et al., 2010) but the complex age patterns are difficult to interpret and there remains the problem of linking zircon data to field relationships. Due to the only very recent deployment of the EBSD technique on zircon, it is possible that lattice distortion may have played a role in these complex age patterns and may yield further information not stored in undistorted zircons.

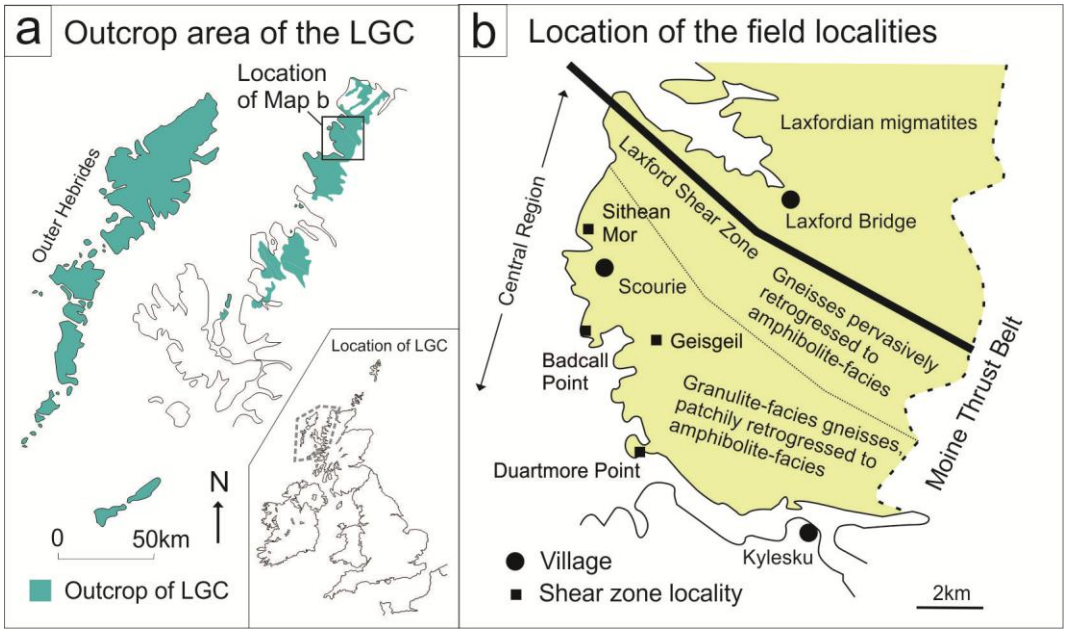

Fig. 5.1 Location maps: **a**: Outline map of NW Scotland, shaded areas denote LGC outcrop and dotted box denotes location of map b; location within British Isles in inset; **b**: Map of Scourie area showing the location and geological context of the field localities.

Methodology

Detailed field maps of localities in the LGC were made to provide a field context of deformation conditions at the whole-rock scale and a framework for sampling. Thin sections and rock chips (~3mm thickness) were cut from samples so that there was a petrographic context for any distorted zircons which could allow speculation as to the cause of lattice distortion. Thin sections and rock chips were polished to 0.25µm grade using progressively finer diamond paste and finally colloidal silica solution. For SIMS analysis, the thin sections were cut up and the relevant parts were mounted onto a one inch glass round with epoxy resin suitable for the ion microprobe sample holder. Zircons were also mechanically separated (see chapter 3 for further details) from the same samples to increase the zircon population size.

BSE and CL imaging were carried out in a Philips XL30 SEM at the University of Liverpool. BSE images were taken at 20kV while CL images were taken at 10kV, both at an emission current of ~3nA in the XL30 SEM. EBSD was conducted on a CamScan X500 crystal probe with a thermionic field emission gun, also at the University of Liverpool. Crystallographic orientation data were automatically indexed using the program Flamenco, part of the CHANNEL5 suite from HKL software. Working conditions were: 20kV acceleration voltage, 20µA beam current and 25mm working distance. A raster step size of 0.5-2µm was used; analytical errors on diffraction angles are ~0.5°. EBSD analytical parameters broadly follow that of Mariani et al. (2009) and Bestmann et al. (2006). The Tango module of CHANNEL5 was used to clean up the data by removing misindexed points and interpolating around good data. The datasets were then displayed as maps in Tango. The maps used here are composites of band contrast (the pattern quality of the EBSD data) and texture component (a false-colour map of crystallographic orientation relative to a given point). EBSD maps are interpreted qualitatively, and quantitatively using a Burgers

Vector analysis, to elucidate possible dislocation types responsible for lattice distortion (Wheeler et al., 2009) – this is the first published use of this method on a mineral.

SIMS analysis of zircon was carried out at the NERC Ion Microprobe Facility, University of Edinburgh. Trace elements were measured using a Cameca ims-4f ion microprobe while U-Th-Pb isotopic measurements were made using a Cameca 1270 ion microprobe. Analytical and correction procedures follow those outlined by Kelly and Harley (2005a) and Kelly et al. (2008). Analytical reproducibility of U/Pb ratios during and between analytical periods was calibrated against the 91500 (Wiedenbeck et al., 1995), SL1 (Maas et al., 1992) and Plesovice (Slama et al., 2008) zircon standards. Plesovice was the primary standard and yielded a mean $^{206}Pb/^{238}U$ ratio of 0.05359±0.00023 (MSWD = 2.4; 95% conf.; 340.5±4.8Ma; *n = 62*). U-Pb age plots and calculation were made using the computer program Isoplot 4.11 (Ludwig, 2003). All $^{207}Pb/^{206}Pb$ ages are quoted at 2σ. Analytical reproducibility of trace elements was calibrated against the 91500 zircon standard. For Ti and most REEs (particularly the heavier ones), the average analytical error was <10% (2σ) but for some for the lighter REEs which have lower concentrations, it was higher. Analytical reproducibility against the NIST SRM610 glass standard (Hinton, 1999) was <7% (2σ) for all trace elements analysed.

Results

Twenty-one samples of tonalitic gneisses and three samples of metasemipelites were collected from localities around the village of Scourie (Fig. 5.1b). These samples were chosen as they recorded a range of different tectonothermal histories: some preserved early Badcallian or Inverian assemblages and structures while others were pervasively altered in the Laxfordian. A population of fifty-five in-situ zircons and forty-four grain-mounted zircons from the twenty-four samples were analysed by EBSD to test for lattice distortion. Some zircons contained fractures that were visible in BSE while most zircons in

the population exhibited no lattice distortion; examples of zircons with no lattice distortion and zircons with brittle fractures are shown in Fig. 5.2. EBSD analysis showed that five zircons out of the ninety-nine have internal lattice distortions of at least 3°. The five distorted zircons are described below in the context of their host rocks; three of these were analysed by ion microprobe for U-Th-Pb, Ti and REEs (Tables 5.1 & 5.2) and compared against undistorted zircons from the same population. Table 5.3 summarises the results for each distorted zircon.

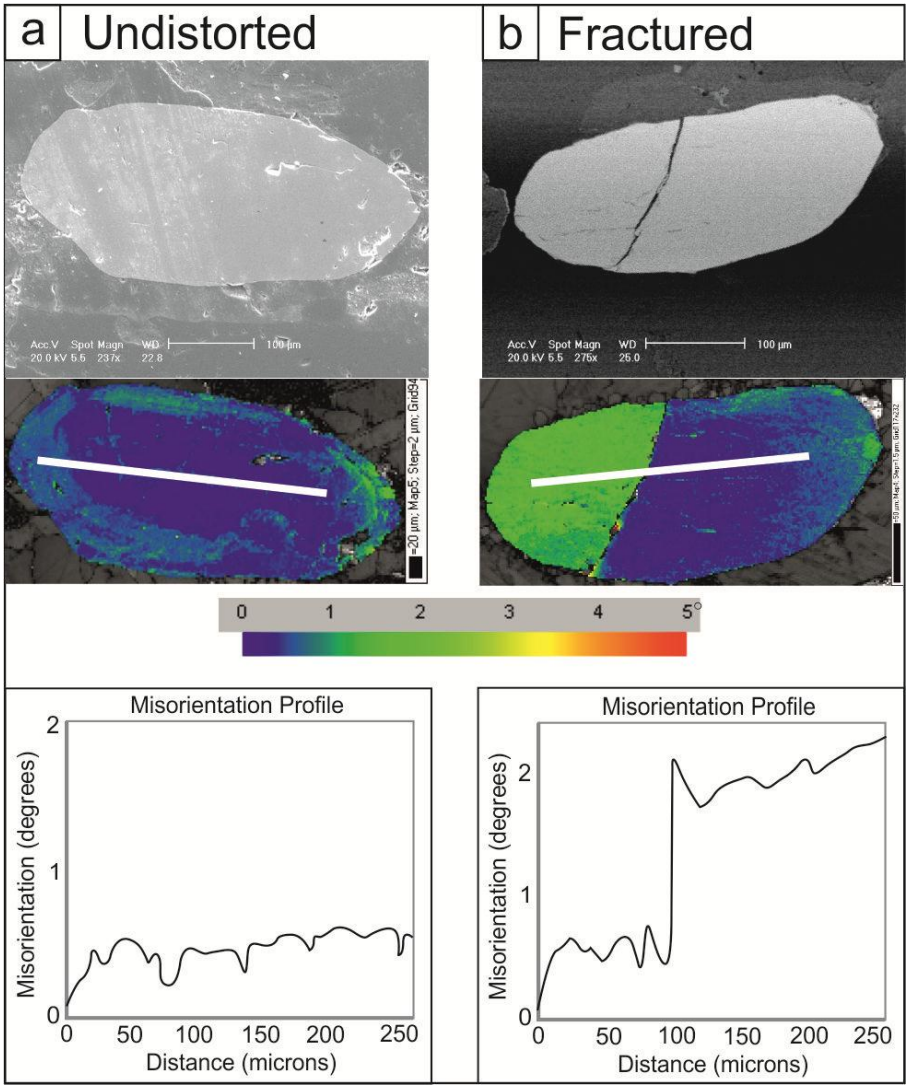

Fig. 5.2 BSE images, lattice misorientation maps and misorientation profiles of examples of zircons without lattice distortion (a) and zircons with fractures (b).

Table 5.1 Ion microprobe U-Th-Pb data for zircons with and without lattice distortion

Spot	U (ppm)	Th (ppm)	Th/U	$^{204}Pb_c$ (ppb)	$^{207}Pb/^{206}Pb$	2σ	$^{206}Pb/^{238}U$	2σ	$^{207}Pb/^{235}U$	2σ	$^{207}Pb/^{206}Pb$ Age	2σ	Disc. (%)
Lattice Distortion													
BP06ChZ3-1	97.1	267.5	2.82	0.3	0.16	0.002	0.46	0.010	10.17	0.237	2453	16	0.26
BP06ChZ3-2	101.6	177.4	1.79	0.3	0.16	0.001	0.48	0.011	10.39	0.259	2437	12	-3.02
BP06ChZ3-3	128.3	400.8	3.20	0.2	0.16	0.001	0.46	0.010	10.05	0.243	2437	14	-0.24
BP06ChZ3-4	114.3	302.7	2.72	0.2	0.16	0.002	0.47	0.010	10.11	0.252	2422	20	-2.10
BP06ChZ3-5	133.5	370.5	2.85	0.2	0.16	0.001	0.46	0.010	10.16	0.225	2440	12	-0.84
DP02Z2-2	86.1	41.3	0.49	0.5	0.15	0.002	0.40	0.010	8.27	0.229	2331	22	6.28
DP02Z7-1	47.1	13.0	0.28	0.7	0.14	0.003	0.38	0.010	7.49	0.263	2266	40	8.49
Undistorted													
BP06ChZ1-2	421.3	294.9	0.72	0.0	0.22	0.001	0.58	0.012	17.41	0.365	2956	8	-0.12
BP06ChZ2-1	72.8	66.1	0.93	0.1	0.22	0.003	0.59	0.014	17.67	0.500	2973	24	0.12
GMBP06Z1-2	20.4	20.2	1.01	0.2	0.18	0.003	0.49	0.016	12.40	0.456	2668	32	2.87
GMBP06Z2-1	24.4	31.3	1.32	0.3	0.17	0.003	0.48	0.013	11.11	0.1360	2526	30	-0.54
GMBP06Z3-1	18.0	12.5	0.71	0.0	0.17	0.004	0.49	0.015	11.70	0.477	2595	42	1.29
GMBP06Z3-2	21.5	12.9	0.61	0.6	0.16	0.003	0.48	0.012	10.69	0.329	2485	30	-1.01
GMBP06Z4-2	19.4	20.2	1.07	0.3	0.18	0.007	0.51	0.015	12.56	0.636	2643	68	-0.34
GMBP06Z4-3	19.8	20.8	1.08	0.3	0.18	0.008	0.51	0.017	12.52	0.684	2650	70	0.53
GMBP06Z6-2	34.0	39.4	1.19	0.1	0.20	0.008	0.53	0.017	14.79	0.756	2848	64	3.86
DP01Z10-2	14.5	5.1	0.36	0.2	0.18	0.008	0.48	0.015	12.21	0.677	2685	74	5.50

(continued)

Table 5.1 (cont) Ion microprobe U-Pb data for zircons with and without lattice distortion

Spot	U (ppm)	Th (ppm)	Th/U	$^{204}Pb_c$ (ppb)	$^{207}Pb/^{206}Pb$	2σ	$^{206}Pb/^{238}U$	2σ	$^{207}Pb/^{235}U$	2σ	$^{207}Pb/^{206}Pb$ Age	2σ	Disc. (%)
DP01Z4-1	15.3	2.2	0.15	0.0	0.17	0.004	0.46	0.013	10.63	0.369	2522	36	2.74
DP01Z4-2	14.0	2.1	0.16	0.2	0.19	0.006	0.51	0.014	13.34	0.541	2725	48	1.82
DP01Z6-1	18.3	11.0	0.62	0.1	0.17	0.003	0.45	0.014	10.61	0.390	2551	30	5.39
DP01Z6-2	17.2	8.8	0.52	0.2	0.17	0.004	0.47	0.014	10.73	0.417	2521	38	1.83
DP01Z6-3	58.0	87.2	1.54	0.0	0.17	0.004	0.46	0.012	10.56	0.359	2521	36	3.21
DP01Z6-4	14.7	9.6	0.67	0.0	0.18	0.005	0.48	0.015	11.73	0.515	2625	50	3.67
DP01Z6-5	18.6	8.9	0.49	0.3	0.17	0.004	0.46	0.014	10.91	0.407	2565	36	4.30
GMDP01Z1-1	36.5	20.8	0.58	0.2	0.17	0.002	0.46	0.011	10.60	0.298	2523	22	3.05
GMDP01Z1-2	27.2	10.4	0.39	0.2	0.16	0.003	0.47	0.012	10.68	0.341	2502	32	0.59
GMDP01Z3-1	15.1	7.1	0.48	0.2	0.19	0.010	0.51	0.020	13.63	0.898	2780	86	4.71
GMDP01Z4-1	14.8	7.8	0.54	0.5	0.16	0.003	0.47	0.015	10.53	0.381	2494	28	1.01
GMDP01Z4-2	12.3	6.0	0.56	0.3	0.16	0.004	0.49	0.017	11.12	0.482	2506	44	-2.41
GMDP01Z6-1	5.4	3.2	0.61	0.8	0.20	0.009	0.52	0.019	14.44	0.822	2849	70	5.83
GMDP01Z6-3	65.7	61.0	0.95	0.1	0.20	0.003	0.55	0.016	15.23	0.475	2836	20	0.58
GMDP01Z7-1	14.7	7.4	0.52	0.3	0.18	0.008	0.49	0.045	12.01	1.237	2624	78	1.71
GMDP01Z8-2	71.0	72.2	1.04	0.2	0.16	0.002	0.45	0.011	10.33	0.281	2505	20	3.55

Table 5.2 Ion microprobe trace element data; element abundances in ppm. REEs are chondrite-normalised against the values of Sun and McDonough (1995). Temperatures are calculated using the Ti-in-zircon geothermometer of Watson et al. (2006).

Spot	La	Ce	Pr	Nd	Sm	Eu	Gd	Tb	Dy	Ho	Er	Tm	Yb	Lu	Yb/Gd	Ti	Temp (°C)
Lattice Distortion																	
BP06ChZ3-1	0.51	84.82	3.65	6.56	16.09	13.42	33	57	102	172	296	448	597	1003	18.3	6.91	709
BP06ChZ3-2	0.55	67.68	2.42	6.26	14.26	9.99	33	58	104	182	316	491	656	1026	20.0	5.72	694
BP06ChZ3-3	0.83	125.39	6.00	13.32	22.66	20.04	34	38	52	73	128	180	233	383	6.8	6.19	700
BP06ChZ3-4	0.61	117.50	6.08	11.13	18.82	18.51	29	44	70	129	223	345	487	804	16.6	10.64	746
BP06ChZ3-5	3.12	116.67	7.82	12.41	19.15	23.16	36	54	81	131	234	335	479	708	13.4	8.10	723
DP02Z2-2	0.81	24.42	2.55	4.03	11.36	11.91	27	34	39	44	60	67	101	137	3.8	20.83	810
DP02Z7-1	0.75	22.10	1.68	3.39	12.57	11.26	35	67	102	166	268	400	494	773	14.1	46.56	897
Undistorted																	
BP06ChZ2-1	0.26	25.21	1.06	2.83	21.87	16.19	92	169	294	476	756	1012	1267	1750	13.7	15.84	793
BP06ChZ2-2	3.20	22.34	1.74	3.08	14.79	15.24	58	109	192	319	531	681	893	1297	15.3	14.53	783
BP06ChZ2-3	0.38	31.64	3.98	12.83	57.67	29.24	160	263	437	677	1040	1338	1684	2406	10.6	18.16	796
BP06ChZ1-2	0.46	46.71	1.57	5.18	20.96	19.17	62	104	180	298	516	814	1178	1977	18.9	14.64	776
GMBP06Z6-2	0.27	34.02	2.36	5.45	19.88	10.68	67	119	186	320	500	636	821	1259	12.3	21.12	811
GMBP06Z3-1	0.29	27.06	0.52	1.65	5.15	4.64	42	67	121	179	295	375	464	740	11.2	15.39	780
GMBP06Z3-3	0.29	26.77	0.52	3.05	8.84	3.43	47	93	138	235	316	476	529	768	11.2	16.38	786
GMBP06Z1-1	0.47	29.77	1.70	4.34	18.42	9.20	58	91	148	235	370	498	690	922	12.0	18.62	799
GMBP06Z1-2	0.33	28.59	1.65	2.79	13.86	8.16	41	62	106	159	262	340	445	621	10.9	17.87	795
GMBP06Z1-3	0.41	23.33	0.60	2.25	8.85	6.16	44	68	132	213	323	453	580	786	13.2	15.66	782
GMBP06Z4-2	0.32	27.08	1.23	3.03	12.24	7.06	38	59	97	151	241	335	442	622	11.5	15.78	783

(continued)

Table 5.2 (cont.) Ion microprobe trace element data; element abundances in ppm. REEs are chondrite-normalised against the values of Sun and McDonough (1995). Temperatures are calculated using the Ti-in-zircon geothermometer of Watson et al. (2006).

Spot	La	Ce	Pr	Nd	Sm	Eu	Gd	Tb	Dy	Ho	Er	Tm	Yb	Lu	Yb/Gd	Ti	Temp (°C)
GMBP06Z4-3	0.31	27.13	1.29	3.79	16.51	11.17	50	82	132	206	331	447	548	818	11.0	13.78	770
BP06ChZ2-9	1.98	69.42	3.62	5.50	19.07	11.54	51	84	143	224	364	543	693	1042	13.6	17.58	793
GMBP06Z2-1	0.28	39.11	1.84	7.05	20.41	13.06	60	97	168	272	386	508	647	1095	10.9	16.72	788
GMBP06Z3-2	0.06	24.41	0.87	1.63	10.50	4.91	36	57	105	156	270	375	393	698	10.9	14.84	777
DP01Z10-1	0.83	32.35	2.10	4.01	15.13	16.79	40	62	97	142	219	280	373	540	9.4	20.28	807
DP01Z10-2	0.38	25.58	1.35	3.44	13.46	9.75	40	60	98	150	221	319	393	565	9.9	19.81	805
DP01Z4-1	0.25	35.50	0.99	2.66	15.05	8.67	55	95	167	257	424	570	725	1074	13.1	17.78	794
DP01Z4-2	0.33	32.36	0.89	2.25	13.18	7.37	49	84	146	232	389	510	626	932	12.9	16.39	786
DP01Z6-1	0.58	29.46	1.80	4.10	16.78	12.57	53	73	118	181	277	365	446	671	8.5	17.14	791
DP01Z6-2	0.35	27.62	1.51	4.11	15.71	12.36	47	74	114	167	262	363	435	648	9.2	15.90	783

Table 5.3 Summary table of data for each zircon with lattice distortion

Zircon	Distortion Pattern	CL	Th/U	$^{207}Pb/^{206}Pb$ Age (Ma)	Ti	REE Pattern
Zircon GG09Z1 from sample JM08/GG09 from Geisgeil	Bending at one corner of the grain	Narrow very bright rim, dark and light zones partially overprinting earlier oscillatory zoning. Two narrow dark lines pass through the area of plastic distortion but do not appear related to the microstructure	-	-	-	-
Zircon ST02Z2 from sample JM09/ST02 from Sithean Mor	Fairly gentle lattice bending across the crystal	Generally quite dark with some irregular lighter patches unrelated to microstructure	-	-	-	-
Zircon BP06ChZ3-1 from sample JM09/BP06 from Badcall Point	Lattice bent in one half of the crystal into a series of subgrains	Generally quite dark with patchy slightly brighter rim, low density of sinuous dark lines	2.8 - much higher than zircons without lattice distortion	2453±16Ma - concordant but slightly younger than youngest ages from zircons without lattice distortion	6.9ppm - well below the main cluster of Ti concentrations	Typical zircon pattern
Zircon BP06ChZ3-2 from sample JM09/BP06 from Badcall Point	Lattice bent in one half of the crystal into a series of subgrains	As BP06ChZ3-1	1.8 - higher than zircons without lattice distortion	2437±12Ma - concordant but slightly younger than youngest ages from zircons without lattice distortion	5.7ppm - well below the main cluster of Ti concentrations	Typical zircon pattern
Zircon BP06ChZ3-3 from sample JM09/BP06 from Badcall Point	Lattice bent in one half of the crystal into a series of subgrains	As BP06ChZ3-1 but with a high density of sinuous black lines	3.2 - about 3x higher than zircons without lattice distortion	2437±14Ma - concordant but slightly younger than youngest ages from zircons without lattice distortion	6.2ppm - well below the main cluster of Ti concentrations	Elevated Pr, depleted in heavy REE (Yb/Gd = 6.8)
Zircon BP06ChZ3-4 from sample JM09/BP06 from Badcall Point	Lattice bent in one half of the crystal into a series of subgrains	As BP06ChZ3-1, this spot covers some of the brighter rim	2.7 - much higher than zircons without lattice distortion	2422±20Ma - concordant but slightly younger than youngest ages from zircons without lattice distortion	10.6ppm - below the main cluster of Ti concentrations	Subdued Eu anomaly, elevated Pr
Zircon BP06ChZ3-5 from sample JM09/BP06 from Badcall Point	Lattice bent in one half of the crystal into a series of subgrains	As BP06ChZ3-1 but with a high density of sinuous black lines	2.8 - much higher than zircons without lattice distortion	2440±12Ma - concordant but slightly younger than youngest ages from zircons without lattice distortion	8.1ppm - well below the main cluster of Ti concentrations	Subdued Eu anomaly, elevated Pr
Zircon DP02Z2 from sample JM09/DP02 from Duartmore Point	Folded pattern across crystal with possibly patchy development of subgrain walls	Medium grey emittance, very bright spot near centre, some irregular dark lines possibly related to microstructure	0.5 - within range of zircons without lattice distortion but below average	2331±22Ma – 6.3% discordance, likely due to Pb-loss during the Laxfordian tectonothermal event, enabled by earlier lattice distortion	20.9ppm - at the higher end of Ti concentrations recorded by undistorted zircons	Subdued Eu anomaly, relatively flat heavy REE pattern (Yb/Gd = 3.8)
Zircon DP02Z7 from sample JM09/DP02 from Duartmore Point	Unusual cross-hatched pattern	Very dark core, very bright rim with dark fracture lines	0.3 - within range of zircons without lattice distortion but well below average	2266±40Ma – 8.5% discordance, likely due to Pb-loss during the Laxfordian tectonothermal event, enabled by earlier lattice distortion	46.6ppm – 25ppm higher than any other recorded Ti concentrations	Subdued Eu anomaly

Distorted Zircons

Zircon GG09Z1 was located on a thin section from sample JM08/GG09, collected at UK Grid Reference NC 17947 41005, ~4.5km southeast of Scourie village (Geisgeil, Fig. 5.1b). At this locality, weakly-banded amphibolite-facies TTG gneiss is cut by a Scourie Dyke, which is in turn cut by a Laxfordian shear zone (Fig. 5.3a). Sample JM08/GG09 is from the pre-dyke banded tonalitic gneiss and is composed of ~40% hornblende aggregates, ~30% plagioclase, ~30% quartz and accessory biotite and opaques; there are no mineral shape fabrics in this rock (Fig. 5.4). It is interpreted to be a Badcallian granulite-facies gneiss that was subsequently pervasively statically retrogressed. Zircon GG09/Z1 (Fig. 5.5a) is a large and unusually squarish-shaped crystal, approximately 200x200µm in size; the lattice distortion is confined to one corner of the crystal, where the lattice gradually bends through 5° out to the tip. The CL pattern for this zircon is irregular – a narrow bright rim partially surrounds a CL-dark zone and fairly uniform lighter zone, which appears to have partially overprinted some earlier oscillatory zoning (Fig. 5.5a). Zircon GG09Z1 was the only zircon found at this locality and so in the absence of undistorted zircons to compare it to, it was not analysed by ion microprobe.

Zircon ST02Z2 was located on a thin section from sample JM09/ST02, collected at UK Grid Reference NC 14970 46124, ~1.5km northwest of Scourie village (Sithean Mor, Fig. 1b). At this locality, an enclave of metasemipelite is surrounded by TTG gneiss; the field relationships suggest the fabric in the metasemipelite may be pre-dyke as the fabric in the surrounding TTG gneiss is cross-cut by a Scourie dyke (Fig. 5.3b). Sample JM09/ST02 is from the metasemipelite and is composed of ~30% plagioclase, ~30% quartz aggregates, ~30% biotite laths and relict garnet porphyroblasts. There is a coarse mineral layering and the quartz aggregates define a shape fabric; biotite laths are not aligned and the garnet porphyroblasts are heavily fractured and retrogressed to biotite around the rims (Fig. 5.4). Zircon ST02Z2 (Fig. 5.5b) is roughly elliptical and approximately 100µm in length along its

long axis; there is lattice misorientation across the crystal of around 3° (Fig. 5.5b). BSE imaging reveals a brittle fracture, which correlates to a certain degree with the microstructure shown in the EBSD map but there is still apparent lattice distortion on either side of this (Fig. 5.5b). The zircon is largely CL-dark with irregular patches of lighter CL response (Fig. 5.5b).

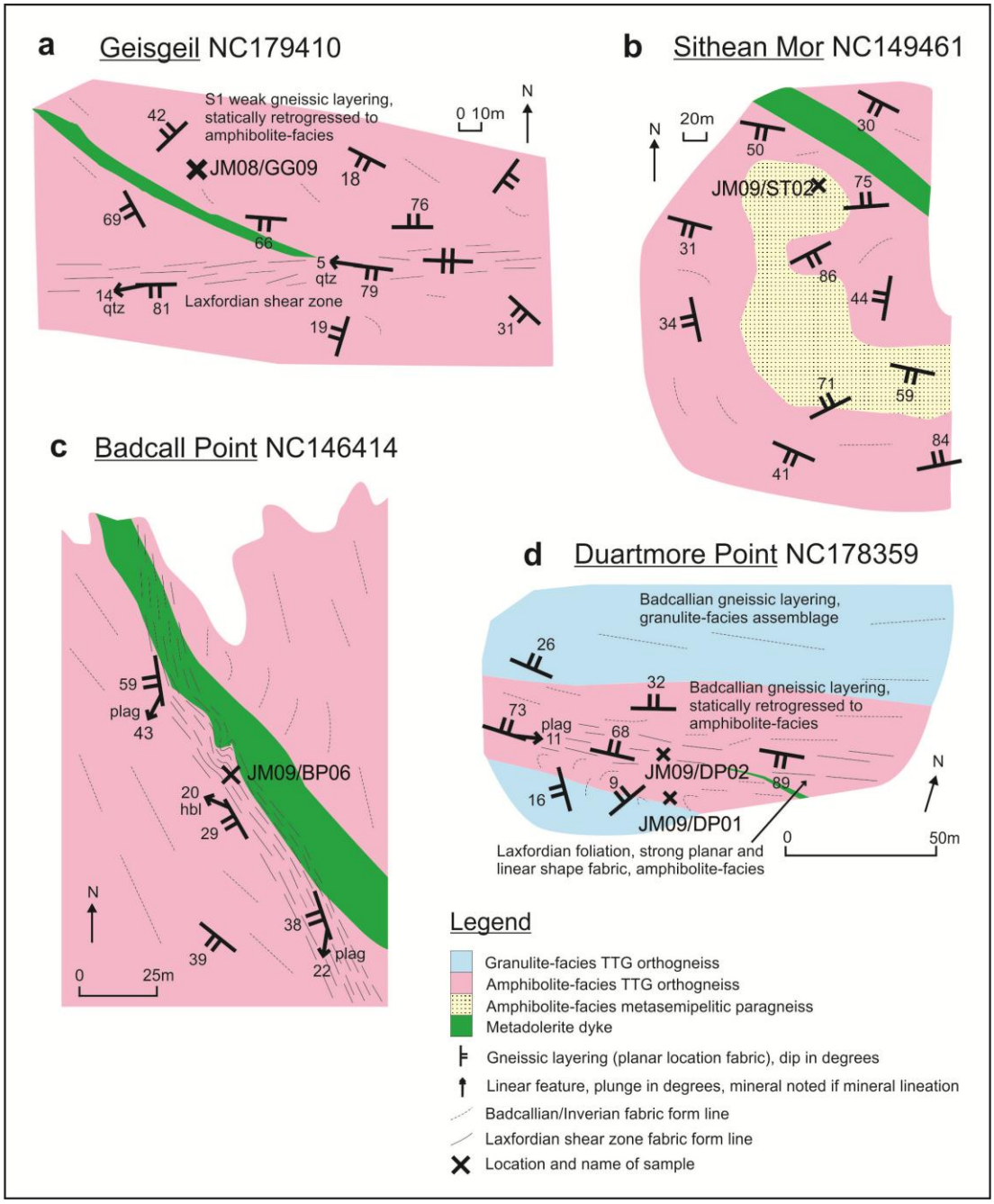

Fig. 5.3 Maps of field areas from which analysed zircons were obtained; **a**: Geisgeil; **b**: Sithean Mor; **c**: Badcall Point; **d**: Duartmore Point; UK grid references given for each locality.

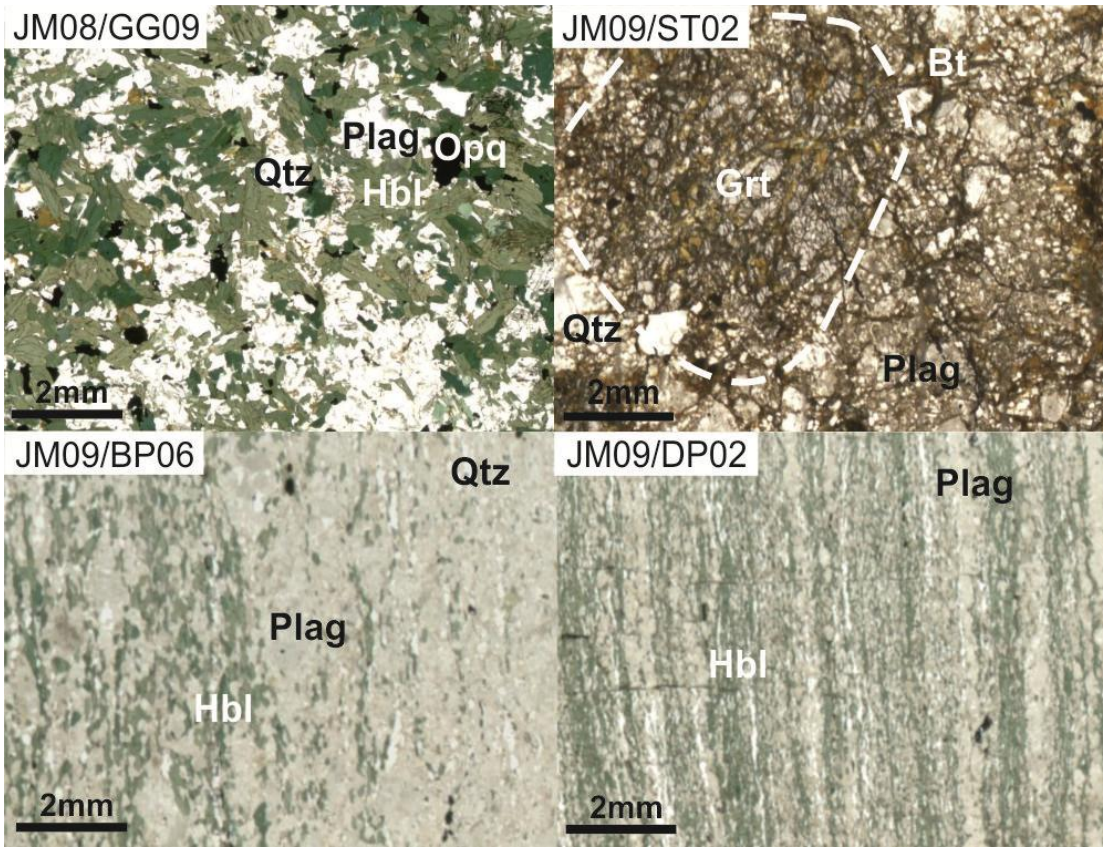

Fig. 5.4 Petrographic context of the distorted zircons: plane polarised light photomicrographs of each sample containing a distorted zircon; Hbl = hornblende, Plag – plagioclase, Qtz = quartz, Grt = garnet, Bt = biotite, Opq = opaque iron oxide.

Zircon BP06ChZ3 was located on a thin section from sample JM09/BP06, collected at UK Grid Reference NC 14565 41561, ~3.5km south-southeast of Scourie village (Badcall Point, Fig. 5.1b). At this locality, an early Badcallian gneissic layering in tonalitic gneiss is cut by a narrow band of possibly Inverian fabric; this is cut by a Laxfordian shear zone, which also cuts a Scourie Dyke (Fig. 5.3c). Sample JM09/BP06 is from the Laxfordian shear zone and is composed of ~75% sericitised plagioclase, ~20% hornblende and ~5% quartz with accessory allanite, titanite, ilmenite and rutile. Sub-millimetre hornblende crystals aggregate to define a moderate mineral aggregate shape fabric (Fig. 5.4). Zircon BP06ChZ3 (Fig. 5.5c) is large and irregularly-shaped, approximately 300x150µm in size; lattice distortion occurs in one half of this elongate crystal, up to 10° from the centre to the tip. The stepped nature of the misorientation profile indicates that this crystal is split into subgrains. BSE imaging shows a small fracture along one edge of the crystal, which is also

picked up by EBSD but is unrelated to the lattice distortion shown by the EBSD (Fig. 5.5c).

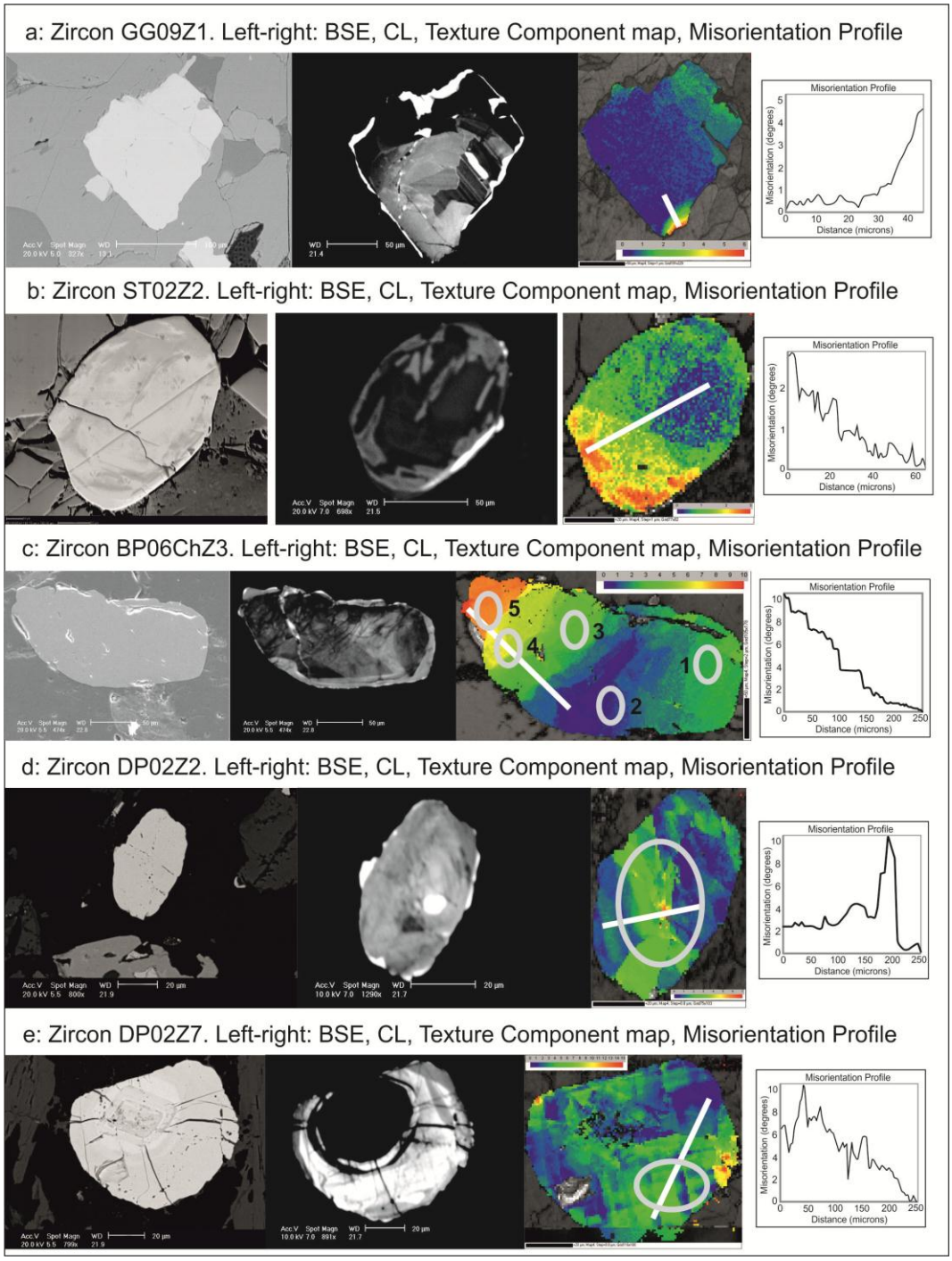

Fig. 5.5 BSE images, CL images, lattice misorientation maps and misorientation profiles of the five zircons with lattice distortion. The lattice misorientation maps were generated using the "Texture Component" function in the "Tango" module of Channel5 software and illustrate crystallographic orientation relative to a given point. The misorientation profiles show this relative change along a transect. The location of the misorientation profiles are shown by the lines on the associated lattice misorientation maps. Ellipses denote ion microprobe analytical spot locations; on zircon BP06ChZ3, numbers denote spot numbers referred to in the text. a GG09Z1; b ST02Z2; c BP06ChZ3; d DP02Z2; e DP02Z7.

The CL pattern is irregular – it is generally CL-dark with a slightly brighter rim (Fig. 5.5c). A brighter linear feature (a fracture) passes through the crystal but appears unrelated to the lattice distortion. There are many sinuous CL-dark lines sub-parallel to the subgrain walls shown by EBSD; these are similar to features noted by Reddy et al. (2006) and Timms et al. (2011), which they interpret to be subgrain walls. Five ion microprobe analytical spots were made on this zircon (see Fig. 5.5c), two of which (4 & 5) were placed on subgrain walls with the other three in different microstructural domains of the crystal; the spot locations were checked after ion microprobe analysis with CL imaging. For the five spots, Th/U ratios range from 1.7-3.1 (Fig. 5.6a) while the $^{207}Pb/^{206}Pb$ ages fall between 2422Ma and 2453Ma (Fig. 5.6b). The five ages are well within error of each other, with discordance of -3.02% to +0.26%. Ti concentrations are between 5.7 and 10.7ppm (Fig. 5.7). Four of the five spots show typical zircon REE patterns (Fig. 5.8); zircons are enriched in heavy REEs relative to light REEs but also have a positive Ce anomaly and a negative Eu anomaly (Kelly and Harley, 2005a; Kelly and Harley, 2005b). However, spot 3 is depleted in heavy REEs with a Lu abundance of only 383ppm; this illustrated by the low Yb/Gd ratio of 6.8 relative to >9 for most undistorted zircons (Table 5.2). Numerous other zircons were found in this sample, including some located within a few millimetres of zircon BP06ChZ3, but all were undistorted.

Zircons DP02Z2 and DP02Z7 were located on a thin section from sample JM09/DP02, collected at UK Grid Reference NC 17923 35972, ~6km west-northwest of Kylesku village (Duartmore Point, Fig. 5.1b). At this locality, a Scourie Dyke cuts across Badcallian granulite-facies tonalitic gneisses but is rotated and sheared by a Laxfordian shear zone (Fig. 5.3d). Sample JM09/DP02 is from the Laxfordian shear zone and is composed of ~60% hornblende aggregates, ~35% sericitised plagioclase and ~5% quartz with accessory rutile, titanite, ilmenite and apatite. Sub-millimetre hornblende crystals aggregate to define strong mineral shape and location fabrics (Fig. 5.4). Only two zircons

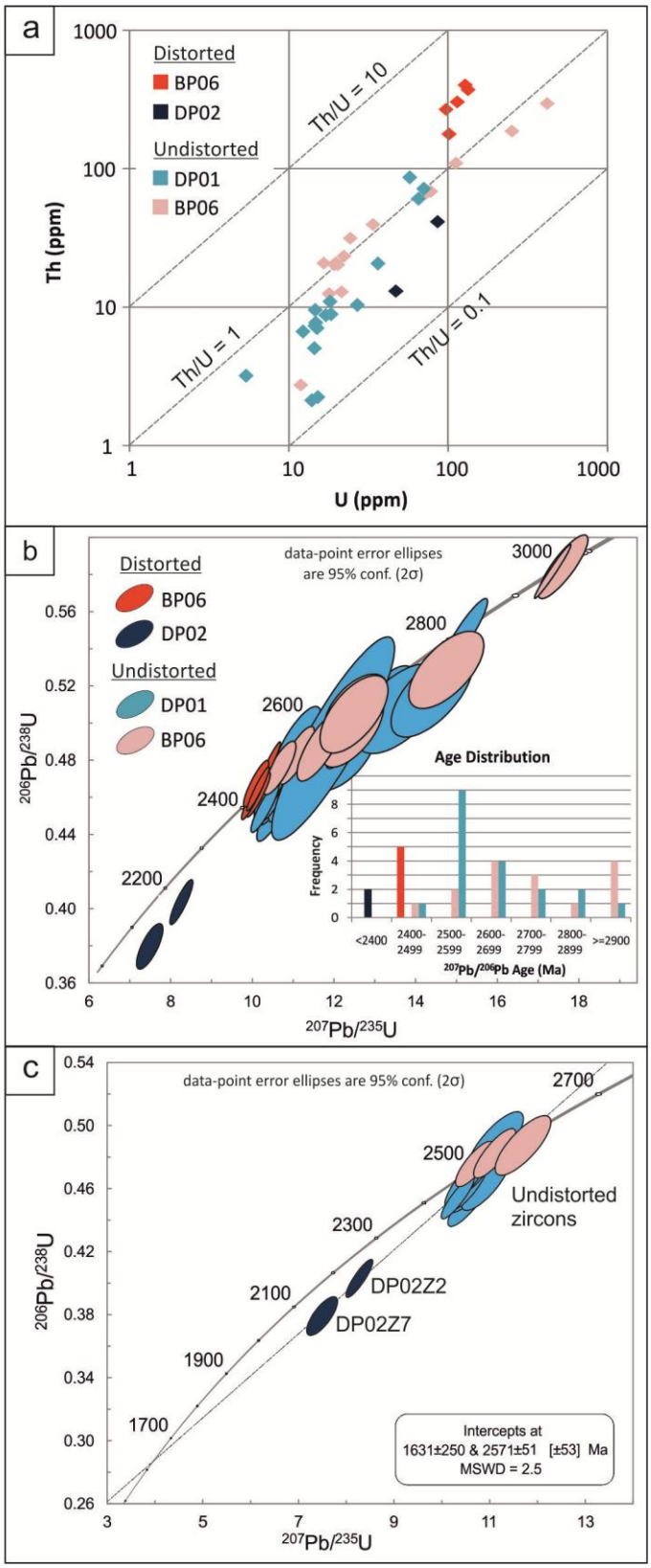

Fig. 5.6 U-Th-Pb data: a Plot showing Th (ppm) against U (ppm) with Th/U ratio contoured of distorted and undistorted zircons; b Wetherill concordia plot showing the age relationship of distorted zircons BP06ChZ3, DP02Z2 and DP02Z7 and undistorted comparison zircons from samples JM09/DP01 and JM09/BP06; c Concordia plot showing a discordia chord through the ellipses for DP02Z2 and DP02Z7 which has a lower intercept within error of the age of the Laxfordian tectonothermal event.

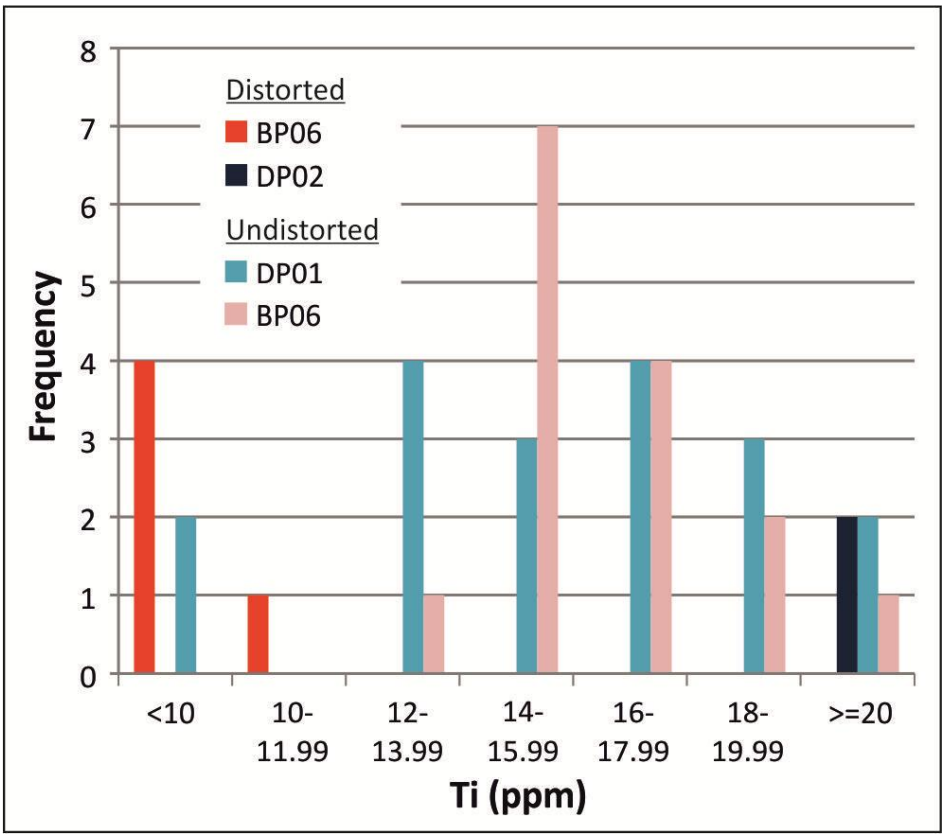

Fig. 5.7 Bar chart showing the concentrations of Ti in zircon in distorted and undistorted zircons.

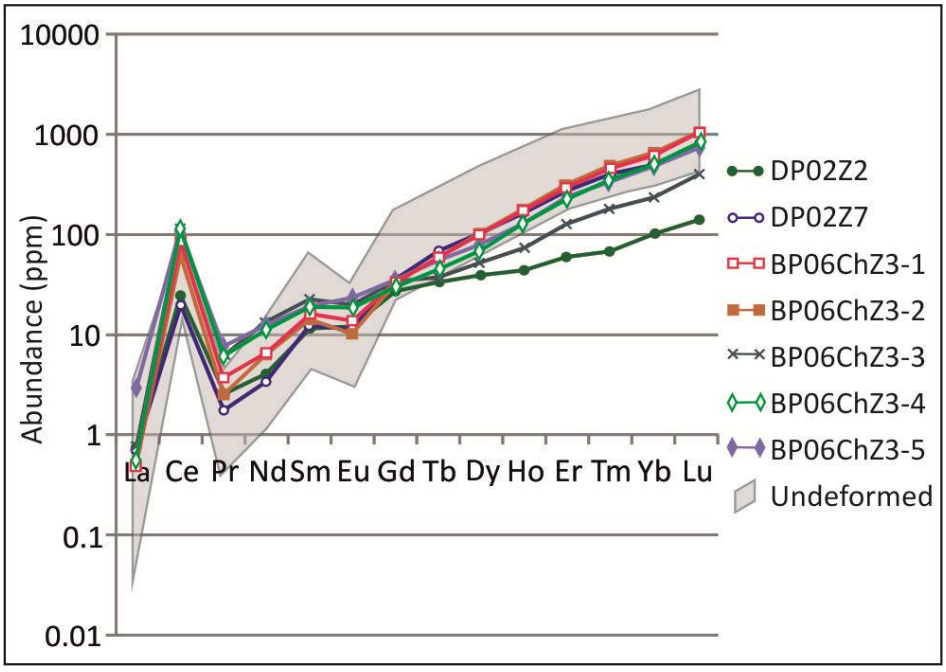

Fig. 5.8 Matsuda diagram showing Rare Earth Element patterns and concentrations. Shaded area denotes analyses of undistorted comparison zircons, solid lines denote distorted zircons. Values are normalised against chondrite (McDonough and Sun, 1995).

were found in this sample big enough for ion microprobe analysis, and both show lattice distortion. Zircon DP02Z2 (Fig. 5.5d) is a small elliptical zircon, approximately 80µm in length along its long axis; there is up to 7° misorientation in a band running diagonally across the crystal with one fairly sharp boundary suggesting a subgrain wall; BSE imaging does not clearly suggest this as a fracture.

Due to the small size of the zircon, it was difficult to get a high-resolution CL image but it shows many sinuous dark lines, as in zircon BP06ChZ3; some of these correlate with lines of dark blebs shown by BSE imaging and with the lattice distortion pattern, and therefore may represent subgrain walls. There is also a bright spot in the centre of the grain, which does not correspond with the microstructure (Fig. 5.5d). Just one ion microprobe analysis was made for this zircon due to its small size. The Th/U ratio is 0.48 (Fig. 5.6a) while the $^{207}Pb/^{206}Pb$ age of 2331±22Ma is discordant by 6.3%, plotting well below concordia (Fig. 5.6b). Ti abundance is 21ppm (Fig. 5.7). Light REEs form a typical zircon pattern but there is no Eu anomaly (concentration of Eu is higher than Sm). The heavy REEs show a flatter profile relative to undistorted zircons (Fig. 5.8), illustrated by a very low Yb/Gd ratio of 3.8; the concentration of Lu is only 137ppm.

Zircon DP02Z7 (Fig. 5.5e) is a squat, slightly elliptical crystal, approximately 100x80µm in size; there is up to 15° variation in lattice orientation across the crystal, with the most extreme deformation occurring in opposite corners. The EBSD analysis also highlights an unusual cross-hatched pattern in lattice orientation in one part of the crystal, with misorientation of up to 7° here (Fig. 5.5e). BSE imaging shows the core of the grain to have some concentric zoning with fractures emanating from this (Fig. 5.5e). CL imaging shows the core to be very CL-dark which suggests high U content; the rim, including area of cross-hatched lattice distortion, is CL-bright (Fig. 5.5e). High U concentrations can induce metamictisation, which causes volume increase resulting in a radial fracture pattern (Corfu

et al., 2003). While the rim has clearly formed before the metamictisation, it is difficult to say whether the cross-hatched lattice distortion occurred before the metamictisation or is related to it. Just one ion microprobe analysis was made for this zircon due to its small size; the spot was placed in an unfractured part of the CL-bright rim showing cross-hatched lattice distortion. The Th/U ratio is 0.28 (Fig. 5.6a) while the $^{207}Pb/^{206}Pb$ age of 2266±40Ma is discordant by 8.5%, plotting well below concordia (Fig. 5.6b). Ti concentration is 46ppm (Fig. 5.7). The REE pattern is typical of that expected for zircon (Kelly and Harley, 2005a) (Fig. 5.8).

Undistorted Zircons

Ion microprobe U-Th-Pb, Ti and REE data from three of the five distorted zircons were compared to undistorted zircons to illustrate the effects of lattice distortion on trace element mobility and isotope systematics, and the geological conclusions drawn from them. The samples to which the distorted zircons were compared, and the reasons why, are given in Table 5.4. Undistorted zircons from sample JM09/BP06 displayed a range of CL patterns comprising dark cores, oscillatory zoning patterns, bright overgrowths and various other patterns. Th/U ratios ranged from 0.2-1.3 (Fig. 5.6a) while $^{207}Pb/^{206}Pb$ ages ranged from 2485±30Ma to 2973±24Ma (Fig. 5.6b); discordance ranged from -1% to +5% (Table 5.1). Ti concentrations were 13-21ppm (Fig. 5.7). The REE patterns are typical of that expected for zircon (Kelly and Harley, 2005a) (Fig. 5.8).

Only two zircons were located and analysed from sample JM09/DP02 and these both had distorted lattices. In order to investigate the effects of lattice distortion on their trace elements and isotopes, undistorted zircons from sample JM09/DP01 were used. This sample was located ~1m away from JM09/DP02 in the marginal part of the shear zone. Sample JM09/DP01 is composed of ~40% quartz, ~40% plagioclase and ~20% sieve-textured hornblende and quartz, after pyroxene, with accessory rutile, allanite, magnetite and

apatite. There is no mineral stretching lineation, only weak gneissic layering and the sample is therefore much less intensely deformed than sample JM09/DP02. Undistorted zircons from sample JM09/DP01 displayed a range of CL patterns comprising dark cores, oscillatory zoning patterns, bright overgrowths and various other patterns. Th/U ratios ranged from 0.1-1.5 (Fig. 5.6a) while $^{207}Pb/^{206}Pb$ ages ranged from 2494±28Ma to 2849±70Ma (Fig. 5.6b); discordance ranged from -2% to +6% (Table 5.1). Ti concentrations were 8-20ppm (Fig. 5.7). The REE patterns are typical of that expected for zircon (Kelly and Harley, 2005a) (Fig. 5.8).

Discussion

Comparison of Distorted and Undistorted Zircons

U-Th-Pb

As U-Pb zircon dating is a widely used technique, it is important to understand the effects of lattice distortion on U-Th-Pb systematics. Th/U ratios of 1.7-3.1 in zircon BP06ChZ3 were up to three times higher than those of the undistorted comparison zircons from the same sample (generally in the range of 0.7-1.2) (Fig. 5.6a). The bulk U and Th contents in this zircon were among the highest in the whole population but this is not interpreted to be related to lattice distortion – an undistorted zircon located ~8mm away also has high Th and U and this is interpreted to be a due to local Th and U availability during growth or metamorphic recrystallization. Zircons DP02Z2 and DP02Z7 had Th/U ratios of 0.28 and 0.48, respectively, which fall within the range of the comparison zircons from sample JM09/DP01 (0.15-1.54) but are lower than the average of 0.63 (Fig. 5.6a).

The $^{207}Pb/^{206}Pb$ ages calculated from distorted zircons are younger than ages from undistorted zircons (Fig. 5.6b). The five ages from zircon BP06ChZ3 are discordant by +0.5% to -3%. Timms et al. (2006b) noted that reverse discordance may be explained by U loss through open-system behaviour during bending of the lattice. In this study, however, the discordance is within error of concordia at 2σ confidence levels. The five ages from this

zircon are slightly younger than previously published ages of ~2490Ma for a tectonothermal event in the Central Region/Assynt Terrane (Corfu et al., 1994; Friend and Kinny, 1995). A small amount of Pb-loss from the lattice during plastic deformation would give an age slightly younger than crystallisation, suggesting plastic deformation occurred at ~2490Ma.

	Sample from which undistorted comparison zircons were obtained			
Distorted Zircon	For U-Pb dating	For Th/U	For REEs	For Ti
BP06ChZ3	**JM09/BP06** – same sample, and **JM09/DP01** – records same age spectrum as **JM09/BP06**	**JM09/BP06** – same sample	**JM09/BP06** – same sample, and **JM09/DP01** – records same compositional range as **JM09/BP06**	**JM09/BP06** – same sample
DP02Z2	**JM09/BP06** – also a Laxfordian shear zone, located 6km away, interpreted to have underwent same tectonothermal history as **JM09/DP02**, and **JM09/DP01** – records same age spectrum as **JM09/BP06**	**JM09/DP01** – located only one metre from **JM09/DP02**. While the host rock is heterogeneous in composition, these zircons are the closest geographically and are interpreted to offer the best comparison of trace element chemistry	**JM09/DP01** – located only one metre from **JM09/DP02**. While the host rock is heterogeneous in composition, these zircons are the closest geographically and are interpreted to offer the best comparison of trace element chemistry, and **JM09/BP06** – records same compositional range as **JM09/DP01**	**JM09/DP01** – located only one metre from **JM09/DP02**. While the host rock is heterogeneous in composition, these zircons are the closest geographically and are interpreted to offer the best comparison of trace element chemistry
DP02Z7	**JM09/BP06** – also a Laxfordian shear zone, located 6km away, interpreted to have underwent same tectonothermal history as **JM09/DP02**, and **JM09/DP01** – records same age spectrum as **JM09/BP06**	**JM09/DP01** – located only one metre from **JM09/DP02**. While the host rock is heterogeneous in composition, these zircons are the closest geographically and are interpreted to offer the best comparison of trace element chemistry	**JM09/DP01** – located only one metre from **JM09/DP02**. While the host rock is heterogeneous in composition, these zircons are the closest geographically and are interpreted to offer the best comparison of trace element chemistry, and **JM09/BP06** – records same compositional range as **JM09/DP01**	**JM09/DP01** – located only one metre from **JM09/DP02**. While the host rock is heterogeneous in composition, these zircons are the closest geographically and are interpreted to offer the best comparison of trace element chemistry

Table 5.4 Samples from which undistorted zircons have been used for comparison with distorted zircons and the justification for sample choice.

Zircons DP02Z2 and DP02Z7 give ages that are younger than all the other analysed zircons in this study, with or without lattice distortion. They are more discordant than any other zircon analyses and plot well below concordia (Fig. 5.6b). CL images of these two zircons do not show any young overgrowths (Fig. 5.5) which the ion microprobe spots could have sampled. Their discordant position on the concordia plot (Fig. 5.6b) is therefore interpreted to be due to Pb-loss. The position and spatial relationship of the ellipses for DP02Z2 and DP02Z7 on a concordia plot line up on a discordia chord with an upper intercept through a cluster of concordant (+5% to -1%) ages of ~2500Ma from undistorted zircons from samples JM09/DP01 and JM09/BP06. This discordia has an upper intercept at 2571±51Ma and a lower intercept at 1631±250Ma with a MSWD of 2.5 at 2σ confidence levels (Fig. 5.6c). The age cluster at ~2500Ma is interpreted to be the age of a tectonothermal event – it is the youngest concordant zircon age recorded in the whole dataset and is also close to the ~2490Ma tectonothermal event (the Inverian of Corfu et al. (1994) and the Badcallian of Kinny et al. (2005)). Although the lower intercept has a large error, it is within error of published ages for the lower amphibolite-facies Laxfordian tectonothermal event. Kinny and Friend (1997) and Corfu et al. (1994) give $^{207}Pb/^{206}Pb$ ages of 1750-1670Ma from rutile and titanite for the Laxfordian. Therefore, these two zircons appear to be recording the Laxfordian event in their U-Pb systematics. An increase in temperature in the Laxfordian may have allowed volume diffusion of Pb out of the zircon and the inherent lattice distortions will have helped this. Laxfordian ages are not recorded in any undistorted zircons in this study or in previous studies which suggests that lattice distortion allows Pb diffusion at lower temperatures than in undistorted zircon, effectively locally lowering the closure temperature.

Ti Thermometry

Ti content in zircon is proportional to the crystallisation temperature – this forms the basis of the Ti-in-zircon geothermometer derived by Watson et al. (2006). The accuracy of the temperatures calculated with the Ti-in-zircon thermometer is controlled by a_{TiO2} – excess rutile in the rock indicates that the $a_{TiO2} = 1$ and Ti content in zircon was buffered. In this case, the calculated temperatures will be accurate. If there is no rutile present during zircon crystallisation, the system is not buffered and the calculated temperature will be a minimum. Quartz and accessory rutile is present in samples BP06, DP02 and DP01 so all zircon temperatures calculated in this study are interpreted to be accurate.

Zircon DP02Z2 yields a crystallisation temperature of 810°C; this is slightly higher than the highest of the temperatures recorded in undistorted zircons from sample JM09/DP01 but is not strikingly different so lattice distortion is interpreted not to have had any extreme or obvious effects on this particular crystal. In zircon DP02Z7, however, the temperature recorded is 897°C, at least 85° higher than the other analysed zircons. The Ti-in-zircon thermometer gives accurate crystallisation temperatures only when buffered by rutile. If rutile is not present and the TiO_2 activity is unconstrained, minimum temperatures will be calculated. The high temperature recorded by zircon DP02Z7 could reflect local Ti buffering with the other zircons only recording minimum temperatures. The temperature recorded by zircon DP02Z7 is in the range of that calculated by Johnson and White (2011) of 875-975°C from major phase equilibrium modelling in mafic gneisses approximately 10km away from our sample JM09/DP02. However, zircon DP02Z2, located ~8mm from DP02Z7 records a temperature 87° lower; this hypothesis would therefore require a considerable variation over that short distance in Ti availability which seems unlikely. Furthermore, accessory rutile is present in samples JM09/DP01 and JM09/DP02 so the thermometer temperatures are interpreted to be accurate.

A more likely explanation is that Ti has moved into the zircon lattice from the matrix along lattice dislocations, perhaps during a thermal event. Impurities in the lattice of a material migrate into lattice dislocations to reduce the stress field around the dislocation (Cottrell and Bilby, 1949) and were found to occur in olivine by Ando et al. (2001) but this concept applies to intracrystal movement. It may be that the grain boundary network was relatively enriched in Ti, perhaps by the breakdown of an adjacent Ti-bearing phase and subgrain walls in the distorted lattice were connected to the grain boundary network. Given that Ti abundance appears to be affected by the presence of lattice dislocations in other zircons, including BP06ChZ3 in this study and the zircon megacryst investigated by Timms et al. (2011), this latter explanation would seem more appropriate.

REEs

The zircons with no lattice distortion from samples JM09/BP06 and JM09/DP01 show a typical chondrite-normalised zircon REE pattern of increasing abundance from light to heavy REE, with positive Ce anomaly and negative Eu anomaly (Kelly and Harley, 2005a). Abundances of the different REEs normally vary by less than half an order of magnitude between analytical spots. The data from samples JM09/BP06 and JM09/DP01 were therefore pooled for comparison against the zircons with lattice distortion. Zircon BP06ChZ3 follows the normal pattern but with some deviation and heterogeneity within the crystal: spot 3 has a relatively low concentration of heavy REEs and a slightly flatter heavy REE profile (Yb/Gd = 6.83); all 5 spots are slightly enriched in Pr relative to undistorted zircons; and the Eu anomaly is subdued, with spot 5 actually having more Eu than Sm, the previous element.

The REE abundances of zircon DP02Z7 fall within the range of zircons with no lattice distortion and it has a similar REE pattern but with a subdued Eu anomaly – the negative Eu anomaly is not as pronounced as in undistorted zircons (Fig. 5.8). Zircon DP02Z2 also has a

subdued Eu anomaly, with more Eu than Sm. It is strongly depleted in heavy REEs: the concentration of Lu, the heaviest REE, was only 137ppm compared to >700ppm among most comparison zircons; it has a relatively flat heavy REE pattern, illustrated by a very low Yb/Gd ratio of 3.8. The variations in REE abundances between zircon DP02Z2 and the comparison undistorted zircons shown in Figure 5.8 are much greater than have been documented previously in distorted zircons.

Cherniak et al. (1997) show that heavy REEs diffuse faster than lighter REEs in an undistorted zircon lattice. Diffusion rates would increase with the enhanced volume diffusion pathways created by lattice distortion and result in the flattening of the middle-heavy REE pattern. The driver for this heavy REE loss is unclear. A change in partition coefficient due to changing pressure-temperature conditions is unlikely as zircon DP02Z7, located no more than a centimetre away from zircon DP02Z2, does not have the same REE pattern. Re-equilibration with another REE-sequestering phase during metamorphism is also a possible driver but garnet is the main metamorphic mineral that incorporates heavy REEs (Kelly and Harley, 2005b; Kelly et al., 2006) and garnet has not been documented in the TTG gneisses of the LGC. Fluids circulating through the rock may also have been a driver for heavy REE loss. Pal et al. (2011) showed that heavy REEs are more strongly complexed with fluorine-rich fluids than light REEs.

Nature of the Lattice Distortion

Crystals with lattice distortion may have grown with defects and therefore have had a distorted lattice from the time of their initial formation; alternatively, post-crystallisation plastic deformation may occur when forces applied to a grain cause the crystal lattice to bend and distort through movement of lattice dislocations. Little is known about zircon deformation so we draw upon the general appearance of microstructures in other minerals to aid our interpretation. We also apply a new method of analysing lattice

distortion, which gives some information on the Burgers vectors of the geometrically necessary dislocations responsible for distortion (Wheeler et al., 2009). In brief, the "integration" version of this method gives the *net* Burgers vector of all the dislocations passing through any chosen area on an EBSD map. These dislocations may be uniformly distributed, non-uniformly distributed or form subgrain walls. The Weighted Burgers Vector (WBV) is expressed crystallographically, and is best presented normalised to the area of the loop (Fig. 5.9 and Table 5.5), so it is measured in $(\mu m)^{-2}$ or 10^{12} m^{-2} (we find the former unit more convenient). An example of the meaning of the WBV in Table 5.5 is as follows. Suppose we have a loop of square outline 10 µm x 5 µm, with a WBV of (1, 0, 4) $(\mu m)^{-2}$. This could mean that we have 50 dislocation lines with Burgers vector [100] *and* 200 lines with Burgers vector [001] passing through the square. Or, it could mean we have 50 dislocation lines with Burgers vector [104]. The WBV is an average over the areas of the loop and the types of dislocation threading through that loop – it proves useful, in trigonal, tetragonal and hexagonal phases, for distinguishing Burgers vectors lying in the basal plane from others. In what follows we focus on the *relative* magnitudes of the (symmetrically equivalent) *a* and *b* components, and the *c* component which lies parallel to the 4-fold symmetry axis.

WBV data are overlaid on Texture Component EBSD maps for each of the distorted crystals (Fig. 5.9). Zircons GG09Z1 and BP06ChZ3 both have lattice distortion patterns suggestive of plastic deformation: the WBV shows variable directions probably due to a mix of dislocations with different Burgers vectors, and there are irregularly shaped subgrain walls. The irregular shapes are indistinguishable from subgrain wall morphologies seen in quartz (e.g. Gleason et al., 1993; Stipp and Tullis, 2003; Heilbronner and Tullis, 2006) and olivine (e.g. Drury, 2005). The distortion of one tip of zircon GG09Z1 suggests that particular part of the crystal has been bent, showing that strain uptake in the zircon lattice was heterogeneous in its distribution. In zircon BP06ChZ3, the subgrain structure with parallel

subgrain walls also indicates bending of the lattice in a similar fashion. Zircon ST02Z2 may also have had its lattice bent by plastic deformation. In zircon DP02Z2, there is a crude radial pattern of subgrain walls around a slightly misoriented part. This could be a deformation microstructure influenced by the strength heterogeneity caused by the misoriented part, or it is conceivably caused by growth defects. The cross-hatched misorientation pattern in zircon DP02Z7 is most unusual, with straight parallel subgrain walls, and it is difficult to see how it can be explained by plastic deformation. In addition the WBV measurements are dominated by components lying in the *a* and *b* plane (the basal plane). We speculate that the cross-hatched misorientation pattern in zircon DP02Z7 is a growth microstructure as the the Burgers vectors are anomalous. Boyle et al. (1998) found similar "checkerboard" microstructures in pyrite which they interpreted as being formed by slip parallel to the [100] planes. This suggests that the microstructure in zircon DP02Z7 may alternatively be a deformation microstructure but the origin of the microstructure remains unclear at present.

Heterogeneous Response of Trace Elements and Isotopes to Lattice Distortion

Reddy et al. (2006), Timms et al. (2006b) and Timms et al. (2011) found that, in general, lattice distortion allowed enhanced volume diffusion along fast pathways such as subgrain walls; this generally led to depletion of trace elements in the zircon. In this study, however, we find that lattice distortion causes heterogeneous behaviour within crystals, within samples and between different localities: trace elements and isotopes are depleted in some analyses but enriched in others. Table 5.6 summarises the differences in response. It would appear that zircons where the crystal may have grown with lattice distortion (DP02Z2 and DP02Z7) are more amenable to later Pb-loss while Ti is not easily lost and may even be gained. However, the effect of this form of lattice distortion on REEs is in itself heterogeneous as shown by the differences in pattern and abundance between zircons

DP02Z2 and DP02Z7. This difference may be due to very local conditions, such as other phases and elements available in the grain boundary network. In zircons where the lattice distortion is caused by plastic deformation, Ti is lost more easily and yet Pb is not while there is variation in REEs even within zircon BP06ChZ3. This variability in chemical response to lattice distortion within grains, within samples and between localities emphasises the need to analyse zircon populations with EBSD prior to trace element and isotope analysis.

Zircon	WBV components $(\mu m)^{-2}$		
	a	b	c
DP02Z7	5.82	-1.53	0.73
DP02Z7	0.67	3.06	-0.66
DP02Z7	-1.54	2.29	0.28
DP02Z7	3.69	-1.09	0.05
DP02Z7	-1.95	-1.00	0.44
DP02Z7	3.47	-0.40	-0.64
BP06ChZ3	-0.39	0.08	-0.47
BP06ChZ3	0.90	0.46	-1.58
BP06ChZ3	-0.06	-0.25	-2.65
BP06ChZ3	-0.82	-0.28	0.05
BP06ChZ3	-1.27	-0.29	-2.05
ST02Z2	-0.14	0.04	-0.96
ST02Z2	-0.35	0.30	0.09
ST02Z2	-0.56	0.72	-1.46
ST02Z2	0.30	-0.22	-0.29
DP02Z2	0.59	-0.33	-0.08
DP02Z2	-2.53	1.25	-0.11
DP02Z2	-2.20	1.15	-4.35
DP02Z2	-1.81	1.04	-0.44
DP02Z2	-0.51	-1.30	0.37
GG09Z1	0.03	-0.01	0.13
GG09Z1	-0.09	0.35	0.19
GG09Z1	1.00	0.17	0.77
GG09Z1	0.06	-0.15	-0.22
GG09Z1	-0.20	0.31	-0.18

Table 5.5 Weighted Burgers Vectors (WBV) components.

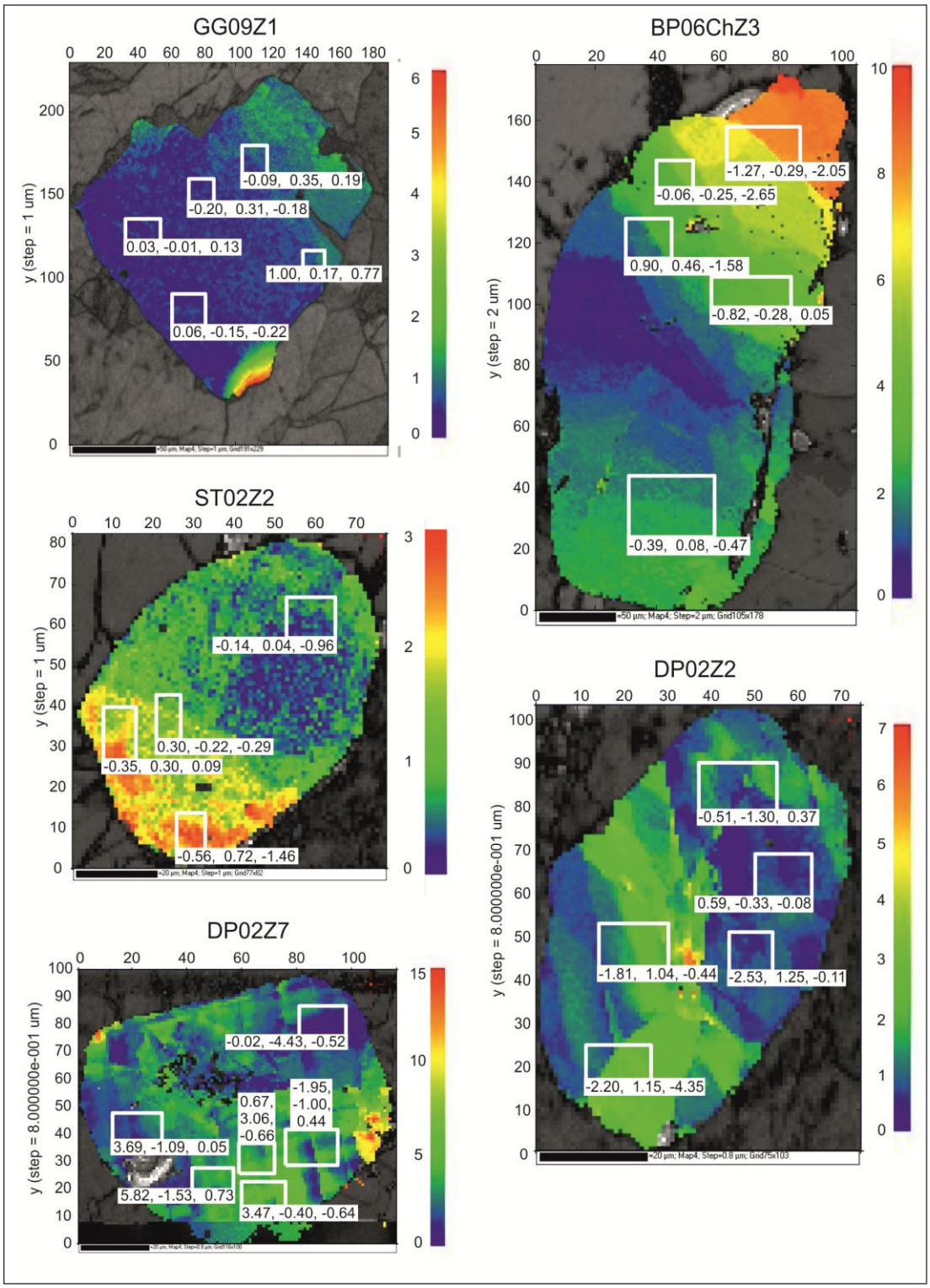

Fig. 5.9 Lattice distortion maps (as in Fig. 5.3) together with the WBV for some example rectangular subareas. The three numbers listed are the *a*, *b* and *c* components of the WBV, measured in $(\mu m)^{-2}$.

Zircons	Distortion	Th/U	$^{207}Pb/^{206}Pb$ Age (Ma)	Ti	REE Pattern
Badcall Point – zircon BP06ChZ3	Plastic Deformation	Relatively high	Concordant but slightly young	Relatively low	Intracrystal heterogeneity in Pr and Eu content and heavy REE pattern and abundance
Duartmore Point – zircons DP02Z2 and DP02Z7	Distortion during crystal growth	Relatively low	Very discordant, young	Variable – average or relatively high	No Eu anomaly, heterogeneity between crystals in heavy REE pattern and abundance

Table 5.6 Summary table of the general and heterogeneous effects of zircon lattice distortion on trace elements and isotopes from Badcall Point and Duartmore Point.

Context of Plastic Deformation

Three of the five distorted zircons were found in samples from Laxfordian shear zones. These are strongly deformed rocks and it would be reasonable to infer that there is a link between deformation at the whole-rock scale and lattice distortion of the zircons. However, the lattice distortion in zircons DP02Z2 and DP02Z7 does not appear to be caused by plastic deformation and is therefore unrelated to the shear zone deformation. Zircon BP06ChZ3 is also from a Laxfordian shear zone and does appear to have been distorted by plastic deformation. However, the link to shearing is not clear as there are plenty of undeformed zircons from the same sample while the other two plastically deformed zircons (GG09Z1 and ST02Z2) are from non-shear zone rocks. There is, therefore, no simple link between macro-scale deformation and intracrystalline zircon distortion.

Conclusions

Analysis of a range of trace elements and isotopes in a population of zircons from the LGC of northwest Scotland has raised the following key points:

1. Five of ninety-nine zircons analysed were found to have distorted lattices, a small but significant proportion, which suggests that lattice distortion of zircon may be more widespread than realised and contests the commonly held assumption that

zircon is mechanically robust.

2. Burgers Vectors analysis suggests that three of the five distorted zircons have undergone post-crystallisation plastic deformation to distort their crystal lattices; the other two have lattice distortion patterns not convincingly explained by plastic deformation and may in fact have grown with distorted lattices.
3. There is heterogeneity in chemical response to lattice distortion within grains, within samples and between localities. Zircon BP06ChZ3 has high Th/U ratios and slightly young ages reflecting minor Pb loss, relative to zircons from the same sample with no lattice distortion. There is intracrystal heterogeneity in Ti content but it is generally relatively low while some analytical spots measure relatively flat chondrite-normalused heavy REE patterns and others no Eu anomaly. Zircons DP02Z2 and DP02Z7 differ from BP06ChZ3 in that Th/U ratios are low and Pb-loss significant. There are differences between zircons DP02Z2 and DP02Z7, however: DP02Z7 has a significantly higher Ti content while DP02Z2 has a relatively flat heavy REE pattern. The flat heavy REE pattern is due to the faster diffusion of the smaller heavy REE ions than their larger light and middle REE neighbours, although the driver for the heavy REE loss is unclear. The variations in REE abundances between zircon DP02Z2 and the comparison undistorted zircons are much greater than have been documented previously in distorted zircons. These heterogeneous effects are summarised in Table 5.3.
4. Discordant $^{207}Pb/^{206}Pb$ ages of 2331±22Ma and 2266±40Ma from two distorted zircons define a discordia lower intercept within error of the previously recorded age of the lower-amphibolite-facies Laxfordian tectonothermal event. Undistorted zircons do not record Laxfordian ages. This suggests that lattice distortion allows Pb diffusion at lower temperatures than in undistorted zircon.

Overall, these findings illustrate the significant and heterogeneous effects of crystal lattice

distortion on trace element mobility and isotope systematics in zircon. It highlights the advantages of conducting EBSD analysis prior to ion microprobe analysis to determine if any zircons in the target population have distorted lattices. Rather than discarding such zircons, they may record information about the thermal evolution of the host rocks not otherwise recorded in undistorted zircons.

Acknowledgements

This work was carried out under UK Natural Environment Research Council DTG NE/G523855/1 and British Geological Survey CASE Studentship 2K08E010 to JMM. Carmel Pinnington and Eddie Dempsey are thanked for assistance with SEM analysis. Ion microprobe analysis at the Edinburgh Ion Microprobe Facility was carried out with funding from NERC grant IMF384/1109; Richard Hinton, Cees-Jan De Hoog and John Craven are thanked for ion microprobe support and Mike Hall for assistance with sample preparation. KMG publishes with the permission of the Executive Director of the Geological Survey.

6. Volume Diffusion of Pb in Zircons from the Lewisian Gneiss Complex, Northwest Scotland

Formatted for submission to *Earth and Planetary Science Letters*

Volume Diffusion of Pb in Zircons from the Lewisian Gneiss Complex, Northwest Scotland

John M. MacDonald[1,*], John Wheeler[1], Kathryn M. Goodenough[2], Quentin Crowley[3], Simon L. Harley[4], Elisabetta Mariani[1], Daniel Tatham[1]

[1] *School of Environmental Sciences, Jane Herdman Laboratories, University of Liverpool, L69 3GP, UK*

[2] *British Geological Survey, Murchison House, West Mains Road, Edinburgh, EH9 3LA, UK*

[3] *School of Natural Sciences, Museum Building, Trinity College Dublin, College Green, Dublin 2, IE*

[4] *School of GeoSciences, Grant Institute, The King's Buildings, West Mains Road, Edinburgh, EH9 3JW, UK*

* Corresponding author at: School of Environmental Sciences, Jane Herdman Laboratories, University of Liverpool, L69 3GP, UK. Tel.: +44 151 794 5201

E-mail address: jmacd@liv.ac.uk (J. M. MacDonald)

Abstract

A population of internally complex zircons from the Lewisian Gneiss Complex (LGC), Northwest Scotland, records a continuous spread of concordant U-Pb ages over a period of ~600myr. We show that this spread of ages has been caused by volume diffusion of radiogenic Pb within and out of the zircon lattice. Eight zircons were found to have a decoupling of chemical zoning pattern and U-Pb ages, which could only be explained by volume diffusion of Pb. This decoupling either took the form of younger cores surrounded by older rims, or single zircon zones recording multiple ages not within uncertainty. Decoupling of age and zoning pattern is only seen in eight grains but may well have

occurred in more as the most concordant data-points in the population (with or without explicit evidence for volume diffusion) define a Pb-loss trajectory on concordia plot. The occurrence of volume diffusion indicates that the host rocks of the LGC were at temperatures of 875-975°C for anything from 3Myr to 500Myr. The widespread occurrence of $^{207}Pb/^{206}Pb$ ages of ~2500Ma in zircon rims in the population suggests this may be a significant age and may be the age around which volume diffusion occurred.

Keywords: volume diffusion, Pb, zircon, Lewisian Gneiss Complex

1. INTRODUCTION

In this study, we illustrate the apparent occurrence of volume diffusion of Pb in zircons from polymetamorphic Archaean-Palaeoproterozoic gneisses of the Lewisian Gneiss Complex (LGC) of Northwest Scotland. Zircon is a key mineral for investigating crustal formation and tectonothermal evolution through its incorporation of geochemical tracers such as the rare earth elements (REEs) and Hf (Kinny et al., 1991; Kinny and Maas, 2003; Whitehouse and Kamber, 2003; Whitehouse and Platt, 2003; Kelly and Harley, 2005a; Gerdes and Zeh, 2009), Ti for geothermometry (Watson et al., 2006), and most notably U for U-Pb isotopic dating (e.g. Davis et al., 2003; Ireland and Williams, 2003; Parrish and Noble, 2003 and references therein). As well as containing these elements, zircon is also able to preserve internal element and isotopic variations through its general physical and chemical durability and its relative insolubility in crustal fluids and melts allowing it to record multiple generations of geochemical information (Cherniak and Watson, 2003).

Radiometric dating using isotopes of U and Pb is probably the most common analysis conducted on zircon. The daughter Pb isotopes have a 2+ valency but sit in a 4+ cation site and have an atomic radius of 1.54Å whereas the U it replaces, and the other tetravalent cations in zircon, have radii nearer 2Å. As a result of this poor fit, Pb will escape from the

lattice if given a chance, for example along fractures or during recrystallisation. This Pb-loss phenomenon results in variable levels of calculated age discordance; in polymetamorphic rocks, such as the Lewisian Gneiss Complex, this can result in a complex U-Pb age spectrum.

1.1. Causes of Pb-loss

Recrystallisation may allow zircon to re-equilibrate with surrounding phases and this open-system process may allow loss of Pb from the zircon lattice. There are three types of recrystallisation: coupled dissolution-reprecipitation; diffusion-driven recrystallisation of radiation-damaged zircon; and solid-state recrystallisation. Coupled dissolution-reprecipitation (Geisler et al., 2007) occurs when a fluid or melt comes into contact with metastable zircon. Zircon will naturally incorporate assorted trace elements but these do not necessarily sit well in the lattice. Radiogenic Pb^{2+} and trivalent REEs sitting in tetravalent sites cause a certain degree of lattice strain. Without interaction with a catalyst such as fluid or melt, the zircon is essentially metastable; but when a fluid or melt is available, the outer parts of the zircon may dissolve and topotactically recrystallize. The recrystallised zircon will often have low REE and U abundances (Geisler et al., 2007). Cathodoluminescence (CL) imaging often reveals irregular inward-penetrating CL-bright zones as pre-existing zircon of certain composition has been preferentially dissolved.

Diffusion-driven recrystallization of radiation-damaged zircon (Geisler et al., 2007) is similar to coupled dissolution-reprecipitation in that it involves metastable zircon lattice moving towards equilibrium on contact with a fluid. Decay of radioactive U and emission of alpha and beta particles causes strain in the crystal lattice, which may become slightly amorphous and effectively metastable. Contact with fluid is the catalyst that allows diffusion of ions to recover the crystallinity of the lattice, although temperature is also an important factor. This process is characterised by irregular curved inward-penetrating zones

visible in CL while pattern quality in Electron Backscatter Diffraction microstructural analysis is poor, reflecting amorphisation of the lattice.

Solid-state recrystallization (Hoskin and Black, 2000) involves internal rearrangement of ions in the crystal lattice, again with the objective of achieving equilibrium. Reaction fronts sweep through the crystal lattice by grain boundary migration or lattice defect diffusion and trace elements are concentrated on these reaction fronts. This mechanism is characterised by CL-bright zones (often rims) transgressing earlier zoning patterns such as oscillatory zoning patterns (OZPs) which are characteristic of magmatic zircon growth. The reaction front itself is seen as a very CL-bright narrow line which reflects the high concentrations of trace elements concentrated on that front.

As well as recrystallisation, Pb can also be lost through distortion of the zircon lattice. Brittle fractures facilitate loss of Pb and other elements from the lattice as they act as fast diffusion pathways (Rimsa et al., 2007). Similarly, plastically deformed zircon lattice has been shown to facilitate fast diffusion of elements (see Chapter 5, Reddy et al., 2006; Timms et al., 2011) and should be tested for with Electron Backscatter Diffraction (EBSD) analysis (Prior et al., 1999).

Metamictisation of zircon promotes easier diffusion of elements (Geisler et al., 2007) but is generally easily visible in CL imaging. Damage accumulates in zircon before complete metamictisation and this is not visible in CL imaging but is unlikely to occur in zircons with less than 700ppm U (Williams, 1992) and can be tested for with EBSD; radiation-damaged zircon will have poor crystallinity and therefore EBSD pattern quality will be low. Similarly, metamictisation is easily recognised by Raman shift in Raman Spectroscopy (Nasdala et al., 2003).

The other possible explanation of Pb-loss in zircon is through volume diffusion of Pb. A range of experimental studies have investigated diffusion of Pb in zircon (e.g. Bogomolov, 1991; Cherniak et al., 1991). Lee et al. (1997) noted an effective closure temperature of

>900°C, broadly in agreement with field-based estimates (e.g. Black et al., 1986; Williams, 1992) while Cherniak and Watson (2001; 2003) noted that closure temperature in crystalline zircon was dependent on a range of factors including temperature, time and distance for ions to diffuse. In their experiments, Cherniak and Watson (2003) analysed the percentage of Pb 'lost' by volume diffusion from crystalline zircons of given radii; they illustrated that as temperature increases, a shorter duration at that temperature is required to instigate volume diffusion, and that the higher the temperature and the longer the duration of time at that temperature, the more Pb is lost (Figure 15, Cherniak and Watson, 2003).

Due to the high closure temperatures determined from the above experimental studies, volume diffusion of Pb in zircon has been regarded as insignificant and unlikely at most crustal conditions in crystalline zircon and may only occur in metamict zircons (e.g. Mezger and Krogstad, 1997; Cherniak and Watson, 2003; Kooijman et al., 2011). However, Ashwal et al. (1999) reported a spread of concordant ages over ~80Myr from a granulite-facies meta-anorthosite from Madagascar and attributed at least some of this age spread to volume diffusion caused by slow cooling at a deep crustal level; this indicates that it can occur at high temperatures for long periods of time, agreeing with the experimentally determined data.

There are, therefore, various explanations for complex age patterns within individual grains. In this paper, we set out criteria for determining if volume diffusion has occurred and illustrate the evidence for volume diffusion of Pb in zircons from the Lewisian Gneiss Complex.

2. GEOLOGICAL SETTING

The Lewisian Gneiss Complex (LGC) of Northwest Scotland (Fig. 6.1a) is composed dominantly of tonalite-trondhjemite-granodiorite (TTG) gneisses with subordinate mafic and metasedimentary units, cross-cut by the mafic Scourie Dyke Swarm (e.g. Sutton and Watson, 1951; Tarney and Weaver, 1987; Goodenough et al., 2010; Wheeler et al., 2010). Three tectonothermal events affected the LGC: the Badcallian event (Park, 1970) was characterised by granulite-facies metamorphism and gneissification of the TTG protoliths; the Inverian event (Evans, 1965) was characterised by regional-scale amphibolite-facies shear zones; and the Laxfordian event (Sutton and Watson, 1951) was characterised by static and dynamic amphibolite-facies metamorphism and heterogeneous deformation across the LGC, either as discrete shear zones several metres wide or as a pervasive composite planar and linear fabric. The Badcallian and Inverian fabrics and assemblages demonstrably pre-date the Scourie Dyke Swarm while the Laxfordian was post-Scourie dyke. Badcallian and Inverian features are best preserved in the Central Region (Sutton and Watson, 1951) (Fig. 6.1b) of the mainland outcrop while the Northern and Southern Regions have been pervasively overprinted in the Laxfordian. U-Pb dating of zircon has allowed precise ages to be attributed to the tectonothermal history of the LGC: protolith crystallisation ~2890-3040Ma (Friend and Kinny, 1995; Whitehouse and Kemp, 2010); Badcallian tectonothermal event ~2710Ma (Corfu et al., 1994); Inverian tectonothermal event ~2490Ma (Corfu et al., 1994).

U-Pb zircon dating, specifically by ion microprobe, has led to the suggestion of an alternative history of the LGC. Analysis of a large population of zircons from across the LGC indicated that different areas had different age spectra (Friend and Kinny, 1995; Kinny and Friend, 1997; Friend and Kinny, 2001; Love et al., 2004; Friend et al., 2007; Love et al., 2010). This was interpreted as meaning that the LGC was composed of disparate terranes (Fig. 6.1c), which possibly accreted in the Inverian event (Goodenough et al., 2010).

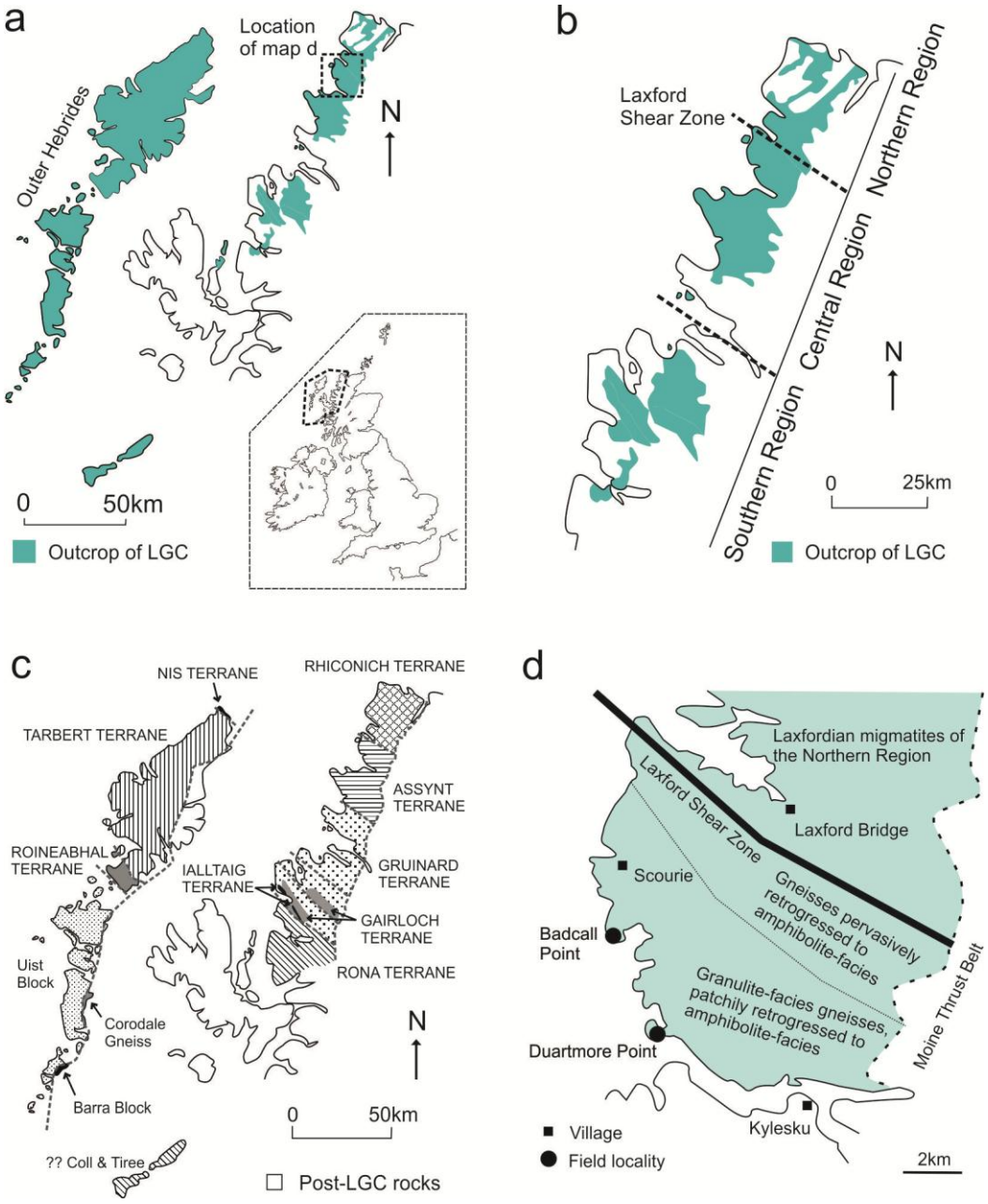

Fig. 6.1 a) Map showing location of the outcrop of the Lewisian Gneiss Complex (LGC) in Northwest Scotland, inset map shows location within British Isles; b) map showing the three-region model of Sutton and Watson (1951) for the mainland LGC; c) map showing the terrane model defined by zircon U-Pb dating, after Kinny et al. (2005); d) map of the northern part of the Assynt Terrane showing the location of the two localities where the samples used in this study were obtained.

It is clear therefore that U-Pb dating of zircons is key to understanding the tectonothermal formation and evolution of Precambrian basement complexes such as the LGC. In this study, we analyse a population of zircons from the Assynt Terrane and to try and further understand the temporal evolution of the LGC. The zircon population was

compiled from seven samples of felsic-intermediate TTG gneisses that reflect the complex tectonothermal history of this part of the LGC. Three samples were taken from Duartmore Point (UK Grid Reference NC 178 359) (Fig. 6.1d): DP01, DP02 and DP03. These reflect Laxfordian shear zone margin, Laxfordian shear zone and pyroxene-bearing Badcallian metamorphic assemblage, respectively. Four samples were taken from Badcall Point (UK Grid Reference NC 146 414) (Fig. 6.1d): BP01 (Inverian), BP02 (statically retrogressed Badcallian), BP04 and BP06 (both Laxfordian shear zone). Detailed field relationships, petrography and geochemistry for all the samples are given in chapter 4 and will not be repeated here.

3. METHODOLOGY

Zircons were located in thin sections of the samples using backscatter electron (BSE) imaging on a Philips XL30 scanning electron microscope (SEM) at the University of Liverpool. To supplement the dataset, the samples were crushed and zircons mechanically and chemically separated using conventional separation procedures. Large crack- and inclusion- free grains were picked from the separated fractions under a reflected light microscope; these were then mounted in an epoxy grain mount and polished to 0.25µm grade with Syton™ colloidal silica.

Zircons were imaged in BSE on the Philips SEM to determine the position of fractures so they could be avoided in subsequent analysis. Electron backscatter diffraction (EBSD) analysis (Prior et al., 1999) was conducted to determine plastic lattice distortion and to test the crystallinity of the zircons as a check for radiation damage. This was done on a Camscan X500 crystal probe SEM with a thermionic field emission gun and data were collected with Flamenco module of HKL CHANNEL5 software and processed in the Tango module. Analytical procedures broadly follow that of Mariani et al. (2009) and Bestmann et al. (2006).

Cathodoluminescence (CL) imaging was conducted in the Philips SEM to show internal chemical zoning within zircon grains. This also acted as a guide for U-Pb dating, which was carried out on a Cameca ims1270 ion microprobe at the NERC Ion Microprobe Facility at the University of Edinburgh; analytical and correction procedures follow those of Kelly et al. (2008). The Plesovice (Slama et al., 2008) zircon standard was used for calibration of U/Pb ratios. During the analytical session, the standard yielded a mean $^{206}Pb/^{238}U$ ratio of 0.05359±0.00023 (MSWD = 2.4; 95% conf.; Fig. 3.1; 340.5±4.8Ma; *n = 62*). Calculation and calibration of ratios and data reduction were conducted using in-house software developed by Richard Hinton at University of Edinburgh. Correction for in-situ common Pb was made using measured ^{204}Pb counts above that of the detector background (typically ~0.2 to 1.5ppb). In the analyses for this project, measured common Pb was generally <5ppb, although occasionally analyses were much higher than this, likely the result of contamination on the sample surface and in exposed cracks.

4. ZIRCON ANALYSIS

The zircons showed a range of CL zoning patterns including cores, oscillatory zoning patterns (indicative of zircon grown in magma (Corfu et al., 2003) and metamorphic rims along with irregular CL patterns not clearly ascribable to any particular formation mechanism. Each of the seven samples displayed a range of CL zoning patterns and no pattern was confined to a particular sample (Table 6.1).

Ion microprobe data (Table 6.1) were filtered to remove analyses that hit fractures, or were from zircons that had been found to have distorted lattices; analyses with >10ppb common ^{204}Pb were also removed as levels higher than this are unlikely to be naturally included in zircon. This resulted in the only two zircons from sample DP02 being analysed. $^{207}Pb/^{206}Pb$ ages range from 2384±46Ma to 3017±56Ma, a span of ~600Myr (Fig. 6.2a); even with conservative discordance limits of ±2% (as Halpin et al., 2012), there is still a ~600Myr

spread of concordant ages (Fig. 6.2b). These minor discordances could easily be caused by volume diffusion (e.g. Mezger and Krogstad, 1997; Kooijman et al., 2011) but the temporal resolution of SIMS analysis and therefore the size of error ellipses on a resulting concordia curve make the data appear relatively concordant, particularly as error ellipses have been plotted at 2σ here.

The dataset of apparent $^{207}Pb/^{206}Pb$ ages was subdivided according to sample to determine if the age spread was due to the temporal evolution in tectonothermal history of the different samples but this failed to show any pattern (Fig. 6.2c). The dataset was also subdivided according to the type of CL zoning pattern at each analytical spot but this too failed to show any age clustering (Fig. 6.2d). If all the ages obtained are real, this implies continuous zircon growth and/or recrystallisation. However, ~600Myr is a very long period for continuous zircon growth to occur; it would require elevated temperatures/pressures and the zircon saturation conditions to be maintained at the right level for continuous growth over this long timescale. Recrystallisation would tend to destroy earlier ages and result in more clustering of zircon ages. All zircons were analysed by EBSD to determine whether there was any plastic lattice distortion present; only three were found to have this and were eliminated from the dataset. The remainder were all found to have good EBSD pattern quality indicating good crystallinity and a lack of lattice radiation damage. U contents of the zircons ranged from tens of parts per million to ~450ppm – well below the 700ppm level suggested by Williams (1992) needed to cause radiation damage of the lattice. Furthermore, no zircons were found to have a mottled CL zoning pattern or radial fractures indicative of metamictisation (Corfu et al., 2003). The elimination of microstructural defects, common Pb contamination, metamictisation and radiation damage in the zircon population leaves volume diffusion of Pb as the only known possible mechanism for Pb-loss and the spread of concordant ages.

Sample/spot	CL Zoning Pattern	U (ppm)	Th (ppm)	Pb (ppm)	Th/U	$^{204}Pb_c$ (ppb)	$^{207}Pb/^{206}Pb$	2σ	$^{207}Pb/^{235}U$	2σ	$^{206}Pb/^{238}U$	2σ	Error Corr.	% Disc.	$^{207}Pb/^{206}Pb$ Age	2σ
Volume diffusion zircons																
GMBP02Z1-1	sp	33.10	82.63	27.88	2.56	4.49	0.188	0.006	13.332	0.587	0.514	0.017	0.732	1.86	2725	48
GMBP02Z1-2	sp	33.55	85.05	31.31	2.60	1.66	0.205	0.005	15.957	0.644	0.564	0.018	0.791	-0.50	2868	40
BP06ChZ2-1	ozp	72.76	66.12	54.21	0.93	2.57	0.219	0.003	17.668	0.500	0.585	0.014	0.850	0.12	2973	24
BP06ChZ2-4	dr	165.93	101.29	101.28	0.63	6.75	0.190	0.003	13.543	0.366	0.518	0.012	0.846	1.79	2739	24
BP06ChZ2-5	ir	35.73	30.51	24.17	0.88	1.61	0.195	0.008	14.633	0.831	0.545	0.020	0.655	-0.82	2782	68
BP06ChZ2-7	ir	29.38	49.56	24.71	1.73	4.38	0.197	0.005	15.864	0.646	0.584	0.018	0.771	-5.76	2802	42
BP06ChZ2-8	ozp	151.28	156.14	110.55	1.06	3.53	0.204	0.002	15.925	0.387	0.566	0.012	0.877	-1.12	2859	18
GMBP06Z4-1	r	32.61	39.32	22.51	1.24	2.37	0.203	0.007	14.444	0.640	0.517	0.014	0.621	5.65	2847	56
GMBP06Z4-2	bc	19.40	20.18	12.59	1.07	1.62	0.179	0.007	12.560	0.636	0.509	0.015	0.573	-0.34	2643	68
GMBP06Z4-3	bc	19.78	20.79	12.78	1.08	1.22	0.180	0.008	12.520	0.684	0.505	0.017	0.624	0.53	2650	70
GMBP06Z4-4	r	22.60	22.98	12.94	1.04	8.06	0.153	0.004	9.690	0.351	0.458	0.011	0.670	-1.96	2384	46
GMDP03Z1-1	br	65.61	52.17	42.71	0.82	2.19	0.188	0.002	13.819	0.379	0.533	0.013	0.881	-1.04	2725	22
GMDP03Z1-2	br	42.13	28.79	26.59	0.70	6.27	0.189	0.003	13.758	0.448	0.528	0.015	0.859	0.00	2733	28
GMDP03Z1-3	ozp	82.66	71.55	47.02	0.89	1.82	0.162	0.001	10.409	0.255	0.466	0.011	0.959	0.29	2475	12
GMDP03Z1-4	br	34.50	24.66	21.87	0.73	1.97	0.194	0.006	14.015	0.578	0.525	0.015	0.700	1.85	2772	48
DP01Z4-1	sp	15.29	2.24	7.41	0.15	0.00	0.166	0.004	10.629	0.369	0.463	0.013	0.788	2.74	2522	36
DP01Z4-2	sp	14.04	2.12	7.69	0.16	0.75	0.188	0.006	13.338	0.541	0.514	0.014	0.664	1.82	2725	48
DP01Z10-1	br	13.87	5.02	7.16	0.37	1.67	0.178	0.007	11.415	0.536	0.465	0.014	0.625	6.53	2634	60
DP01Z10-2	br	14.54	5.07	7.79	0.36	0.79	0.184	0.008	12.208	0.677	0.482	0.015	0.574	5.50	2685	74
DP01Z10-3	br	15.54	6.57	7.58	0.43	4.85	0.158	0.004	9.575	0.368	0.441	0.012	0.725	3.14	2430	44
DP01Z10-4	dc	39.05	35.39	22.26	0.93	5.30	0.182	0.004	11.457	0.439	0.457	0.014	0.803	9.16	2670	38
GMDP01Z2-1	br	15.09	11.70	12.08	0.80	0.00	0.225	0.008	19.960	1.007	0.643	0.023	0.715	-6.12	3017	56
GMDP01Z2-2	dc	89.07	105.38	53.54	1.21	2.28	0.163	0.001	10.372	0.264	0.463	0.011	0.942	1.23	2482	14
GMDP01Z2-4	dc	149.86	173.21	103.04	1.19	2.17	0.192	0.002	13.849	0.360	0.524	0.013	0.952	1.59	2758	12
GMDP01Z2-5	br	21.17	8.45	12.12	0.41	0.26	0.187	0.006	13.130	0.580	0.509	0.016	0.710	2.42	2717	52
GMDP01Z6-1	br	5.41	3.20	3.31	0.61	1.08	0.203	0.009	14.440	0.822	0.516	0.019	0.651	5.83	2849	70
GMDP01Z6-2	br	24.23	19.41	16.76	0.82	1.15	0.200	0.003	15.491	0.506	0.561	0.016	0.882	-1.60	2827	24
GMDP01Z6-3	dc	65.70	61.02	45.59	0.95	2.38	0.201	0.003	15.229	0.475	0.549	0.016	0.916	0.58	2836	20

(continued)

Sample/spot	CL Zoning Pattern	U (ppm)	Th (ppm)	Pb (ppm)	Th/U	204Pbc (ppb)	207Pb/ 206Pb	2σ	207Pb/ 235U	2σ	206Pb/ 238U	2σ	Error Corr.	% Disc.	207Pb/206Pb Age	2σ
Other zircons																
GMBP02Z2-1	ir	51.03	59.13	32.96	1.19	1.06	0.179	0.003	12.224	0.360	0.495	0.012	0.857	1.98	2644	26
GMBP02Z2-2	ir	49.84	61.14	33.11	1.26	1.44	0.182	0.004	12.579	0.441	0.502	0.014	0.805	1.71	2668	34
BP01Z1-1	ir	47.98	26.41	26.43	0.56	2.61	0.169	0.003	11.200	0.331	0.480	0.012	0.854	0.85	2549	26
BP01Z1-2	ir	44.44	23.85	24.32	0.55	1.13	0.172	0.004	11.339	0.369	0.477	0.011	0.731	2.58	2581	36
GMBP01Z2-1	ir	171.81	272.79	113.48	1.63	2.30	0.167	0.002	10.839	0.285	0.471	0.012	0.931	1.49	2526	16
BP06ChZ1-1	br	49.48	38.36	27.89	0.80	2.48	0.170	0.003	10.953	0.333	0.468	0.012	0.810	3.09	2554	30
BP06ChZ1-2	ozp	421.30	294.94	299.81	0.72	0.00	0.217	0.001	17.415	0.365	0.583	0.012	0.977	-0.12	2956	8
BP06Z3-1	ir	88.81	4.38	50.43	0.05	2.22	0.195	0.002	14.604	0.375	0.543	0.013	0.934	-0.31	2786	14
BP06Z3-2	ir	24.46	3.43	15.87	0.14	0.73	0.223	0.008	18.255	0.910	0.594	0.019	0.653	-0.10	3002	60
BP06Z3-3	ir	23.45	9.87	13.17	0.43	5.10	0.179	0.008	12.310	0.631	0.500	0.014	0.542	1.04	2640	70
BP06Z3-4	ir	2.61	0.99	1.39	0.39	0.77	0.169	0.009	11.213	0.796	0.480	0.022	0.637	0.98	2552	90
BP06Z3-5	ir	209.28	8.36	124.24	0.04	2.45	0.208	0.002	16.112	0.398	0.563	0.012	0.886	0.31	2887	18
GMBP06Z1-2	br	20.42	20.19	12.79	1.01	1.00	0.182	0.003	12.399	0.456	0.495	0.016	0.858	2.87	2668	32
GMBP06Z2-1	ir	24.40	31.31	15.62	1.32	1.51	0.167	0.003	11.107	0.360	0.483	0.013	0.820	-0.54	2526	30
GMBP06Z2-2	ozp	30.23	39.97	22.13	1.36	0.12	0.189	0.004	14.106	0.514	0.543	0.015	0.757	-2.38	2729	40
GMBP06Z3-1	br	18.00	12.48	10.42	0.71	0.00	0.174	0.004	11.699	0.477	0.488	0.015	0.778	1.29	2595	42
GMBP06Z3-2	br	21.50	12.85	11.81	0.61	2.73	0.163	0.003	10.688	0.329	0.476	0.012	0.808	-1.01	2485	30
GMBP06Z5-1	br	12.79	7.76	6.94	0.62	2.48	0.170	0.004	10.923	0.467	0.467	0.016	0.785	3.14	2552	44
GMBP06Z5-2	dc	52.42	111.53	41.06	2.18	1.21	0.186	0.006	12.960	0.532	0.506	0.013	0.609	2.29	2703	54
GMBP06Z6-1	ir	37.75	40.14	25.22	1.09	1.49	0.219	0.006	15.330	0.592	0.508	0.015	0.741	10.90	2972	42
GMBP04Z1-1	br	35.34	48.52	24.83	1.41	5.24	0.189	0.006	13.421	0.576	0.515	0.015	0.669	2.08	2734	52
GMBP04Z1-2	br	35.24	49.49	27.80	1.44	4.20	0.213	0.005	16.677	0.565	0.568	0.015	0.776	0.90	2927	34
GMBP04Z2-1	br	23.51	24.05	13.66	1.05	6.27	0.167	0.005	10.594	0.434	0.460	0.012	0.628	3.54	2528	54
GMBP04Z2-2	br	35.08	32.98	20.40	0.96	1.47	0.168	0.003	10.807	0.326	0.468	0.010	0.742	2.33	2533	34

(continued)

Sample/spot	CL Zoning Pattern	U (ppm)	Th (ppm)	Pb (ppm)	Th/U	204Pbc (ppb)	207Pb/ 206Pb	2σ	207Pb/ 235U	2σ	206Pb/ 238U	2σ	Error Corr.	% Disc.	207Pb/206Pb Age	2σ
Other zircons (cont.)																
GMBP04Z3-1	bc	16.46	21.09	10.03	1.31	0.49	0.173	0.007	10.886	0.583	0.457	0.015	0.615	6.02	2583	70
GMBP04Z3-2	bc	21.05	25.57	13.85	1.25	3.94	0.173	0.005	11.932	0.450	0.501	0.013	0.709	-1.41	2583	44
GMBP04Z4-1	br	23.11	29.88	13.83	1.33	0.10	0.168	0.004	10.430	0.364	0.449	0.011	0.702	5.89	2541	42
GMBP04Z4-2	br	21.63	26.78	13.27	1.27	2.43	0.160	0.004	10.352	0.366	0.468	0.011	0.650	-0.66	2459	46
GMBP04Z4-3	dc	127.60	55.92	66.72	0.45	4.59	0.163	0.001	10.516	0.239	0.469	0.010	0.948	0.10	2482	12
GMBP04Z5-1	sp	20.13	24.51	15.47	1.25	1.53	0.201	0.008	15.977	0.997	0.577	0.027	0.738	-3.69	2832	68
GMBP04Z5-2	sp	28.26	24.28	18.60	0.88	1.17	0.190	0.008	13.890	0.750	0.531	0.016	0.572	-0.32	2738	72
GMBP04Z6-1	br	15.38	14.35	9.58	0.96	0.76	0.179	0.007	12.277	0.625	0.499	0.016	0.623	1.24	2640	64
GMBP04Z6-2	ozp	34.99	49.14	28.31	1.44	1.73	0.211	0.009	16.985	0.888	0.584	0.019	0.634	-1.83	2912	64
GMBP04Z7-1	sp	18.32	19.41	10.71	1.09	1.69	0.167	0.004	10.582	0.431	0.459	0.014	0.753	3.61	2528	44
GMBP04Z7-2	sp	12.54	9.88	7.24	0.81	2.17	0.164	0.003	10.849	0.362	0.481	0.012	0.775	-1.45	2494	34
GMBP04Z7-3	sp	16.48	18.01	10.64	1.12	4.32	0.167	0.005	11.649	0.536	0.505	0.018	0.791	-4.19	2530	46
GMBP04Z7-4	sp	30.80	41.16	21.78	1.37	2.11	0.191	0.005	13.705	0.512	0.521	0.014	0.720	1.54	2747	42
GMBP04Z8-2	sp	13.39	8.05	7.78	0.62	2.27	0.206	0.009	13.864	0.861	0.487	0.021	0.680	11.02	2876	74
GMBP04Z8-3	sp	28.76	20.31	16.61	0.72	1.92	0.179	0.006	11.960	0.511	0.484	0.013	0.615	3.94	2647	54
GMBP04Z9-1	sp	21.87	29.00	16.12	1.36	3.31	0.188	0.007	14.128	0.900	0.546	0.028	0.799	-3.33	2720	62
GMBP04Z9-2	sp	30.11	20.81	17.56	0.71	3.67	0.185	0.010	12.413	0.829	0.488	0.018	0.546	4.93	2694	90
GMDP03Z2-1	ozp	33.96	12.58	21.94	0.38	0.93	0.219	0.010	17.060	0.974	0.564	0.019	0.599	3.00	2974	74
DP03Z2-1	sp	439.84	358.71	257.43	0.84	4.50	0.178	0.002	11.763	0.303	0.480	0.011	0.926	4.09	2633	16
DP01Z6-1	br	18.27	11.02	9.64	0.62	0.35	0.169	0.003	10.605	0.390	0.454	0.014	0.866	5.39	2551	30
DP01Z6-2	br	17.20	8.79	9.14	0.52	0.59	0.166	0.004	10.734	0.417	0.468	0.014	0.793	1.83	2521	38
DP01Z6-3	dc	57.95	87.23	36.86	1.54	0.32	0.166	0.004	10.556	0.359	0.460	0.012	0.780	3.21	2521	36
DP01Z6-4	br	14.72	9.57	8.34	0.67	0.00	0.177	0.005	11.725	0.515	0.480	0.015	0.733	3.67	2625	50
DP01Z6-5	br	18.57	8.94	9.75	0.49	1.25	0.171	0.004	10.911	0.407	0.463	0.014	0.797	4.30	2565	36

(continued)

Sample/spot	CL Zoning Pattern	U (ppm)	Th (ppm)	Pb (ppm)	Th/U	204Pbc (ppb)	207Pb/ 206Pb	2σ	207Pb/ 235U	2σ	206Pb/ 238U	2σ	Error Corr.	% Disc.	207Pb/206Pb Age	2σ
Other zircons (cont.)																
GMDP01Z1-1	br	36.48	20.76	19.37	0.58	1.29	0.167	0.002	10.596	0.298	0.461	0.011	0.885	3.05	2523	22
GMDP01Z1-2	br	27.15	10.41	14.10	0.39	1.14	0.164	0.003	10.677	0.341	0.471	0.012	0.800	0.59	2502	32
GMDP01Z3-1	sp	15.12	7.08	8.83	0.48	0.72	0.194	0.010	13.629	0.898	0.508	0.020	0.594	4.71	2780	86
GMDP01Z4-1	sp	14.84	7.77	7.87	0.54	1.52	0.164	0.003	10.532	0.381	0.467	0.015	0.876	1.01	2494	28
GMDP01Z4-2	sp	12.34	6.70	6.89	0.56	0.96	0.165	0.004	11.116	0.482	0.489	0.017	0.782	-2.41	2506	44
GMDP01Z5-1	dc	81.03	33.84	50.53	0.43	5.62	0.198	0.002	14.929	0.398	0.548	0.013	0.916	-0.44	2805	18
GMDP01Z5-2	br	11.57	6.02	6.12	0.53	0.30	0.168	0.004	10.783	0.389	0.464	0.011	0.673	3.29	2542	44
GMDP01Z7-1	sp	14.67	7.37	8.24	0.52	0.98	0.177	0.008	12.006	1.237	0.492	0.045	0.887	1.71	2624	78
GMDP01Z8-1	br	19.81	13.34	11.37	0.69	0.86	0.184	0.007	12.209	0.578	0.482	0.012	0.542	5.59	2686	66
GMDP01Z9-3	ir	58.50	27.94	30.01	0.49	1.33	0.164	0.002	10.285	0.281	0.456	0.011	0.898	2.88	2493	20

Table 6.1 U-Th-Pb zircon data for zircons analysed in this study; 'volume diffusion zircons' are those where age and cathodoluminescence zoning pattern are clearly decoupled while 'other zircons' are those where they are not decoupled; in the 'CL zoning pattern' column: sp = single phase, ozp = oscillatory zoning pattern, dr = dark rim, br = bright rim, dc = dark core, bc = bright core, ir = irregular, r = rim.

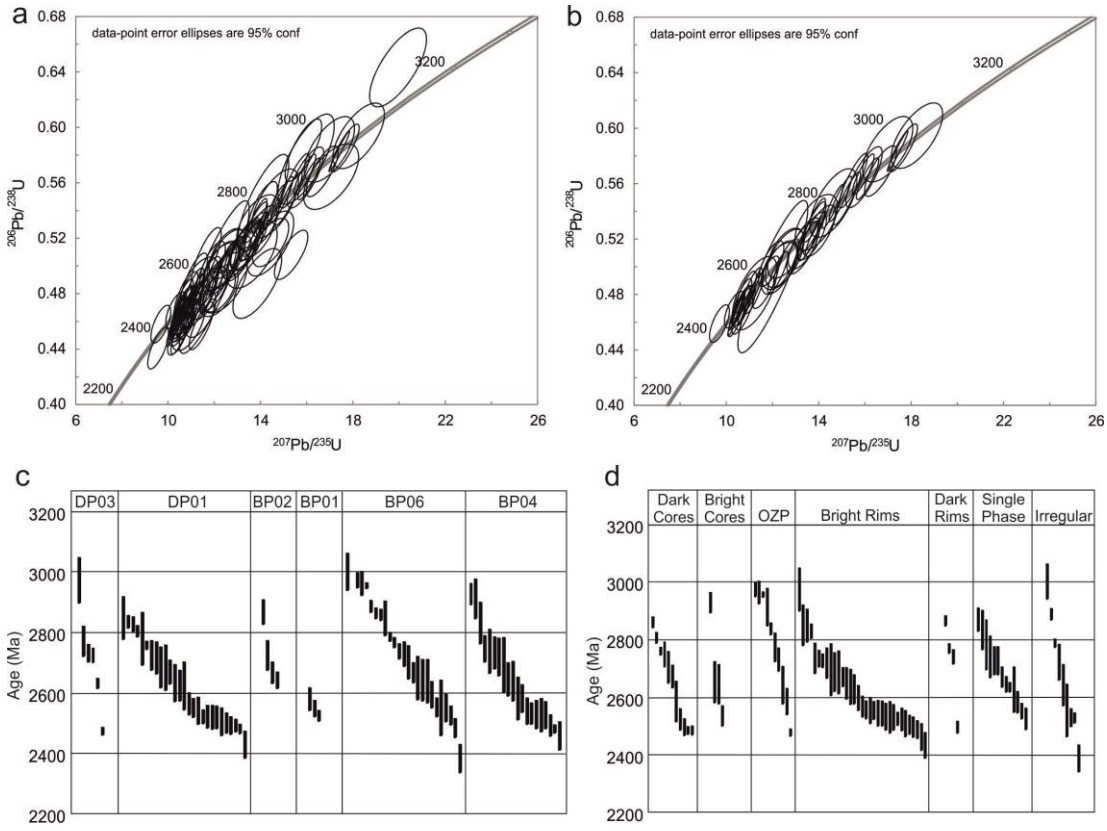

Fig. 6.2 a) Wetherill concordia plot of zircon U-Pb ages from the zircon population analysed in this study; b) as a) but with 98-102% concordance limits imposed; c) plot showing spread of ages in different samples collected; d) plot showing lack of correlation between age and cathodoluminescence zoning pattern.

Explicit evidence for volume diffusion of Pb in the zircons was sought by examining the relationship between $^{207}Pb/^{206}Pb$ ages and CL zoning patterns in individual zircon crystals. The main criterion for determining that volume diffusion of Pb has occurred in zircon is decoupling of $^{207}Pb/^{206}Pb$ ages from CL zoning patterns. This decoupling can take one of two forms. It may be a zone of uniform CL intensity, interpreted to reflect a single age, but with multiple $^{207}Pb/^{206}Pb$ ages recorded that are not within error of each other. This zone may be a rim or a whole crystal. The other form is where $^{207}Pb/^{206}Pb$ ages are older at the edge of a crystal than those in the centre. Normally, the centre of a grain would be expected to be the oldest part of the crystal with the edge being the youngest. However, with volume diffusion of Pb, it is possible to have a core with a younger age than its surrounding rim. If a new low U rim grows around a core in which some of the U has already decayed to Pb, Pb

will then diffuse from the core to the new rim, which will have started with no Pb. After diffusion stops, Pb will continue to build up in both the rim and the core but because the rim has gained Pb and the core lost Pb, and because there is less U in the rim, the ratio of Pb to U will be higher causing an increase in percentage discordance values and older ages. As this evolves over time the $^{207}Pb/^{206}Pb$ ages will also show a decoupling from the core and rim zoning pattern.

Of the 35 analysed zircon grains in the population, 9 had only a single analytical point (either due to their small size or to other points being excluded for high common Pb) and so the presence of volume diffusion could not be proven. 12 grains had what could be termed a 'meaningful' age/zoning pattern relationship where age and zoning pattern are coupled, for example a core with an old age surrounded by a bright rim with a younger age, or a uniform CL grain with two spots the same age. In this group of 12 zircons, there is clustering of ages from CL-bright rims at ~2500Ma (Fig. 6.3), suggesting this may be a real age for a metamorphic event. There were 6 grains where recrystallisation could potentially explain the decoupling between age and zoning pattern, or the CL pattern was unclear. In the remaining 8 grains, age was decoupled from zoning pattern but in such a way that recrystallisation cannot be invoked to explain the age/zoning pattern relationship. Many of the data-points from these zircons with volume diffusion are 98-102% concordant (Fig. 6.4). CL images annotated with $^{207}Pb/^{206}Pb$ ages of these eight grains are shown in Figure 6.5 and described below:

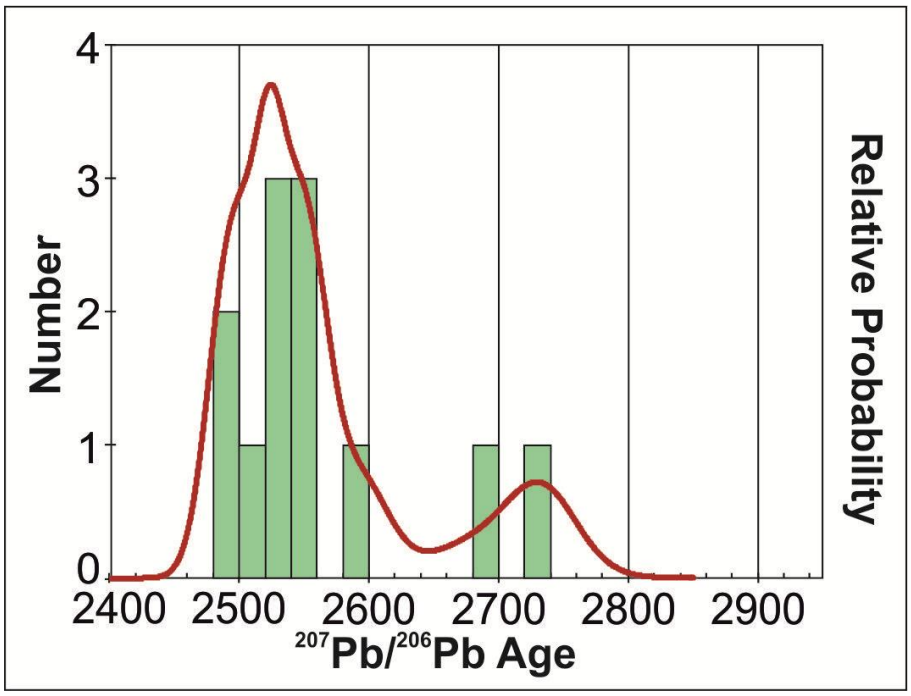

Fig. 6.3 Probability-density plot (2σ confidence levels) of $^{207}Pb/^{206}Pb$ ages from CL-bright zircon rims; the peak at ~2500Ma is interpreted to represent the age of a tectonothermal event.

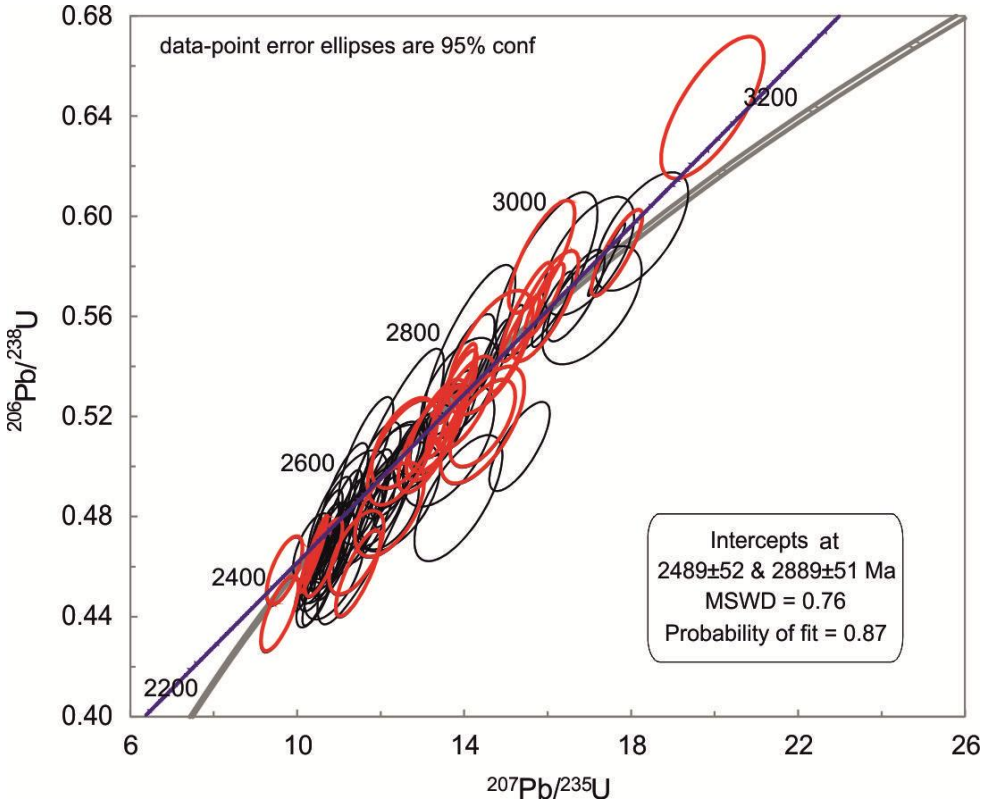

Fig. 6.4 Wetherill concordia plot of zircon U-Pb ages from the zircon population analysed in this study; red ellipses denote analyses from zircons with decoupling of age and cathodoluminescence zoning pattern; the blue line denotes a possible Pb-loss trajectory (line parameters in inset box), the lower intercept is interpreted to approximately mark the timing of the cessation of volume diffusion.

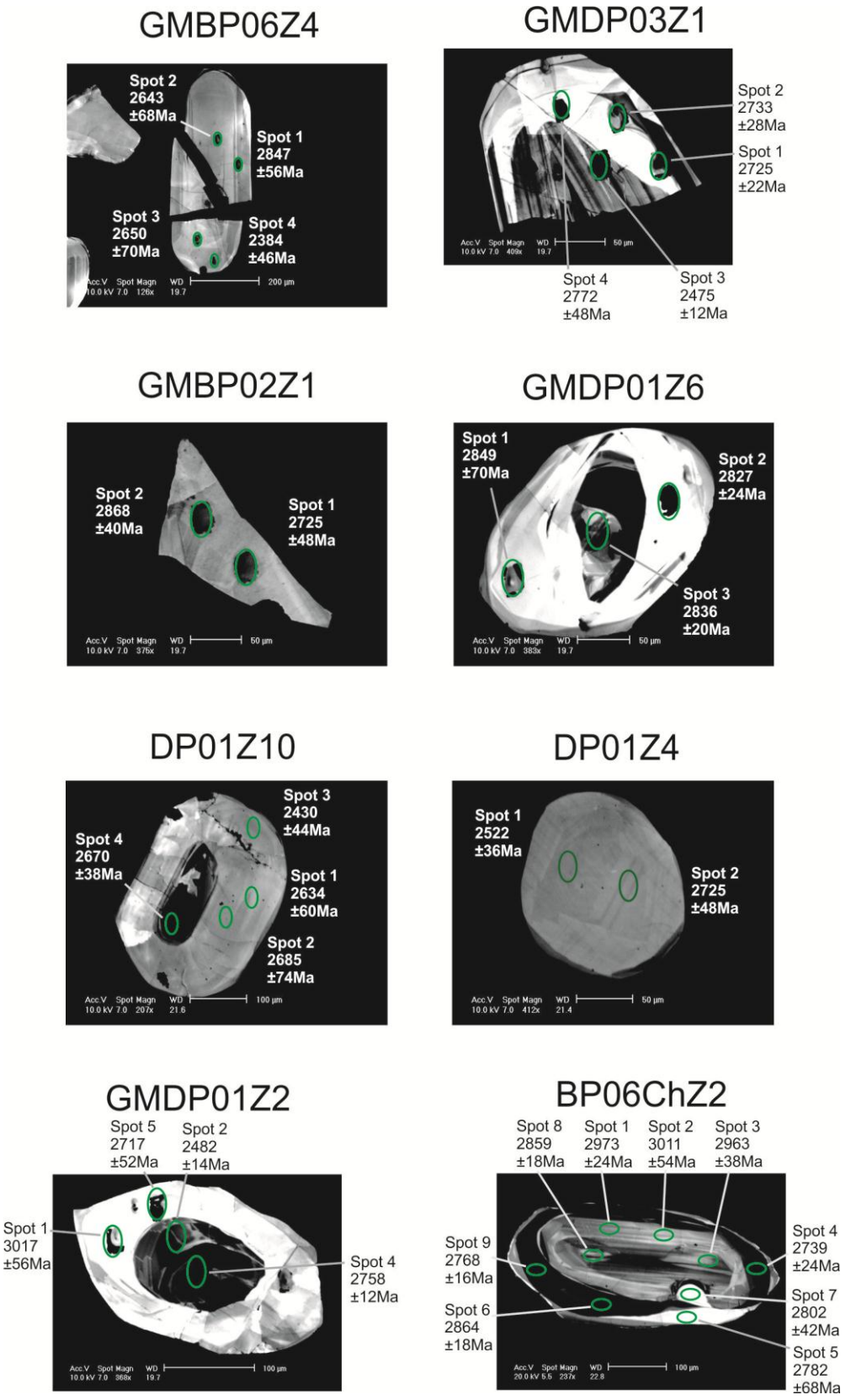

Fig. 6.5 Cathodoluminescence (CL) images of zircons, annotated with $^{207}Pb/^{206}Pb$ ages, where the decoupling between age and CL zoning is interpreted to have been caused by volume diffusion.

GMBP06Z4 CL imaging suggests some faint remnant zoning, possibly OZP around a homogeneous core. The oldest age of 2847Ma is recorded at the edge of the crystal while younger ages of ~2650Ma are recorded towards the centre. A young and moderately discordant age is recorded at one tip of the grain although the chemical zoning is irregular here.

GMDP03Z1 CL imaging shows this zircon to have some well-preserved OZP surrounded by a mainly bright rim. Ages from this rim are within error of each other but are ~300myr older than that from the OZP domain.

GMBP02Z1 This zircon is uniform in CL intensity suggesting a single age domain but the two ages recorded are ~150myr apart, even though they are located only 30µm from each other. This difference would surely require very local diffusion gradients for Pb, possibly controlled by local variations of Pb concentration at the grain boundary.

GMDP01Z6 The core of this zircon is heterogeneous in CL response indicating it has not been swept by a recrystallisation front; it is surrounded by bright rim. One age from the core and two ages from the rim are all within error of each other. One possible explanation for this overlap in ages is that the rim formed as a late-magmatic feature hence the proximity of ages from core and rim. However, late-magmatic alteration in zircon tends to take the form of patchy internal replacement in CL (Corfu et al., 2003); CL-bright rims are much more commonly a metamorphic feature (Corfu et al., 2003), suggesting the proximity of ages between core and rim may be due to volume diffusion of Pb.

DP01Z10 CL imaging shows this zircon has a plain dark core surrounded by a moderately bright rim. The age from the core is within error of two ages from the rim; this may be just due to recrystallisation, and hence U-Pb resetting, of the core at the time of rim formation. However, the third age from the apparently single-event rim is ~200myr younger than the other rim ages.

DP01Z4 This zircon is uniform in CL intensity suggesting a single age domain but the two ages recorded are ~200myr apart, even though they are located only 40µm from each other. This difference would surely require very local diffusion gradients for Pb, possibly controlled by local variations of Pb concentration at the grain boundary.

GMDP01Z2 CL imaging shows this zircon to have a dark core, possibly with some OZP, surrounded by a bright rim. There is heterogeneity of ages within the core of ~300myr and the two ages from the rim are older than one of the core ages. Indeed one of the CL-bright rim ages is 3017Ma – the oldest age recorded in the whole population although it is moderately normally discordant.

BP06ChZ2 CL imaging shows this zircon has an early core, possibly with some OZP, surrounded by a domain of OZP which is in turn surrounded by a dark rim; there are some CL-bright replacement domains at the rim, likely from fluid alteration. Multiple ages from the main OZP zone are within error but they are older than the early core surrounded by the OZP domain; this does not make sense as innermost domains should be older than those around them. Furthermore, there is heterogeneity in age in the dark rim, even though CL suggests it should be a single age domain.

In 4 of the 8 zircons (GMDP03Z1, GMDP01Z6, GMDP01Z2 and BP06ChZ2), total U concentration varied within a single CL zone. The variable U concentration did not affect the calculated age as Pb concentration varied accordingly; while this may suggest limited volume diffusion, intra-zone diffusion may be masked by uncertainties in the analysis. Variable U concentration was therefore not considered to be a factor in the overall age/zoning pattern relationship. If volume diffusion of Pb occurred in these 8 grains, then it would be expected to have occurred in all zircons in the population. Grains that have been affected by volume diffusion are not concentrated in a single sample and are located within millimetres of other zircons that show no direct evidence for volume diffusion. Volume diffusion cannot be disproved in the 8 grains with only a single analytical point but there

remain 20 grains in the population that show no clear evidence of volume diffusion. This type of phenomenon has been described previously as 'variable' Pb-loss, although not explicitly invoking volume diffusion (e.g. Friend and Kinny, 1995; Whitehouse and Kemp, 2010; Halpin et al., 2012). If Pb-loss by volume diffusion occurred in all zircons in the population, one might expect to see a cluster of ages representing a cooling age (which there is not, see Fig. 6.2) or a correlation between grain size and age. The smallest zircons would record the youngest ages as there is a shorter distance for the Pb to diffuse out of the grain, therefore it would occur quicker than in larger grains, which would retain more Pb. This is not the case in this population (Fig. 6.6). One possible explanation for this 'variable' volume diffusion is heterogeneous spatial distribution of Pb in the grain boundary network. If, for example, there was no Pb in the grain boundary network at one end of a prismatic zircon grain, the radiogenic Pb in the zircon would diffuse out of the zircon and into the grain boundary network. But, if at the other end of the zircon there was a high concentration of Pb in the grain boundary network, this would act as a buffer to volume diffusion of Pb out of the zircon. At present, this remains only a theory as Pb concentrations in other minerals in the host TTG gneisses such as iron-titanium oxides were below detection limit of the electron microprobe.

However, with discordance limits of ±2%, a Pb-loss trajectory passes through the datapoints on concordia with intercepts at 2489±52Ma and 2889±51Ma (2σ confidence levels, MSWD = 0.76, probability of fit = 0.87) (Fig. 6.4). Friend and Kinny (1995) also proposed a Pb-loss trajectory from ~3000Ma to ~2500Ma through their apparently concordant dataset from LGC zircons, although they did not attribute it to volume diffusion. Even though there is not explicit evidence for volume diffusion (in the form of decoupling of age and CL zoning) in all zircons in this study, this chord suggests that many or all underwent Pb-loss which may have been caused by volume diffusion.

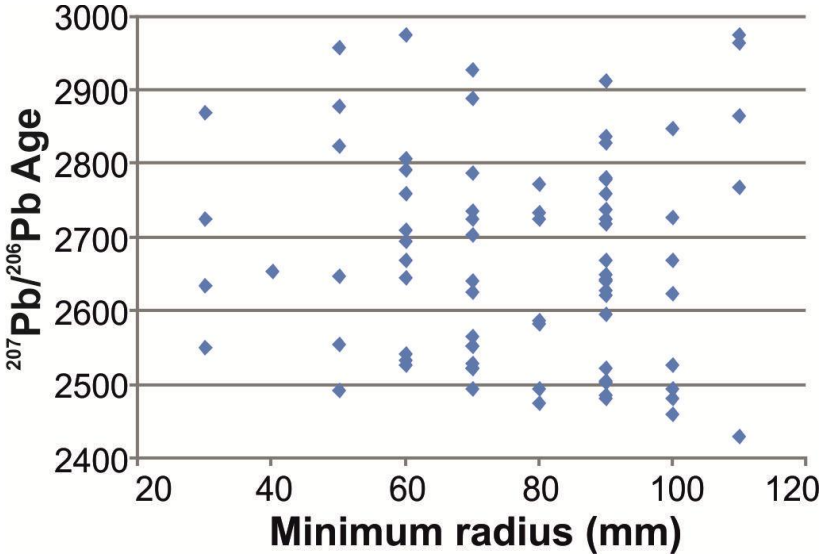

Fig. 6.6 Scatter plot of $^{207}Pb/^{206}Pb$ age against minimum crystal radius of zircons in the population in this study; lack of correlation indicates the age spread in Fig. 6.2 is not related to cooling.

5. CONDITIONS FOR VOLUME DIFFUSION OF PB IN ZIRCON

The experiments of Cherniak and Watson (2001; 2003) indicate that volume diffusion of Pb in zircon requires a combination of temperatures in excess of 700°C for millions to hundreds of millions of years, depending on grain size (the diffusion distance). In the eight zircons interpreted to have clear evidence of volume diffusion, Pb would have to travel at least 50µm in some grains to give the resultant age pattern. The hottest period in the history of the rocks of the Assynt Terrane, where the zircons in this study were sampled, was the Badcallian tectonothermal event. Johnson and White (2011) calculated peak Badcallian temperatures of 875-975°C by mineral equilibria modelling methods while Sills and Rollinson (1987) calculated a temperature range of ~750-1000°C using a range of ion exchange geothermometers. Using the modelling of Pb diffusion of Cherniak and Watson (2001; 2003) and a diffusion distance of 50µm, diffusion of Pb out of the zircons would have taken between 3Myr and 500Myr based on the temperature estimates of Johnson and White (2011) (Fig. 6.7). 500Myr at 875°C would allow diffusion of 50% of the Pb out of a zircon of 50µm diameter while only 3Myr would be required at 975°C for the same amount of diffusional Pb loss (Fig. 6.7).

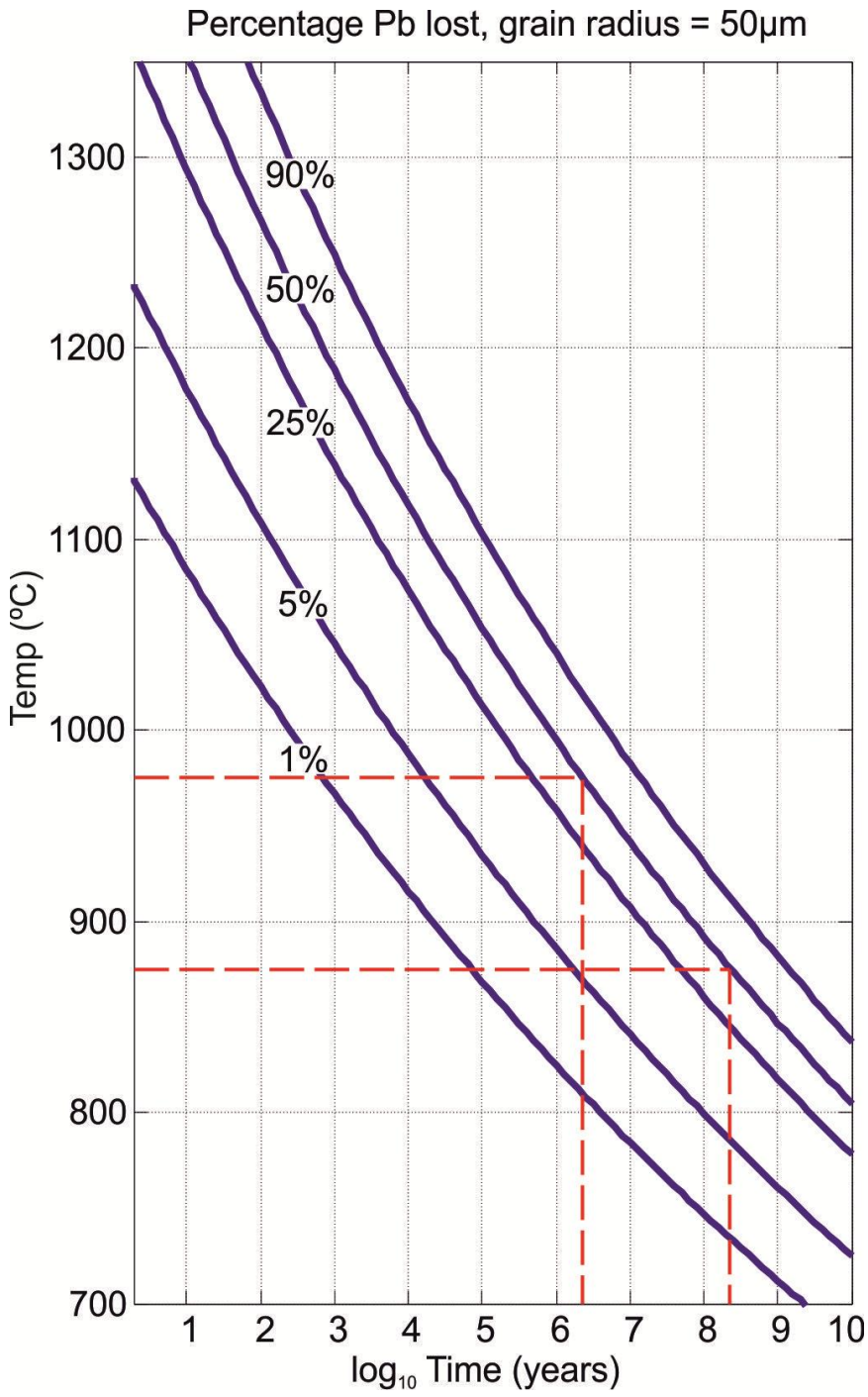

Fig. 6.7 Percentage Pb lost over a diffusion distance of 50µm at variable temperatures and times, after Cherniak and Watson (2001); dashed lines denote the time taken for 50% Pb-loss at the temperature range of 875-975°C (Johnson and White, 2011).

The time differences here are significant and the exact temperature-time history of the Assynt Terrane cannot be resolved further without more precise temperature estimates. The widespread occurrence of $^{207}Pb/^{206}Pb$ ages of ~2500Ma in CL-bright rims throughout

the zircon population is interpreted to represent a metamorphic event and may reflect the timing of the volume diffusion. Friend and Kinny (1995) interpreted a major metamorphic event to have occurred around this time and suggested this was the time at which the Badcallian granulite-facies metamorphic assemblage formed. Furthermore, the lower intercept of a Pb-loss trajectory (Fig. 6.4) is around the 2500Ma age. If the whole zircon population has been affected by volume diffusion then it must have been occurring at ~2500Ma as volume diffusion cannot produce apparent ages younger than the time it is occurring at. However, it has also been suggested that the Badcallian 'event' occurred at ~2730Ma (Corfu et al., 1994; Whitehouse and Kemp, 2010). These ages may perhaps represent the beginning and end of a period of elevated temperature. Given that the spread of ages along concordia in Figure 3 is ~500myr, it is possible that variable volume diffusion may have occurred over this length of time. It is, however, equally possible that the Badcallian was a short ultra-high temperature metamorphic event (e.g. Brown, 2007). Further constraints on peak Badcallian temperature would help to further elucidate the temperature-time history of the Assynt Terrane.

6. CONCLUSIONS

This study has shown that it is possible for volume diffusion of Pb to occur in natural crystalline zircon over long timescales at high temperatures. The example zircons from the Lewisian Gneiss Complex (LGC) of northwest Scotland exhibit a decoupling between the chemical zoning patterns and $^{207}Pb/^{206}Pb$ ages; methodical elimination of various possible explanations has indicated that this is due to volume diffusion of Pb. Direct evidence is only seen in eight grains but may well have occurred in more as the most concordant data-points in the population (with or without explicit evidence for volume diffusion) define a Pb-loss trajectory on concordia plot. Volume diffusion of Pb in these zircons could represent anything between 3Myr and 500Myr at temperatures of 875-975°C in the Assynt

Terrane of the LGC. The widespread occurrence of $^{207}Pb/^{206}Pb$ ages of ~2500Ma in CL-bright zircon rims may reflect the occurrence of a short period of ultra-high temperature during which volume diffusion occurred or may reflect the end of a longer period at lower temperatures during which volume diffusion occurred. The latter scenario would entail a radically different interpretation of the tectonothermal history but this requires further work to constrain the temperature history of these rocks better.

ACKNOWLEDGEMENTS

This work was carried out under UK Natural Environment Research Council DTG NE/G523855/1 and British Geological Survey CASE Studentship 2K08E010 to JMM. Carmel Pinnington and Eddie Dempsey are thanked for assistance with SEM analysis. Ion microprobe analysis at the Edinburgh Ion Microprobe Facility was carried out with funding from NERC grant IMF384/1109; Richard Hinton, Cees-Jan De Hoog and John Craven are thanked for ion microprobe support and Mike Hall for assistance with sample preparation. KMG publishes with the permission of the Executive Director of the Geological Survey.

7. New Insights on the Assynt Terrane of the Lewisian Gneiss Complex of Northwest Scotland from Zircon U-Th-Pb, REEs and Ti-Thermometry

Formatted for submission to *Precambrian Research*

New Insights on the Assynt Terrane of the Lewisian Gneiss Complex of Northwest Scotland from Zircon U-Th-Pb, REEs and Ti-Thermometry

John M. MacDonald[1], John Wheeler[1], Kathryn M. Goodenough[2], Quentin Crowley[3], Simon L. Harley[4], Elisabetta Mariani[1], Daniel Tatham[1]

[1] School of Environmental Sciences, Jane Herdman Laboratories, University of Liverpool, L69 3GP, UK

[2] British Geological Survey, Murchison House, West Mains Road, Edinburgh, EH9 3LA, UK

[3] School of Natural Sciences, Museum Building, Trinity College Dublin, College Green, Dublin 2, IE

[4] School of GeoSciences, Grant Institute, The King's Buildings, West Mains Road, Edinburgh, EH9 3JW, UK

Corresponding author: John M. MacDonald

Postal: School of Environmental Sciences, University of Liverpool, L69 3GP, UK.

Email: jmacd@liv.ac.uk

Telephone: 01517945201

ABSTRACT

The Lewisian Gneiss Complex (LGC) of Northwest Scotland is a classic Precambrian basement gneiss complex. The LGC is divided into a number of terranes, the most well-studied of which is the Assynt Terrane. Field evidence shows that it has a complex tectonothermal history comprising the Badcallian granulite-facies metamorphism followed by the Inverian and Laxfordian amphibolite-facies tectonothermal events. In this contribution we analyse zircons from tonalite-trondhjemite-granodiorite (TTG) gneisses and metasediments and supplement U-Th-Pb data with REE profiling and Ti thermometry which

help to constrain the geochemical and thermal history of the Assynt Terrane. We apply Ti-in-zircon thermometry to the LGC for the first time and zircon REE profiling for the first time to the mainland LGC. Volume diffusion of Pb (see Chapter 6) in zircons across the analysed population has made it difficult to confidently interpret magmatic and metamorphic ages as zircon U-Pb data form a relatively concordant ~500Myr age spread. The oldest three cores yield a mean age of 2958±7Ma (MSWD = 1.00, probability = 0.37), a possible minimum magmatic protolith crystallisation age. The period of volume diffusion of Pb in zircon is interpreted to have ended at ~2482Ma with the peak of the Badcallian granulite-facies metamorphism shortly before this. Zircons in the metasediments have relatively flat chondrite-normalised heavy REE profiles (low Yb/Gd ratios) which suggest they equilibrated with Badcallian metamorphic garnet. Although the REE profiling links these zircons to the Badcallian metamorphic assemblage, volume diffusion of Pb means that the U-Pb systematics do not record an accurate age for the Badcallian tectonothermal event. Ti-in-zircon thermometry records crystallisation temperatures of at least ~760-820°C for zircons in the magmatic protolith to the TTG gneisses. Zircons in the metasediments generally record higher minimum temperatures, with an average of 823°C compared to 790°C in the TTG gneisses. The zircons in the metasediments are interpreted to be detrital and the calculated temperatures record zircon crystallisation in a currently unknown protolith. Through this combination of zircon U-Th-Pb, REE and Ti data, this study provides further insight into the formation and tectonothermal evolution of the Assynt Terrane.

Keywords: Lewisian Gneiss Complex, Assynt Terrane, zircon, U-Th-Pb, REEs, Ti-in-zircon thermometry

1. Introduction

The Lewisian Gneiss Complex (LGC) of Northwest Scotland (Fig. 7.1a) is a classic example of a basement gneiss complex and is an important location for understanding the tectonothermal evolution of lower crustal rocks. Field relationships and mineral assemblages allowed Peach et al. (1907) and Sutton and Watson (1951) to determine a relative chronology of events in the LGC, providing a framework for the large number of geochemical and geochronological investigations that have been carried out since then (as summarised by Wheeler et al., 2010). The dominant lithologies in the LGC are tonalite-trondhjemite-granodiorite (TTG) gneisses, with subordinate mafic and ultramafic gneisses and rare metasediments. In the area around the village of Scourie (Fig. 7.1b), three major sets of structures and associated mineral assemblages have been recognised and attributed to three tectonothermal events. Sutton and Watson (1951) used the heterogeneous preservation of these structures and assemblages to subdivide the mainland outcrop of the LGC into three regions (Fig. 7.1a). The area around Scourie was termed the Central Region, bounded to the north and south by the Northern and Southern Regions, respectively.

In parts of the Central Region, such as around Scourie, all three tectonothermal events are preserved. The earliest is expressed as granulite-facies gneissic layering, which represents the gneissification of the TTG magmatic protoliths, and is named the Badcallian (Park, 1970). The subsequent Inverian event is characterised by an amphibolite-facies assemblage and localised shear zones up to a few kilometres wide (e.g. Canisp (Evans, 1965; Jensen, 1984; Attfield, 1987)). Following the Inverian event came the intrusion of the mafic Scourie Dyke Swarm, an important chronological marker. Post-dyke, the Laxfordian amphibolite-facies event heterogeneously overprinted earlier assemblages and structures (Sutton and Watson, 1951). Around Scourie, it is represented by discrete shear zones a few metres wide, or static overprinting of earlier granulite-facies assemblages. The terms Badcallian, Inverian and Laxfordian are used here to refer to the structures and mineral

assemblages and the tectonothermal activity they represent; the attributes of each are summarised in Table 7.1.

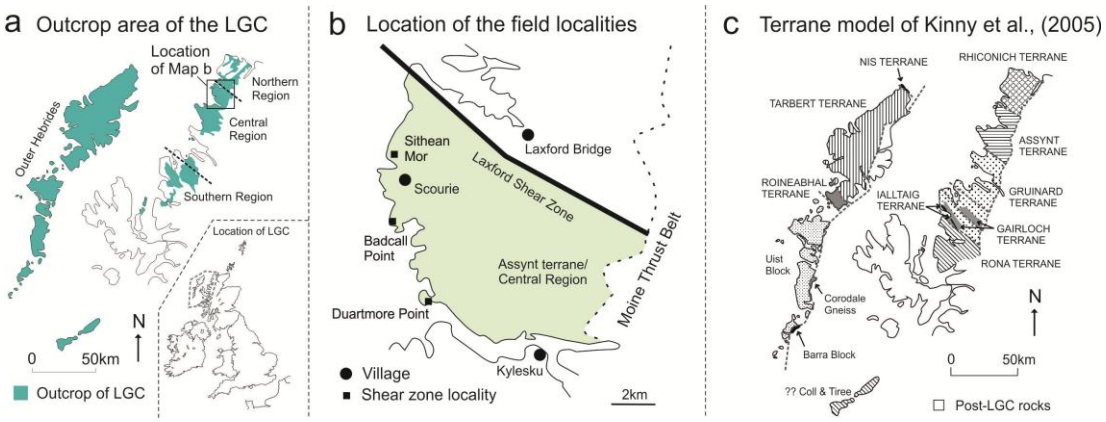

Fig. 7.1 (a) Location of the outcrop area of the LGC (Lewisian Gneiss Complex) in Northwest Scotland, inset map shows location in the British Isles; mainland outcrop regions are after Peach et al. (1907). (b) Localities where zircons analysed in this study were taken from. (c) The terrane model of Kinny et al. (2005) showing the different terranes interpreted to make up the LGC.

Table 7.1 Summary of the structures and mineral assemblages that characterise the Badcallian, Inverian and Laxfordian tectonothermal events in the Scourie area.

Name	Characteristics
Badcallian	Pyroxene-bearing granulite-facies mineral assemblage, gneissification of TTG protoliths and formation of gneissic layering, generally no lineation
Inverian	Kilometre-wide shear zones with amphibolite-facies planar and linear fabrics
Laxfordian	Discrete shear zones several metres wide with amphibolite-facies planar and linear fabrics, static retrogression of pyroxene to hornblende

The relationship of the metasedimentary rocks, found mainly in the Central Region, to the rest of the LGC is not wholly clear. They tend to be spatially associated with mafic and ultramafic gneisses, which Davies (1976) interpreted to represent an ocean floor supracrustal package. Based on field evidence, Davies (1976) and Goodenough et al. (2010) suggested that the juxtaposition of the metasediments, whether depositional or tectonic, with the TTG gneisses pre-dated the Badcallian tectonothermal. In support of this, dating of monazites from the metasediments by Zhu et al. (1997) suggested they were metamorphosed in the Badcallian while detailed petrographic analysis by Zirkler et al. (2012) recorded partial melting of the metasediments in the Badcallian.

Early workers such as Peach and Horne (1907) and Sutton and Watson (1951) assumed that the LGC was a single block of crust and the three tectonothermal events had affected each of the three regions. Radiometric dating meant that precise ages could be attributed to these tectonothermal events. Corfu et al. (1994) obtained U-Pb zircon ages of ~2710Ma and ~2490Ma from near Badcall Point (Fig. 7.1b) which they attributed to the Badcallian and Inverian respectively. Corfu et al. (1994) and Kinny and Friend (1997) attributed U-Pb titanite ages of ~1750Ma to the Laxfordian event. However, a large suite of high spatial resolution ion microprobe U-Pb zircon dating from across the LGC has led to a new interpretation of the formation and tectonothermal evolution of the LGC (Friend and Kinny, 1995; Kinny and Friend, 1997; Friend and Kinny, 2001; Love et al., 2004; Kinny et al., 2005; Love et al., 2010). At first, U-Pb zircon ages from the Central Region led Friend and Kinny (1995) to suggest a magmatic protolith age for the LGC of 2960-3030Ma with a major metamorphic event at ~2490Ma; they did not find a significant age cluster at ~2710Ma. This led them to interpret that the granulite-facies Badcallian event actually occurred at ~2490Ma with the Inverian occurring soon after but not recorded in the zircons.

Following this, they obtained magmatic protolith ages of 2680-2840Ma from the Northern Region and no record of metamorphism at ~2490Ma (Kinny and Friend, 1997). The difference in age profile for magmatic protolith formation and subsequent tectonothermal activity led them to believe that the Northern Region and Central Region were separate crustal blocks. Friend and Kinny (2001) found that different parts of the Outer Hebrides also had different magmatic protolith formation and tectonothermal activity ages while Love et al. (2004) found that the southern part of the Central Region recorded different magmatic protolith formation and tectonothermal activity ages to those in the northern part of the Central Region found by Friend and Kinny (1995). These findings were formalised into a model of disparate terranes with different magmatic protolith ages and tectonothermal histories, which then accreted during or before the Laxfordian event

(Kinny et al., 2005) (Fig. 7.1c). Further work by Love et al. (2010) indicated that the Southern Region was also composed of multiple terranes with varying histories. The Central Region was re-named the Assynt Terrane, and the Northern Region the Rhiconich Terrane (Fig. 7.1c) (Kinny et al., 2005). Goodenough et al. (2010) investigated field relationships in the Laxford Shear Zone (Fig. 7.1a), the boundary between the Assynt and Rhiconich Terranes, and suggested that the two terranes were accreted during the Inverian event.

Large U-Pb zircon datasets in studies such as those by Friend and Kinny (1995) and Whitehouse and Kemp (2010) show a spread of relatively concordant ages over several hundred million years. It is difficult to interpret magmatic and metamorphic ages from these data and this has fuelled debate over the details of the terrane model (Kinny et al., 2005; Park, 2005; Park et al., 2005; Corfu, 2007). Understanding the formation and tectonothermal evolution of the LGC continues to be a challenge, with many pieces of incremental evidence contributing to the development of an overarching history. In this contribution we analyse zircons from TTG gneisses and metasediments and supplement U-Pb data with REE and Ti concentration data which help to constrain the geochemical and thermal history of the Assynt Terrane. We apply Ti-in-zircon thermometry to the LGC for the first time and zircon REE profiling for the first time to the mainland LGC.

2. Sample Characterisation

Zircons were collected from 8 samples, 6 from the TTG gneisses which dominate the Assynt Terrane, and 2 from the metasediments. The samples of TTG gneiss were taken from two localities: Badcall Point and Duartmore Point (Fig. 7.1b; 7.2a&b), and chosen to reflect the tectonothermal history of the Assynt Terrane. At Badcall Point, Badcallian gneissic layering is the dominant structure but the Badcallian granulite-facies metamorphic assemblage has been retrogressed, as is typical across much of the Assynt Terrane. Sieve-textured hornblende and quartz have replaced pyroxenes; plagioclase is the other main

mineral. Sample JM09/BP02 was taken from this. The Badcallian gneissic layering is cross-cut by a ~0.5m-wide zone of planar fabric, interpreted to be Inverian in age. Sieve-textured hornblende and quartz have replaced pyroxenes; plagioclase is the other main mineral. Sample JM09/BP01 was taken from this. The Inverian and Badcallian fabrics are cross-cut by a Laxfordian shear zone from which samples JM09/BP06 and JM09/BP04 were taken. Both have moderate to strong planar and linear fabrics and an amphibolite-facies hornblende+plagioclase+quartz assemblage. At Duartmore Point, the Badcallian gneissic layering retains granulite-facies clinopyroxene but orthopyroxene has largely been replaced by epidote and biotite; plagioclase and quartz are the other major minerals. Sample JM09/DP03 was taken from this. The Badcallian gneissic layering is cross-cut by a Laxfordian shear zone from which sample JM09/DP02 was taken. The shear zone has moderate to strong planar and linear fabrics and an amphibolite-facies hornblende+plagioclase+quartz assemblage. On either side of the shear zone is a zone where granulite-facies gneissic layering has been statically retrogressed to amphibolite-facies. Sample JM09/DP01 and was taken from this.

Two samples were taken from the body of metasediments at Sithean Mor (Fig. 7.1b & 7.2c). The package of metasediments is internally heterogeneous with biotite- and garnet-rich zones, and more quartzose areas. This outcrop of metasediments is enclosed by TTG gneisses with Badcallian gneissic layering. The strike of the layering runs into the metasediment outcrop and continues in the form of a moderately-developed planar fabric comprising biotite-rich and biotite-poor layers. Sample JM08/22 has a garnet+biotite+plagioclase+quartz assemblage. The garnet is highly fractured and partially replaced with biotite and quartz. Sample JM08/23 is composed of: lensoid- or arcuate-shaped quartz aggregates, 2-5mm long and composed of equant 0.5mm-diameter crystals, possibly porphyroclasts; large partially sericitised plagioclase crystals, possibly also porphyroclasts; a very fine matrix of quartz, feldspar and muscovite; and very high relief

kyanite. The kyanite is either acicular or equant in shape when viewed in thin section, with the different shapes representing different sections through the crystals. The kyanite indicates an amphibolite-facies overprint. Full details of sample petrography and geochemistry can be found in chapter 4.

3. Results

3.1. Analytical Methods

Internal chemical zoning in zircons was revealed by cathodoluminescence (CL) imaging. This was carried out in a Philips XL30 scanning electron microscope at the University of Liverpool (see Chapter 3 for full details). The zircons were then analysed by ion microprobe at the Edinburgh Ion Microprobe Facility (EIMF) at the University of Edinburgh. U-Pb isotope analysis was conducted using a Cameca IMS 1270 ion microprobe and analytical procedures follow those of Kelly et al. (2008). U/Pb ratios were calibrated against the Plesovice (Slama et al., 2008) zircon standard. During the analytical session, the standard yielded a mean $^{206}Pb/^{238}U$ ratio of 0.05359±0.00023 (MSWD = 2.4; 95% conf.; $^{206}Pb/^{238}U$ age = 340.5±4.8Ma; *n = 62*). Calculation of ratios and data reduction were conducted using in-house software developed by Richard Hinton at University of Edinburgh.

A common Pb correction was also applied in-house. Common Pb surface contamination was reduced by rastering the sample with the ion microprobe beam immediately prior to isotope measurement and by production of flat-bottom analysis pits through carefully tuned beam conditions. Correction for in-situ common Pb was made using measured ^{204}Pb counts above that of the detector background (typically ~0.2 to 1.5ppb). In the analyses for this project, measured common Pb was generally in the range of <5ppb, although occasionally analyses were much higher than this, likely the result of contamination on the sample surface and in exposed cracks; such analyses were discarded.

Uncertainties on all isotopic ratios and ages are quoted at the 2σ level. Plots and age calculations have been made using the computer program ISOPLOT (Ludwig, 2003).

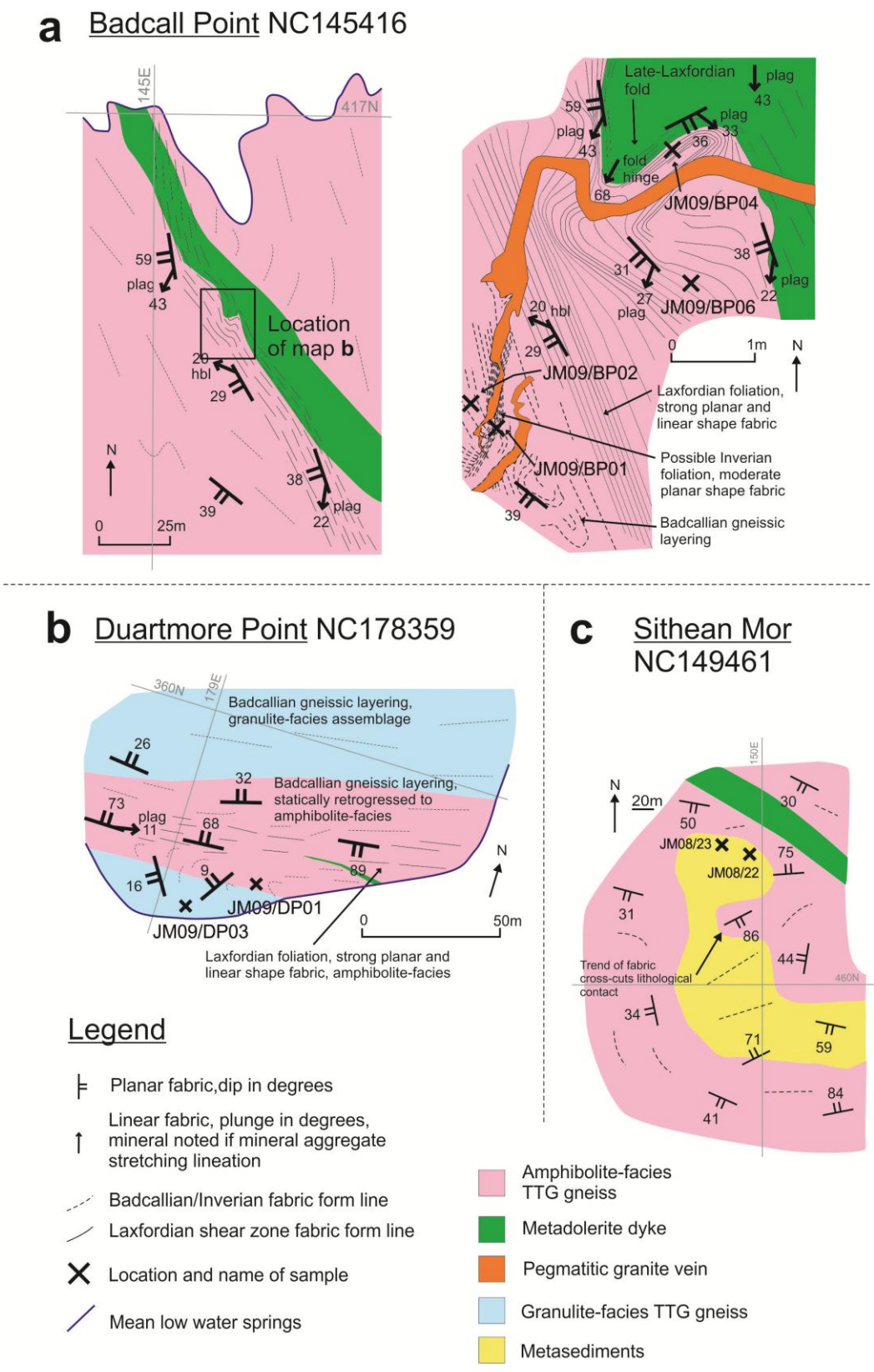

Fig. 7.2 Field maps showing structures, mineral assemblages and sample localities: (a) Badcall Point, with context map (left) and detail map (right); (b) Duartmore Point; (c) Sithean Mor.

Trace elements were measured using a Cameca 4f ion microprobe, following the analytical procedures of Kelly and Harley (2005). Analytical reproducibility during the analytical session was tested by regular measurement of REEs and Ti in the 91500 zircon standard (Wiedenbeck et al., 1995) and NIST SRM610 glass standard. The analyses from the 91500 zircon show an expected, smooth increase in chondrite-normalised values of trivalent REEs as ionic radius decreases from La to Lu, together with large positive Ce anomaly and small negative Eu anomaly. Good agreement is obtained between the SIMS measurements for zircon 91500 presented here and those of Whitehouse and Platt (2003) and Hoskin (1998) although there is some variation in REE concentrations in the analyses of 91500, also encountered by Hoskin (1998). For most REEs (particularly the heavier ones), the average analytical error is <10% (2σ) but for some of the lighter REEs which have lower concentrations, it can be significantly higher. This is interpreted to be partly due to a lack of reproducibility from the spectrometer but also to heterogeneity in the 91500 standard as noted above. Error on Ti is ~10% (2σ). Analytical reproducibility against the NIST SRM610 glass standard was <6% (2σ) for the elements analysed. Raw data were reduced using the JCION6 software written by John Craven at the University of Edinburgh. REE data were chondrite-normalised against the values of McDonough and Sun (1995).

3.2. Zircon Cathodoluminescence

When imaged by CL, the population of zircons showed a range of chemical zoning patterns typical of complex zircons from high-grade metamorphic rocks (Fig. 7.3). Sub-rounded cores, both CL-bright and CL-dark, are found in many crystals. Some cores have distinctive oscillatory zoning patterns (e.g. GMBP04Z6 and BP06ChZ1 in Fig. 7.3), indicative of growth from a magma (Corfu et al., 2003). Other cores may be homogenous in CL response (e.g. DP01Z6 in Fig. 7.3) or may show some irregular zoning. All cores tend to be surrounded by rims which are usually CL-bright (e.g. GMDP01Z2 and BP06ChZ1 in Fig. 7.3)

but may in some cases have medium or low CL response (CL-dark). Each rim is generally homogeneous in CL response and they are interpreted to have formed during metamorphism (Corfu et al., 2003). Some crystals do not have any discernible internal zoning patterns – these are termed single phase (e.g. GMBP04Z5 and GMBP02Z1 in Fig. 7.3), although it cannot be ruled out that they contain distinct zones beneath the level of polishing. A number of crystals are irregular in their CL zoning pattern – they have no recognisable core or rim structures and cannot be assigned to any known formation mechanism (e.g. GM23Z2 and BP06Z3 in Fig. 7.3). For the purposes of analysing zircon U-Pb and trace elements to gain further insight into the formation and evolution of the Assynt Terrane, the CL zoning patterns were divided into four groups: cores (oscillatory-zoned, homogeneous or heterogeneous zoning, CL-bright or CL-dark); rims (CL-bright or CL-dark); single phase; and irregular. Zircons in all the different samples have a range of zoning patterns (Table 7.2).

3.3. Zircon U-Th-Pb

103 spot analyses in 44 zircon grains were conducted by ion microprobe for U-Th-Pb. U contents range from a few to 440ppm while Th ranges from 1 to 360ppm, although the majority of analyses are 10-100ppm for both Th and U (Table 7.2). There is a wide range in Th and U contents within each sample although zircons from the metasedimentary rocks from Sithean Mor (samples JM08/22 and JM08/23) cluster towards the top of the range for Th and U (Fig. 7.4a; Table 7.2). There is no correlation between Th or U contents and CL zoning pattern; each of the four categories record a wide range (Fig. 7.4b; Table 7.2). Th/U is generally in the range 0.5-2, although some analyses from an irregularly-zoned zircon from sample JM09/BP06 are as low as 0.04 (Fig. 7.4a-b; Table 7.2). As well as a range in Th and U concentrations, there is also a range in $^{207}Pb/^{206}Pb$ ages from 2384±46Ma to 3017±56Ma (Table 7.2). There is no correlation between age and U content or Th/U either

between samples or between CL zoning pattern category (Fig. 7.4c-f; Table 7.2). Each sample records a range of $^{207}Pb/^{206}Pb$ ages as do the zoning pattern categories (Fig. 7.5a&b). The ages are mainly concordant (-2% to +5%) although some are more discordant (Table 7.2) and the data define a spread along concordia with no obvious clustering representing protolith or metamorphic ages (Fig. 7.5c&d).

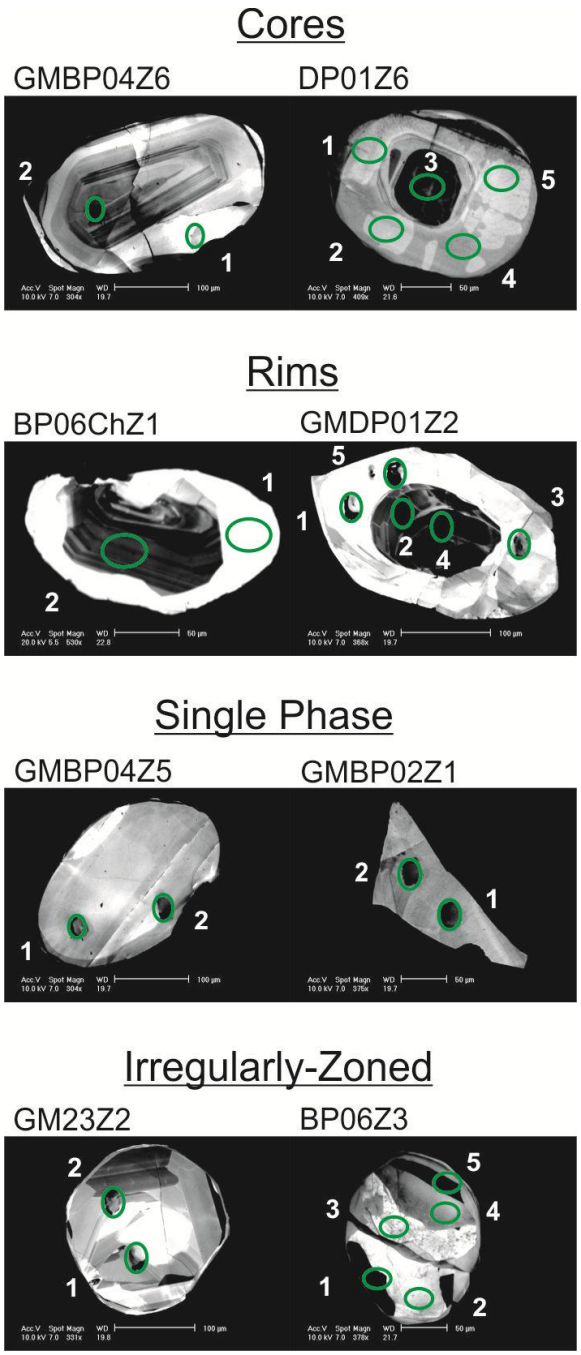

Fig. 7.3 Representative images showing the four cathodoluminescence (CL) categories of zircons from the population analysed in this study, with crystal names and ion microprobe spot numbers annotated.

Table 7.2 Ion microprobe U-Th-Pb data for zircons analysed in this study. CL (cathodoluminescence) zoning pattern identifiers: sp = single phase; ir = irregular; ir (emb) = irregular embayment; r = rim; r (br) = bright rim; r (dr) = dark rim; c (ozp) = oscillatory zoned core; c (bc) = bright core; c (dc) = dark core.

Sample/spot	CL Zoning Pattern	U (ppm)	Th (ppm)	Pb (ppm)	Th/U	$^{204}Pb_c$ (ppb)	$^{207}Pb/^{206}Pb$	2σ	$^{207}Pb/^{235}U$	2σ	$^{206}Pb/^{238}U$	2σ	Error Corr.	% Disc.	$^{207}Pb/^{206}Pb$ Age	2σ
JM09/BP02																
GMBP02Z1-1	sp	33.10	82.63	27.88	2.56	4.49	0.188	0.006	13.332	0.587	0.514	0.017	0.732	1.86	2725	48
GMBP02Z1-2	sp	33.55	85.05	31.31	2.60	1.66	0.205	0.005	15.957	0.644	0.564	0.018	0.791	-0.50	2868	40
GMBP02Z2-1	ir	51.03	59.13	32.96	1.19	1.06	0.179	0.003	12.224	0.360	0.495	0.012	0.857	1.98	2644	26
GMBP02Z2-2	ir	49.84	61.14	33.11	1.26	1.44	0.182	0.004	12.579	0.441	0.502	0.014	0.805	1.71	2668	34
JM09/BP01																
BP01Z1-1	ir	47.98	26.41	26.43	0.56	2.61	0.169	0.003	11.200	0.331	0.480	0.012	0.854	0.85	2549	26
BP01Z1-2	ir	44.44	23.85	24.32	0.55	1.13	0.172	0.004	11.339	0.369	0.477	0.011	0.731	2.58	2581	36
GMBP01Z2-1	ir	171.81	272.79	113.48	1.63	2.30	0.167	0.002	10.839	0.285	0.471	0.012	0.931	1.49	2526	16
JM09/BP06																
BP06ChZ1-1	r (br)	49.48	38.36	27.89	0.80	2.48	0.170	0.003	10.953	0.333	0.468	0.012	0.810	3.09	2554	30
BP06ChZ1-2	c (ozp)	421.30	294.94	299.81	0.72	0.00	0.217	0.001	17.415	0.365	0.583	0.012	0.977	-0.12	2956	8
BP06ChZ2-1	c (ozp)	72.76	66.12	54.21	0.93	2.57	0.219	0.003	17.668	0.500	0.585	0.014	0.850	0.12	2973	24
BP06ChZ2-4	r (dr)	165.93	101.29	101.28	0.63	6.75	0.190	0.003	13.543	0.366	0.518	0.012	0.846	1.79	2739	24
BP06ChZ2-5	ir (emb)	35.73	30.51	24.17	0.88	1.61	0.195	0.008	14.633	0.831	0.545	0.020	0.655	-0.82	2782	68
BP06ChZ2-7	ir (emb)	29.38	49.56	24.71	1.73	4.38	0.197	0.005	15.864	0.646	0.584	0.018	0.771	-5.76	2802	42
BP06ChZ2-8	c (ozp)	151.28	156.14	110.55	1.06	3.53	0.204	0.002	15.925	0.387	0.566	0.012	0.877	-1.12	2859	18
BP06Z3-1	ir	88.81	4.38	50.43	0.05	2.22	0.195	0.002	14.604	0.375	0.543	0.013	0.934	-0.31	2786	14
BP06Z3-2	ir	24.46	3.43	15.87	0.14	0.73	0.223	0.008	18.255	0.910	0.594	0.019	0.653	-0.10	3002	60
BP06Z3-3	ir	23.45	9.87	13.17	0.43	5.10	0.179	0.008	12.310	0.631	0.500	0.014	0.542	1.04	2640	70
BP06Z3-4	ir	2.61	0.99	1.39	0.39	0.77	0.169	0.009	11.213	0.796	0.480	0.022	0.637	0.98	2552	90
BP06Z3-5	ir	209.28	8.36	124.24	0.04	2.45	0.208	0.002	16.112	0.398	0.563	0.012	0.886	0.31	2887	18
GMBP06Z1-2	r (br)	20.42	20.19	12.79	1.01	1.00	0.182	0.003	12.399	0.456	0.495	0.016	0.858	2.87	2668	32
GMBP06Z2-1	ir (emb)	24.40	31.31	15.62	1.32	1.51	0.167	0.003	11.107	0.360	0.483	0.013	0.820	-0.54	2526	30
GMBP06Z2-2	c (ozp)	30.23	39.97	22.13	1.36	0.12	0.189	0.004	14.106	0.514	0.543	0.015	0.757	-2.38	2729	40
GMBP06Z3-1	r (br)	18.00	12.48	10.42	0.71	0.00	0.174	0.004	11.699	0.477	0.488	0.015	0.778	1.29	2595	42
GMBP06Z3-2	r (br)	21.50	12.85	11.81	0.61	2.73	0.163	0.003	10.688	0.329	0.476	0.012	0.808	-1.01	2485	30

(continued)

Table 7.2 (cont.)

Sample/spot	CL Zoning Pattern	U (ppm)	Th (ppm)	Pb (ppm)	Th/U	$^{204}Pb_c$ (ppb)	$^{207}Pb/^{206}Pb$	2σ	$^{207}Pb/^{235}U$	2σ	$^{206}Pb/^{238}U$	2σ	Error Corr.	% Disc.	$^{207}Pb/^{206}Pb$ Age	2σ
JM09/BP06 (continued)																
GMBP06Z4-1	r	32.61	39.32	22.51	1.24	2.37	0.203	0.007	14.444	0.640	0.517	0.014	0.621	5.65	2847	56
GMBP06Z4-2	c (bc)	19.40	20.18	12.59	1.07	1.62	0.179	0.007	12.560	0.636	0.509	0.015	0.573	-0.34	2643	68
GMBP06Z4-3	c (bc)	19.78	20.79	12.78	1.08	1.22	0.180	0.008	12.520	0.684	0.505	0.017	0.624	0.53	2650	70
GMBP06Z4-4	r	22.60	22.98	12.94	1.04	8.06	0.153	0.004	9.690	0.351	0.458	0.011	0.670	-1.96	2384	46
GMBP06Z5-1	r (br)	12.79	7.76	6.94	0.62	2.48	0.170	0.004	10.923	0.467	0.467	0.016	0.785	3.14	2552	44
GMBP06Z5-2	c (dc)	52.42	111.53	41.06	2.18	1.21	0.186	0.006	12.960	0.532	0.506	0.013	0.609	2.29	2703	54
GMBP06Z6-1	ir	37.75	40.14	25.22	1.09	1.49	0.219	0.006	15.330	0.592	0.508	0.015	0.741	10.90	2972	42
JM09/BP04																
GMBP04Z1-1	r (br)	35.34	48.52	24.83	1.41	5.24	0.189	0.006	13.421	0.576	0.515	0.015	0.669	2.08	2734	52
GMBP04Z1-2	r (br)	35.24	49.49	27.80	1.44	4.20	0.213	0.005	16.677	0.565	0.568	0.015	0.776	0.90	2927	34
GMBP04Z2-1	r (br)	23.51	24.05	13.66	1.05	6.27	0.167	0.005	10.594	0.434	0.460	0.012	0.628	3.54	2528	54
GMBP04Z2-2	r (br)	35.08	32.98	20.40	0.96	1.47	0.168	0.003	10.807	0.326	0.468	0.010	0.742	2.33	2533	34
GMBP04Z3-1	c (bc)	16.46	21.09	10.03	1.31	0.49	0.173	0.007	10.886	0.583	0.457	0.015	0.615	6.02	2583	70
GMBP04Z3-2	c (bc)	21.05	25.57	13.85	1.25	3.94	0.173	0.005	11.932	0.450	0.501	0.013	0.709	-1.41	2583	44
GMBP04Z4-1	r (br)	23.11	29.88	13.83	1.33	0.10	0.168	0.004	10.430	0.364	0.449	0.011	0.702	5.89	2541	42
GMBP04Z4-2	r (br)	21.63	26.78	13.27	1.27	2.43	0.160	0.004	10.352	0.366	0.468	0.011	0.650	-0.66	2459	46
GMBP04Z4-3	c (dc)	127.60	55.92	66.72	0.45	4.59	0.163	0.001	10.516	0.239	0.469	0.010	0.948	0.10	2482	12
GMBP04Z5-1	sp	20.13	24.51	15.47	1.25	1.53	0.201	0.008	15.977	0.997	0.577	0.027	0.738	-3.69	2832	68
GMBP04Z5-2	sp	28.26	24.28	18.60	0.88	1.17	0.190	0.008	13.890	0.750	0.531	0.016	0.572	-0.32	2738	72
GMBP04Z6-1	r (br)	15.38	14.35	9.58	0.96	0.76	0.179	0.007	12.277	0.625	0.499	0.016	0.623	1.24	2640	64
GMBP04Z6-2	c (ozp)	34.99	49.14	28.31	1.44	1.73	0.211	0.009	16.985	0.888	0.584	0.019	0.634	-1.83	2912	64
GMBP04Z7-1	sp	18.32	19.41	10.71	1.09	1.69	0.167	0.004	10.582	0.431	0.459	0.014	0.753	3.61	2528	44
GMBP04Z7-2	sp	12.54	9.88	7.24	0.81	2.17	0.164	0.003	10.849	0.362	0.481	0.012	0.775	-1.45	2494	34
GMBP04Z7-3	sp	16.48	18.01	10.64	1.12	4.32	0.167	0.005	11.649	0.536	0.505	0.018	0.791	-4.19	2530	46
GMBP04Z7-4	sp	30.80	41.16	21.78	1.37	2.11	0.191	0.005	13.705	0.512	0.521	0.014	0.720	1.54	2747	42
GMBP04Z8-2	sp	13.39	8.05	7.78	0.62	2.27	0.206	0.009	13.864	0.861	0.487	0.021	0.680	11.02	2876	74
GMBP04Z8-3	sp	28.76	20.31	16.61	0.72	1.92	0.179	0.006	11.960	0.511	0.484	0.013	0.615	3.94	2647	54

(continued)

Table 7.2 (cont.)

Sample/spot	CL Zoning Pattern	U (ppm)	Th (ppm)	Pb (ppm)	Th/U	$^{204}Pb_c$ (ppb)	$^{207}Pb/^{206}Pb$	2σ	$^{207}Pb/^{235}U$	2σ	$^{206}Pb/^{238}U$	2σ	Error Corr.	% Disc.	$^{207}Pb/^{206}Pb$ Age	2σ
JM09/BP04 (continued)																
GMBP04Z9-1	sp	21.87	29.00	16.12	1.36	3.31	0.188	0.007	14.128	0.900	0.546	0.028	0.799	-3.33	2720	62
GMBP04Z9-2	sp	30.11	20.81	17.56	0.71	3.67	0.185	0.010	12.413	0.829	0.488	0.018	0.546	4.93	2694	90
JM09/DP03																
GMDP03Z1-1	r (br)	65.61	52.17	42.71	0.82	2.19	0.188	0.002	13.819	0.379	0.533	0.013	0.881	-1.04	2725	22
GMDP03Z1-2	r (br)	42.13	28.79	26.59	0.70	6.27	0.189	0.003	13.758	0.448	0.528	0.015	0.859	0.00	2733	28
GMDP03Z1-3	c (ozp)	82.66	71.55	47.02	0.89	1.82	0.162	0.001	10.409	0.255	0.466	0.011	0.959	0.29	2475	12
GMDP03Z1-4	r (br)	34.50	24.66	21.87	0.73	1.97	0.194	0.006	14.015	0.578	0.525	0.015	0.700	1.85	2772	48
GMDP03Z2-1	c (ozp)	33.96	12.58	21.94	0.38	0.93	0.219	0.010	17.060	0.974	0.564	0.019	0.599	3.00	2974	74
DP03Z2-1	sp	439.84	358.71	257.43	0.84	4.50	0.178	0.002	11.763	0.303	0.480	0.011	0.926	4.09	2633	16
JM09/DP01																
DP01Z4-1	sp	15.29	2.24	7.41	0.15	0.00	0.166	0.004	10.629	0.369	0.463	0.013	0.788	2.74	2522	36
DP01Z4-2	sp	14.04	2.12	7.69	0.16	0.75	0.188	0.006	13.338	0.541	0.514	0.014	0.664	1.82	2725	48
DP01Z6-1	r (br)	18.27	11.02	9.64	0.62	0.35	0.169	0.003	10.605	0.390	0.454	0.014	0.866	5.39	2551	30
DP01Z6-2	r (br)	17.20	8.79	9.14	0.52	0.59	0.166	0.004	10.734	0.417	0.468	0.014	0.793	1.83	2521	38
DP01Z6-3	c (dc)	57.95	87.23	36.86	1.54	0.32	0.166	0.004	10.556	0.359	0.460	0.012	0.780	3.21	2521	36
DP01Z6-4	r (br)	14.72	9.57	8.34	0.67	0.00	0.177	0.005	11.725	0.515	0.480	0.015	0.733	3.67	2625	50
DP01Z6-5	r (br)	18.57	8.94	9.75	0.49	1.25	0.171	0.004	10.911	0.407	0.463	0.014	0.797	4.30	2565	36
DP01Z10-1	r (br)	13.87	5.02	7.16	0.37	1.67	0.178	0.007	11.415	0.536	0.465	0.014	0.625	6.53	2634	60
DP01Z10-2	r (br)	14.54	5.07	7.79	0.36	0.79	0.184	0.008	12.208	0.677	0.482	0.015	0.574	5.50	2685	74
DP01Z10-3	r (br)	15.54	6.57	7.58	0.43	4.85	0.158	0.004	9.575	0.368	0.441	0.012	0.725	3.14	2430	44
DP01Z10-4	c (dc)	39.05	35.39	22.26	0.93	5.30	0.182	0.004	11.457	0.439	0.457	0.014	0.803	9.16	2670	38
GMDP01Z1-1	r (br)	36.48	20.76	19.37	0.58	1.29	0.167	0.002	10.596	0.298	0.461	0.011	0.885	3.05	2523	22
GMDP01Z1-2	r (br)	27.15	10.41	14.10	0.39	1.14	0.164	0.003	10.677	0.341	0.471	0.012	0.800	0.59	2502	32
GMDP01Z2-1	r (br)	15.09	11.70	12.08	0.80	0.00	0.225	0.008	19.960	1.007	0.643	0.023	0.715	-6.12	3017	56
GMDP01Z2-2	c (dc)	89.07	105.38	53.54	1.21	2.28	0.163	0.001	10.372	0.264	0.463	0.011	0.942	1.23	2482	14
GMDP01Z2-4	c (dc)	149.86	173.21	103.04	1.19	2.17	0.192	0.002	13.849	0.360	0.524	0.013	0.952	1.59	2758	12
GMDP01Z2-5	r (br)	21.17	8.45	12.12	0.41	0.26	0.187	0.006	13.130	0.580	0.509	0.016	0.710	2.42	2717	52

(continued)

Table 7.2 (cont.)

Sample/spot	CL Zoning Pattern	U (ppm)	Th (ppm)	Pb (ppm)	Th/U	$^{204}Pb_c$ (ppb)	$^{207}Pb/^{206}Pb$	2σ	$^{207}Pb/^{235}U$	2σ	$^{206}Pb/^{238}U$	2σ	Error Corr.	% Disc.	$^{207}Pb/^{206}Pb$ Age	2σ
JM09/DP01 (continued)																
GMDP01Z3-1	sp	15.12	7.08	8.83	0.48	0.72	0.194	0.010	13.629	0.898	0.508	0.020	0.594	4.71	2780	86
GMDP01Z4-1	sp	14.84	7.77	7.87	0.54	1.52	0.164	0.003	10.532	0.381	0.467	0.015	0.876	1.01	2494	28
GMDP01Z4-2	sp	12.34	6.70	6.89	0.56	0.96	0.165	0.004	11.116	0.482	0.489	0.017	0.782	-2.41	2506	44
GMDP01Z5-1	c (dc)	81.03	33.84	50.53	0.43	5.62	0.198	0.002	14.929	0.398	0.548	0.013	0.916	-0.44	2805	18
GMDP01Z5-2	r (br)	11.57	6.02	6.12	0.53	0.30	0.168	0.004	10.783	0.389	0.464	0.011	0.673	3.29	2542	44
GMDP01Z6-1	r (br)	5.41	3.20	3.31	0.61	1.08	0.203	0.009	14.440	0.822	0.516	0.019	0.651	5.83	2849	70
GMDP01Z6-2	r (br)	24.23	19.41	16.76	0.82	1.15	0.200	0.003	15.491	0.506	0.561	0.016	0.882	-1.60	2827	24
GMDP01Z6-3	c (dc)	65.70	61.02	45.59	0.95	2.38	0.201	0.003	15.229	0.475	0.549	0.016	0.916	0.58	2836	20
GMDP01Z7-1	sp	14.67	7.37	8.24	0.52	0.98	0.177	0.008	12.006	1.237	0.492	0.045	0.887	1.71	2624	78
GMDP01Z8-1	r (br)	19.81	13.34	11.37	0.69	0.86	0.184	0.007	12.209	0.578	0.482	0.012	0.542	5.59	2686	66
GMDP01Z9-3	ir	58.50	27.94	30.01	0.49	1.33	0.164	0.002	10.285	0.281	0.456	0.011	0.898	2.88	2493	20
JM08/22																
GM22Z1-1	c (ozp)	98.42	112.96	72.56	1.18	0.00	0.206	0.004	15.870	0.521	0.558	0.014	0.781	0.63	2876	34
GM22Z1-2	c (bc)	152.83	181.19	111.25	1.22	0.94	0.200	0.003	15.121	0.389	0.549	0.012	0.835	0.05	2823	24
GM22Z2-1	c (ozp)	172.11	246.58	96.22	1.47	6.30	0.165	0.002	9.292	0.240	0.409	0.010	0.903	11.84	2506	18
GM22Z3-1	c (ozp)	409.93	185.31	225.64	0.46	0.74	0.173	0.002	11.660	0.271	0.489	0.010	0.908	0.86	2587	16
JM08/23																
GM23Z2-1	ir	110.41	78.14	66.20	0.73	1.14	0.177	0.004	12.247	0.367	0.503	0.011	0.746	-0.27	2620	34
GM23Z2-2	ir	78.76	69.45	47.04	0.90	0.70	0.177	0.003	11.807	0.323	0.483	0.011	0.797	3.27	2627	26
GM23Z4-1	r (br)	138.07	290.26	108.04	2.16	1.57	0.182	0.003	12.754	0.350	0.509	0.011	0.811	0.58	2668	26
GM23Z4-2	r (br)	136.05	233.58	103.19	1.76	2.65	0.188	0.003	13.602	0.387	0.524	0.012	0.784	0.33	2726	28
GM23Z5-1	sp	74.92	73.40	50.93	1.01	0.30	0.196	0.005	14.420	0.504	0.534	0.013	0.698	1.23	2792	40
GM23Z5-2	sp	61.85	57.41	40.43	0.95	1.99	0.186	0.004	13.405	0.443	0.522	0.014	0.784	0.15	2710	34
GM23Z6-2	ir	144.50	87.46	85.49	0.62	4.87	0.174	0.003	12.187	0.385	0.508	0.012	0.778	-2.08	2595	34
GM23Z6-3	ir	88.35	88.90	60.25	1.03	1.43	0.194	0.004	14.276	0.480	0.533	0.014	0.759	0.75	2777	34

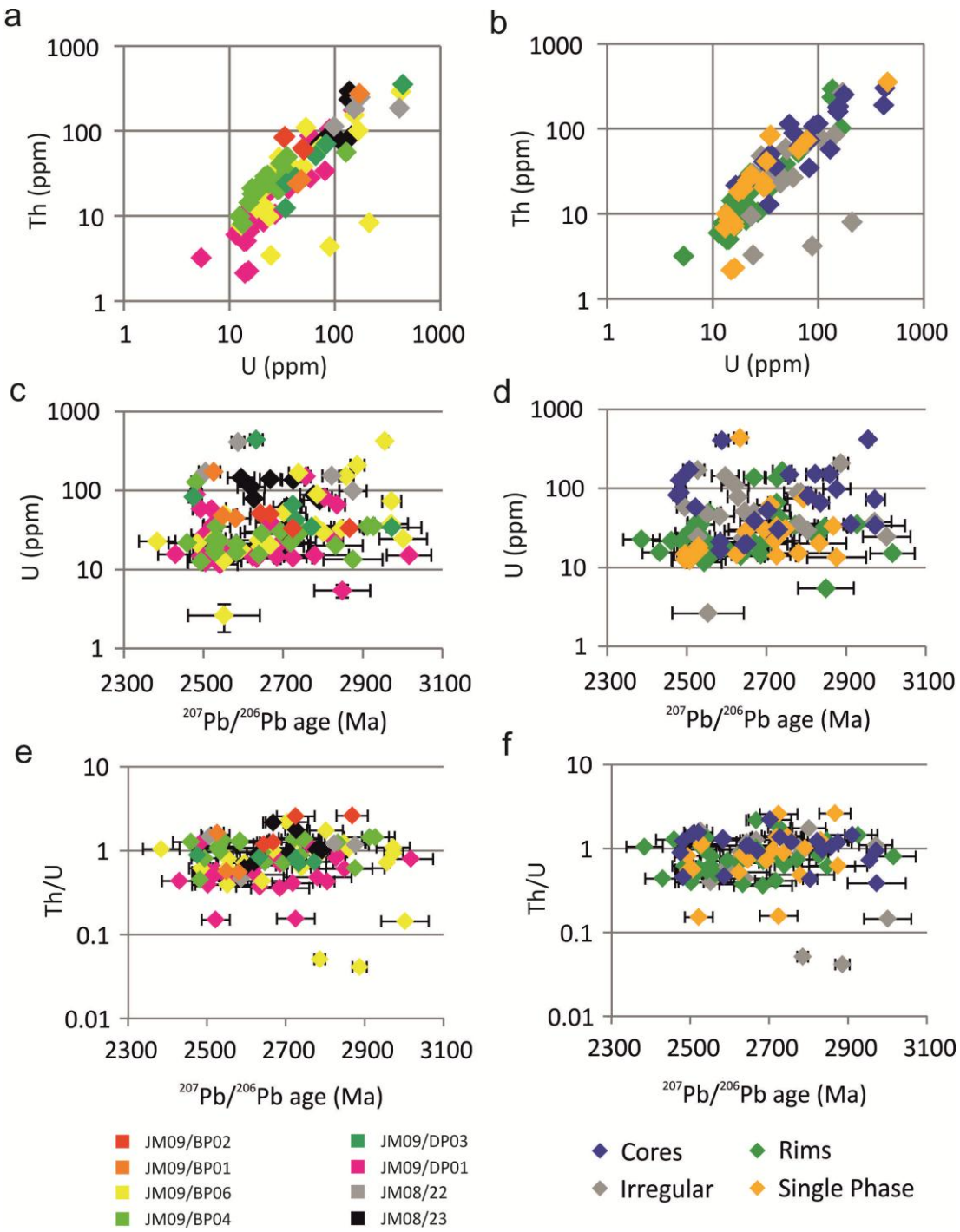

Fig. 7.4 U-Th-Pb chemistry of zircons from this study plotted as: Th concentration (ppm) vs. U concentration (ppm) colour-coded by sample (a) and by cathodoluminescence zoning pattern (b); U concentration (ppm) vs. ^{207}Pb/^{206}Pb age colour-coded by sample (c) and by cathodoluminescence zoning pattern (d); Th/U ratio vs. ^{207}Pb/^{206}Pb age colour-coded by sample (e) and by cathodoluminescence zoning pattern (f).

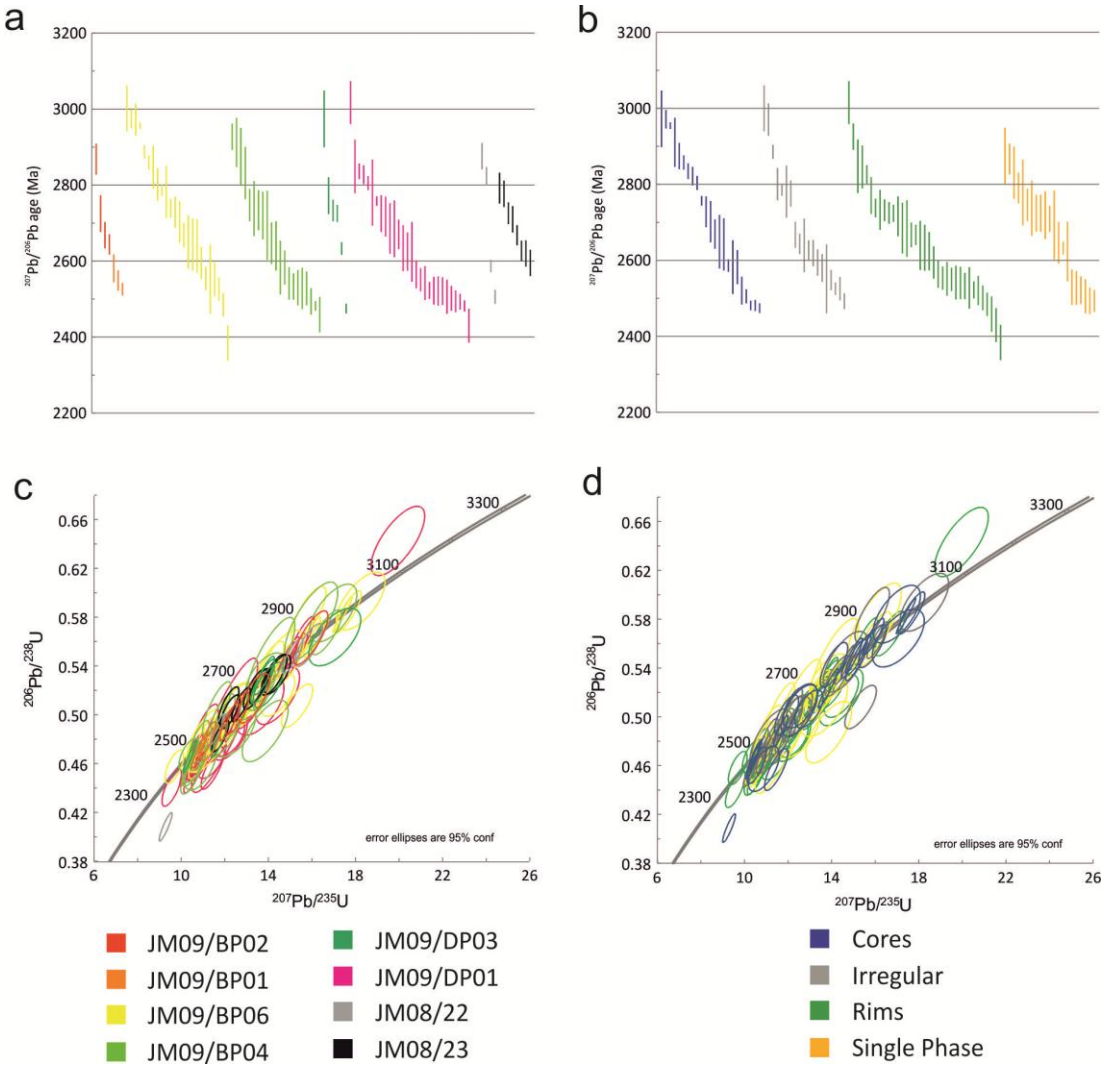

Fig. 7.5 Spread of ^{207}Pb/^{206}Pb ages recorded by zircons in this study: (a) ^{207}Pb/^{206}Pb ages with 2σ errors colour-coded by sample; (b) ^{207}Pb/^{206}Pb ages with 2σ errors colour-coded by cathodoluminescence zoning pattern; (c) Wetherill concordia plot of zircon Pb/U ratios colour-coded by sample; (d) Wetherill concordia plot of zircon Pb/U ratios colour-coded by cathodoluminescence zoning pattern.

In order to obtain a protolith age for the Assynt Terrane from this potentially confusing array of data, a starting point is to look for the oldest age in the population, as was done by Friend and Kinny (1995) in their analysis of the Assynt Terrane. This study includes zircons of unknown provenance from metasedimentary rocks and these are therefore excluded when trying to determine a protolith age for the TTG gneisses which make up the majority of the Assynt Terrane. The oldest age in the TTG gneiss zircon population is 3017±56Ma, although this age is reversely discordant by 6%. This degree of reverse discordance is interpreted to be beyond the level of an analytical artefact affecting the U/Pb ratio calibration so this particular age may be overestimated.

An alternative approach used by Whitehouse and Kemp (2010) to determine a protolith age is to assume that there is a single magmatic age and that the spread of ages has been caused by later Pb-loss. Successive rejection of the youngest ages is performed until the mean square of weighted deviates (MSWD) of the weighted average age of the population falls below a limit, below which analytical error can account for the observed scatter. This objective approach does not take account of the CL zoning pattern, however. The oldest age in the TTG gneiss zircon population is from a rim which is unlikely to reflect protolith formation whereas cores are much more likely to reflect the early stages of zircon history, possibly growth from a protolith magma (Corfu et al., 2003). Taking the threshold MSWD to be 1 (Whitehouse and Kemp, 2010), the oldest three cores yield a mean age of 2958±7Ma (MSWD = 1.00, probability = 0.37). Including the next youngest core increases the MSWD to only 1.3 which is still acceptable and yields a mean age of 2957±14Ma. These four oldest cores are all oscillatory zoned and thus are likely to have formed by crystallisation from a magma (Corfu et al., 2003). Cores with younger ages do not all show oscillatory zoning, and also greatly increase the MSWD. This age is ~100Myr older than the protolith age suggested by Whitehouse and Kemp (2010) from a similar dataset, which was also calculated from oscillatory zoned zircons, but is within error of the 2960Ma age suggested by Friend and Kinny (1995) for the formation of the protolith to the Assynt Terrane.

Any attempt to pick out ages for metamorphic events from the zircon population in this study is hampered by the spread of concordant ages. There is no clear clustering of ages in any sample (Fig. 7.5a) or CL zoning pattern category (Fig. 7.5b). The fact that not all of the oldest ages in the population are from cores as might be expected, coupled with the spread of ages of up to ~600Myr in the different CL zoning pattern categories, makes interpretation of the chronological history of the Assynt Terrane extremely difficult. In chapter 6, possible explanations for this spread of ages and lack of correlation between age,

sample and CL zoning pattern were explored and volume diffusion of Pb was considered to be the most likely explanation. The evidence for this was presented and discussed in detail in chapter 6 and will not be repeated here.

3.4. Zircon Rare Earth Elements

The relative abundance of the different rare earth elements in zircon has been shown to vary according to the environment in which the zircon formed or was modified (e.g. Bea et al., 1994; Rubatto, 2002; Whitehouse and Kamber, 2003; Rubatto and Hermann, 2006). For example, zircon grown from a felsic-intermediate magma typically has a steeply positive chondrite-normalised La-Lu profile due to a preference for the smaller ionic radius heavier REEs over the larger lighter REEs (Murali et al., 1983; Hinton and Upton, 1991; Hoskin and Ireland, 2000; Whitehouse and Kamber, 2003). Zircon formed or modified during metamorphism, however, may deviate from this pattern (e.g. Kelly and Harley, 2005a). The REE composition of zircon that grows or is modified during metamorphism will be affected by concurrent growth or resorption of other REE-sequestering minerals such as garnet, which sequesters heavy REEs (Rubatto, 2002; Whitehouse and Platt, 2003), monazite, which sequesters light REEs (Bea and Montero, 1999; Schaltegger et al., 1999; Rubatto et al., 2001), or amphibole, which sequesters middle REEs (Davidson et al., 2007). Therefore, REE profiles of zircons can assist in investigations of zircon petrogenesis and potentially link zircon CL domains to metamorphic assemblages in the host rock (e.g. Whitehouse and Kamber, 2003; Kelly and Harley, 2005a).

The majority of zircon analyses from Badcall Point show a typical magmatic zircon REE profile of increasing chondrite-normalised La-Lu with a positive Ce anomaly and a negative Eu anomaly (Table 7.3; Fig. 7.6a). Yb/Gd is generally 10-15 (Fig. 7.7) which is lower than that measured by Kelly and Harley (2005a) for magmatic zircon (Yb/Gd = 20-30). There is no clear distinction in REE profile between the different CL zoning pattern categories (Fig.

7.6d). A few analyses from Badcall Point deviate from this pattern. A couple of core analyses from samples JM09/BP06 and JM09/BP04 are enriched in Pr-Eu relative to other analyses (Figs. 7.6a&d) and this core analysis from JM09/BP04 has virtually no Eu anomaly (Eu/Eu* = 6.34) (Figs. 7.6a&d, 7.8 & 7.9; Table 7.4). A single analysis from an irregularly-zoned zircon from sample JM09/BP01 has a flat heavy REE profile (Yb/Gd = 1.87) (Table 7.4; Figs. 7.6a&d, 7.8 & 7.9). Four analyses from a an irregularly-zoned zircon from sample JM09/BP06 are relatively depleted in light and middle REEs and have very high Yb/Gd ratios of 72-323 (Table 7.4; Figs. 7.6a&d, 7.8 & 7.9). They also have low Eu contents and no Eu anomaly (Table 7.4; Figs. 7.6a&d).

The majority of zircon analyses from Duartmore Point also show a typical magmatic zircon REE profile, regardless of sample or CL zoning pattern (Table 7.4; Figs. 7.6b&e). Like at Badcall Point, typical Yb/Gd ratios are lower than those reported by Kelly and Harley (2005a) for magmatic zircon with the majority in the range of ~8-15 (Table 7.4; Figs. 7.8 & 7.9). One core analysis from sample JM09/DP01 has a lower Yb/Gd of 3.28 and therefore has a relatively flat heavy REE profile (Table 7.4; Figs. 7.6b&e, 7.8 & 7.9). Eu/Eu* values are generally higher than at Badcall Point (almost all are >1) and Eu anomalies are generally less pronounced (Table 7.4; Figs. 7.6b&e, 7.8 & 7.9).

There is more variety in REE profile in zircons from Sithean Mor. The majority of analyses, especially the irregularly-zoned zircons from sample JM08/23, have pronounced negative Eu anomalies and Eu/Eu* values of <0.5 (Table 7.4; Figs. 7.8 & 7.9). The negative Eu anomaly is also found in zircons from sample JM08/22 but is not as pronounced. Most notable in the analyses from Sithean Mor is the presence of flat heavy REE patterns; in all bar two of the analyses Yb/Gd is <7 (Table 7.4; Figs. 7.6c&f, 7.8 & 7.9). The highest two Yb/Gd values are from a single phase zircon while the two analyses from zircon rims have Yb/Gd of <1. Zircon cores and irregularly-zoned zircons have a range of Yb/Gd values of ~1-7 (Table 7.4; Fig. 7.8 & 7.9).

Table 7.3 Ion microprobe zircon trace element data (ppm). CL zoning pattern identifiers as Table 7.2.

Sample/spot	CL Zoning Pattern	Ti	Ba	La	Ce	Pr	Nd	Sm	Eu	Gd	Tb	Dy	Ho	Er	Tm	Yb	Lu	Yb/Gd	Eu/Eu*	Ce/Ce*
JM09/BP02																				
GMBP02Z1-1	sp	15.43	0.834	0.248	35.8	1.36	2.51	10.96	6.91	42.1	63.0	114.0	181.2	306.1	418.7	548.7	833.5	13.04	0.95	28.18
GMBP02Z1-2	sp	15.90	1.109	0.251	34.5	1.25	2.65	12.01	8.34	39.3	63.7	114.0	175.8	292.5	431.7	517.3	821.5	13.16	1.16	28.19
GMBP02Z2-1	ir	17.75	0.741	0.160	25.8	1.10	2.65	8.83	8.16	24.4	41.9	63.8	111.4	167.5	248.7	308.1	498.3	12.64	1.42	22.98
GMBP02Z2-2	ir	16.89	0.614	0.191	26.2	1.31	2.47	9.57	7.97	25.4	42.6	73.6	106.1	169.7	247.1	299.3	463.8	11.79	1.35	21.39
JM09/BP01																				
BP01Z1-1	ir	18.66	0.917	0.313	20.3	1.15	2.21	8.88	6.47	21.2	24.1	30.6	32.4	40.3	43.2	39.7	58.2	1.87	1.18	16.79
GMBP01Z2-1	ir	14.53	0.465	0.420	26.7	1.56	3.53	10.43	7.68	38.0	66.7	121.9	204.1	362.9	511.3	661.6	997.2	17.41	1.10	18.97
JM09/BP06																				
BP06ChZ1-1	r (br)	17.13	0.317	0.303	31.3	1.24	2.64	8.30	8.76	21.1	24.0	35.5	46.0	64.5	84.2	107.8	165.9	5.10	1.62	25.22
BP06ChZ1-2	c (ozp)	14.64	0.352	0.456	46.7	1.57	5.18	20.96	19.17	62.3	104.1	180.1	298.4	515.8	814.1	1177.9	1976.7	18.91	2.10	32.82
BP06ChZ2-1	c (ozp)	15.84	0.987	0.262	25.2	1.06	2.83	21.87	16.19	92.2	168.9	294.1	476.4	755.8	1011.6	1266.6	1750.1	13.73	1.52	21.93
BP06ChZ2-2	c (ozp)	14.53	0.977	3.202	22.3	1.74	3.08	14.79	15.24	58.2	108.7	191.8	318.6	530.7	681.4	893.1	1297.2	15.33	1.78	10.05
BP06ChZ2-3	c (ozp)	18.16	0.699	0.380	31.6	3.98	12.83	57.67	29.24	159.6	263.4	436.6	676.6	1039.9	1337.9	1684.1	2405.9	10.55	1.98	15.15
BP06ChZ2-6	r (dr)	19.42	0.451	1.008	45.1	1.99	4.67	20.35	8.80	60.6	106.7	177.6	287.0	493.5	698.2	878.2	1317.1	14.50	0.98	26.06
BP06ChZ2-7	ir (emb)	12.15	0.804	0.163	14.3	0.61	0.77	5.66	4.45	20.5	40.5	79.7	145.3	243.3	364.2	492.3	826.2	23.97	0.87	16.22
BP06ChZ2-9	r (dr)	17.58	0.808	1.983	69.4	3.62	5.50	19.07	11.54	50.9	83.9	143.5	224.1	364.0	542.8	692.7	1042.1	13.62	1.38	29.33
BP06Z3-1	ir	12.61	0.502	0.649	6.7	0.59	0.29	1.49	3.13	6.2	21.0	70.8	183.1	459.7	850.6	1358.7	2354.3	219.13	1.13	6.05
BP06Z3-2	ir	16.84	0.627	0.493	5.6	0.54	0.34	1.68	3.82	6.3	27.0	95.6	269.1	709.2	1370.3	2042.0	3485.7	322.94	1.35	5.55
BP06Z3-3	ir	10.52	0.485	0.775	34.6	2.02	3.31	12.20	9.47	32.8	47.0	82.4	146.8	329.5	597.0	889.7	1646.8	27.16	1.41	20.74
BP06Z3-4	ir	14.23	0.557	0.093	1.6	0.25	0.13	1.15	1.70	2.1	3.6	11.9	30.9	75.1	125.0	213.2	359.9	100.05	0.94	2.81
BP06Z3-5	ir	14.81	0.354	0.224	5.3	0.67	0.29	2.26	2.81	6.6	15.9	39.4	90.5	189.3	318.7	478.3	783.7	72.02	0.94	5.64
GMBP06Z1-1	r (br)	18.62	0.711	0.473	29.8	1.70	4.34	18.42	9.20	57.7	91.4	148.2	235.4	370.4	497.8	690.1	922.1	11.96	1.05	20.20
GMBP06Z1-2	r (br)	17.87	0.549	0.331	28.6	1.65	2.79	13.86	8.16	40.9	62.5	106.2	159.3	261.6	339.8	444.6	621.5	10.88	1.10	20.34
GMBP06Z1-3	c (bc)	15.66	0.954	0.412	23.3	0.60	2.25	8.85	6.16	44.0	68.5	131.7	213.3	323.4	453.4	580.0	786.1	13.19	0.85	23.23
GMBP06Z2-1	ir (emb)	16.72	0.392	0.280	39.1	1.84	7.05	20.41	13.06	59.6	97.2	168.1	271.7	385.9	507.9	647.3	1094.6	10.86	1.46	26.86
GMBP06Z2-2	c (ozp)	18.75	0.428	0.157	38.7	1.46	5.09	27.35	18.71	113.0	182.7	298.1	456.1	675.5	889.8	1014.7	1678.2	8.98	1.58	30.39
GMBP06Z3-1	r (br)	15.39	0.611	0.295	27.1	0.52	1.65	5.15	4.64	41.5	67.2	121.2	179.0	295.4	375.0	464.3	739.7	11.18	0.68	30.06
GMBP06Z3-2	r (br)	14.84	0.635	0.063	24.4	0.87	1.63	10.50	4.91	36.0	56.8	104.8	155.6	270.3	375.0	393.2	697.6	10.92	0.72	25.30
GMBP06Z3-3	c (dc)	16.38	0.315	0.291	26.8	0.52	3.05	8.84	3.43	47.4	92.9	138.2	235.1	315.9	475.5	529.3	767.8	11.17	0.46	29.70

(continued)

Table 7.3 (cont.)

Sample/spot	CL Zoning Pattern	Ti	Ba	La	Ce	Pr	Nd	Sm	Eu	Gd	Tb	Dy	Ho	Er	Tm	Yb	Lu	Yb/Gd	Eu/Eu*	Ce/Ce*
JM09/BP06 (continued)																				
GMBP06Z4-1	r	15.00	0.885	0.284	30.0	2.04	4.50	24.92	15.07	80.8	127.7	212.8	330.7	514.8	657.8	853.0	1130.7	10.56	1.47	19.68
GMBP06Z4-2	c (bc)	15.78	0.604	0.322	27.1	1.23	3.03	12.24	7.06	38.4	59.3	97.0	151.3	241.4	335.1	441.8	622.5	11.50	0.99	21.73
GMBP06Z4-3	c (bc)	13.78	0.617	0.315	27.1	1.29	3.79	16.51	11.17	50.0	81.8	131.7	206.0	331.2	447.5	548.4	818.4	10.97	1.37	21.38
GMBP06Z4-4	r	14.48	0.606	0.188	29.7	1.94	4.86	23.39	14.24	76.0	128.2	211.3	336.4	508.1	661.0	872.7	1179.0	11.48	1.43	20.33
GMBP06Z5-1	r (br)	15.83	0.316	0.435	25.9	0.40	2.03	9.89	3.15	33.5	61.5	93.8	166.1	276.0	377.1	447.6	773.9	13.38	0.48	28.38
GMBP06Z5-2	c (dc)	14.60	0.450	0.283	43.2	0.72	2.95	12.67	5.72	70.2	111.8	212.4	365.3	565.4	860.9	1101.4	1763.6	15.70	0.63	42.99
GMBP06Z6-1	ir	23.72	0.511	0.246	36.1	1.70	5.50	16.56	8.14	74.7	111.7	199.9	317.9	491.0	653.4	806.6	1222.3	10.80	0.85	25.88
JM09/BP04																				
GMBP04Z1-1	r (br)	17.26	0.206	0.325	38.8	1.03	6.42	15.54	8.33	54.8	84.0	149.4	229.3	368.8	500.3	592.0	934.0	10.80	0.99	33.33
GMBP04Z1-2	r (br)	18.30	0.233	0.178	44.2	1.44	4.77	22.46	12.84	73.8	124.9	210.4	316.4	530.1	697.1	835.8	1320.1	11.33	1.31	34.75
GMBP04Z2-1	r (br)	16.95	0.389	0.178	33.2	0.89	2.14	11.31	7.67	24.8	40.4	57.3	78.2	124.7	200.8	238.4	349.9	9.61	1.28	32.17
GMBP04Z2-2	r (br)	11.89	0.488	0.030	36.9	1.33	2.84	11.89	6.61	40.2	76.2	128.8	198.2	296.2	485.3	576.3	861.0	14.34	0.92	31.66
GMBP04Z3-1	c (bc)	16.13	1.254	1.899	33.1	10.21	22.42	79.01	99.26	166.1	215.9	280.3	380.0	541.0	684.6	814.0	1135.2	4.90	6.34	9.51
GMBP04Z3-2	c (bc)	16.25	1.439	0.353	34.3	1.26	2.66	12.53	7.91	35.9	66.3	110.3	171.4	284.9	382.2	492.9	701.0	13.71	1.14	26.95
GMBP04Z4-1	r (br)	13.81	0.935	0.435	42.7	2.87	7.89	18.80	8.42	43.7	69.8	122.0	190.9	293.5	385.9	488.0	808.8	11.18	1.07	23.50
GMBP04Z4-2	r (br)	14.81	0.166	0.287	42.6	2.51	7.14	14.26	9.27	50.7	76.6	115.7	185.7	239.2	346.7	478.1	781.8	9.43	1.15	25.47
GMBP04Z4-3	c (dc)	8.58	0.148	1.305	32.1	1.88	3.98	6.78	8.18	27.2	47.7	75.3	128.6	204.9	343.2	429.8	697.5	15.80	1.40	17.97
GMBP04Z5-1	sp	17.10	0.242	0.338	33.0	1.53	4.85	17.50	8.09	50.3	78.9	142.9	222.3	316.5	466.2	574.6	922.4	11.42	0.98	24.16
GMBP04Z5-2	sp	17.30	0.664	0.228	31.8	1.36	5.71	18.21	12.77	57.6	89.8	138.1	247.7	350.5	512.9	533.8	994.8	9.26	1.47	25.22
GMBP04Z6-1	r (br)	18.91	0.243	0.189	30.8	1.35	4.12	12.19	4.90	38.6	74.3	113.8	187.9	278.8	415.1	513.6	820.2	13.30	0.69	24.79
GMBP04Z6-2	c (ozp)	19.13	0.304	0.142	39.9	1.95	5.06	21.07	12.72	65.1	108.7	187.8	304.8	483.1	603.0	781.6	1184.7	12.01	1.37	27.63
GMBP04Z7-1	sp	21.06	0.277	0.141	32.3	0.90	2.99	12.50	7.75	33.9	57.4	100.3	151.8	246.0	309.4	440.5	674.4	13.01	1.14	31.64
GMBP04Z7-2	sp	18.59	0.007	0.258	32.9	1.15	4.09	15.07	6.57	46.9	67.7	125.7	180.5	273.9	416.6	515.7	824.6	10.99	0.83	27.76
GMBP04Z7-3	sp	20.74	0.109	0.186	29.8	1.31	1.90	17.59	4.44	38.2	56.6	102.9	167.1	269.2	391.6	426.6	770.9	11.17	0.59	24.35
GMBP04Z8-2	sp	19.12	0.928	0.313	30.5	1.63	3.62	15.61	9.84	48.7	78.5	130.2	201.4	324.5	433.4	526.6	808.3	10.81	1.23	21.86
GMBP04Z8-3	sp	16.61	0.828	0.252	32.4	1.62	3.80	15.34	12.65	55.8	88.7	141.1	225.9	341.9	479.5	608.7	866.6	10.91	1.50	23.74
GMBP04Z9-1	sp	16.60	0.220	0.196	32.8	1.48	3.53	14.04	7.79	47.8	83.2	124.4	211.3	306.2	437.9	523.9	901.5	10.96	0.99	25.33
GMBP04Z9-2	sp	14.82	0.159	0.185	34.2	1.33	3.66	11.61	8.00	38.7	62.9	75.3	126.4	217.4	266.2	324.6	558.0	8.39	1.13	27.79

(continued)

Table 7.3 (cont.)

Sample/spot	CL Zoning Pattern	Ti	Ba	La	Ce	Pr	Nd	Sm	Eu	Gd	Tb	Dy	Ho	Er	Tm	Yb	Lu	Yb/Gd	Eu/Eu*	Ce/Ce*
JM09/BP04 (continued)																				
JM09/DP03																				
GMDP03Z1-1	r (br)	13.09	0.380	0.207	29.0	1.14	2.11	13.05	10.24	43.9	71.8	112.4	192.3	314.7	450.7	607.2	879.2	13.84	1.36	24.97
GMDP03Z1-2	r (br)	12.66	0.601	0.236	24.6	0.91	2.32	9.96	9.25	33.1	52.0	83.7	137.4	222.7	320.4	431.0	645.8	13.03	1.41	23.02
GMDP03Z1-3	c (ozp)	6.71	0.655	0.385	34.2	0.88	3.28	16.41	18.27	62.4	94.4	168.1	267.0	445.9	621.2	818.0	1186.9	13.10	2.06	30.34
GMDP03Z1-4	r (br)	14.07	0.251	0.357	27.0	1.01	2.23	11.11	10.21	34.3	53.2	92.5	145.9	244.3	343.9	459.1	686.6	13.38	1.51	23.14
GMDP03Z1-5	r (br)	13.03	1.335	0.538	28.4	1.99	4.00	16.92	16.06	45.2	71.6	112.6	173.2	294.5	420.4	575.8	874.4	12.73	2.04	17.89
GMDP03Z2-1	c (ozp)	19.64	0.435	0.580	8.3	1.02	1.92	10.59	20.72	49.7	97.4	177.0	311.6	516.6	733.2	1000.7	1492.3	20.15	2.67	6.59
DP03Z2-1	sp	19.41	0.698	2.283	32.1	3.98	7.48	16.61	18.49	34.8	41.8	60.4	74.9	123.3	155.4	224.8	303.6	6.46	2.58	12.81
JM09/DP01																				
DP01Z4-1	sp	17.78	0.663	0.252	35.5	0.99	2.66	15.05	8.67	55.4	94.5	167.4	257.2	424.1	569.6	724.5	1073.9	13.09	1.03	31.92
DP01Z4-2	sp	16.39	0.647	0.334	32.4	0.89	2.25	13.18	7.37	48.7	84.2	145.7	232.1	389.0	510.3	626.4	932.5	12.86	0.94	29.25
DP01Z6-1	r (br)	17.14	1.115	0.577	29.5	1.80	4.10	16.78	12.57	52.5	73.4	117.6	180.9	276.9	364.6	446.3	671.0	8.50	1.51	19.13
DP01Z6-2	r (br)	15.90	0.811	0.348	27.6	1.51	4.11	15.71	12.36	47.4	73.5	114.4	166.5	262.2	363.1	435.0	648.4	9.17	1.55	20.25
DP01Z6-3	c (dc)	15.09	0.584	0.357	31.4	1.03	2.49	9.47	7.09	24.0	32.1	53.1	74.7	101.4	136.6	159.8	253.1	6.65	1.22	26.64
DP01Z6-4	r (br)	17.78	0.529	0.470	26.4	1.82	3.03	14.73	12.85	40.3	60.4	95.1	142.0	220.2	304.1	377.0	547.7	9.36	1.73	17.48
DP01Z6-5	r (br)	18.59	0.581	0.610	26.9	1.53	4.18	16.49	14.28	48.5	72.5	113.8	171.5	252.7	355.0	452.9	624.4	9.34	1.77	18.42
DP01Z10-1	r (br)	20.28	0.908	0.835	32.4	2.10	4.01	15.13	16.79	39.5	62.2	96.9	141.8	219.1	279.8	372.9	540.4	9.43	2.27	18.87
DP01Z10-2	r (br)	19.81	0.613	0.380	25.6	1.35	3.44	13.46	9.75	39.5	59.7	98.3	149.9	221.4	318.8	393.0	565.1	9.95	1.34	19.43
DP01Z10-3	r (br)	15.75	1.028	0.144	24.5	1.20	2.30	11.07	9.49	28.6	44.0	68.7	113.4	168.6	222.3	280.4	403.4	9.79	1.51	21.12
GMDP01Z1-1	r (br)	13.32	0.639	0.286	27.2	0.78	1.18	7.36	4.66	27.7	50.5	82.0	131.7	222.5	341.8	435.8	690.4	15.74	0.79	26.29
GMDP01Z1-2	r (br)	8.32	0.834	0.211	26.6	0.98	1.59	8.07	7.52	23.1	46.2	83.1	135.1	232.3	340.5	467.3	697.6	20.26	1.35	24.40
GMDP01Z2-1	r (br)	14.94	0.338	0.283	20.9	0.89	2.29	10.76	8.53	32.7	51.1	82.1	120.7	186.0	255.7	339.4	475.4	10.39	1.29	19.34
GMDP01Z2-2	c (dc)	14.87	0.649	0.253	25.2	0.90	1.48	5.81	6.28	17.1	30.2	46.9	67.6	111.5	154.2	205.6	304.6	12.00	1.31	23.49
GMDP01Z2-4	c (dc)	14.15	0.539	0.297	28.0	1.08	3.06	16.49	16.55	50.2	69.0	94.2	109.6	130.6	140.8	164.7	181.0	3.28	2.03	23.82
GMDP01Z2-5	r (br)	15.15	0.428	0.284	19.8	1.16	2.10	9.16	7.69	28.5	44.7	72.5	110.4	172.4	245.6	309.4	491.0	10.87	1.25	16.46
GMDP01Z3-1	sp	20.75	0.957	0.554	24.7	1.74	3.68	14.71	13.21	46.4	78.7	118.4	184.5	288.7	371.7	478.1	714.3	10.31	1.69	16.33
GMDP01Z4-1	sp	9.95	0.532	0.237	27.2	1.58	3.69	12.89	10.67	36.2	54.6	87.6	131.6	198.6	270.3	334.2	463.8	9.24	1.52	20.19
GMDP01Z4-2	sp	12.78	0.136	0.497	26.1	1.92	3.51	15.31	12.82	42.6	58.4	93.0	139.5	217.2	293.2	378.8	533.6	8.89	1.68	16.81

(continued)

Table 7.3 (cont.)

Sample/spot	CL Zoning Pattern	Ti	Ba	La	Ce	Pr	Nd	Sm	Eu	Gd	Tb	Dy	Ho	Er	Tm	Yb	Lu	Yb/Gd	Eu/Eu*	Ce/Ce*
JM09/DP01 (continued)																				
GMDP01Z5-1	c (dc)	10.81	0.894	0.469	14.9	0.62	2.04	8.01	9.60	27.9	44.0	72.1	108.1	174.9	241.3	302.8	490.6	10.85	1.60	14.29
GMDP01Z5-2	r (br)	17.20	1.265	0.346	21.1	1.17	2.53	8.11	5.61	22.5	35.5	55.9	84.8	133.3	166.3	222.9	338.4	9.90	1.01	17.08
GMDP01Z6-1	r (br)	13.70	0.755	0.142	24.1	0.72	1.98	9.97	7.38	29.1	50.0	86.0	137.3	218.9	312.2	428.9	599.3	14.74	1.18	25.98
GMDP01Z6-2	r (br)	14.19	0.748	0.262	21.3	0.76	1.55	7.87	8.52	28.6	47.3	80.7	134.9	224.7	321.7	433.8	644.9	15.17	1.41	21.07
GMDP01Z6-3	c (dc)	13.87	0.408	0.293	24.9	0.80	1.88	8.03	8.25	26.4	44.1	71.3	114.2	186.2	272.3	379.4	583.4	14.38	1.41	23.86
GMDP01Z7-1	sp	19.31	0.641	0.403	25.0	1.55	3.89	12.37	12.06	40.3	64.8	97.5	148.9	238.0	308.6	391.3	568.7	9.72	1.66	17.89
GMDP01Z8-1	r (br)	15.34	1.410	0.215	24.6	0.73	2.12	11.50	8.74	33.5	59.0	105.2	173.2	280.5	387.5	531.9	846.1	15.86	1.30	25.30
GMDP01Z9-3	ir	13.42	1.287	0.080	25.9	1.05	1.92	10.33	7.30	27.1	42.2	59.2	84.9	124.6	158.8	213.1	293.0	7.87	1.19	24.38
JM08/22																				
GM22Z1-1	c (ozp)	21.31	0.145	0.623	27.8	4.98	16.33	87.52	42.92	230.9	314.3	444.7	583.3	759.4	985.4	1013.3	1667.5	4.39	2.41	11.76
GM22Z1-2	c (bc)	19.97	0.110	0.284	40.2	6.69	19.49	90.32	48.48	245.6	343.9	477.5	619.2	807.7	1041.6	1137.0	1789.9	4.63	2.65	15.22
GM22Z2-1	c (ozp)	22.97	0.063	0.202	5.0	1.51	2.86	19.80	3.19	50.1	44.7	64.2	62.2	60.1	66.1	84.1	94.2	1.68	0.38	3.80
GM22Z3-1	c (ozp)	19.39	0.193	0.277	7.7	1.27	3.56	19.99	15.92	74.3	131.6	199.9	269.7	362.9	452.0	519.5	840.4	6.99	1.64	6.17
GM22Z4-1	ir	19.84	0.156	0.419	19.2	1.01	3.09	17.73	9.63	40.3	61.7	87.5	102.6	132.6	164.6	170.1	204.7	4.22	1.26	16.02
JM08/23																				
GM23Z1-1	ir	17.80	0.872	0.444	28.6	3.82	10.31	48.06	2.85	151.7	212.6	286.9	308.6	330.6	342.1	364.7	428.3	2.40	0.20	13.83
GM23Z2-1	ir	19.54	0.138	0.385	27.9	2.42	6.41	44.56	1.66	136.7	218.9	254.2	303.3	315.9	334.3	365.1	410.7	2.67	0.12	16.65
GM23Z2-2	ir	24.39	0.103	0.573	30.8	3.10	8.75	36.74	5.28	117.5	190.4	284.3	407.7	547.7	696.2	790.7	1063.9	6.73	0.43	16.04
GM23Z4-1	r (br)	24.32	0.098	0.045	11.0	1.77	7.86	25.21	4.49	60.6	58.1	62.5	66.3	62.4	62.5	46.7	69.2	0.77	0.49	8.15
GM23Z4-2	r (br)	25.19	0.263	1.430	14.5	2.80	8.88	28.35	14.41	55.5	58.4	57.7	54.3	50.4	50.1	53.7	61.2	0.97	1.57	7.04
GM23Z5-1	sp	20.55	0.340	0.581	30.9	4.52	13.11	26.78	6.80	102.5	167.9	288.0	460.0	693.2	898.2	908.6	1538.6	8.87	0.60	13.68
GM23Z5-2	sp	17.94	0.129	0.153	31.1	2.17	7.58	24.43	4.92	78.3	144.6	220.2	362.9	571.1	605.0	844.0	1248.2	10.78	0.49	20.39
GM23Z6-1	ir	26.69	0.028	0.238	25.9	1.71	7.34	28.61	2.58	95.9	143.8	185.8	224.7	244.5	247.9	259.1	321.9	2.70	0.23	18.54
GM23Z6-2	ir	22.06	0.218	0.325	31.8	3.46	9.97	56.00	3.34	162.6	258.4	317.3	346.0	339.0	318.7	306.0	314.9	1.88	0.23	16.33
GM23Z6-3	ir	24.48	0.230	0.395	36.6	3.02	7.98	48.48	6.60	145.6	233.1	353.8	493.6	703.5	871.8	1001.1	1412.0	6.88	0.47	19.80

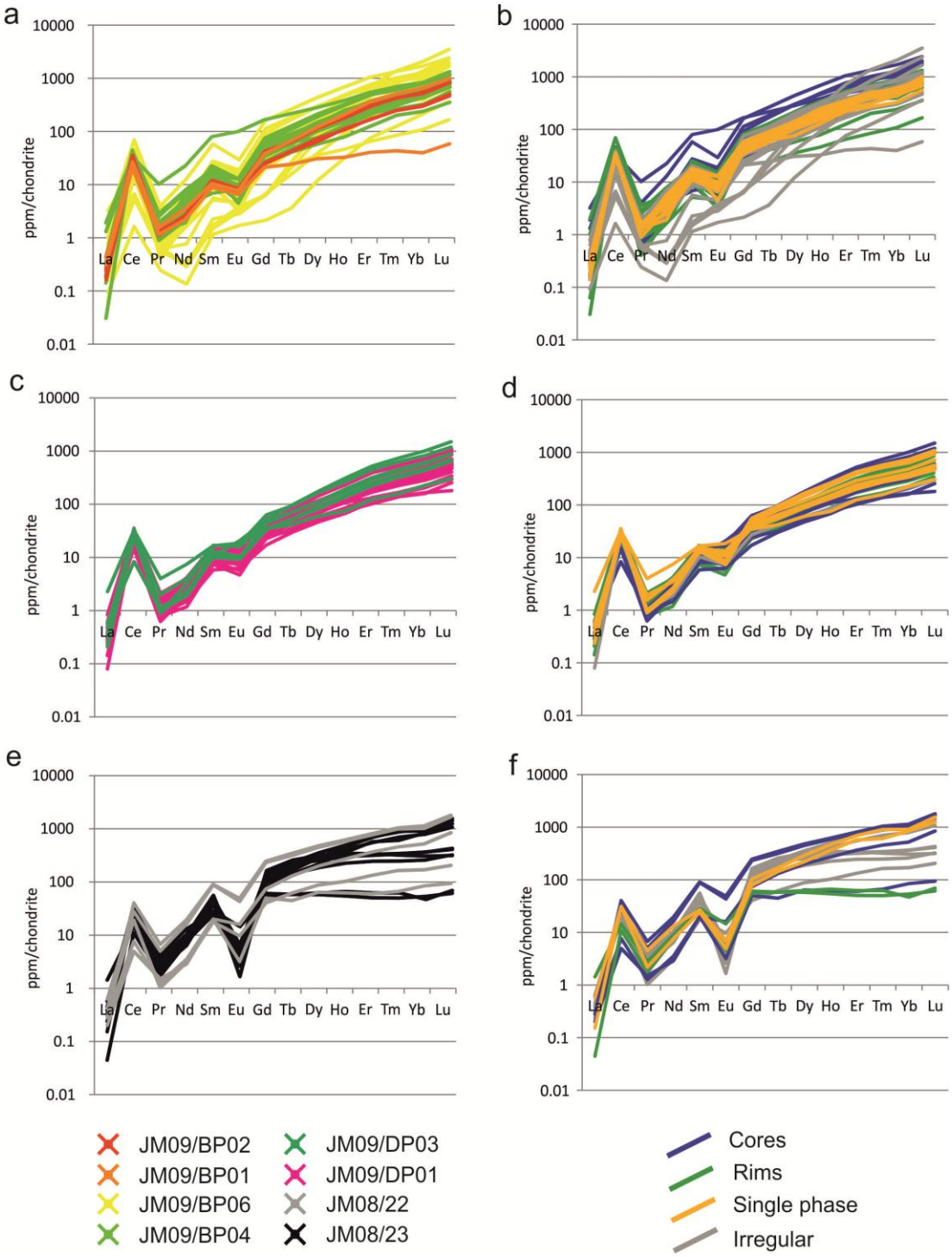

Fig. 7.6 Matsuda plots of zircon rare earth element profiles for: (a) Badcall Point colour-coded by sample; (b) Badcall Point colour-coded by cathodoluminescence zoning pattern; (c) Duartmore Point colour-coded by sample; (d) Duartmore Point colour-coded by cathodoluminescence zoning pattern; (e) Sithean Mor colour-coded by sample; (f) Sithean Mor colour-coded by cathodoluminescence zoning pattern; values normalised against chondrite values of Sun and McDonough (1995).

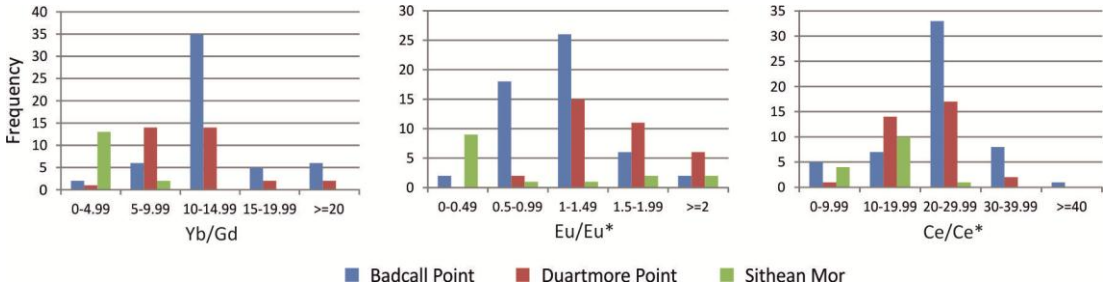

Fig. 7.7 Histograms comparing rare earth element ratios of zircons from Badcall Point, Duartmore Point and Sithean Mor.

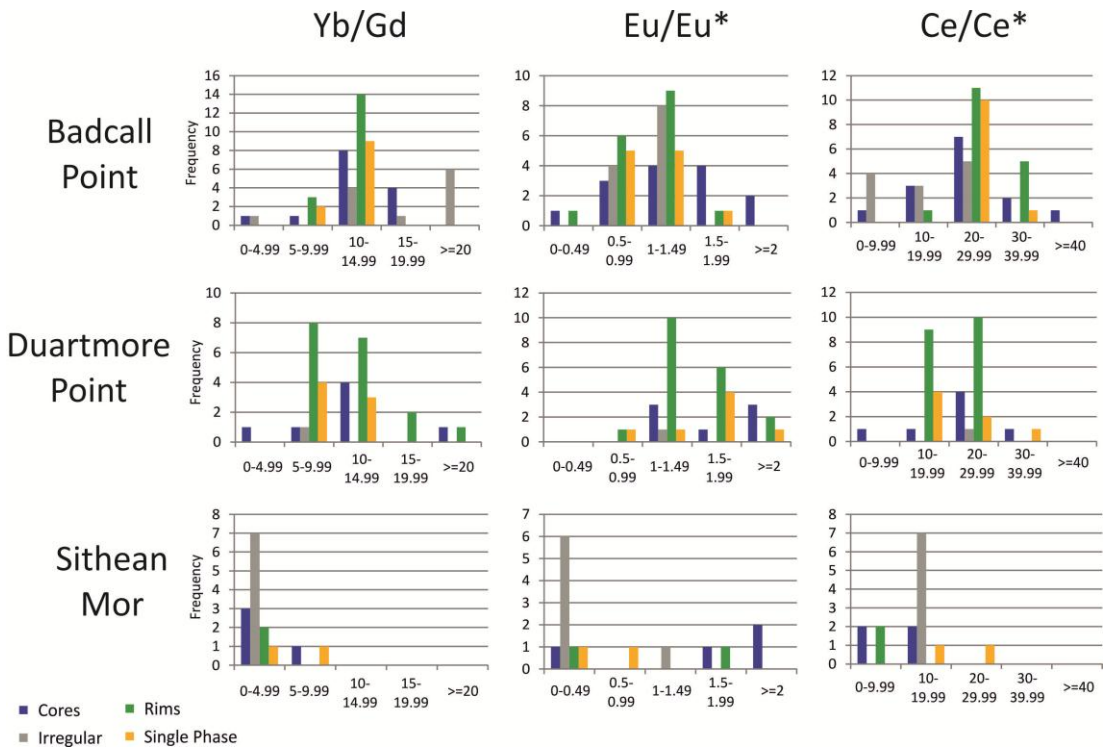

Fig. 7.8 Histograms comparing rare earth element ratios of zircon domains with different cathodoluminescence zoning patterns from Badcall Point, Duartmore Point and Sithean Mor.

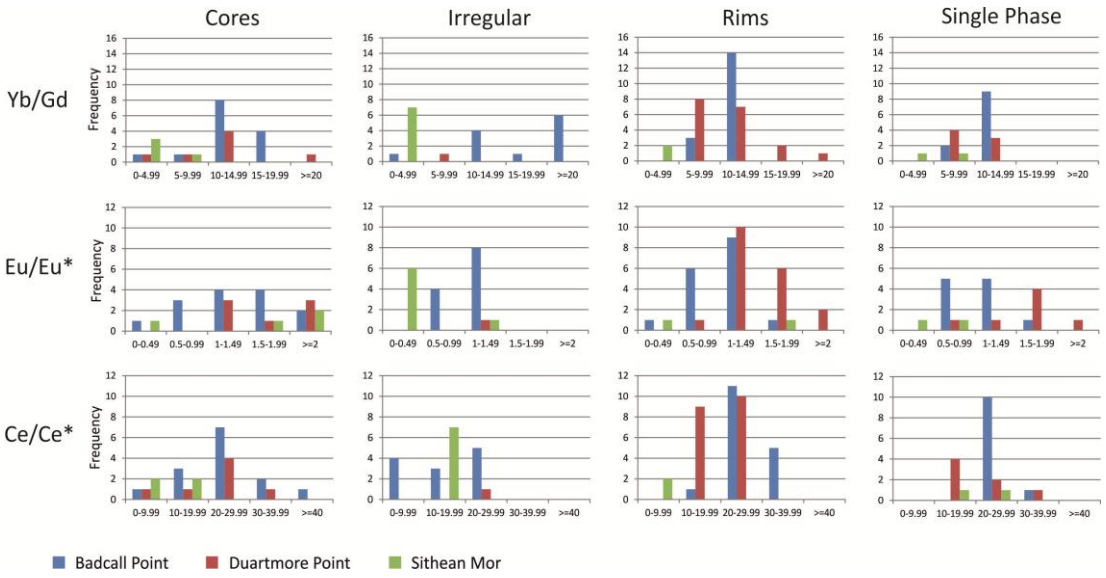

Fig. 7.9 Histograms comparing rare earth element ratios of zircons from Badcall Point, Duartmore Point and Sithean Mor for different categories of cathodoluminescence zoning patterns.

3.5. Zircon Ti

Ti contents of zircons were measured along with U-Th-Pb and REEs so that Ti-in-zircon thermometry (Watson and Harrison, 2005; Watson et al., 2006) could be applied to the LGC for the first time to further the understanding of the temperature history of the Assynt terrane. Ti contents ranged from 6 to 27ppm (Table 7.3). Zircons from Sithean Mor had higher average Ti concentration than Badcall Point and Duartmore Point (Fig. 7.10a; Table 7.5) although there was no clear distinction between the two samples from this locality (Fig. 7.10b; Table 7.5). Zircons from Duartmore Point and Badcall Point had a similar range of Ti concentrations and again there was no clear distinction between samples at each locality (Fig. 7.10b; Table 7.5). There was also no clear correlation between CL zoning pattern category and Ti content (Figs. 7.11a&b; Table 7.5).

Table 7.4 Range, mean and standard deviation on rare earth element ratios of each sample, locality and cathodoluminescence zoning pattern. 1SD denotes 1 standard deviation, %SD denotes the standard deviation as a percentage of the mean. Values in parts per million.

	Yb/Gd				Eu/Eu*				Ce/Ce*			
	Range	Mean	1SD	SD%	Range	Mean	1SD	SD%	Range	Mean	1SD	SD%
JM09/BP02 (n=4)	11.79-13.16	12.66	*0.62*	*4.89*	0.95-1.42	1.22	*0.21*	*17.16*	21.39-28.19	25.19	*3.52*	*13.98*
JM09/BP01 (n=2)	1.87-17.41	9.64	*10.99*	*113.93*	1.10-1.18	1.14	*0.05*	*4.68*	16.79-18.97	17.88	*1.54*	*8.60*
JM09/BP06 (n=28)	5.19-322.94	36.81	*70.51*	*191.58*	0.46-2.10	1.18	*0.43*	*36.43*	2.81-42.99	21.57	*9.27*	*42.97*
JM09/BP04 (n=20)	4.90-15.80	11.17	*2.33*	*20.86*	0.59-6.34	1.38	*1.19*	*86.77*	9.51-34.75	25.98	*5.69*	*21.92*
JM09/DP03 (n=7)	6.46-13.84	13.24	*3.97*	*29.96*	1.36-2.67	1.95	*0.54*	*27.87*	6.59-30.34	19.82	*8.02*	*40.47*
JM09/DP01 (n=27)	3.28-20.26	11.02	*3.41*	*30.98*	0.94-2.27	1.43	*0.33*	*22.82*	14.29-31.92	21.46	*4.36*	*20.30*
JM08/22 (n=5)	1.68-4.63	4.38	*1.88*	*43.01*	0.38-2.65	1.67	*0.91*	*54.64*	3.80-16.02	10.59	*5.43*	*51.25*
JM08/23 (n=10)	0.77-10.78	4.46	*3.55*	*79.49*	0.12-1.57	0.48	*0.41*	*85.85*	7.04-20.39	15.05	*4.52*	*30.02*
Badcall Point (all analyses) (n=54)	1.87-322.94	17.57	*21.11*	*120*	0.46-6.34	1.23	*0.47*	*38*	2.81-42.99	22.65	*5.01*	*22*
Duartmore Point (all analyses) (n=34)	3.28-20.26	12.13	3.69	*30*	0.94-2.67	1.69	0.43	*26*	6.59-31.92	20.64	6.19	*30*
Sithean Mor (all analyses) (n=15)	0.77-10.78	4.42	2.72	*61*	0.12-2.65	1.07	0.66	*62*	3.80-20.39	12.82	4.97	*39*
<u>Badcall Point</u>												
Cores (n=14)	4.90-18.91	12.60	*3.43*	*27*	0.46-6.34	1.68	*1.42*	*85*	9.51-42.99	23.67	*9.06*	*38*
Irregular (n=12)	1.87-322.94	69.22	*100.98*	*146*	0.85-1.46	1.17	*0.23*	*19*	2.81-26.86	15.82	*8.61*	*54*
Rims (n=17)	5.10-14.50	11.39	*2.23*	*20*	0.48-1.62	1.08	*0.32*	*29*	19.68-34.75	26.50	*4.85*	*18*
Single Phase (n=11)	8.39-13.16	11.19	*1.50*	*13*	0.59-1.50	1.09	*0.26*	*24*	21.86-31.64	26.20	*2.77*	*11*
<u>Duartmore Point</u>												
Cores (n=7)	3.28-20.15	11.49	*5.44*	*47*	1.22-2.67	1.76	*0.52*	*30*	6.49-30.34	21.29	*8.10*	*38*
Irregular (n=1)	7.87	7.87			1.19	1.19			24.38	24.38		
Rims (n=18)	8.50-20.26	12.18	*3.15*	*26*	0.79-2.27	1.45	*0.34*	*23*	16.46-26.29	21.03	*3.21*	*15*
Single Phase (n=7)	6.46-13.09	10.08	*2.32*	*23*	0.94-2.58	1.59	*0.54*	*34*	12.81-31.92	20.74	*7.11*	*34*
<u>Sithean Mor</u>												
Cores (n=4)	1.68-6.99	4.42	*2.17*	*49*	0.38-2.65	1.77	*1.02*	*58*	3.80-15.22	9.24	*5.20*	*56*
Irregular (n=7)	1.88-6.88	3.93	*2.09*	*53*	0.12-1.26	0.42	*0.39*	*93*	6.17-19.80	16.74	*1.92*	*11*
Rims (n=2)	0.77-0.97	0.87	*0.14*	*16*	0.49-1.57	1.03	*0.77*	*75*	7.04-8.15	7.59	*0.79*	*10*
Single Phase (n=2)	8.87-10.78	9.82	*1.35*	*14*	0.49-0.60	0.54	*0.08*	*15*	13.68-20.39	17.04	*4.75*	*28*
Cores (all analyses) (n=25)	1.68-20.15	28.51	11.04	*39*	0.38-6.34	5.20	2.96	*57*	3.80-42.99	54.20	22.37	*41*
Irregular (all analyses) (n=20)	1.87-322.94	81.02	103.07	*127*	0.12-1.46	2.78	0.62	*22*	2.81-26.86	56.95	10.53	*18*
Rims (all analyses) (n=38)	0.77-20.26	24.44	5.52	*23*	0.48-2.27	3.56	1.42	*40*	7.04-34.75	55.13	8.85	*16*
Single Phase (all analyses) (n=20)	6.46-13.16	31.10	5.17	*17*	0.49-2.58	3.22	0.88	*27*	12.81-31.92	63.98	14.63	*23*

4. Discussion

4.1. U-Th-Pb

The occurrence of volume diffusion has several implications for determining the chronology of the Assynt Terrane. Firstly, volume diffusion of Pb in zircon potentially compromises the accuracy of the protolith formation age calculated here. If Pb was able to move out of zircons, this could have affected Pb/U ratios in the crystals that yielded the oldest core ages from which the protolith formation age was calculated. Pb loss would generate artificially young ages so the calculated protolith formation age for the TTG gneisses of 2958±7Ma would be a minimum; the true age may be older than this. Volume diffusion would also suggest that the protolith formation ages determined by Whitehouse and Kemp (2010) and Friend and Kinny (1995) are minimum ages.

Second, the depositional age of the metasedimentary rocks at Sithean Mor cannot be constrained. When using zircons to constrain the depositional ages of metasediments, the youngest core age (interpreted to be detrital) is the maximum depositional age while the oldest rim age (interpreted to be metamorphic) is the minimum depositional age. However, at Sithean Mor the oldest rim age (2726±28Ma) is older than the youngest core age (2506±18Ma) so this approach cannot be applied. This is further evidence of volume diffusion of Pb in zircons having occurred.

Third, the age of metamorphic events occurring in the Assynt Terrane cannot be confidently determined. There is field evidence for at least one granulite-facies metamorphism (the Badcallian) and this would be expected to be recorded in the zircon U-Pb systematics, as well as potentially the amphibolite-facies Inverian event. However, the absolute timing of these events has been obscured by volume diffusion. Friend and Kinny (1995) concluded that the youngest age in their spread of concordant zircon ages represented a metamorphic event which caused major Pb-loss, and they suggested that this was the age of the Badcallian metamorphism. Corfu et al. (1994) had previously

suggested the Badcallian occurred at ~2710Ma and Whitehouse and Kemp (2010) attempted to determine if this was a statistically significant age in their concordant age spread but were unable to do so with any confidence.

Table 7.5 Range, mean and standard deviation of zircon Ti from each sample, locality and cathodoluminescence zoning pattern category. 1SD denotes 1 standard deviation, %SD denotes the standard deviation as a percentage of the mean. Values in parts per million.

	Range	Mean	1SD	SD%
Samples				
JM09/BP02 (n=4)	15.43-17.75	16.49	*1.04*	*6.29*
JM09/BP01 (n=2)	14.53-16.89	16.59	*2.92*	*17.58*
JM09/BP06 (n=28)	10.52-23.72	15.92	*2.55*	*16.03*
JM09/BP04 (n=20)	8.58-21.06	16.70	*2.94*	*17.60*
JM09/DP03 (n=7)	6.71-19.64	14.09	*4.43*	*31.44*
JM09/DP01 (n=27)	8.32-20.75	15.43	*3.05*	*19.74*
JM08/22 (n=5)	19.39-22.97	20.70	*1.46*	*7.05*
JM08/23 (n=10)	17.80-26.69	22.30	*3.18*	*14.25*
Badcall Point				
Cores (n=14)	8.58-19.13	15.59	*2.57*	*16.50*
Irregular (n=12)	10.52-23.72	15.78	*3.49*	*22.13*
Rims (n=17)	11.89-19.42	16.36	*2.06*	*12.62*
Single Phase (n=11)	14.82-21.06	17.57	*2.07*	*11.77*
Duartmore Point				
Cores (n=7)	6.71-19.64	13.59	*4.00*	*29.40*
Irregular (n=1)	13.42			
Rims (n=18)	8.32-20.28	15.28	*2.84*	*18.57*
Single Phase (n=7)	9.95-20.75	16.63	*3.93*	*23.64*
Sithean Mor				
Cores (n=4)	19.39-2.97	20.91	*1.59*	*7.61*
Irregular (n=7)	17.80-26.69	22.12	*3.22*	*14.56*
Rims (n=2)	24.32-25.19	24.76	*0.61*	*2.47*
Single Phase (n=2)	17.94-20.55	19.24	*1.84*	*9.56*
Localities				
Badcall Point (all analyses) (n=54)	8.58-23.72	16.43	*2.36*	*14.38*
Duartmore Point (all analyses) (n=34)	6.71-20.75	14.76	*3.74*	*25.32*
Sithean Mor (all analyses) (n=15)	17.80-26.69	21.50	*2.32*	*10.78*
CL Zoning Pattern Categories				
Cores (n=25)	6.71-22.97	15.88	*3.70*	*23.30*
Irregular (n=20)	10.52-26.69	17.88	*4.56*	*25.48*
Rims (n=38)	8.32-25.19	16.26	*3.19*	*19.61*
Single Phase (n=20)	9.95-21.06	17.41	*2.81*	*16.15*

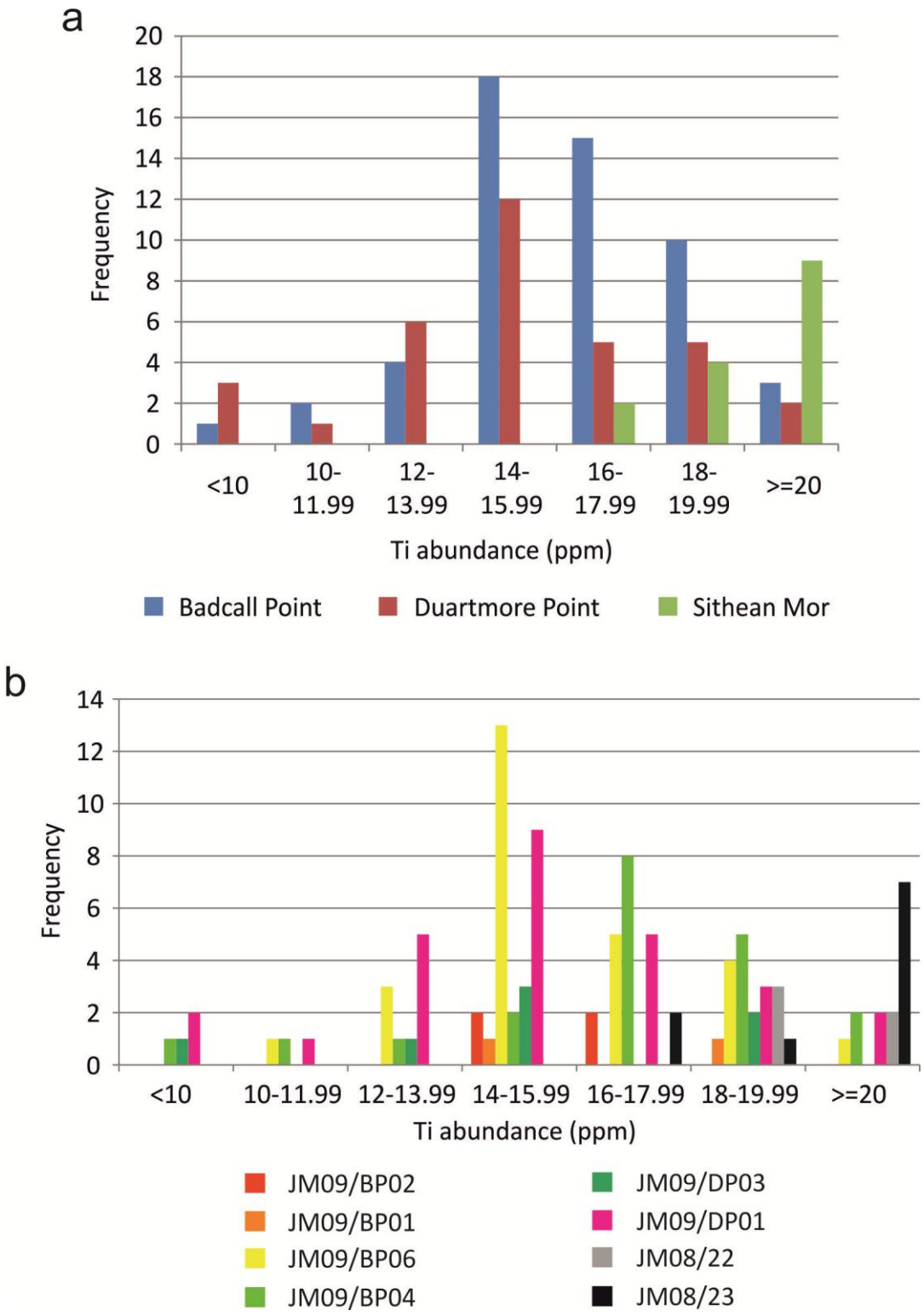

Fig. 7.10 (a) Histogram of Ti concentration (ppm) in zircons from each locality. (b) Histogram of Ti concentration in zircons from each sample.

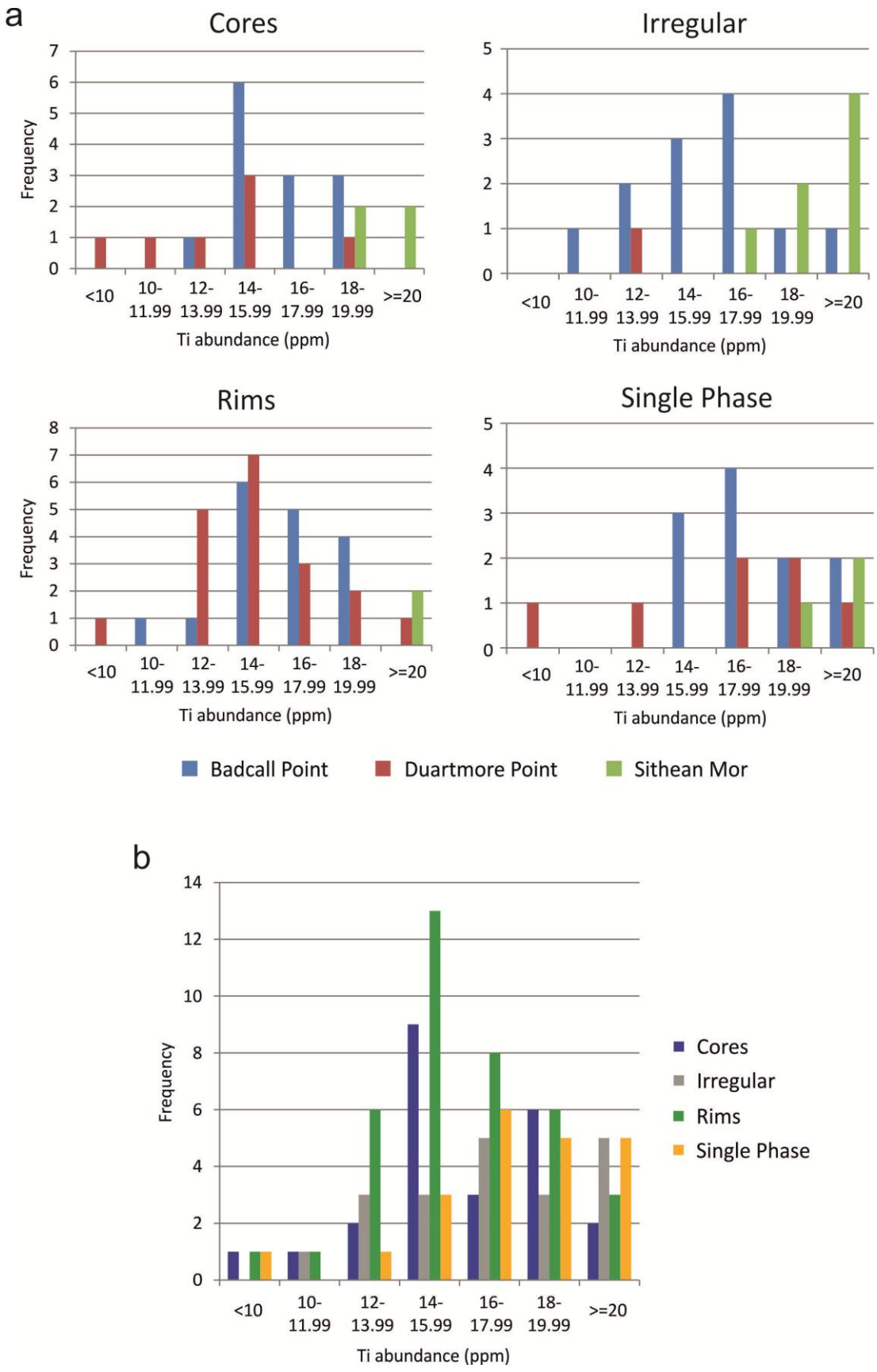

Fig. 7.11 (a) Histogram comparing Ti concentration (ppm) in zircons with different cathodoluminescence zoning patterns from each locality. (b) Histogram of Ti concentration in zircons for each cathodoluminescence zoning patterns from each locality.

The youngest age of the spread caused by volume diffusion in this study represents the time at which volume diffusion of Pb in zircon ceased. The youngest age in this population (2384±46Ma) is from a zircon rim from sample JM09/BP06 but is 46Myr younger than the next youngest age and is reversely discordant by 2%. Adopting the approach used above to attempt to determine a protolith formation age but rejecting the oldest ages until a MSWD threshold is reached, the youngest ten ages (those <2500Ma) yields a mean age of 2479±12Ma (MSWD = 3.1, probability 0.001). As more ages are excluded, the MSWD only increases but by rejecting the 2384±46Ma and taking the next nine oldest ages, the MSWD drops to 1.3. Only by rejecting the next youngest age (2430±44Ma) as well, however, does the MSWD drop below 1 – the next eight oldest ages (ranging from 2459±46Ma to 2494±28Ma) yield a mean age of 2482±6Ma (MSWD = 0.69, probability = 0.68). This age is interpreted to reflect the cessation of volume diffusion of Pb in zircons.

Volume diffusion would not have ceased at peak metamorphic conditions. A post-peak drop in temperature would cause volume diffusion of Pb in zircon to cease (Cherniak and Watson, 2001; Cherniak and Watson, 2003). This cessation appears to have taken place at ~2482Ma indicating the peak metamorphic conditions of a major tectonothermal event may have shortly predated this. Which tectonothermal event was responsible for the volume diffusion? Zirkler et al. (2012) calculated PT conditions for the Inverian tectonothermal event (characterised by an amphibolite-facies assemblage in the TTG gneisses) of 5-6.5kbar and 520-550°C. Cherniak and Watson (2003) showed that volume of diffusion of Pb in zircon required temperatures of at least ~700°C and over a billion years would be required at that temperature for it to occur. This rules out volume diffusion during the Inverian event. Johnson and White (2011) calculated peak temperatures for the Badcallian tectonothermal event (characterised by a granulite-facies assemblage in the TTG gneisses) of 875-975°C; a temperature of 875°C for 500Myr would allow significant volume diffusion, falling to only 3Myr at a temperature of 975°C. Therefore, the Badcallian clearly

reached temperatures which made volume diffusion of Pb in zircon possible. It remains unclear whether the Badcallian was a short 'event' or a longer high temperature episode, without improved temperature constraints. As volume diffusion of Pb in zircon ceased at ~2482Ma, the Badcallian tectonothermal 'event' would have occurred prior to this. Friend and Kinny (1995) and Whitehouse and Kemp (2010) suggested it occurred at ~2500Ma, an age which would fit with post-peak cessation of volume diffusion at ~2482Ma. The occurrence of high-grade metamorphism at ~2700Ma remains uncertain.

4.2. REEs

The interpretation that there was volume diffusion of Pb in zircon raises the question of whether the REEs were also able to diffuse around or out of the zircons. At the conditions required for volume diffusion of Pb in the Assynt Terrane (3Myr at 975°C to 500Myr at 875°C), there would not be significant diffusion of REEs, perhaps only over a few microns (Cherniak et al., 1997). This is borne out by sharp and fine-scale CL zoning patterns, for example the oscillatory zoning in zircon GMBP04Z6 or the sharp boundary between the CL-bright rim and the core in zircon BP06ChZ1 (Fig. 7.3). This indicates that the REE profiles of the zircons in this population are representative of the zircon petrogenesis.

The similarity in REE profiles and REE abundances between the majority of core and rim analyses at Badcall Point and Duartmore Point indicates that zircon REEs did not interact with REEs in other metamorphic minerals. The presence of REE-sequestering metamorphic minerals such as garnet causes deviation in the pattern of metamorphic zircon rims from that in zircon cores (e.g. Kelly and Harley, 2005a). The general absence of any such deviation, for example a flat chondrite-normalised heavy REE profile if the rim formed in the presence of metamorphic garnet, is best explained by little or no interaction between REEs in zircon and any other minerals in the majority of cases. This is commonly observed in solid-state recrystallization (Hoskin and Black, 2000).

The flat heavy REE profile in one of the two analyses from zircons from sample JM09/BP01 (Inverian TTG gneiss, Badcall Point) suggests that this irregularly-zoned zircon may have formed its current REE profile in the presence of garnet. Garnet has not been documented in the TTG gneisses of the Assynt Terrane, however, and is not stable in tonalites (the dominant rock type in the Assynt Terrane) below 15kbar (Knudsen and Andersen, 1999); such pressures have not been documented in the Assynt Terrane. The cause of this and the few other low Yb/Gd values from zircons from Badcall Point and Duartmore Point remains unclear. Similarly, the relative depletion in Pr-Dy of a single irregularly-zoned zircon from sample JM09/BP06 is also unclear. Amphibole sequesters middle REEs (Davidson et al., 2007) such as those depleted in this zircon, but amphibole is abundant in the TTG gneisses in the Inverian and Laxfordian assemblages and does not seem to have had a similar effect on the REE pattern of any of the other 36 zircons analysed from Badcall Point and Duartmore Point.

The majority of zircons from the TTG gneisses from Badcall Point and Duartmore Point have REE profiles typical of magmatic growth. Zircons from the metasedimentary rocks from Sithean Mor, however, do not. The prevalence of relatively low Yb/Gd ratios and relatively flat chondrite-normalised heavy REE profiles suggests that REE abundance in these zircons has been affected by garnet. Garnet is present in sample JM08/22, and although it was not found in sample JM08/23, it is widely distributed at this locality. The link with garnet has the potential to allow zircon CL zones to be linked to the tectonothermal evolution of the Assynt Terrane (Rubatto, 2002; Whitehouse and Platt, 2003). Phase equilibria modelling by Zirkler et al. (2012) showed that garnet in similar metasedimentary rocks from elsewhere in the Assynt Terrane was part of the Badcallian assemblage. This suggests that the zircon CL zones from Sithean Mor with relatively flat heavy REE profiles re-equilibrated in the presence of garnet during the Badcallian tectonothermal event. Unfortunately there is not a clear correlation between Yb/Gd ratio

and CL zoning pattern as rims, irregularly-zoned crystals and a core analysis all have Yb/Gd ratio of <3. Perhaps a larger number of analyses from this locality (n = 15 in this study) would show a more statistically significant relationship between CL zoning pattern and Yb/Gd. It is also possible, however, that these detrital zircons may have acquired their low Yb/Gd ratios in the source rock and were not significantly reset in the Badcallian but without knowing the composition of the source rock, this is impossible to determine. Kelly and Harley (2005a) used REE profiles to link ages from zircon domains to whole rock assemblages to determine which zircon ages represented magmatic and metamorphic episodes in the Napier Complex in Antarctica but volume diffusion of Pb in zircon in this study means that this approach is not possible due to the heterogeneous resetting of zircon ages.

The zircons from Duartmore Point generally have relatively high Eu/Eu* values. Eu can occur as a divalent or trivalent cation and this is controlled by the oxygen fugacity of the parent magma (e.g. Schreiber et al., 1980; Hinton and Upton, 1991; Hoskin and Schaltegger, 2003). In reducing conditions, there will be more divalent Eu which is relatively incompatible with the tetravalent Zr site and hence there will be a negative Eu anomaly. More oxidising conditions mean more trivalent Eu, which is more compatible in zircon, so that the Eu anomaly will be of a lesser magnitude. The lower magnitude Eu anomaly (i.e. Eu/Eu* is higher) suggesting that the protolith magma at Duartmore Point may have been more oxidised than at Badcall Point. However, a more oxidising magma would result in a greater magnitude of positive Ce anomaly but the Ce/Ce* values for Duartmore Point are not markedly higher than those for Badcall Point (Fig. 7.7). This indicates that the oxygen fugacity of the magma alone is not responsible for the high Eu/Eu*. Furthermore, a positive Ce anomaly indicates oxidising magma conditions while a negative Eu anomaly indicates reducing magma conditions. This paradox may be explained by plagioclase fractionation which depletes divalent Eu from the magma (Snyder et al., 1993; Hoskin, 1998; Hoskin et

al., 2000). Plagioclase is ubiquitous in the TTG gneisses of the Assynt Terrane and wider LGC, both in current metamorphic assemblages and in the protolith magmatic assemblages calculated by CIPW norm (see Chapter 4b). The TTG gneiss samples from Duartmore Point have slightly lower modal percentages of plagioclase than the Badcall Point samples. If the protolith magmas at Duartmore Point were less evolved than those at Badcall Point at the time of zircon crystallisation, less plagioclase would have crystallised and the Eu anomaly in the magma, and the zircon, would be less pronounced.

4.3. Ti-in-Zircon Thermometry

Ti content in zircon is proportional to the crystallisation temperature – this forms the basis of the Ti-in-zircon geothermometer derived by Watson et al. (2006). The thermometer has so far been used mainly to calculate crystallisation temperatures for magmatic zircon in igneous rocks but Baldwin et al. (2007) also used it to calculate the temperature of ultra-high temperature metamorphic zircon from Brazil. Ti contents of zircons were measured along with U-Th-Pb and REEs in this study in this study to investigate zircon crystallisation temperatures in the Assynt Terrane of the LGC.

The accuracy of the temperatures calculated with the Ti-in-zircon thermometer is controlled by a_{TiO2} – the presence of rutile in the rock indicates that $a_{TiO2} = 1$ and Ti content in zircon was buffered. In this situation, the calculated temperatures will be accurate. If there is no rutile present during zircon crystallisation, the system is not buffered and the calculated temperature will be a minimum. However, Ferry and Watson (2007) calibrated the thermometer equation to take into account sub-unity a_{TiO2}; the lowest temperatures are calculated if zircon is assumed to be in equilibrium with rutile ($a_{TiO2} = 1$) while temperature increases as a_{TiO2} decreases.

Accurate temperatures can therefore be calculated for zircons in this study if a_{TiO2} is known but the host rocks are polymetamorphic with field evidence for three

tectonothermal events after protolith formation. Which of these four assemblages was coeval with the Ti-in-zircon thermometer temperature? At a_{TiO2} = 1, the lowest calculated temperature is 710°C but the majority are ~780-800°C (Table 7.6). This is well above the best available peak pressure-temperature estimates for the Inverian (520-550°C, 5-6.5kbar (Zirkler et al., 2012)) and Laxfordian (510-660°C, 5-8kbar (Droop et al., 1999)) tectonothermal events. This leaves the Badcallian tectonothermal event and the magmatic protolith formation as temperatures that could be recorded by the Ti-in-zircon thermometer.

Different rocks may have different a_{TiO2} and zircons from the metasedimentary rocks from Sithean Mor and the TTG gneisses from Badcall Point and Duartmore Point are dealt with separately. For the TTG gneisses, a sample of typical pristine Badcallian granulite-facies gneiss with granoblastic texture and an opx+cpx+plag+qtz assemblage has rutile in its assemblage indicating that a_{TiO2} was 1 in the Badcallian. At a_{TiO2} = 1, the maximum calculated temperature was 834±34°C from an irregularly-zoned zircon from sample JM09/BP06 (Table 7.6). This is below the most recent reliable peak Badcallian temperature estimates of Johnson and White (2011) of 875-975°C and below previously calculated Badcallian peaks (e.g. O' Hara and Yarwood, 1978; Savage and Sills, 1980; Barnicoat, 1987; Sills and Rollinson, 1987). Cherniak and Watson (2007) showed that Ti does not diffuse in zircon at temperatures below 1000°C.

Diffusion is controlled by temperature and time and Cherniak and Watson (2007) showed that to diffuse a distance of 50µm (an approximate average diameter of a rim in zircons in this study) over a period of 10Myr, a temperature of ~1200°C would need to be sustained for this length of time. This is much hotter than the peak Badcallian temperatures of Johnson and White (2011) and so magmatic zircon recrystallizing at Badcallian peak temperatures appears not to have had its Ti signature reset. Any anatectic zircon grown in the Badcallian (for which there is no clear CL evidence, Fig. 7.3) would be expected to

record temperatures within the peak Badcallian temperature range calculated by Johnson and White (2011) but this is not the case.

Table 7.6 Ti-in-zircon crystallisation temperatures calculated using the thermometer of Watson et al. (2006) for TiO_2 activities of 0.5 and 1 reflecting the presence or absence of rutile as a buffer to the thermometer system. CL zoning pattern identifiers as Table 7.2.

Sample/spot	CL Zoning Pattern	Ti (ppm)	T (°C) at a_{TiO2} = 0.5	2σ	T (°C) at a_{TiO2} = 1	2σ
JM09/BP02						
GMBP02Z1-1	sp	863.99	30.73	29	788	28
GMBP02Z1-2	sp	867.54	31.11	29	791	28
GMBP02Z2-1	ir	880.64	32.54	31	803	30
GMBP02Z2-2	ir	874.66	31.88	30	798	29
JM09/BP01						
BP01Z1-1	ir	886.65	33.21	31	808	30
GMBP01Z2-1	ir	857.01	29.99	28	782	27
JM09/BP06						
BP06ChZ1-1	r (br)	876.37	32.07	30	799	29
BP06ChZ1-2	c (ozp)	857.86	30.08	28	783	27
BP06ChZ2-1	c (ozp)	867.09	31.06	29	791	28
BP06ChZ2-2	c (ozp)	857.04	29.99	28	782	27
BP06ChZ2-3	c (ozp)	883.42	32.85	31	805	30
BP06ChZ2-6	r (dr)	891.56	33.77	32	812	31
BP06ChZ2-7	ir (emb)	836.72	27.91	26	765	26
BP06ChZ2-9	r (dr)	879.46	32.41	30	802	30
BP06Z3-1	ir	840.88	28.33	27	768	26
BP06Z3-2	ir	874.31	31.84	30	797	29
BP06Z3-3	ir	820.89	26.37	25	751	24
BP06Z3-4	ir	854.58	29.73	28	780	27
BP06Z3-5	ir	859.21	30.22	28	784	28
GMBP06Z1-1	r (br)	886.44	33.19	31	808	30
GMBP06Z1-2	r (br)	881.44	32.63	31	804	30
GMBP06Z1-3	c (bc)	865.72	30.91	29	790	28
GMBP06Z2-1	ir (emb)	873.46	31.75	30	797	29
GMBP06Z2-2	c (ozp)	887.28	33.28	31	809	30
GMBP06Z3-1	r (br)	863.67	30.69	29	788	28
GMBP06Z3-2	r (br)	859.44	30.24	28	784	28
GMBP06Z3-3	c (dc)	871.01	31.48	30	794	29
GMBP06Z4-1	r	860.70	30.38	29	785	28
GMBP06Z4-2	c (bc)	866.63	31.01	29	791	28
GMBP06Z4-3	c (bc)	850.91	29.35	28	777	27
GMBP06Z4-4	r	856.61	29.95	28	782	27
GMBP06Z5-1	r (br)	866.97	31.05	29	791	28
GMBP06Z5-2	c (dc)	857.56	30.05	28	783	27
GMBP06Z6-1	ir	916.61	36.69	34	834	33

(continued)

Table 7.6 (cont.)

Sample/spot	CL Zoning Pattern	Ti (ppm)	T (°C) at a_{TiO2} = 0.5	2σ	T (°C) at a_{TiO2} = 1	2σ
JM09/BP04						
GMBP04Z1-1	r (br)	877.29	32.17	30	800	29
GMBP04Z1-2	r (br)	884.33	32.95	31	806	30
GMBP04Z2-1	r (br)	875.10	31.93	30	798	29
GMBP04Z2-2	r (br)	834.30	27.67	26	762	25
GMBP04Z3-1	c (bc)	869.24	31.29	29	793	29
GMBP04Z3-2	c (bc)	870.08	31.38	29	794	29
GMBP04Z4-1	r (br)	851.14	29.38	28	777	27
GMBP04Z4-2	r (br)	859.23	30.22	28	784	28
GMBP04Z4-3	c (dc)	799.32	24.38	23	732	22
GMBP04Z5-1	sp	876.16	32.05	30	799	29
GMBP04Z5-2	sp	877.57	32.20	30	800	29
GMBP04Z6-1	r (br)	888.28	33.40	31	809	30
GMBP04Z6-2	c (ozp)	889.70	33.56	31	811	31
GMBP04Z7-1	sp	901.62	34.92	33	821	32
GMBP04Z7-2	sp	886.21	33.16	31	808	30
GMBP04Z7-3	sp	899.67	34.70	33	819	32
GMBP04Z8-2	sp	889.65	33.55	31	811	31
GMBP04Z8-3	sp	872.72	31.67	30	796	29
GMBP04Z9-1	sp	872.62	31.66	30	796	29
GMBP04Z9-2	sp	859.33	30.23	28	784	28
JM09/DP03						
GMDP03Z1-1	r (br)	845.05	28.75	27	772	26
GMDP03Z1-2	r (br)	841.33	28.37	27	769	26
GMDP03Z1-3	c (ozp)	774.35	22.24	21	710	20
GMDP03Z1-4	r (br)	853.28	29.60	28	779	27
GMDP03Z1-5	r (br)	844.61	28.71	27	771	26
GMDP03Z2-1	c (ozp)	892.92	33.92	32	813	31
DP03Z2-1	sp	891.51	33.76	32	812	31
JM09/DP01						
DP01Z4-1	sp	880.85	32.56	31	803	30
DP01Z4-2	sp	871.08	31.49	30	794	29
DP01Z6-1	r (br)	876.44	32.08	30	799	29
DP01Z6-2	r (br)	867.53	31.11	29	791	28
DP01Z6-3	c (dc)	861.41	30.45	29	786	28
DP01Z6-4	r (br)	880.86	32.56	31	803	30
DP01Z6-5	r (br)	886.25	33.17	31	808	30
DP01Z10-1	r (br)	896.90	34.38	32	817	31
DP01Z10-2	r (br)	894.01	34.05	32	814	31
DP01Z10-3	r (br)	866.42	30.99	29	790	28
GMDP01Z1-1	r (br)	847.08	28.96	27	774	26
GMDP01Z1-2	r (br)	796.04	24.09	23	729	22
GMDP01Z2-1	r (br)	860.28	30.33	28	785	28

(continued)

Table 7.6 (cont.)

Sample/spot	CL Zoning Pattern	Ti (ppm)	T (°C) at a_{TiO2} = 0.5	2σ	T (°C) at a_{TiO2} = 1	2σ
GMDP01Z2-2	c (dc)	859.73	30.27	28	785	28
GMDP01Z2-4	c (dc)	853.93	29.67	28	780	27
GMDP01Z2-5	r (br)	861.85	30.50	29	786	28
GMDP01Z3-1	sp	899.75	34.71	33	819	32
GMDP01Z4-1	sp	814.95	25.81	24	745	24
GMDP01Z4-2	sp	842.38	28.48	27	769	26
GMDP01Z5-1	c (dc)	823.88	26.65	25	753	24
GMDP01Z5-2	r (br)	876.85	32.12	30	800	29
GMDP01Z6-1	r (br)	850.30	29.29	28	776	27
GMDP01Z6-2	r (br)	854.32	29.71	28	780	27
GMDP01Z6-3	c (dc)	851.70	29.43	28	778	27
GMDP01Z7-1	sp	890.88	33.69	32	812	31
GMDP01Z8-1	r (br)	863.32	30.66	29	788	28
GMDP01Z9-3	ir	847.95	29.05	27	774	27
JM08/22						
GM22Z1-1	c (ozp)	903.08	35.09	33	822	32
GM22Z1-2	c (bc)	895.00	34.16	32	815	31
GM22Z2-1	c (ozp)	912.53	36.21	34	830	33
GM22Z3-1	c (ozp)	891.39	33.75	32	812	31
GM22Z4-1	ir	894.17	34.06	32	815	31
JM08/23						
GM23Z1-1	ir	880.94	32.57	31	803	30
GM23Z2-1	ir	892.34	33.86	32	813	31
GM23Z2-2	ir	920.22	37.13	35	837	34
GM23Z4-1	r (br)	919.86	37.08	35	837	34
GM23Z4-2	r (br)	924.37	37.63	35	841	34
GM23Z5-1	sp	898.52	34.56	32	818	31
GM23Z5-2	sp	881.94	32.68	31	804	30
GM23Z6-1	ir	931.95	38.56	36	847	35
GM23Z6-2	ir	907.43	35.60	33	826	32
GM23Z6-3	ir	920.71	37.18	35	838	34

The lack of peak Badcallian temperatures recorded by Ti-in-zircon thermometry and the unlikelihood of Ti resetting in recrystallizing zircon suggests that the zircons from TTG gneiss samples did not record Badcallian metamorphic temperatures in their Ti systematics but instead retain the crystallisation temperature of the magmatic protolith. A CIPW normative mineralogy calculated from a dry pristine Badcallian granulite-facies TTG gneiss indicates that rutile was not present in the protolith magmatic rock. In addition to this,

modelling of the fractionation of TTG magmas indicates that any rutile would be left in the mafic restite (e.g. Xiong et al., 2005; Xiong, 2006). The titanium-bearing mineral ilmenite is present in the CIPW normative assemblage and the majority of igneous rocks have an a_{TiO2} of ≥0.5 (Watson and Harrison, 2005) but the protolith a_{TiO2} cannot be well-constrained. Therefore, temperatures calculated at a_{TiO2} = 1 will be minimum temperatures. Maximum temperatures would be calculated at a_{TiO2} = 0.5 and the accurate temperature will be somewhere in between the two. Figure 12 shows the Ti-in-zircon thermometer temperatures at a_{TiO2} = 1 and 0.5 for each zircon analysis. The upper bar in each pair is the maximum temperature (a_{TiO2} = 0.5) and the lower bar is the minimum (a_{TiO2} = 1); the bars include 2σ errors on the temperature calculations.

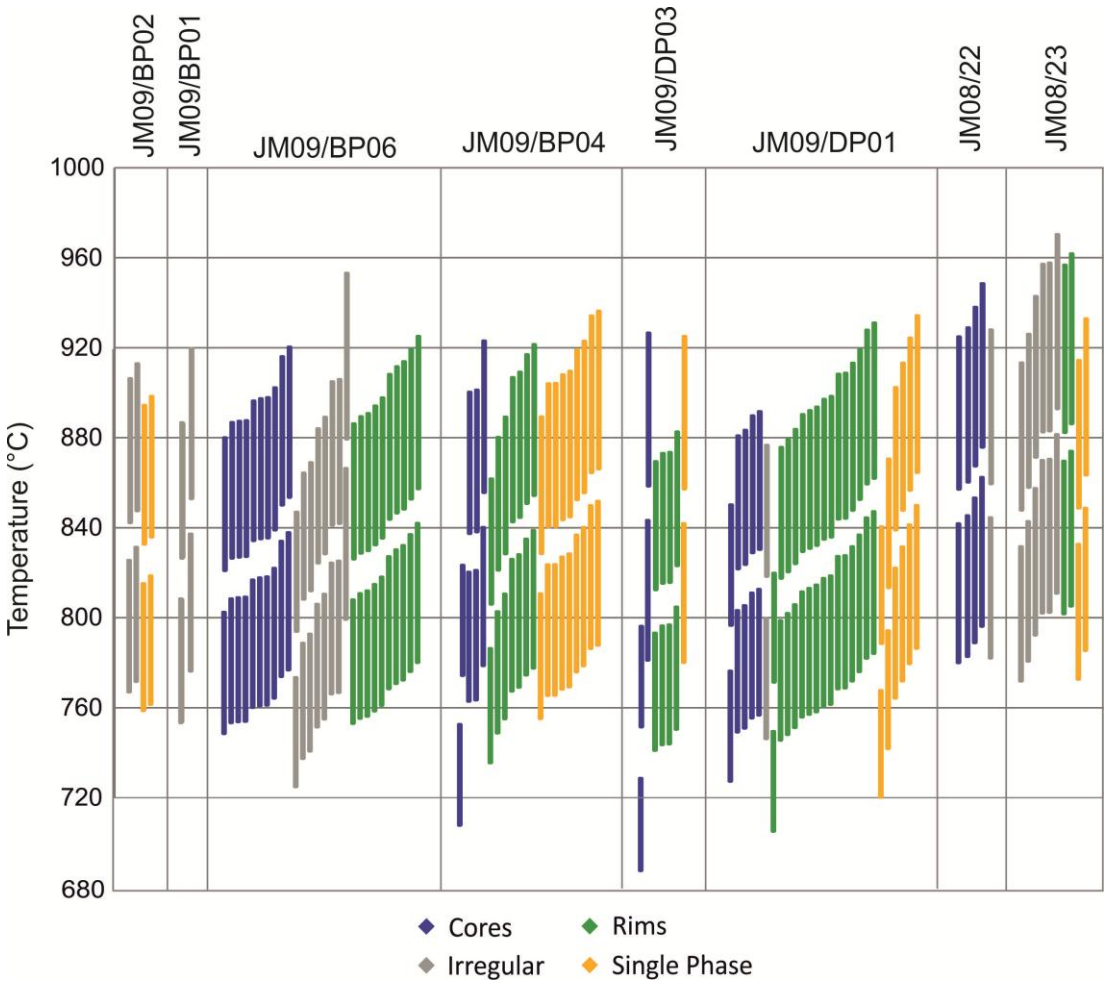

Fig. 7.12 Plot showing temperatures with 2σ errors for zircon analyses from each sample (colour-coded by cathodoluminescence zoning pattern) at TiO_2 activities of both 0.5 and 1 (reflecting the absence or presence of rutile, respectively); the upper bar in each vertical pair denotes the temperature at a_{TiO2} = 0.5, the lower one a_{TiO2} = 1.

Over the 6 TTG samples, minimum temperatures ranged from 710°C to 834°C with an average minimum temperature of 790°C (Table 7.7). Maximum temperatures ranged from 774°C to 917°C with an average maximum temperature of 865°C (Table 7.7). Fu et al. (2008) calculated crystallisation temperatures of <800-850°C for a wide range of igneous rocks and the crystallisation temperatures presented here are in broad agreement with this. The zircons record a range of temperatures of >100° at both a_{TiO2} values although the majority of analyses fall in a 60° window (760-820°C at a_{TiO2} = 1 and 840-900°C at a_{TiO2} = 0.5) (Fig. 7.13). Watson et al. (2006) found a wide range of temperatures recorded by zircon in their Adirondack migmatite sample and suggested this may reflect a mix of inherited and magmatic temperatures. However, the average 2σ error on the temperatures calculated in this study is ~±30° and so the 60° range in temperatures is not believed to reflect a mixture of protolith and metamorphic temperatures but rather uncertainty in the calibration and analytical error (Watson et al., 2006).

Zircons from the metasedimentary rocks from Sithean Mor record higher Ti-in-zircon temperatures than from the TTG gneisses from Badcall Point and Duartmore Point. At a_{TiO2} = 1, the average temperature is 823°C compared to 790°C in the TTG gneisses and the minimum recorded temperature from Sithean Mor of 803±30°C is much higher than the lowest from the TTG gneisses (710±20°C) (Table 7.7). The garnet in the metasediments is interpreted to be Badcallian (see section 4.2 of this chapter) so the rocks as a whole were involved in the Badcallian metamorphism. It is therefore possible that the zircons recorded this metamorphism in their Ti systematics. However, only one of the nine zircons analysed from the metasedimentary samples has a convincingly metamorphic CL zoning pattern. Three have fine oscillatory zoning, suggesting they grew from a magma. These are interpreted to be detrital zircons that preserve their original igneous zoning. Another four of the studied zircons have irregular CL zoning which is difficult to interpret. The metasediment samples have been retrogressed from their peak Badcallian assemblage and

it is not clear if the rutile that is present in one of the samples would have been in equilibrium with zircon during the Badcallian metamorphism. Ghent and Stout (1984) found that a_{TiO2} in metapelites is normally at or close to 1 but this would mean that calculated zircon temperatures would be generally lower than the peak Badcallian conditions calculated by Johnson and White (2011). On the whole, given that the zircons in the TTG gneisses are interpreted not to have recorded the Badcallian granulite-facies metamorphism in their Ti systematics, there is no reason to believe that the zircons in the metasediments would have done so either.

Table 7.7 Range, mean and standard deviation of Ti-in-zircon thermometer temperatures (Watson et al., 2006) from each sample at TiO_2 activities of both 0.5 and 1 (reflecting the absence or presence of rutile, respectively). 1SD denotes 1 standard deviation; values in °C.

Sample	Range	Mean	1SD	Average error (2σ)
At a_{TiO2} = 0.8				
JM09/BP02 (n=4)	864-881	872	*7*	*32*
JM09/BP01 (n=2)	857-887	872	*21*	*32*
JM09/BP06 (n=28)	821-917	867	*19*	*31*
JM09/BP04 (n=20)	800-902	872	*23*	*32*
JM09/DP03 (n=7)	774-893	849	*40*	*29*
JM09/DP01 (n=27)	796-900	862	*24*	*31*
All TTG Samples	774-917	866		
JM08/22 (n=5)	894-913	899	*9*	*35*
JM08/23 (n=10)	881-924	908	*18*	*36*
All Metasediments	881-924	904		
At a_{TiO2} = 1				
JM09/BP02 (n=4)	788-803	795	*6*	*29*
JM09/BP01 (n=2)	782-808	795	*18*	*29*
JM09/BP06 (n=28)	751-834	791	*16*	*28*
JM09/BP04 (n=20)	732-821	795	*20*	*29*
JM09/DP03 (n=7)	710-812	775	*35*	*27*
JM09/DP01 (n=27)	753-819	787	*21*	*28*
All TTG Samples	710-834	790		
JM08/22 (n=5)	812-830	819	*7*	*32*
JM08/23 (n=10)	803-847	826	*16*	*32*
All Metasediments	803-847	823		

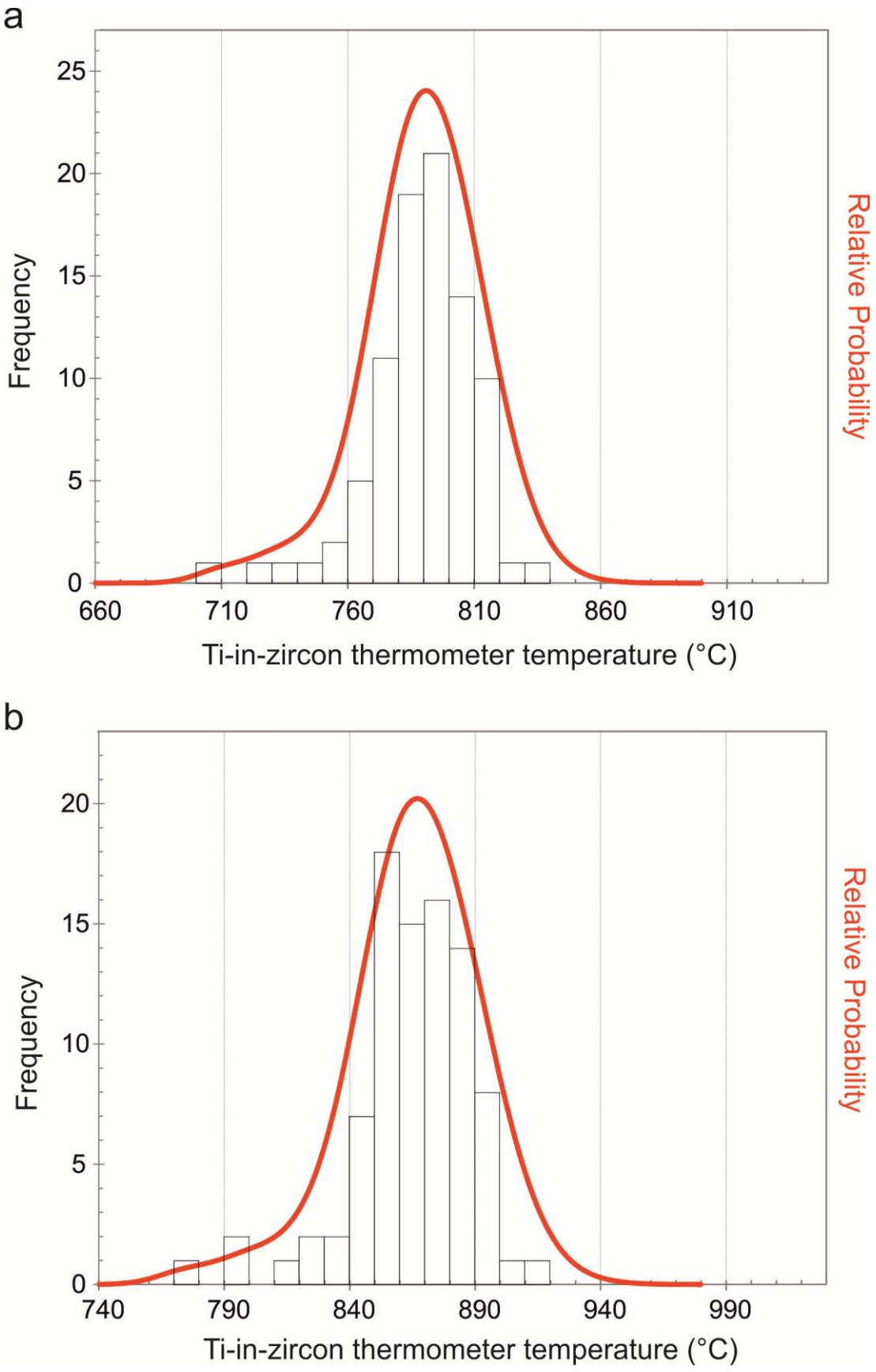

Fig. 7.13 Probability density histograms of Ti-in-zircon thermometer (Watson et al., 2006) temperatures at a_{TiO2} = 1 (a) and a_{TiO2} = 0.5 (b).

The protolith of the zircons in the metasediments at Sithean Mor is unknown and so the Ti-in-zircon thermometer offers the opportunity to fingerprint the crystallisation temperature of these rocks. Similar to the attempts of Watson and Harrison (2005) to determine the crystallisation temperature of the Jack Hills zircons, the lack of any constraint on a_{TiO2} means that an a_{TiO2} value of 1 is used and the calculated temperatures are minima. This results in a range of 803°C to 847°C with an average of 823°C (n=15). Assuming the protolith was an igneous rock, the crystallisation temperatures are relatively high, suggesting it may have been relatively mafic. This is just speculation and a constraint on a_{TiO2}, perhaps through analysis of mineral inclusions in zircons (as used by Watson and Harrison (2005) to aid their interpretation of the crystallisation temperature of the Jack Hills zircons), is required to improve the accuracy of the Ti-in-zircon thermometry in this case.

5. Conclusions

Zircons from a range of TTG gneisses and metasediments from the Assynt Terrane, a significant part of the Precambrian Lewisian Gneiss Complex (LGC) of Northwest Scotland, have been analysed for U-Th-Pb, REEs and Ti. This contribution has presented the first application of Ti-in-zircon thermometry (Watson et al., 2006) to the LGC and the first analysis of zircon REEs on the mainland LGC. Analysis of these trace elements and isotopes in the context of field and petrographic characterisation and cathodoluminescence imaging of internal chemical zoning has raised the following key points about the history of the Assynt Terrane:

- The oldest three cores yield a mean age of 2958±7Ma (MSWD = 1.00, probability = 0.37), a possible minimum magmatic protolith crystallisation age and close to that derived by Friend and Kinny (1995) for the formation of the protolith to the Assynt Terrane.

- A period of volume diffusion of Pb in zircon is interpreted to have ended at ~2482Ma with the peak of the Badcallian granulite-facies metamorphism shortly before this. The length of the Badcallian metamorphism (calculated to be anything from 3Myr to 500Myr based on diffusion rates) remains unclear without further temperature constraints.
- A general lack of variation between cores and rims suggests that zircon REEs may have been a closed system in many cases. Occasional zircon analyses from TTG gneisses deviate from the typical zircon REE profile which may have been caused by equilibration with other phases such as amphibole but this remains unclear.
- Zircons in the metasediments have relatively flat chondrite-normalised heavy REE profiles (low Yb/Gd ratios) which suggest they equilibrated with Badcallian metamorphic garnet. Volume diffusion of Pb in the zircons, however, means that a definitive age for the Badcallian cannot be determined from these zircons.
- Ti-in-zircon thermometry (Watson et al., 2006) records crystallisation temperatures of ~760-820°C for zircons in the magmatic protolith to the TTG gneisses, although this may be higher as the activity of TiO_2 is unconstrained. Zircons in the metasediments record generally higher minimum temperatures, with an average of 823°C compared to 790°C in the TTG gneisses. The zircons in the metasediments are interpreted to be detrital and the calculated temperatures are interpreted to record zircon crystallisation in a currently unknown protolith.

Acknowledgements

This work was carried out under UK Natural Environment Research Council DTG NE/G523855/1 and British Geological Survey CASE Studentship 2K08E010 to JMM. Richard Holme assisted with thermometry calculations. Ion microprobe analysis at the Edinburgh Ion Microprobe Facility was carried out with funding from NERC grant IMF384/1109;

Richard Hinton, Cees-Jan De Hoog and John Craven are thanked for ion microprobe support and Mike Hall for assistance with sample preparation. KMG publishes with the permission of the Executive Director of the Geological Survey.

8. Synthesis and Future Work

In this chapter, the conclusions from the previous three chapters are summarised and related to the aims of the thesis. The overall aim in this PhD was to undertake a detailed and systematic characterisation of the response of zircon to overprinting. Under this, there are both process- and regionally-motivated objectives:

- a generic understanding of how radiometric ages and other geochemical systems in zircon are affected by multiple and varying intensities of metamorphism and deformation i.e. process-motivated
- a better understanding of the formation and evolution of the case study rocks, the Lewisian Gneiss Complex, through geological mapping, petrography, microstructure and element/isotope zircon measurements i.e. regionally-motivated

In order to try and understand the effects of overprinting on zircon (the process-motivated aim), the research in this project evolved to look at the effects of deformation at the grain-scales on zircon and the effects of aspects of metamorphic history on zircon. Initially, it was planned to investigate the effects of macro-scale deformation on zircon by comparing zircons from inside and outside shear zones and linking their isotope and trace element systematics to the evolution of the host samples. However, as discussed in chapter 4c, the heterogeneity of the LGC rocks and the samples themselves meant that any understanding of zircon chemistry in the context of the whole rock could not be replicated from one sample to the next.

To investigate the effects of micro-scale deformation on zircon, the frequency of lattice distortion in a zircon population and its effects on zircon geochemistry was examined. In terms of the effects of metamorphism, evidence was found to suggest that there had been volume diffusion of Pb in some zircons which gave some constraint on the metamorphic history of the rocks. In order to gain a better understanding of the Lewisian Gneiss Complex (the regionally-motivated aim), zircon U-Th-Pb, REEs and Ti were analysed

to investigate zircon crystallisation temperatures, links with other minerals and the absolute chronology of the Assynt Terrane of the LGC. The outcomes of the research into these points are outlined here.

The Effects of Deformation on Zircon

The effects of deformation at the micro-scale were considered in Chapter 5. Five of ninety-nine zircons analysed in a population of zircons from the LGC were found to have distorted lattices, a small but significant proportion, which suggests that lattice distortion of zircon may be more widespread than generally realised and contests the commonly held assumption that zircon is mechanically robust. Weighted Burgers vectors (WBV) analysis (Wheeler et al., 2009) suggests that three of the five distorted zircons have undergone post-crystallisation plastic deformation to distort their crystal lattices; the other two have lattice distortion patterns not easily explained by plastic deformation and are instead suggested to have grown with distorted lattices.

There is heterogeneity in chemical response to lattice distortion within grains, within samples and between localities. Lattice distortion was found to have caused both loss and gain of Pb and Ti while chondrite-normalised REE profiles varied between and within distorted crystals. Discordant ages from two distorted zircons define a discordia lower intercept within error of the age of the lower-amphibolite-facies Laxfordian tectonothermal event, previously dated by U-Pb titanite methods (Corfu et al., 1994; Kinny and Friend, 1997). Undistorted zircons do not record Laxfordian ages. This suggests that lattice distortion allows Pb diffusion at lower temperatures than in undistorted zircon.

Overall, these findings illustrate the significant and heterogeneous effects of crystal lattice distortion on trace elements and isotopes in zircon. It highlights the importance of conducting EBSD analysis prior to ion microprobe analysis to determine if any zircons in the target population have distorted lattices. Zircons with distorted lattices may record lower temperature tectonothermal events that undistorted zircons do not.

Further Study of the Effects of Deformation on Zircon

Extending the study of the effects of micro-scale deformation on zircon in other basement complexes and other host rock lithologies would help to prove whether the findings noted here are widely applicable or if there is just too much heterogeneity to develop any model of the effects of deformation on zircon.

Hf isotope petrogenetic tracing is a widely used technique and a major zircon isotope system not analysed in this study. Although the Hf isotope system is regarded as robust (Kinny et al., 1991), systematic investigation into the effects of lattice distortion of Hf in zircon could be illuminating.

One thing this study has revealed is that some zircons had crystal lattice distortion but others did not. In one sample, a plastically deformed zircon was located approximately two millimetres from an entirely undeformed one. Why did some zircons plastically deform while others didn't? The answer may well lie in the surrounding minerals. Barrie et al. (2009) and Boyle et al. (1998) showed that impingement on pyrite of another pyrite, rather than a different softer sulphide phase gave rise to greater plastic deformation. Perhaps a similar scenario explains why some zircons have distorted lattices and other do not. Further petrographic and EBSD analysis could potentially confirm this.

The necessity of analysing zircons with EBSD prior to geochemical and geochronological analysis is clear. The technique could therefore be applied to other mineral chronometers such as monazite, titanite, rutile, baddeleyite, etc to determine if trace element mobility and isotope systematics are affected by lattice distortion. As well as mineral chronometers, other geochemical applications could benefit from prior EBSD analysis. EBSD could test for lattice distortion that could compromise thermobarometric phases such as garnet, rutile, titanite, pyroxenes, etc.

The Weighted Burgers Vector (WBV) (Wheeler et al., 2009) is newly applied to zircon here. It offers new insight into the cause of lattice distortion whether it is through

plastic deformation or a growth microstructure or some other cause. This technique could be incorporated into future EBSD studies of zircon and other mineral chronometers and thermobarometers as well as being deployed on other phases to help determine deformation histories at the micro-scale.

Volume Diffusion of Pb in Zircons

Part of the process-motivated aim of this project was to investigate the effects of multiple metamorphic events on zircon. A significant result came in the form of evidence for volume diffusion of Pb in zircons. Chapter 6 systematically illustrated the evidence for volume diffusion of Pb having occurred in a population of complex zircons from the LGC. Other potential explanations for a spread of concordant ages of ~600Myr, including radiation-damage, lattice distortion and recrystallisation, were methodically eliminated. Decoupling of age and chemical zoning pattern suggested that volume diffusion of Pb in the zircons may have been responsible for the age spread. For an average grain radius of 50µm, volume diffusion would have required anything between ~3Myr and ~500Myr to occur at the 875-975°C temperatures estimated as peak metamorphic conditions in the host rock by Johnson and White (2011). The length of time at high temperature cannot be further constrained without more precise temperature estimates.

Further Study of Volume Diffusion of Pb in Zircons

The hypothesis that volume diffusion of Pb occurred in zircons from the Assynt Terrane of the LGC is based on the relationship between catholuminescence (CL) zoning patterns and ion microprobe analytical spots that are ~30µm in diameter. In order to strengthen the evidence for volume diffusion having occurred, a higher resolution picture of Pb distribution throughout the zircon crystals would be advantageous. This would show if there was a decoupling of U and Pb isotopes and provide a higher spatial resolution map of the extent of decoupling between U-Pb dates and chemical zoning. NanoSIMS is

essentially a higher resolution ion microprobe with a spot size of ~10µm; it has previously been applied to zircons where there was a decoupling between U-Pb dates and chemical zoning but volume diffusion was not invoked as an explanation for the decoupling (Flowers et al., 2010). The efficacy of the technique has been demonstrated though and could be applied to the zircon population in this study.

Another technique that could provide an even higher spatial resolution Pb isotope map of the zircons is TOFSIMS (time-of-flight secondary ion mass spectrometry) (Henkel et al., 2007). TOFSIMS measures a complete spectrum of isotopes and elements simultaneously and rasters across a specified area pixel by pixel; pixels can be sub-micron in diameter and so it offers the possibility of a very high spatial resolution map of not just Pb isotopes but all isotopes that are present in the crystal. Investigation of one zircon in the population was started using the TOFSIMS instrument at the University of Manchester but the gold source was not good enough to resolve the small mass differences b
etween the different Pb isotopes and interferences from ionised hafnium oxides. However, a new electron source is to be installed in late 2012 that should provide the mass resolution required to resolve Pb isotopes from interferences, and so this work may yet be carried out.

As well as gathering more data, modelling the Pb diffusion pathways and conditions would help to visualise the volume diffusion. This work is currently being undertaken by one of the project supervisors (JW), where a model developed in Matlab will model the diffusion of Pb ions over time where the grain radius, parent isotope concentration and temperature history can be varied. The model is currently being refined but may prove a valuable addition in further developing the volume diffusion hypothesis.

Volume diffusion of Pb in zircon is generally regarded as unlikely or impossible in normal crustal conditions (Mezger and Krogstad, 1997; Cherniak and Watson, 2003). However, a hotter Archaean geotherm would make it more likely for high temperatures to be sustained for long periods. Therefore, it would be interesting to test the volume

diffusion hypothesis on other zircon populations from Archaean basement complexes around the world. This would require high quality CL images for each zircon with analytical spots clearly marked and this is not always available in material already published so new studies would be required. With more precise temperature estimates, the length of time required for volume diffusion of Pb in zircon can be better constrained. If relatively long high temperature periods of ~500Ma are required, there will be implications for Archaean tectonics and the origination of the continental crust, and this therefore merits further investigation.

Tectonothermal History of the Lewisian Gneiss Complex

The regionally-motivated aim of this thesis was to understand better the tectonothermal history of the Lewisian Gneiss Complex (LGC), and was covered in Chapter 7. A suite of tonalite-trondhjemite-granodiorite (TTG) gneisses and metasediments from the Assynt Terrane of the LGC were analysed for zircon U-Th-Pb, REEs and Ti. Volume diffusion of Pb in zircons (chapter 6) across the analysed population made it difficult to confidently interpret magmatic and metamorphic ages. The oldest three cores yield a mean age of 2958±7Ma (MSWD = 1.00, probability = 0.37), a possible minimum magmatic protolith crystallisation age but caution is required as the oldest age in this study is from a zircon rim, which is not interpreted to reflect magmatic crystallisation. The period of volume diffusion of Pb in zircon is interpreted to have ended at ~2482Ma with the peak of the Badcallian granulite-facies metamorphism shortly before this. Zircons in the metasediments have relatively flat chondrite-normalised heavy REE profiles (low Yb/Gd ratios) which suggest their REE profiles were affected by Badcallian metamorphic garnet sequestering heavy REEs. Ti-in-zircon thermometry (Watson et al., 2006) records crystallisation temperatures of ~760-820°C for zircons in the magmatic protolith to the TTG gneisses, although this may be higher as a_{TiO2} is not tightly constrained. Zircons in the metasediments generally record higher temperatures, with an average of 823°C compared

to 790°C in the TTG gneisses. The zircons in the metasediments are interpreted to be detrital and the calculated temperatures are interpreted to record zircon crystallisation in a currently unknown protolith.

Further Study of the Tectonothermal History of the Lewisian Gneiss Complex

The Assynt Terrane (Kinny et al., 2005), part of the Central Region of Sutton and Watson (1951) is the most studied part of the LGC. Metamorphic mineral assemblages and structures from three tectonothermal events can be seen here and this was the reason for the work in this study being carried out on samples from the Assynt Terrane. Formerly the same tectonothermal history was thought to apply to the whole of the LGC with different degrees of overprinting in different areas. However, the terrane hypothesis of Kinny et al. (2005) suggested that different parts of the LGC had completely different histories.

Volume diffusion of Pb in zircon is hypothesised to have occurred in the Assynt Terrane but what about other parts of the LGC? The available published data are sparse and do not really allow investigation of the possibility of volume diffusion. A new suite of data from different parts of the LGC would help to determine if volume diffusion occurred elsewhere. This would potentially inform the debate over the terrane model hypothesis of Kinny et al. (2005) and lead to a better understanding of the evolution of the whole of the LGC.

9. Bibliography

Anders, E., Grevesse, N., 1989. Abundances of the Elements - Meteoritic and Solar. Geochimica Et Cosmochimica Acta, 53(1): 197-214.

Ando, J. et al., 2001. Striped iron zoning of olivine induced by dislocation creep in deformed peridotites. Nature, 414(6866): 893-895.

Andrews, J.R., 1973. Stratigraphic, structural and metamorphic features of Archaean (pre-Ketilidian) rocks in the Frederikshab district, South-West Greenland. In: Park, R.G., Tarney, J. (Eds.), The Early Precambrian of Scotland and Related Rocks of Greenland. University of Keele.

Andrews, J.R. et al., 1973. The Precambrian of South-East Greenland. In: Park, R.G., Tarney, J. (Eds.), The Early Precambrian of Scotland and Related Rocks of Greenland. University of Keele.

Ashwal, L.D., Tucker, R.D., Zinner, E.K., 1999. Slow cooling of deep crustal granulites and Pb-loss in zircon. Geochimica Et Cosmochimica Acta, 63(18): 2839-2851.

Attfield, P., 1987. The structural history of the Canisp shear zone. In: Park, R.G., Tarney, J. (Eds.), Evolution of the Lewisian and Comparable Precambrian High-Grade Terrains.

Baba, S., 1998. Proterozoic anticlockwise P-T path of the Lewisian Complex of South Harris, Outer Hebrides, NW Scotland. Journal of Metamorphic Geology, 16(6): 819-841.

Baba, S., 1999. Sapphirine-bearing orthopyroxene-kyanite/sillimanite granulites from South Harris, NW Scotland: evidence for proterozoic UHT metamorphism in the Lewisian. Contributions to Mineralogy and Petrology, 136(1-2): 33-47.

Baldwin, J.A., Brown, M., Schmitz, M.D., 2007. First application of titanium-in-zircon thermometry to ultrahigh-temperature metamorphism. Geology, 35(4): 295-298.

Barnicoat, A.C., 1987. The causes of high-grade metamorphism of the Scourie complex, NW Scotland. In: Park, R.G., Tarney, J. (Eds.), Evolution of the Lewisian and Comparable Precambrian High-Grade Terrains. Blackwells.

Barnicoat, A.C., Cartwright, I., Ohara, M.J., 1987. Kyanite in the Mainland Lewisian Complex. Scottish Journal of Geology, 23: 209-213.

Barrie, C.D., Boyle, A.P., Salter, M., 2009. How low can you go? - Extending downwards the limits of plastic deformation in pyrite. Mineralogical Magazine, 73(6): 895-913.

Bea, F., Montero, P., 1999. Behavior of accessory phases and redistribution of Zr, REE, Y, Th, and U during metamorphism and partial melting of metapelites in the lower crust: An example from the Kinzigite Formation of Ivrea-Verbano, NW Italy. Geochimica Et Cosmochimica Acta, 63(7-8): 1133-1153.

Bea, F., Pereira, M.D., Stroh, A., 1994. Mineral/leucosome trace-element partitioning in a peraluminous migmatite (a laser ablation-ICP-MS study). Chemical Geology, 117(1-4): 291-312.

Beach, A., 1973. Mineralogy of High-Temperature Shear Zones at Scourie, NW Scotland. Journal of Petrology, 14(2): 231-248.

Beach, A., 1974. Amphibolitization of Scourian granulites. Scottish Journal of Geology, 10(1): 35-43.

Beach, A., 1976. Interrelations of Fluid Transport, Deformation, Geochemistry and Heat-Flow in Early Proterozoic Shear Zones in Lewisian Complex. Philosophical Transactions of the Royal Society of London Series a-Mathematical Physical and Engineering Sciences, 280(1298): 569-604.

Beach, A., Coward, M.P., Graham, R.H., 1974. An interpretation of the structural evolution of the Laxford Front, north-west Scotland. Scottish Journal of Geology, 9(4): 297-308.

Belousova, E.A., Reid, A.J., Griffin, W.L., O'Reilly, S.Y., 2009. Rejuvenation vs. recycling of Archean crust in the Gawler Craton, South Australia: Evidence from U-Pb and Hf isotopes in detrital zircon. Lithos, 113(3-4): 570-582.

Bestmann, M., Prior, D.J., Grasemann, B., 2006. Characterisation of deformation and flow mechanics around porphyroclasts in a calcite marble ultramylonite by means of EBSD analysis. Tectonophysics, 413(3-4): 185-200.

Bingen, B., Austrheim, H., Whitehouse, M., 2001. Ilmenite as a source for zirconium during high-grade metamorphism? Textural evidence from the Caledonides of western Norway and implications for zircon geochronology. Journal of Petrology, 42(2): 355-375.

Black, L.P., Williams, I.S., Compston, W., 1986. Four zircon ages from one rock: the history of a 3930 Ma-old granulite from Mount Sones, Enderby Land, Antarctica. Contributions to Mineralogy and Petrology, 94(4): 427-437.

Bogomolov, Y., 1991. Migration of lead in non-metamict zircon. Earth and Planetary Science Letters, 107(3-4): 625-633.

Bott, M.H.P., Holland, J.G., Storry, P.G., Watts, A.B., 1972. Geophysical evidence concerning the structure of the Lewisian of Sutherland. Journal of the Geological Society, 128: 599-612.

Bowes, D.R., 1978. Shield formation in early Precambrian times: the Lewisian. In: Bowes, D.R., Leake, B.E. (Eds.), Crustal evolution in northwestern Britain and adjacent regions. Special Issue of the Geological Journal. Seel House Press, Liverpool, pp. 39-80.

Boyle, A.P., Prior, D.J., Banham, M.H., Timms, N.E., 1998. Plastic deformation of metamorphic pyrite: new evidence from electron-backscatter diffraction and forescatter orientation-contrast imaging. Mineralium Deposita, 34(1): 71-81.

Brown, M., 2007. Metamorphic Conditions in Orogenic Belts: A Record of Secular Change. International Geology Review, 49(3): 193-234.

Burton, K.W., Cohen, A.S., Onions, R.K., O' Hara, M.J., 1994. Archean Crustal Development in the Lewisian Complex of Northwest Scotland. Nature, 370(6490): 552-555.

Cartwright, I., Barnicoat, A.C., 1987. Petrology of Scourian supracrustal rocks and orthogneisses from Stoer, NW Scotland: implications for the geological evolution of the Lewisian complex. In: Park, R.G., Tarney, J. (Eds.), Evolution of the Lewisian and Comparable Precambrian High-Grade Terrains. Blackwells.

Castro, A., 2004. The source of granites: inferences from the Lewisian complex. Scottish Journal of Geology, 40: 49-65.

Chamberlain, V.E., Lambert, R.S., Holland, J.G., 1986. Rb-Sr and Zircon Study of Approximately 2800 Ma Lewisian Silicic Gneisses from the Torridon Inlier of NW Scotland - Dyke Intrusion and an Open System. Geochimica Et Cosmochimica Acta, 50(1): 37-47.

Cherniak, D.J., Hanchar, J.M., Watson, E.B., 1997. Rare-earth diffusion in zircon. Chemical Geology, 134(4): 289-301.

Cherniak, D.J., Lanford, W.A., Ryerson, F.J., 1991. Lead diffusion in apatite and zircon using ion implantation and Rutherford Backscattering techniques. Geochimica Et Cosmochimica Acta, 55(6): 1663-1673.

Cherniak, D.J., Watson, E.B., 2001. Pb diffusion in zircon. Chemical Geology, 172(1-2): 5-24.

Cherniak, D.J., Watson, E.B., 2003. Diffusion in Zircon. In: Hanchar, J.M., Hoskin, P.W.O. (Eds.), Zircon. Reviews in Mineralogy and Geochemistry. Mineralogical Society of America and The Geochemical Society.

Cherniak, D.J., Watson, E.B., 2007. Ti diffusion in zircon. Chemical Geology, 242(3-4): 473-483.

Chowdhary, P.K., Bowes, D.R., 1972. Structure of Lewisian rocks between Loch Inchard and Loch Laxford, Sutherland, Scotland. Krystalinikum, 9: 21-51.

Clark, C., Collins, A.S., Santosh, M., Taylor, R., Wade, B.P., 2009. The P-T-t architecture of a Gondwanan suture: REE, U-Pb and Ti-in-zircon thermometric constraints from the Palghat Cauvery shear system, South India. Precambrian Research, 174(1-2): 129-144.

Cliff, R.A., Rex, D.C., Guise, P.G., 1998. Geochronological studies of Proterozoic crustal evolution in the northern Outer Hebrides. Precambrian Research, 91(3-4): 401-418.

Cohen, A.S., Onions, R.K., O' Hara, M.J., 1991. Chronology and Mechanism of Depletion in Lewisian Granulites. Contributions to Mineralogy and Petrology, 106(2): 142-153.

Condie, K., 2005. Earth as an Evolving Planetary System. Elsevier Academic Press, Burlington, 447 pp.

Corfu, F., 2007. Comment to paper: Timing of magmatism and metamorphism in the Gruinard Bay area of the Lewisian gneiss complex: comparison with the Assynt Terrane and implications for terrane accretion by G.J. Love, P.D. Kinny and C.R.L. Friend (Contr Mineral Petrol (2004) 146 : 620-636). Contributions to Mineralogy and Petrology, 153(4): 483-488.

Corfu, F., Crane, A., Moser, D., Rogers, G., 1998. U-Pb zircon systematics at Gruinard Bay, northwest Scotland: implications for the early orogenic evolution of the Lewisian complex. Contributions to Mineralogy and Petrology, 133: 329-345.

Corfu, F., Hanchar, J.M., Hoskin, P.W.O., Kinny, P.D., 2003. Atlas of Zircon Textures. In: Hanchar, J.M., Hoskin, P.W.O. (Eds.), Zircon. Reviews in Mineralogy and Geochemistry. Mineralogical Society of America and The Geochemical Society.

Corfu, F., Heaman, L.M., Rogers, G., 1994. Polymetamorphic Evolution of the Lewisian Complex, Nw Scotland, as Recorded by U-Pb Isotopic Compositions of Zircon, Titanite and Rutile. Contributions to Mineralogy and Petrology, 117(3): 215-228.

Corfu, F., Noble, S.R., 1992. Genesis of the Southern Abitibi Greenstone-Belt, Superior-Province, Canada - Evidence from Zircon Hf Isotope Analyses Using a Single Filament Technique. Geochimica Et Cosmochimica Acta, 56(5): 2081-2097.

Cottrell, A.H., Bilby, B.A., 1949. Dislocation Theory of Yielding and Strain Ageing of Iron Proceedings of the Physical Society Section A, 62(1): 49-62.

Coward, M., Park, R.G., 1987. The role of mid-crustal shear zones in the Early Proterozoic evolution of the Lewisian. In: Park, R.G., Tarney, J. (Eds.), Evolution of the Lewisian and Comparable Precambrian High-Grade Terrains. Blackwells.

Coward, M.P., 1975. Flat-lying structures within the Lewisian basement gneiss complex of NW. Scotland. Proceedings of the Geologists' Association, 85(4): 459-472.

Coward, M.P., 1984. Major shear zones in the Precambrian crust: examples from NW Scotland and southern Africa. In: Kroner, A., Greiling, R. (Eds.), Precambrian Tectonics Illustrated. E. Schweizerbart'sche, pp. 419.

Coward, M.P., 1990. Shear Zones at the Laxford Front, Nw Scotland and Their Significance in the Interpretation of Lower Crustal Structure. Journal of the Geological Society, 147: 279-286.

Cresswell, D., 1972. The structural development of the Lewisian rocks on the north shore of Loch Torridon, Ross-shire. Scottish Journal of Geology, 8(4): 293-308.

Cresswell, D., Park, R.G., 1973. The metamorphic history of the Lewisian rocks of the Torridon area in relation to that of the remainder of the southern Laxfordian belt. In: Park, R.G., Tarney, J. (Eds.), The Early Precambrian of Scotland and Related Rocks of Greenland. University of Keele.

Dash, B., 1969. Structure of the Lewisian rocks between Strath Dionard and Rhiconich, Sutherland, Scotland. Scottish Journal of Geology, 5: 347-374.

Davidson, C.F., 1944. The Archaean Rocks of the Rodil district, South Harris. Transactions of the Royal Society of Edinburgh, 61: 71-112.

Davidson, J., Turner, S., Handley, H., Macpherson, C., Dosseto, A., 2007. Amphibole “sponge” in arc crust? Geology, 35(9): 787-790.

Davies, F.B., 1976. Early Scourian structures in the Scourie-Laxford region and their bearing on the evolution of the Laxford Front. Journal of the Geological Society, 132: 543-554.
Davis, D.W., Williams, I.S., Krogh, T.E., 2003. Historical Development of Zircon Geochronology. In: Hanchar, J.M., Hoskin, P.W.O. (Eds.), Zircon. Reviews in Mineralogy and Geochemistry. Mineralogical Society of America and The Geochemical Society.
Degeling, H., Eggins, S., Ellis, D.J., 2001. Zr budgets for metamorphic reactions, and the formation of zircon from garnet breakdown. Mineralogical Magazine, 65(6): 749-758.
Droop, G.T.R., Fernandes, L.A.D., Shaw, S., 1999. Laxfordian metamorphic conditions of the Palaeoproterozoic Loch Maree Group, Lewisian Complex, NW Scotland. Scottish Journal of Geology, 35: 31-50.
Drury, M.R., 2005. Dynamic recrystallization and strain softening of olivine aggregates in the laboratory and the lithosphere. Geological Society, London, Special Publications, 243(1): 143-158.
Drury, S.A., 1973. The geochemistry of Precambrian granulite facies rocks from the Lewisian complex of Tiree, Inner Hebrides, Scotland. Chemical Geology, 11(3): 167-188.
Drury, S.A., 1974. Chemical changes during retrogressive metamorphism of Lewisian granulite facies rocks from Coll and Tiree. Scottish Journal of Geology, 10(3): 237-256.
Evans, C.R., 1965. Geochronology of the Lewisian Basement near Lochinver, Sutherland. Nature, 204: 638-641.
Evans, C.R., Lambert, R.S., 1974. The Lewisian of Lochinver, Sutherland: the type area for the Inverian metamorphism. Journal of the Geological Society, 130: 125-150.
Ewing, R.C., Meldrum, A., Wang, L., Weber, W.J., Corrales, L.R., 2003. Radiation effects in zircon. In: Hanchar, J., Hoskin, P.W.O. (Eds.), Zircon. Mineralogical Society of America and The Geochemical Society, pp. 387-425.
Faure, G., Mensing, T.M., 2005. Isotopes: Principles and Applications. John Wiley & Sons, 897 pp.
Ferry, J.M., Watson, E.B., 2007. New thermodynamic models and revised calibrations for the Ti-in-zircon and Zr-in-rutile thermometers. Contributions to Mineralogy and Petrology, 154(4): 429-437.
Fettes, D.J., Mendum, J.R., Smith, D.I., Watson, J.V., 1992. Geology of the Outer Hebrides: memoir for 1: 100 000 (solid edition) geological sheets, Lewis and Harris, Uist and Barra (Scotland). Memoirs of the British Geological Survey.
Finch, R.J., Hanchar, J., 2003. Structure and Chemistry of Zircon and Zircon-group Minerals. In: Hanchar, J., Hoskin, P.W.O. (Eds.), Zircon. Reviews in Mineralogy and Geochemistry. Mineralogical Society of America and The Geochemical Society.
Fitton, J.G., Saunders, A.D., Larsen, L.M., Hardarson, B.S., Norry, M.J., 1998. Volcanic Rocks from the Southeast Greenland Margin at 63°N: Composition, Petrogenesis, and Mantle Sources. In: Saunders, A.D., Larsen, H.C., Wise, S.W.J. (Editors), Proceedings of the Ocean Drilling Program, Scientific Results, pp. 332-350.
Flinn, D., 1965. On the symmetry principle in the deformational ellipsoid. Geological Magazine 102: 36-45.
Flowers, R.M., Schmitt, A.K., Grove, M., 2010. Decoupling of U-Pb dates from chemical and crystallographic domains in granulite facies zircon. Chemical Geology, 270(1-4): 20-30.
Fraser, G., Ellis, D., Eggins, S., 1997. Zirconium abundance in granulite-facies minerals, with implications for zircon geochronology in high-grade rocks. Geology, 25(7): 607-610.
Friend, C.R.L., Kinny, P.D., 1995. New Evidence for Protolith Ages of Lewisian Granulites, Northwest Scotland. Geology, 23(11): 1027-1030.

Friend, C.R.L., Kinny, P.D., 2001. A reappraisal of the Lewisian Gneiss Complex: geochronological evidence for its tectonic assembly from disparate terranes in the Proterozoic. Contributions to Mineralogy and Petrology, 142(2): 198-218.
Friend, C.R.L., Kinny, P.D., Love, G.J., 2007. Timing of magmatism and metamorphism in the Gruinard Bay area of the Lewisian Gneiss Complex: comparison with the Assynt Terrane and implications for terrane accretion - reply. Contributions to Mineralogy and Petrology, 153(4): 489-492.
Fu, B. et al., 2008. Ti-in-zircon thermometry: applications and limitations. Contributions to Mineralogy and Petrology, 156(2): 197-215.
Geisler, T., Schaltegger, U., Tomaschek, F., 2007. Re-equilibration of Zircon in Aqueous Fluids and Melts. Elements, 3(1): 43-50.
Gerdes, A., Zeh, A., 2009. Zircon formation versus zircon alteration — New insights from combined U–Pb and Lu–Hf in-situ LA-ICP-MS analyses, and consequences for the interpretation of Archean zircon from the Central Zone of the Limpopo Belt. Chemical Geology, 261(3-4): 230-243.
Ghent, E.D., Stout, M.Z., 1984. TiO2 Activity in Metamorphosed Pelitic and Basic Rocks - Principles and Applications to Metamorphism in Southeastern Canadian Cordillera. Contributions to Mineralogy and Petrology, 86(3): 248-255.
Giletti, B.J., 1959. Rubidium-Strontium Ages of Lewisian Rocks from North-West Scotland. Nature, 184(4701): 1793-1794.
Gilletti, B.J., Moorbath, S., Lambert, R.S., 1961. A geochronological study of the metamorphic complexes of the Scottish Highlands. Quarterly Journal of the Geological Society, 117: 233-272.
Gleason, G.C., Tullis, J., Heidelbach, F., 1993. The role of dynamic recrystallization in the development of lattice preferred orientations in experimentally deformed quartz aggregates. Journal of Structural Geology, 15(9–10): 1145-1168.
Glikson, A., 2006. Comment on "Zircon thermometer reveals minimum melting conditions on earliest Earth" I. Science, 311(5762): 779.
Goodenough, K.M. et al., 2010. The Laxford Shear Zone: an end-Archaean terrane boundary? In: Law, R.D., Butler, R.W.H., Holdsworth, R.E., Krabbendam, M., Strachan, R.A. (Eds.), Continental Tectonics and Mountain Building. Special Publications. Geological Society, London.
Govindaraju, K., 1994. 1994 Compilation of Working Values and Sample Description for 383 Geostandards (Vol 18, Pg 53, 1994). Geostandards Newsletter, 18(2): 331-331.
Graham, R.H., Coward, M., 1973. The Laxfordian of the Outer Hebrides. In: Park, R.G., Tarney, J. (Eds.), The Early Precambrian of Scotland and Related Rocks of Greenland. University of Keele.
Halpin, J., Daczko, N., Milan, L., Clarke, G., 2012. Decoding near-concordant U–Pb zircon ages spanning several hundred million years: recrystallisation, metamictisation or diffusion? Contributions to Mineralogy and Petrology, 163: 67-85.
Hamilton, P.J., Evensen, N.M., Onions, R.K., Tarney, J., 1979. Sm-Nd Systematics of Lewisian Gneisses - Implications for Origin of Granulites. Nature, 277(5691): 25-28.
Hanchar, J., Watson, E.B., 2003. Zircon saturation thermometry. In: Hanchar, J., Hoskin, P.W.O. (Eds.), Zircon. Mineralogical Society of America and The Geochemical Society, pp. 89-112.
Harley, S.L., Kelly, N.M., 2007. The impact of zircon-garnet REE distribution data on the interpretation of zircon U-Pb ages in complex high-grade terrains: An example from the Rauer Islands, East Antarctica. Chemical Geology, 241(1-2): 62-87.
Harley, S.L., Kelly, N.M., Moller, A., 2007. Zircon behaviour and the thermal histories of mountain chains. Elements, 3(1): 25-30.
Heaman, L.M., Tarney, J., 1989. U-Pb Baddeleyite Ages for the Scourie Dyke Swarm, Scotland - Evidence for 2 Distinct Intrusion Events. Nature, 340(6236): 705-708.

Heilbronner, R., Tullis, J., 2006. Evolution of c axis pole figures and grain size during dynamic recrystallization: Results from experimentally sheared quartzite. J. Geophys. Res., 111(B10): B10202.
Henkel, T., Tizard, J., Blagburn, D.J., Lyon, I.C., 2007. Interstellar dust laser explorer: A new instrument for elemental and isotopic analysis and imaging of interstellar and interplanetary dust. Review of Scientific Instruments, 78: 1-9.
Hiess, J., Condon, D.J., McLean, N., Noble, S.R., 2012. U-238/U-235 Systematics in Terrestrial Uranium-Bearing Minerals. Science, 335(6076): 1610-1614.
Hinton, R.W., 1999. NIST SRM 610, 611 and SRM 612, 613 multi-element glasses: Constraints from element abundance ratios measured by microprobe techniques. Geostandards Newsletter-the Journal of Geostandards and Geoanalysis, 23(2): 197-207.
Hinton, R.W., Upton, B.G.J., 1991. The chemistry of zircon: Variations within and between large crystals from syenite and alkali basalt xenoliths. Geochimica Et Cosmochimica Acta, 55(11): 3287-3302.
Hofmann, A.W., 1988. Chemical Differentiation of the Earth - the Relationship between Mantle, Continental-Crust, and Oceanic-Crust. Earth and Planetary Science Letters, 90(3): 297-314.
Holland, J.G., Lambert, R.S., 1973. Comparative major element geochemistry of the Lewisian of the mainland of Scotland. In: Park, R.G., Tarney, J. (Eds.), The Early Precambrian of Scotland and Related Rocks of Greenland. University of Keele.
Holland, T.J.B., Powell, R., 1998. An internally consistent thermodynamic data set for phases of petrological interest. Journal of Metamorphic Geology, 16(3): 309-343.
Hoskin, P.W.O., 1998. Minor and trace element analysis of natural zircon (ZrSiO4) by SIMS and laser ablation ICPMS: A consideration and comparison of two broadly competitive techniques. Journal of Trace and Microprobe Techniques, 16(3): 301-326.
Hoskin, P.W.O., Black, L.P., 2000. Metamorphic zircon formation by solid-state recrystallization of protolith igneous zircon. Journal of Metamorphic Geology, 18(4): 423-439.
Hoskin, P.W.O., Ireland, T.R., 2000. Rare earth element chemistry of zircon and its use as a provenance indicator. Geology, 28(7): 627-630.
Hoskin, P.W.O., Kinny, P.D., Wyborn, D., Chappell, B.W., 2000. Identifying accessory mineral saturation during differentiation in granitoid magmas: an integrated approach. Journal of Petrology, 41(9): 1365-1396.
Hoskin, P.W.O., Schaltegger, U., 2003. The composition of zircon and igneous and metamorphic petrogenesis. In: Hanchar, J., Hoskin, P.W.O. (Eds.), Zircon. Mineralogical Society of America and The Geochemical Society, pp. 27-62.
Humphries, F.J., Cliff, R.A., 1982. Sm-Nd Dating and Cooling History of Scourian Granulites, Sutherland. Nature, 295(5849): 515-517.
Ireland, T.R., Williams, I.S., 2003. Considerations in Zircon Geochronology by SIMS. In: Hanchar, J.M., Hoskin, P.W.O. (Eds.), Zircon. Reviews in Mineralogy and Geochemistry. Mineralogical Society of America and The Geochemical Society.
Jehu, T.J., Craig, R.M., 1923-1934. Geology of the Outer Hebrides, parts I-V. Transactions of the Royal Society of Edinburgh.
Jehu, T.J., Craig, R.M., 1924. Geology of the Outer Hebrides Part I—The Barra Isles. Transactions of the Royal Society of Edinburgh: Earth Sciences, 53: 419-441.
Jehu, T.J., Craig, R.M., 1925. Geology of the Outer Hebrides. Part II. South Uist and Eriskay. Transactions of the Royal Society of Edinburgh: Earth Sciences 53: 615-641.
Jehu, T.J., Craig, R.M., 1926. Geology of the Outer Hebrides. Part III. North Uist and Benbecula. Transactions of the Royal Society of Edinburgh: Earth Sciences 54: 467-489.

Jehu, T.J., Craig, R.M., 1927. Geology of the Outer Hebrides. Part IV. South Harris. Transactions of the Royal Society of Edinburgh: Earth Sciences 55: 457-488.
Jehu, T.J., Craig, R.M., 1934. Geology of the Outer Hebrides. Part V. North Harris and Lewis. Transactions of the Royal Society of Edinburgh: Earth Sciences, 57: 839-874.
Jensen, L.N., 1984. Quartz Microfabric of the Laxfordian Canisp Shear Zone, Nw Scotland. Journal of Structural Geology, 6(3): 293-302.
Johnson, T.E., Fischer, S., White, R.W., Brown, M., Rollinson, H.R., 2012. Archaean Intracrustal Differentiation from Partial Melting of Metagabbro-Field and Geochemical Evidence from the Central Region of the Lewisian Complex, NW Scotland. Journal of Petrology, 53(10): 2115-2138.
Johnson, T.E., White, R.W., 2011. Phase equilibrium constraints on conditions of granulite-facies metamorphism at Scourie, NW Scotland. Journal of the Geological Society, 168(1): 147-158.
Johnstone, G.S., Mykura, W., 1989. The Northern Highlands of Scotland. Her Majesty's Stationery Office, London, 219 pp.
Kalsbeek, F. et al., 1993. Geochronology of Archean and Proterozoic Events in the Ammassalik Area, South-East Greenland, and Comparisons with the Lewisian of Scotland and the Nagssugtoqidian of West Greenland. Precambrian Research, 62(3): 239-270.
Kelly, N.M., Harley, S.L., 2005a. An integrated microtextural and chemical approach to zircon geochronology: refining the Archaean history of the Napier Complex, east Antarctica. Contributions to Mineralogy and Petrology, 149(1): 57-84.
Kelly, N.M., Harley, S.L., 2005b. Timing of zircon growth during highgrade metamorphism: Constraints from garnet-zircon REE. Geochimica Et Cosmochimica Acta, 69(10): A22-A22.
Kelly, N.M., Harley, S.L., Hinton, R.W., 2006. Zircon-garnet REE distribution: events and processes in high grade terrains. Geochimica Et Cosmochimica Acta, 70(18): A312-A312.
Kelly, N.M., Hinton, R.W., Harley, S.L., Appleby, S.K., 2008. New SIMS U-Pb zircon ages from the Langavat Belt, South Harris, NW Scotland: implications for the Lewisian terrane model. Journal of the Geological Society, 165: 967-981.
Kinny, P.D., Compston, W., Williams, I.S., 1991. A reconnaissance ion-probe study of hafnium isotopes in zircons. Geochimica Et Cosmochimica Acta, 55(3): 849-859.
Kinny, P.D., Friend, C.R.L., 1997. U-Pb isotopic evidence for the accretion of different crustal blocks to form the Lewisian Complex of northwest Scotland. Contributions to Mineralogy and Petrology, 129: 326-340.
Kinny, P.D., Friend, C.R.L., Love, G.J., 2005. Proposal for a terrane-based nomenclature for the Lewisian Gneiss Complex of NW Scotland. Journal of the Geological Society, 162: 175-186.
Kinny, P.D., Maas, R., 2003. Lu-Hf and Sm-Nd isotope systems in zircon. In: Hanchar, J.M., Hoskin, P.W.O. (Eds.), Zircon. Reviews in Mineralogy and Geochemistry.
Knudsen, T.L., Andersen, T., 1999. Petrology and geochemistry of the Tromoy gneiss complex, South Norway, an alleged example of Proterozoic depleted lower continental crust. Journal of Petrology, 40(6): 909-933.
Kooijman, E. et al., 2011. Response of the U–Pb chronometer and trace elements in zircon to ultrahigh-temperature metamorphism: The Kadavur anorthosite complex, southern India. Chemical Geology, 290(3-4): 177-188.
Korstgard, J., Ryan, B., Wardle, R., 1987. The boundary between Proterozoic and Archaean crustal blocks in central West Greenland and northern Labrador. In: Park, R.G., Tarney, J. (Eds.), Evolution of the Lewisian and Comparable Precambrian High Grade Terrains. Blackwell Scientific.

Kosler, J., Sylvester, P.J., 2003. Present Trends and the Future of Zircon in Geochronology: Laser Ablation ICPMS. In: Hanchar, J.M., Hoskin, P.W.O. (Eds.), Zircon. Reviews in Mineralogy and Geochemistry. Mineralogical Society of America and The Geochemical Society.

Krogh, T.E., 1982. Improved Accuracy of U-Pb Zircon Ages by the Creation of More Concordant Systems Using an Air Abrasion Technique. Geochimica Et Cosmochimica Acta, 46(4): 637-649.

Lee, J.K.W., Tromp, J., 1995. Self-Induced Fracture Generation in Zircon. Journal of Geophysical Research-Solid Earth, 100(B9): 17753-17770.

Lee, J.K.W., Williams, I.S., Ellis, D.J., 1997. Pb, U and Th diffusion in natural zircon. Nature, 390(6656): 159-162.

Lindsley, D.H., 1983. Pyroxene Thermometry. American Mineralogist, 68(5-6): 477-493.

Lloyd, G.E., Hall, M.G., 1981. Application of Scanning Electron-Microscopy to the Study of Deformed Rocks. Tectonophysics, 78(1-4): 687-698.

Love, G.J., Friend, C.R.L., Kinny, P.D., 2010. Palaeoproterozoic terrane assembly in the Lewisian Gneiss Complex on the Scottish mainland, south of Gruinard Bay: SHRIMP U-Pb zircon evidence. Precambrian Research, 183(1): 89-111.

Love, G.J., Kinny, P.D., Friend, C.R.L., 2004. Timing of magmatism and metamorphism in the Gruinard Bay area of the Lewisian Gneiss Complex: comparisons with the Assynt Terrane and implications for terrane accretion. Contributions to Mineralogy and Petrology, 146(5): 620-636.

Ludwig, K.R., 2003. User's manual for Isoplot 3.00: a geochronological toolkit for Excel. Special Publications, 4. Berkeley Geochronological Center.

Lyon, T.D.B., Pidgeon, R.T., Bowes, D.R., Hopgood, A.M., 1973. Geochronological investigation of the quartzofeldspathic rocks of the Lewisian of Rona, Inner Hebrides. Journal of the Geological Society, 129: 389-402.

Maas, R., Kinny, P.D., Williams, I.S., Froude, D.O., Compston, W., 1992. The Earths Oldest Known Crust - a Geochronological and Geochemical Study of 3900-4200 Ma Old Detrital Zircons from Mt Narryer and Jack Hills, Western-Australia. Geochimica Et Cosmochimica Acta, 56(3): 1281-1300.

Mariani, E., Mecklenburgh, J., Wheeler, J., Prior, D.J., Heidelbach, F., 2009. Microstructure evolution and recrystallization during creep of MgO single crystals. Acta Materialia, 57(6): 1886-1898.

Martin, H., 1994. The Archean Grey Gneisses and the Genesis of the Continental Crust. In: Condie, K. (Ed.), Archean Crustal Evolution. Developments in Precambrian Geology. Elsevier, Amsterdam.

Mason, A.J., 2012. Major early thrusting as a control on the Palaeoproterozoic evolution of the Lewisian Complex: evidence from the Outer Hebrides, NW Scotland. Journal of the Geological Society, 169(2): 201-212.

Mason, A.J., Parrish, R.R., Brewer, T.S., 2004. U-Pb geocbronology of Lewisian orthogneisses in the Outer Hebrides, Scotland: implications for the tectonic setting and correlation of the South Harris Complex. Journal of the Geological Society, 161: 45-54.

Mattinson, J.M., 2005. Zircon U-Pb chemical abrasion ("CA-TIMS") method: Combined annealing and multi-step partial dissolution analysis for improved precision and accuracy of zircon ages. Chemical Geology, 220(1-2): 47-66.

McDonough, W.F., Sun, S.s., 1995. The composition of the Earth. Chemical Geology, 120(3-4): 223-253.

Mezger, K., Krogstad, E.J., 1997. Interpretation of discordant U-Pb zircon ages: An evaluation. Journal of Metamorphic Geology, 15(1): 127-140.

Muir, R.J., Fitches, W.R., Maltman, A.J., Bentley, M.R., 1994. Precambrian rocks of the southern Inner Hebrides-Malin Sea region: Colonsay, west Islay, Inishtrahull and

Iona. In: Gibbons, W., Harris, A.L. (Eds.), A revised correlation of Precambrian rocks in the British Isles. Geological Society of London Special Report.
Murali, A.V., Parthasarathy, R., Mahadevan, T.M., Das, M.S., 1983. Trace-Elements Characteristics, Ree Patterns and Partition-Coefficients of Zircons from Different Geological Environments - a Case-Study on Indian Zircons. Geochimica Et Cosmochimica Acta, 47(11): 2047-2052.
Myers, J.S., 1971. The Late Laxfordian granite-migmatite complex of western Harris, Outer Hebrides. Scottish Journal of Geology, 7: 254-284.
Myers, J.S., 1987. The East Greenland Nagssugtoqidian mobile belt compared with the Lewisian complex. In: Park, R.G., Tarney, J. (Eds.), Evolution of the Lewisian and Comparable Precambrian High Grade Terrains. Blackwell Scientific.
Nasdala, L. et al., 2003. Spectroscopic Methods Apllied to Zircon. In: Hanchar, J.M., Hoskin, P.W.O. (Eds.), Zircon. Reviews in Mineralogy & Geochemistry. Mineralogical Society of America and The Geochemical Society.
Nutman, A.P., 2006. Comment on "Zircon thermometer reveals minimum melting conditions on earliest Earth" II. Science, 311(5762): 779.
O' Hara, M.J., Yarwood, G., 1978. High Pressure-Temperature Point on an Archaean Geotherm, Implied Magma Genesis by Crustal Anatexis, and Consequences for Garnet-Pyroxene Thermometry and Barometry. Philosophical Transactions of the Royal Society of London Series a-Mathematical Physical and Engineering Sciences, 288(1355): 441-453.
Okeke, P.O., Borley, G.D., Watson, J., 1983. A Geochemical Study of Lewisian Meta-Sedimentary Granulites and Gneisses in the Scourie-Laxford Area of the Northwest Scotland. Mineralogical Magazine, 47(342): 1-9.
Oxburgh, E.R., Turcotte, D.L., 1974. Thermal Gradients and Regional Metamorphism in Overthrust Terranes. Transactions-American Geophysical Union, 55(4): 442-442.
Pal, D.C., Chaudhuri, T., McFarlane, C., Mukherjee, A., Sarangi, A.K., 2011. Mineral Chemistry and In Situ Dating of Allanite, and Geochemistry of Its Host Rocks in the Bagjata Uranium Mine, Singhbhum Shear Zone, India-Implications for the Chemical Evolution of REE Mineralization and Mobilization. Economic Geology, 106(7): 1155-1171.
Park, R.G., 1970. Observations on Lewisian Chronology. Scottish Journal of Geology, 6(4): 379-399.
Park, R.G., 1973. The Laxfordian belts of the Scottish mainland. In: Park, R.G., Tarney, J. (Eds.), The Early Precambrian of Scotland and Related Rocks of Greenland. University of Keele.
Park, R.G., 1994. Early Proterozoic Tectonic Overview of the Northern British-Isles and Neighboring Terrains in Laurentia and Baltica. Precambrian Research, 68(1-2): 65-79.
Park, R.G., 2002. The Lewisian Geology of Gairloch, NW Scotland. Geological Society Memoirs, 26. The Geological Society, London, 80 pp.
Park, R.G., 2005. The Lewisian terrane model: a review. Scottish Journal of Geology, 41: 105-118.
Park, R.G., Cresswell, D., 1973. The dykes of the Laxfordian belts. In: Park, R.G., Tarney, J. (Eds.), The Early Precambrian of Scotland and Related Rocks of Greenland. University of Keele.
Park, R.G., Kinny, P.D., Friend, C.R.L., Love, G.J., 2005. Discussion on a terrane-based nomenclature for the Lewisian Gneiss complex of NW Scotland. Journal of the Geological Society, 162: 893-895.
Parrish, R.R., Noble, S.R., 2003. Zircon U-Th-Pb Geochronology by Isotope Dilution - Thermal Ionisation Mass Spectrometry (ID-TIMS). In: Hanchar, J.M., Hoskin, P.W.O. (Eds.),

Zircon. Reviews in Mineralogy and Geochemistry. Mineralogical Society of America and The Geochemical Society.
Patchett, P.J., 1983. Importance of the Lu-Hf Isotopic System in Studies of Planetary Chronology and Chemical Evolution. Geochimica Et Cosmochimica Acta, 47(1): 81-91.
Patchett, P.J., Kouvo, O., Hedge, C.E., Tatsumoto, M., 1981. Evolution of Continental-Crust and Mantle Heterogeneity - Evidence from Hf Isotopes. Contributions to Mineralogy and Petrology, 78(3): 279-297.
Patchett, P.J., Tatsumoto, M., 1980. Hafnium Isotope Variations in Oceanic Basalts. Geophysical Research Letters, 7(12): 1077-1080.
Peach, B.N., Horne, J., Gunn, W., Clough, C.T., Hinxman, L.W., 1907. The Geological Structure of the Northwest Highlands of Scotland. Memoirs of the Geological Survey. H.M.S.O., London.
Pidgeon, R.T., Bowes, D.R., 1972. Zircon U-Pb Ages of Granulites from Central Region of Lewisian, Northwest Scotland. Geological Magazine, 109: 247-258.
Potts, G.J., Hunter, R.H., Harris, A.L., Fraser, F.M., 1995. Late-Orogenic Extensional Tectonics at the NW Margin of the Caledonides in Scotland. Journal of the Geological Society, 152: 907-910.
Prior, D.J. et al., 1999. The application of electron backscatter diffraction and orientation contrast imaging in the SEM to textural problems in rocks. American Mineralogist, 84(11-12): 1741-1759.
Prior, D.J., Mariani, E., Wheeler, J., 2009. EBSD in the Earth Sciences: applications, common practice and challenges. In: Schwartz, A.J., Kumar, M., Adams, B.L., Field, D.P. (Eds.), Electron Backscatter Diffraction in Materials Science. Springer.
Ramsay, J.G., Graham, R.H., 1970. Strain Variation in Shear Belts. Canadian Journal of Earth Sciences, 7: 786-813.
Reddy, S.M. et al., 2006. Crystal-plastic deformation of zircon: A defect in the assumption of chemical robustness. Geology, 34(4): 257-260.
Rimsa, A., Whitehouse, N., Johansson, L., Piazolo, S., 2007. Brittle fracturing and fracture healing of zircon: An integrated cathodoluminescence, EBSD, U-Th-Pb, and REE study. American Mineralogist, 92(7): 1213-1224.
Rollinson, H., Gravestock, P., 2012. The trace element geochemistry of clinopyroxenes from pyroxenites in the Lewisian of NW Scotland: insights into light rare earth element mobility during granulite-facies metamorphism. Contributions to Mineralogy and Petrology, 163: 319-335.
Rollinson, H.R., 1979. Ilmenite-Magnetite Geothermometry in Trondhjemites from the Scourian Complex of Nw Scotland. Mineralogical Magazine, 43(325): 165-170.
Rollinson, H.R., Fowler, M.B., 1987. The magmatic evolution of the Scourian complex at Gruinard Bay. In: Park, R.G., Tarney, J. (Eds.), Evolution of the Lewisian and Comparable Precambrian High-Grade Terrains. Blackwells.
Rollinson, H.R., Windley, B.F., 1980. An Archean Granulite-Grade Tonalite-Trondhjemite-Granite Suite from Scourie, NW Scotland - Geochemistry and Origin. Contributions to Mineralogy and Petrology, 72(3): 265-281.
Rubatto, D., 2002. Zircon trace element geochemistry: partitioning with garnet and the link between U-Pb ages and metamorphism. Chemical Geology, 184(1-2): 123-138.
Rubatto, D., Hermann, J., 2006. Zircon/garnet trace element partitioning: A tool for P-T-time paths. Geochimica Et Cosmochimica Acta, 70(18): A542-A542.
Rubatto, D., Hermann, J., 2007. Zircon behaviour in deeply subducted rocks. Elements, 3(1): 31-35.
Rubatto, D., Williams, I.S., Buick, I.S., 2001. Zircon and monazite response to prograde metamorphism in the Reynolds Range, central Australia. Contributions to Mineralogy and Petrology, 140(4): 458-468.

Savage, D., Sills, J.D., 1980. High-Pressure Metamorphism in the Scourian of NW Scotland - Evidence from Garnet Granulites. Contributions to Mineralogy and Petrology, 74(2): 153-163.
Schaltegger, U. et al., 1999. Growth, annealing and recrystallization of zircon and preservation of monazite in high-grade metamorphism: conventional and in-situ U-Pb isotope, cathodoluminescence and microchemical evidence. Contributions to Mineralogy and Petrology, 134(2-3): 186-201.
Schreiber, H.D., Lauer, H.V., Thanyasiri, T., 1980. The Redox State of Cerium in Basaltic Magmas - an Experimental-Study of Iron-Cerium Interactions in Silicate Melts. Geochimica Et Cosmochimica Acta, 44(10): 1599-1612.
Schuiling, R.D., Kreulen, R., 1979. Are Thermal Domes Heated by CO2-Rich Fluids from the Mantle. Earth and Planetary Science Letters, 43(2): 298-302.
Sheraton, J.W., 1970. Origin of Lewisian Gneisses of Northwest Scotland, with Particular Reference to Drumbeg Area, Sutherland. Earth and Planetary Science Letters, 8: 301-310.
Sheraton, J.W., Skinner, A.C., Tarney, J., 1973a. The geochemistry of the Scourian gneisses of the Assynt district. In: Park, R.G., Tarney, J. (Eds.), The Early Precambrian of Scotland and Related Rocks of Greenland. University of Keele.
Sheraton, J.W., Tarney, J., Wheatley, T.J., Wright, A.E., 1973b. The structural history of the Assynt district. In: Park, R.G., Tarney, J. (Eds.), The Early Precambrian of Scotland and Related Rocks of Greenland. University of Keele.
Sills, J.D., Rollinson, H.R., 1987. Metamorphic evolution of the mainland Lewisian complex. In: Park, R.G., Tarney, J. (Eds.), Evolution of the Lewisian and Comparable Precambrian High-Grade Terrains. Blackwells.
Slama, J. et al., 2008. Plesovice zircon - A new natural reference material for U-Pb and Hf isotopic microanalysis. Chemical Geology, 249(1-2): 1-35.
Snyder, G.A., Taylor, L.A., Crozaz, G., 1993. Rare-Earth Element Selenochemistry of Immiscible Liquids and Zircon at Apollo-14 - an Ion Probe Study of Evolved Rocks on the Moon. Geochimica Et Cosmochimica Acta, 57(5): 1143-1149.
Stipp, M., Tullis, J., 2003. The recrystallized grain size piezometer for quartz. Geophysical Research Letters, 30: 2088-2093.
Streckeisen, A.L., 1974. Classification and Nomenclature of Plutonic Rocks: Recommendations of the IUGS Subcommission on the Systematics of Igneous Rocks. Geologische Rundschau, 63: 773-785.
Sutton, J., Watson, J., 1951. The pre-Torridonian metamorphic history of the Loch Torridon and Scourie areas in the North-West Highlands, and its bearing on the chronological classification of the Lewisian. Quarterly Journal of the Geological Society, 106: 241-296.
Tailby, N.D. et al., 2011. Ti site occupancy in zircon. Geochimica Et Cosmochimica Acta, 75(3): 905-921.
Tarney, J., 1973. The Scourie dyke suite and the nature of the Inverian event in Assynt. In: Park, R.G., Tarney, J. (Eds.), The Early Precambrian of Scotland and Related Rocks of Greenland. University of Keele.
Tarney, J., Weaver, B.L., 1987. Geochemistry of the Scourian Complex: petrogenesis and tectonic models. In: Park, R.G., Tarney, J. (Eds.), Evolution of the Lewisian and Comparable Precambrian High-Grade Terrains. Blackwells.
Taylor, R.J.M., Harley, S.L., Hinton, R.W., Elphick, S., 2007. Experimental determination of trace element partition coefficients between zircon, garnet and melt. Geochimica Et Cosmochimica Acta, 71(15): A1008-A1008.
Teall, J.J.H., 1885. Metamorphosis of dolerite into hornblende schist. Quarterly Journal of the Geological Society, 41: 133-145.

Timms, N.E., Kinny, P.D., Reddy, S.M., 2006a. Deformation-related modification of U and Th in zircon. Geochimica Et Cosmochimica Acta, 70(18): A651-A651.
Timms, N.E., Kinny, P.D., Reddy, S.M., 2006b. Enhanced diffusion of Uranium and Thorium linked to crystal plasticity in zircon. Geochemical Transactions, 7: 1-16.
Timms, N.E. et al., 2011. Relationship among titanium, rare earth elements, U-Pb ages and deformation microstructures in zircon: Implications for Ti-in-zircon thermometry. Chemical Geology, 280(1-2): 33-46.
Valley, J.W., 2003. Oxygen Isotopes in Zircon. In: Hanchar, J., Hoskin, P.W.O. (Eds.), Zircon. Reviews in Mineralogy and Geochemistry. Mineralogical Society of America and The Geochemical Society.
Vavra, G., 1993. A Guide to Quantitative Morphology of Accessory Zircon. Chemical Geology, 110(1-3): 15-28.
Vavra, G., Gebauer, D., Schmid, R., Compston, W., 1996. Multiple zircon growth and recrystallization during polyphase Late Carboniferous to Triassic metamorphism in granulites of the Ivrea Zone (Southern Alps): An ion microprobe (SHRIMP) study. Contributions to Mineralogy and Petrology, 122(4): 337-358.
Waters, F.G., Cohen, A.S., Onions, R.K., Ohara, M.J., 1990. Development of Archean Lithosphere Deduced from Chronology and Isotope Chemistry of Scourie Dykes. Earth and Planetary Science Letters, 97(3-4): 241-255.
Watkins, J.M., Clemens, J.D., Treloar, P.J., 2007. Archaean TTGs as sources of younger granitic magmas: melting of sodic metatonalites at 0.6-1.2 GPa. Contributions to Mineralogy and Petrology, 154(1): 91-110.
Watson, E.B., Harrison, T.M., 2005. Zircon thermometer reveals minimum melting conditions on earliest Earth. Science, 308(5723): 841-844.
Watson, E.B., Harrison, T.M., 2006. Response to comments on "Zircon thermometer reveals minimum melting conditions on earliest Earth". Science, 311(5762): 779.
Watson, E.B., Wark, D.A., Thomas, J.B., 2006. Crystallization thermometers for zircon and rutile. Contributions to Mineralogy and Petrology, 151(4): 413-433.
Wells, P.R.A., 1977. Pyroxene Thermometry in Simple and Complex Systems. Contributions to Mineralogy and Petrology, 62(2): 129-139.
Westbrook, G.K., 1972a. Structure and metamorphism of the Lewisian of east Tiree, Inner Hebrides. Scottish Journal of Geology, 8(1): 13-30.
Westbrook, G.K., 1972b. Structure and metamorphism of the Lewisian of east Tiree, Inner Hebrides. Scottish Journal of Geology, 8: 13-30.
Wheeler, J., 2007. A major high-strain zone in the Lewisian Complex in the Loch Torridon area, NW Scotland: insights into deep crustal deformation. In: Ries, A.C., Butler, R.W.H., Graham, R.H. (Eds.), Deformation of the Continental Crust: The Legacy of Mike Coward. The Geological Society Publishing House.
Wheeler, J. et al., 2009. The weighted Burgers vector: a new quantity for constraining dislocation densities and types using electron backscatter diffraction on 2D sections through crystalline materials. Journal of Microscopy, 233(3): 482-494.
Wheeler, J., Park, R.G., Rollinson, H.R., Beach, A., 2010. The Lewisian Complex: Insights into Deep Crustal Evolution. In: Law, R.D., Butler, R.W.H., Holdsworth, R.E., Krabbendam, M., Strachan, R.A. (Eds.), Continental Tectonics and Mountain Building. The Geological Society Publishing House.
Wheeler, J., Windley, B.F., Davies, F.B., 1987. Internal evolution of the major Precambrian shear belt at Torridon, NW Scotland. In: Park, R.G., Tarney, J. (Eds.), Evolution of the Lewisian and Comparable Precambrian High-Grade Terrains. Blackwells.
Whitehouse, M., Kemp, A.I.S., 2010. On the difficulty of assigning crustal residence, magmatic protolith and metamorphic ages to Lewisian granulites: constraints from combined in-situ U-Pb and Lu-Hf isotopes. In: Law, R.D., Butler, R.W.H., Holdsworth, R.E., Krabbendam, M., Strachan, R.A. (Eds.), Continental Tectonics and Mountain

Building: The Legacy of Peach and Horne. Special Publications. The Geological Society Publishing House.
Whitehouse, M.J., 1989. Sm-Nd Evidence for Diachronous Crustal Accretion in the Lewisian Complex of Northwest Scotland. Tectonophysics, 161(3-4): 245-256.
Whitehouse, M.J., 1993. Age of the Corodale Gneisses, South Uist. Scottish Journal of Geology, 29(1): 1-7.
Whitehouse, M.J., Bridgwater, D., 2001. Geochronological constraints on Paleoproterozoic crustal evolution and regional correlations of the northern Outer Hebridean Lewisian complex, Scotland. Precambrian Research, 105(2-4): 227-245.
Whitehouse, M.J., Bridgwater, D., Park, R.G., 1997a. Detrital zircons from the Loch Maree Group, Lewisian Complex, NW Scotland and their significance for Palaeoproterozoic Laurentia-Baltica. Terra Nova, 9: 260-263.
Whitehouse, M.J., Claesson, S., Sunde, T., Vestin, J., 1997b. Ion microprobe U-Pb zircon geochronology and correlation of Archaean gneisses from the Lewisian Complex of Gruinard Bay, northwestern Scotland. Geochimica Et Cosmochimica Acta, 61(20): 4429-4438.
Whitehouse, M.J., Fowler, M.B., Friend, C.R.L., 1996. Conflicting mineral and whole-rock isochron ages from the Late-Archaean Lewisian Complex of northwestern Scotland: Implications for geochronology in polymetamorphic high-grade terrains. Geochimica Et Cosmochimica Acta, 60(16): 3085-3102.
Whitehouse, M.J., Kamber, B.S., 2003. A rare earth element study of complex zircons from early Archaean Amitsoq gneisses, Godthabsfjord, south-west Greenland. Precambrian Research, 126(3-4): 363-377.
Whitehouse, M.J., Platt, J.P., 2003. Dating high-grade metamorphism - constraints from rare-earth elements in zircon and garnet. Contributions to Mineralogy and Petrology, 145(1): 61-74.
Whitehouse, M.J., Robertson, C.J., 1995. Isotopic evolution of the Lewisian Complex of Tiree, Inner Hebrides and correlation with the mainland. Scottish Journal of Geology, 31(2): 131-137.
Whitehouse, M.J., Russell, J., 1997. Isotope systematics of Precambrian marbles from the Lewisian complex of northwest Scotland: implications for Pb---Pb dating of metamorphosed carbonates. Chemical Geology, 136(3-4): 295-307.
Wiedenbeck, M. et al., 1995. Three natural zircon standards for U-Th-Pb, Lu-Hf, trace element and REE analyses. Geostandards Newsletter, 19(1): 1-23.
Williams, I.S., 1992. Some observations on the use of zircon U-Pb geochronology in the study of granitic rocks. Transactions of the Royal Society of Edinburgh: Earth Sciences, 83(1-2): 447-458.
Windley, B., Bridgwater, D., 1971. The evolution of Archaean low- and high-grade terrains, Special Publication. Geological Society of Australia, pp. 33-46.
Wood, B.J., Banno, S., 1973. Garnet-Orthopyroxene and Orthopyroxene-Clinopyroxene Relationships in Simple and Complex Systems. Contributions to Mineralogy and Petrology, 42(2): 109-124.
Wright, A.E., Tarney, J., Palmer, K.F., Moorlock, B.S.P., Skinner, A.C., 1973. The Geology of the Angmagssalik Area, East Greenland and possible relationships with the Lewisian of Scotland. In: Park, R.G., Tarney, J. (Eds.), The Early Precambrian of Scotland and Related Rocks of Greenland. University of Keele.
Wynn, T.J., 1995. Deformation in the mid to lower continental crust: analogues from Proterozoi shear zones in NW Scotland. In: Coward, M.P., Ries, A.C. (Eds.), Early Precambrian Processes. The Geological Society Publishing House.
Xiong, X.-L., 2006. Trace element evidence for growth of early continental crust by melting of rutile-bearing hydrous eclogite. Geology, 34(11): 945-948.

Xiong, X.L., Adam, J., Green, T.H., 2005. Rutile stability and rutile/melt HFSE partitioning during partial melting of hydrous basalt: Implications for TTG genesis. Chemical Geology, 218(3–4): 339-359.

Zhu, X.K., ONions, R.K., Belshaw, N.S., Gibb, A.J., 1997. Lewisian crustal history from in situ SIMS mineral chronometry and related metamorphic textures. Chemical Geology, 136(3-4): 205-218.

Zirkler, A., Johnson, T.E., White, R.W., Zack, T., 2012. Polymetamorphism in the mainland Lewisian complex, NW Scotland - phase equilibria and geochronological constraints from the Cnoc an t'Sidhean suite. Journal of Metamorphic Geology, 30(8): 865-885.